

# Hydrogen Effects in Austenitic Stainless Steel Microstructures validated by ToF-SIMS and EBSD

## Dissertation

Zur Erlangung des akademischen Grades

**Doktoringenieur**

**(Dr.-Ing.)**

von Dipl.-Ing. Andreas Röhler  
geboren am 13. Mai 1988 in Görlitz  
genehmigt durch die Fakultät für Maschinenbau  
der Otto-von-Guericke-Universität Magdeburg

Gutachter:

Hon.-Prof. Dr.-Ing. habil. Thomas Böllinghaus

Prof. Dr. Hannu Hänninen

Dr.-Ing. Oded Sobol

Promotionskolloquium am 13. Juli 2021

*...C'est pourquoi aussi jamais des mesures pourront confirmer ni infirmer directement une hypothèse; elles pourront seulement en faire ressortir la convenance plus ou moins grande.*

Max Planck



## Abstract

Hydrogen-assisted cracking (HAC) of iron alloys are a long known, yet not fully understood phenomenon. However, it is of great relevance for a multitude of different industries and has been investigated for decades. One reason for this is the dependency of our economy on fossil energy carriers, i.e. carbohydrates, such as oil and gas. Hydrogen-assisted damages frequently occur along the whole value-added chain: During production of the raw material, processing and manufacturing of components and life time. One example for this is the cathodic corrosion protection of pipelines. Locally, high concentrations of hydrogen might develop, enter the material and damage it. Hydrogen-assisted damages are a risk not to be underestimated, not only in the field of fossil fuels, but in the chemical industry and increasingly in the renewable energy sector.

The degradation of the mechanical properties of steels is commonly and, imprecise, called *hydrogen embrittlement*. It mainly effects toughness and ductility and less the mechanical strength. For hydrogen-assisted cracking occurs always as an interaction of the influencing factors *material* (microstructure etc.), *hydrogen concentration* and *mechanical load*, these must be considered in the assessment of HAC.

The present study aims to make a contribution to a better understanding of hydrogen related damages and transport phenomena in an often neglected group of metallic materials, i.e. high alloyed austenitic stainless steels, which often are regarded as "resistant" against hydrogen-assisted cracking. To gain a closer insight into hydrogen-assisted damages and failures of components made of such materials, the austenitic stainless steels AISI 304L (EN 1.4307) and AISI 316L (EN 1.4404) were charged with the hydrogen isotope deuterium and subsequently analysed by scanning electron microscopy (SEM), electron backscatter diffraction (EBSD) and time-of-flight secondary ion mass spectrometry (ToF-SIMS).

The SEM investigations proved intergranular (grain boundary cracks) and transgranular crack formation (along slip bands and twins). The analyses of the structure before and after electrochemical charging displayed the partial transformation of the austenitic base material into hexagonal  $\epsilon$ - and body-centred cubic(BCC)  $\alpha'$ -martensite. This can be attributed to the impact of deuterium.

The localisation of deuterium in the sample's microstructure was realised by ToF-SIMS. In connection with EBSD information, deuterium was shown to be situated both in the austenite and in newly-formed martensite. This can indicate both a solution of deuterium within the supersaturated BCT lattice and trapping of deuterium by dislocations and other lattice defects that formed during martensite formation. As already shown previously, it further shows that deuterium (and thus hydrogen) can initiate such phase transformations in the investigated materials and by that also might initiate cracking.

A self-developed sample holder enabled the *in-situ* analysis of the behaviour of deuterium by ToF-SIMS during simultaneous external mechanical load. The stress-induced motion of deuterium towards the direction of highest (tensile) stress could be observed in both materials by that. This is providing some indication for the so-called *Gorsky effect*.

## Kurzbeschreibung

Wasserstoffunterstützter Schäden von Eisenlegierungen sind ein lange bekanntes, obgleich noch immer nicht vollständig durchdrungenes Phänomen. Es ist jedoch von großer Relevanz für eine Vielzahl unterschiedlicher Industriezweige und wird daher seit Jahrzehnten stark beforscht. Ein Grund hierfür liegt in der Abhängigkeit unserer Wirtschaft von fossilen Energieträgern, also Kohlenwasserstoffen, wie Erdöl und Erdgas. Entlang der gesamten Wertschöpfungskette kommt es immer wieder zu wasserstoffunterstützten Materialschäden. Der kathodische Korrosionsschutz von Pipelines ist ein typisches Beispiel hierfür. Dabei können lokal hohe Konzentrationen von Wasserstoff entstehen, in das Material eindringen und dieses schädigen. Doch nicht nur im Gebiet fossiler Energieträger, sondern auch in der chemischen Industrie und in zunehmendem Maße im Bereich erneuerbarer Energieträger, sind wasserstoffinduzierte Schäden eine nicht zu unterschätzende Gefahr.

Die Degradation der mechanischen Eigenschaften von Stahl, umgangssprachlich *Wasserstoffversprödung*, wirkt sich dabei vor allem negativ auf Festigkeit, Zähigkeit und Duktilität aus. Da es sich hierbei stets um ein Zwischenspiel verschiedener Gegebenheiten, wie Material (Mikrostruktur etc.), Wasserstoffkonzentration und mechanischer Beanspruchung handelt, müssen diese Faktoren für die Beurteilung wasserstoffunterstützter Schäden berücksichtigt werden.

Die vorliegende Arbeit soll einen Beitrag leisten, um derlei Schäden besser zu verstehen. Dafür wurden die hochlegierten austenitischen Stähle AISI 304L (EN 1.4307) und AISI 316L (EN 1.4404) mit dem Wasserstoffisotop Deuterium beladen und anschließend mittels Rasterelektronenmikroskopie (REM), Rückstreulektronenbeugung (EBSD), und Sekundärionenmassenspektrometrie (ToF-SIMS) untersucht.

REM-Untersuchungen wiesen interkristalline und transkristalline Rissbildung (an Gleitbändern und Zwillingen) nach. Analysen der Gitterstruktur vor und nach der elektrochemischen Beladung legten die teilweise Umwandlung des austenitischen Ausgangsmaterials in hexagonalen  $\epsilon$ - und kubisch raumzentrierten (krz)  $\alpha'$ -Martensit an den Tag. Dies konnte auf die Wirkung des Deuteriums zurückgeführt werden.

Die genaue Lokalisierung von Deuterium innerhalb der Mikrostruktur der Proben wurde mit ToF-SIMS realisiert. In Verbindung mit EBSD Untersuchungen konnte gezeigt werden, dass Deuterium sowohl im Austenit, als auch im neugebildeten Martensit vorliegt. Dies kann einerseits auf eine Zwangslösung im übersättigten krz Gitter des Martensits und andererseits auf *trapping* an Versetzungen und anderen Gitterdefekten hindeuten, die während der Martensitbildung entstanden.

Ein selbstentwickelter Probenhalter ermöglichte des Weiteren die *in-situ* Analyse des Deuteriumverhaltens im ToF-SIMS bei gleichzeitiger äußerer mechanischer Biegelast. Somit konnte in beiden Werkstoffen eine spannungsinduzierte Bewegung des Deuteriums in Richtung der höchsten (Zug-)Spannung beobachtet werden. Dies ist ein Indiz für den sogenannten *Gorsky Effekt*.

# Table of contents

<b>1. Introduction</b>	<b>1</b>
<b>2. Hydrogen-assisted failure cases</b>	<b>4</b>
<b>3. State of knowledge</b>	<b>6</b>
3.1. Metastable austenitic steels . . . . .	6
3.1.1. Phase stability . . . . .	6
3.1.2. Classification . . . . .	11
3.1.3. Hardening behaviour in metastable steels . . . . .	12
3.1.3.1. Underlying processes . . . . .	14
3.1.3.2. Influencing factors on the strain-hardening behaviour . . . . .	18
3.1.4. Applications . . . . .	24
3.2. Fundamentals of hydrogen-assisted damage . . . . .	25
3.2.1. Sources of hydrogen and its uptake . . . . .	25
3.2.2. Transport of hydrogen . . . . .	27
3.2.2.1. Diffusion-assisted transport . . . . .	27
3.2.2.2. Dislocation-assisted transport . . . . .	28
3.2.3. Trapping . . . . .	30
3.2.4. Effects of hydrogen on steels . . . . .	31
3.2.4.1. Degradation of mechanical properties . . . . .	32
3.2.4.2. Loss of surface integrity . . . . .	34
3.2.5. Mechanisms of hydrogen-assisted damage . . . . .	35
3.2.5.1. Hydrogen-Enhanced Localised Plasticity - HELP . . . . .	35
3.2.5.2. Hydrogen-Enhanced Decohesion - HEDE . . . . .	36
3.2.5.3. Adsorption-Induced Dislocation Emission - AIDE . . . . .	36
3.2.5.4. Phase transformations . . . . .	38
3.3. Approaches to evaluate hydrogen-assisted damage . . . . .	38
3.3.1. Mechanical characterisation . . . . .	38
3.3.2. Microscopic analyses . . . . .	39
3.3.3. Hydrogen mapping techniques . . . . .	41
3.3.3.1. Secondary ion mass spectrometry . . . . .	41
3.3.4. Quantitative examination methods . . . . .	48
<b>4. Objectives of the present investigations</b>	<b>49</b>
<b>5. Experimental</b>	<b>50</b>
5.1. Materials and sample preparation . . . . .	50
5.1.1. Alloys . . . . .	50
5.1.2. Sample preparation . . . . .	52
5.1.3. Electrochemical charging . . . . .	54

5.2. Scanning electron microscopy . . . . .	55
5.3. Electron backscatter diffraction . . . . .	55
5.4. Time-of-flight secondary ion mass spectrometry . . . . .	57
5.5. Combination of four-point-bending test and ToF-SIMS . . . . .	58
5.6. Data treatment . . . . .	61
5.7. Determination of the hydrogen content . . . . .	61
<b>6. Results and discussion</b>	<b>65</b>
6.1. Experimental challenges and drawbacks . . . . .	65
6.1.1. Influence of recombination poison on the surface and the deuterium uptake	65
6.1.2. Sputter-induced artefacts . . . . .	66
6.2. Systematic analyses of sputter-induced martensite formation . . . . .	68
6.3. Ex-situ experiments . . . . .	76
6.3.1. Deuterium-induced (micro-)structural changes . . . . .	76
6.3.2. Distribution of deuterium . . . . .	78
6.4. In-situ experiments . . . . .	81
6.4.1. Deuterium-induced cracking of the surface . . . . .	81
6.4.2. Deuterium-induced phase transformation . . . . .	84
6.4.3. Accumulation of hydrogen at grain boundaries . . . . .	108
6.4.4. Accumulation of deuterium at interfaces and sputter-induced martensite .	110
6.4.5. Distribution of deuterium in the material . . . . .	115
6.4.6. Behaviour of deuterium during mechanical load . . . . .	120
<b>7. Conclusions</b>	<b>130</b>
<b>8. Perspectives</b>	<b>133</b>
<b>A. Appendix</b>	<b>i</b>
A.1. Results of the sputter tests . . . . .	i
A.2. SEM micrographs . . . . .	xiii
A.3. EBSD results . . . . .	xvii
A.4. ToF-SIMS results . . . . .	xxvi
<b>B. List of Figures</b>	<b>xl</b>
<b>C. List of Tables</b>	<b>xli</b>

# List of Symbols and abbreviations

## Abbreviations, Acronyms

<b>4PB</b>	<b>f</b> our- <b>p</b> oint- <b>b</b> ending test
<b>AIDE</b>	<b>a</b> bsorption- <b>i</b> nduced <b>d</b> islocation <b>e</b> mission
<b>AISI</b>	<b>A</b> merican <b>I</b> ron and <b>S</b> teel <b>I</b> nstitute
<b>AMT</b>	<b>a</b> thermal <b>m</b> artensite <b>t</b> ransformation
<b>ASS</b>	<b>a</b> ustenitic stainless steel
<b>BAM</b>	<b>B</b> undesanstalt für <b>M</b> aterialforschung und -prüfung
<b>BCC</b>	<b>b</b> ody- <b>c</b> entred <b>c</b> ubic
<b>BCT</b>	<b>b</b> ody- <b>c</b> entred <b>t</b> etragonal
<b>BKDP</b>	<b>b</b> ackscatter <b>K</b> ikuchi <b>d</b> iffraction <b>p</b> attern
<b>EBS</b>	<b>e</b> lectron <b>b</b> ackscatter <b>d</b> iffraction
<b>DIM</b>	<b>d</b> eformation- <b>i</b> nduced <b>m</b> artensite
<b>DIMT</b>	<b>d</b> eformation- <b>i</b> nduced <b>m</b> artensitic <b>t</b> ransformation
<b>FCC</b>	<b>f</b> ace- <b>c</b> entred <b>c</b> ubic
<b>FIB</b>	<b>f</b> ocused ion <b>b</b> eam
<b>HE</b>	<b>h</b> ydrogen <b>e</b> mbrittlement
<b>HELP</b>	<b>h</b> ydrogen- <b>e</b> nhanced localised <b>p</b> lasticity
<b>HEDE</b>	<b>h</b> ydrogen- <b>e</b> nhanced <b>d</b> ecoherence
<b>HCP</b>	<b>h</b> exagonal close <b>p</b> acked
<b>LMIG</b>	<b>l</b> iquid <b>m</b> etal ion <b>g</b> un
$M_d$	<b>d</b> eformation- <b>i</b> nduced <b>m</b> artensite start temperature
$M_{d30}$	temperature at which 50% of the original austenite transforms into martensite after a plastic deformation of 30%.
$M_S$	<b>m</b> artensite <b>s</b> tart temperature
<b>OES</b>	<b>o</b> ptical <b>e</b> mission <b>s</b> pectrometry
<b>PTFE</b>	<b>p</b> olytetrafluoroethylene

<b>ROI</b>	region of interest
<b>SB</b>	slip band
<b>SEM</b>	scanning electron microscopy
<b>SF</b>	stacking fault
<b>SFE</b>	stacking fault energy
<b>TEM</b>	transmission electron microscopy
<b>ToF-SIMS</b>	time-of-flight secondary ion mass spectrometry
<b>TRIP</b>	transformation-induced plasticity
<b>TWIP</b>	twinning-induced plasticity
<b>XRD</b>	X-ray diffraction

### Symbols

$\alpha$	linear coefficient of thermal expansion
$\alpha'$	BCC/BCT martensite
$\delta$	BCC ferrite
$\epsilon$	HCP martensite/ densely packed stacking faults
$\gamma$	FCC austenite
$\gamma_{SFE}$	stacking fault energy
<b>G</b>	Gibb's free energy
$\Delta G_{chem}$	chemical driving force for martensite formation
$W_{mech}$	mechanical work as additional driving force for martensite formation

### Units

$\mu\text{m}$	micrometer ( $10^{-6}\text{m}$ )
<b>nm</b>	nanometer ( $10^{-9}\text{m}$ )
<b>R</b>	ideal gas constant $R=8.315\text{ J/mol}\cdot\text{K}$
<b>ppm</b>	parts per million

## 1. Introduction

*On some remarkable changes produced in iron and steel by the action of hydrogen and acids* is the title of perhaps the very first systematic investigations of the influence of hydrogen on metals published in 1874 [1]. This ground breaking work by William Johnson pioneered numberless studies on what is commonly called *hydrogen embrittlement* (HE). Correctly, this phenomena describes the degradation of the mechanical properties of metals. This includes the decrease of mechanical strength and ductility as well as toughness and fatigue strength. This is a problem of crucial importance since metallic alloys, and here especially steels, are commonly used as structural elements for a variety of industrial applications where they encounter aggressive hydrogen-containing media. Typical examples where (highly alloyed) steels are used are the chemical and petrochemical sector, but also marine and offshore industry.

Hydrogen-assisted damages and the assessment of the life expectancy of parts and components used in these "conventional" applications have been the focus of materials research for many years. Only during the last two decades, other technologies such as fuel cells and power-to-gas dragged some attention of the hydrogen community. The safe and efficient production, storage and transportation of hydrogen as energy carrier made research on the compatibility of e.g. austenitic stainless steels with liquid and gaseous hydrogen inevitable.

These technologies received a boost when, recently, global warming was acknowledged by the international community. Although researchers already warned against climate change in the 1970s, only the "special report on the impacts of global warming of 1.5°C above pre-industrial levels", published by the Intergovernmental Panel on Climate Change (IPCC) together with massive civic engagement, brought this topic back to the agendas of policy-makers [2, 3].

Man-made global warming ultimately causes extinction of species, desertification, poverty and migration and its ramifications will affect mankind as a whole. Taking action to reduce emissions of greenhouse gases in sectors such as energy production, transportation, mobility and industry are now more important than ever. Among other measures, the transition towards renewable energy sources like wind and solar power is necessary and inevitable to mitigate the emission of greenhouse gases. However, these technologies face us with the problem of storing the generated electricity. Converting electrical energy into chemical energy through the formation of hydrogen and methane, is a suitable way for this purpose. These gases can be stored, transported and used to re-generate electrical energy. Establishing a reliable infrastructure for this power-to-gas grid requires further investigation in every aspect of the chain, from conversion efficiency to safety of components such as pipelines exposed to high concentrations of hydrogen. This is necessary because the suitability of materials used for this hydrogen-infrastructure is still not fully clarified [4]. Moreover, hydrogen-induced degradation of such components can cause high economic and environmental costs.

Some parts of this grid can be manufactured from the austenitic stainless steel grades AISI 304 and 316, respectively. Figure 1.1 shows for instance an element of a hydrogen fuel station built by *Linde GmbH* in cooperation with *H2 Mobility Deutschland GmbH & Co. KG*. Gaseous hydrogen is stored underground in large vessels at about 300 bar. From this vessels it gets to

the compressor unit shown in the picture. The compressor increases the pressure up to 860 bar; a process accompanied by a temperature rise. That is why most of the tubes are cooled from outside (visible by the blue jackets). All of the pipes into and out from the compressor and in addition to that other parts such as filters and valves, are made from the austenitic steel grade 316. Compressed hydrogen is distributed from the compressor to the dispenser.

High alternating pressures and varying temperatures apply a fatigue load on the material. In addition to that ingress and accumulation of hydrogen makes the steel prone to hydrogen-assisted cracking (HAC) and the reduction of its life time. Targeted research on the influence of hydrogen on this steel grade is therefore essential.



Figure 1.1: *Hydrogen compressor unit as part of a hydrogen fuel station engineered by Linde GmbH and run by H2 Mobility Deutschland GmbH & Co. KG [5]. Hydrogen is compressed up to 860 bar and pumped to the dispenser. All the piping is manufactured from austenitic stainless steel AISI 316.*



The present study aims on providing new information on the behaviour of the austenitic stainless steel grades AISI 304L and 316L under the influence of hydrogen. For this reason, Chapter 3.1 introduces the family of austenitic stainless steels and their remarkable ability to change their crystal structure when subjected to mechanical load.

Chapter 3.2 focuses on hydrogen-assisted damages on (austenitic stainless) steels and presents the main theories behind the mechanisms that govern the deteriorative impact hydrogen can inflict on steels. As part of this chapter, possible sources of hydrogen into the material and its interaction with the lattice are presented as well.

As hydrogen is the smallest chemical element of the universe and might affect steels in various ways, a large toolbox of analytical methods and experimental approaches was developed. Section 3.3 gives a brief overview of different methods used to evaluate hydrogen-assisted damages.

Chapter 4 draws conclusions from the state of the art of hydrogen research and the properties and behaviour of austenitic stainless steels subjected to hydrogen. The aims of the present study are introduced there.

Chapter 5, the experimental part, describes the investigated alloys, the applied methods and the experimental procedures within the framework of the present study. Analytical methods to identify structural and microstructural changes of the investigated alloys that result from the introduction of the hydrogen isotope deuterium are done by scanning electron microscopy (SEM) and electron backscatter diffraction (EBSD). These are combined with a technique that is able to map its distribution in the sub-micron scale, time-of-flight secondary ion mass spectrometry (ToF-SIMS). Subsequent principal component analysis (PCA) and data fusion allows to draw conclusion towards the behaviour of both the material and deuterium located inside of it.

The results generated in this way are presented and interpreted in the following section, Chapter 6. They are divided into *ex-situ* and *in-situ* experiments, according the sample geometry and treatment used. Main objectives are the identification of (I.) structural and (II.) microstructural changes of the investigated materials, (III.) the identification of deuterium accumulation sites inside the metal lattice and (IV.) the validation of a sample holder that should enable to investigate the re-distribution of deuterium due to the application of external mechanical load. This sample holder was developed within the scope of the doctoral thesis by O. Sobol [6]. Chapter 6 addresses and evaluates the difficulties and drawbacks arisen during the progression of the study, as well.

Chapter 7 summarises the insights of the present work and tries to set them in context with results from the literature. Chapter 8 gives perspectives of possible further research that can follow recent findings. Proposals for the improvement of the present experimental approach are given. It outlines additional experiments to answer newly raised questions as well.

## 2. Hydrogen-assisted failure cases

For the EXPO 2005 in Nagoya, Japan, the *Japan Hydrogen & Fuel Cell Demonstration Project* established and operated refuelling stations to provide hydrogen for the operating fleet of fuel cell buses. Undoubtedly, Japan was and still is on a leading position in hydrogen research and use alike. That is why, this project was also carried out at that time to prove the feasibility and reliability of Japanese hydrogen technologies.

However, after refuelling 280 buses a leakage occurred in a dispenser made from the austenitic stainless steel AISI 316L (EN 1.4404). Murakami *et al.* investigated this failure case and found that the damage arose from fatigue fracture. The predominant stress amplitude was higher than expected, causing the fatigue crack growth rate in the material also to be much faster than predicted, culminating in this premature failure [7].

In the case of the broken dispenser serious harm to people and huge economic costs did not occur. Yet, Woodtli and Kieselbach reported of the collapse of a hydrogen storage tank, generating an insurance loss of about 50 million dollar [8]. Analyses of this failure case revealed that large fatigue cracks, induced by hydrogen and high pressure, caused the vessel explosion. An impression of the destructive forces unleashed gives Figure 2.1.



Figure 2.1: *The explosion of a hydrogen storage tank destroyed big parts of a factory, causing immense economic costs [8].*

Failure cases connected to hydrogen do not only occur in hydrogen-related industries: Djukic *et al.* [9] described the breakdown of a boiler evaporator tube inside a fossil fuel power plant. After 73000 h of operation, the wall of an evaporator, made from plain carbon steel, was severely damaged when heating to 350°C with a pressure of 15.5 MPa. This is shown in Figure 2.2.

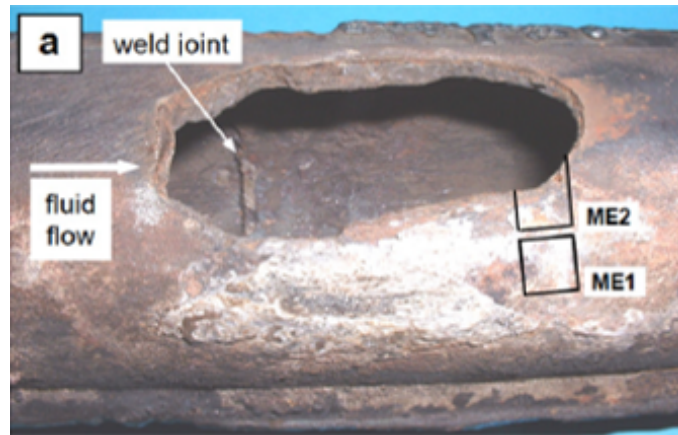


Figure 2.2: *Failure of a boiler tube as part of a power plant, investigated by Djukic et al. [9].*

The authors claim that the damage was caused by a combination of factors of which the localised enrichment with hydrogen was a part of. During service, hydrogen-induced corrosion simultaneously appeared with high temperature hydrogen attack.

### 3. State of knowledge

#### 3.1. Metastable austenitic steels

Steels are metallic materials with iron as their main alloying element and an amount of carbon of not more than 2:06 wt.-%. This fraction is given by a line in the iron-carbon diagram (Fe-C-diagram) that is shown in Figure 3.1. This diagram shows furthermore the structural composition of the steel in dependence of temperature and carbon content. As it can be seen, only at a temperature above 723°C (P-K-line) the face-centred cubic austenite exists. Below this temperature, only body-centred cubic ferrite, pearlite and cementite prevail.

##### 3.1.1. Phase stability

The structural constitution of metastable austenitic steels deviates from that of low-alloyed BCC steels have. Because of the high amounts of alloying elements like manganese, nickel, this steel grade consists even at room temperature of an austenitic fraction [11]. The influence of important alloying elements on the phase composition is shown in Table 3.1.

Table 3.1: *Influence of alloying elements on the phase stability [10].*

effect	element
FCC stabilising	Ni, Mn, Co, C, N, Cu, Zn, H
BCC stabilising	Al, Cr, W, P, Ti, Nb, Ta, V

Elements, like nitrogen or carbon, whose atomic radius is smaller than that of iron occupy *interstitial* sites within the host lattice. Despite of a higher packing density, the FCC phase offers more space for interstitial alloying elements than the BCC phase. Like the Fe-C-diagram in Figure 3.1 for the steel side shows, the high temperature austenite decomposes at 723°C into ferrite, pearlite and Fe<sub>3</sub>C cementite with almost no carbon in the ferrite at room temperature. The maximum solubility for carbon in the  $\alpha$ -iron amounts to only 0.025% at 723°C. Interstitial alloying elements stabilise the austenite phase and lead to solid solution strengthening. This, apart from its several negative effects on steel, holds true for hydrogen as well [12].

*Substitutional* alloying elements, like nickel and manganese replace iron atoms from its lattice sites. It is commonly assumed that they enhance the austenite stability because of their similar crystal structure: FCC alloying elements stabilise the FCC phase in steel [13].

Both interstitial and substitutional alloying elements alter entropy, enthalpy and free energy of the system.

In the following, the influence of the most important alloying elements in metastable steels shall be discussed more in detail.

**Carbon:** Carbon is the most important single alloying element in steels [14]. As an interstitial alloying element, it occupies the octahedral lattice sites and leads to solid-solution hardening of the material. Like other interstitials, it increases the FCC stability. Additionally, studies show that it decreases the so-called *stacking fault energy* SFE which describes the deformation

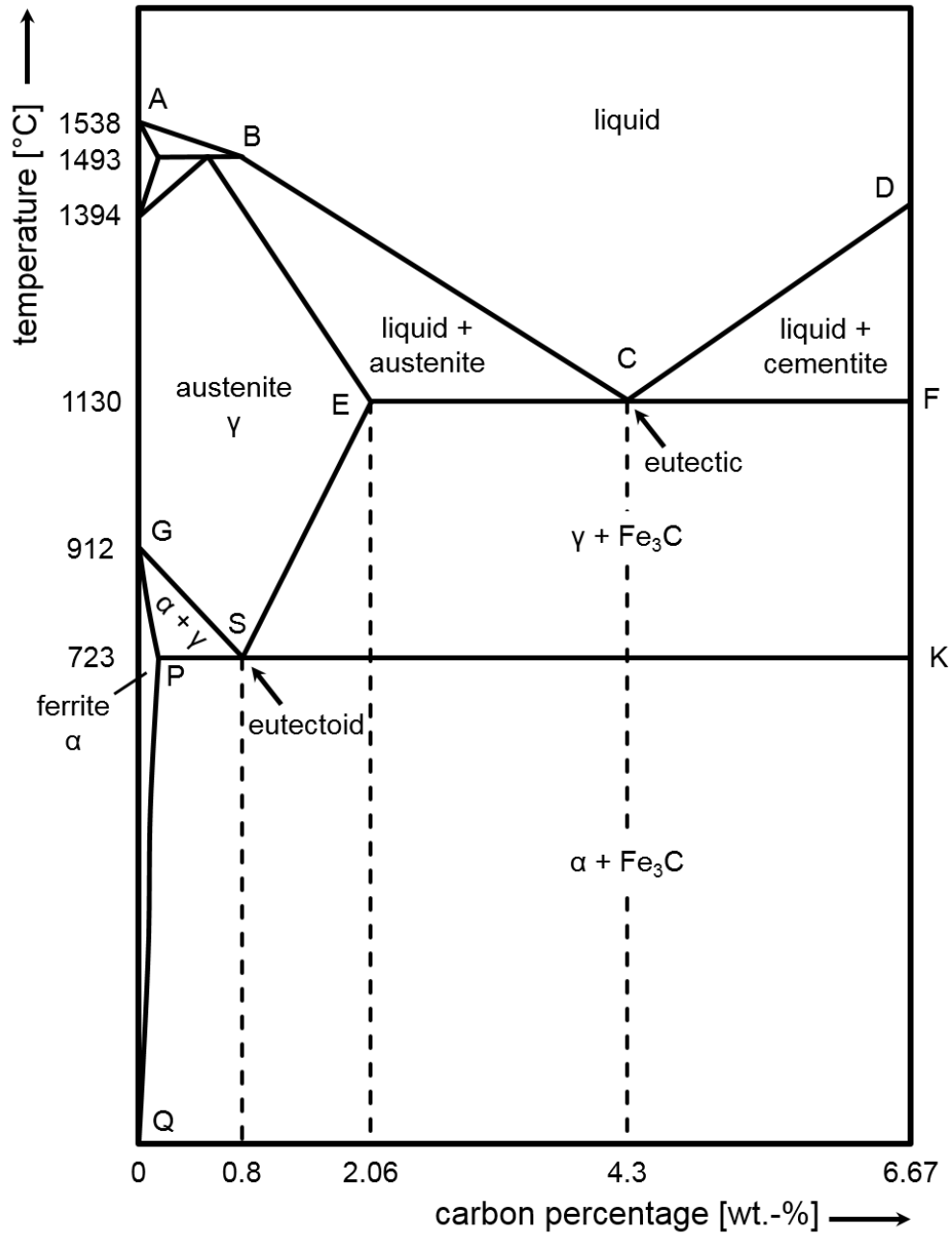


Figure 3.1: The iron-carbon phase diagram showing the areas of different phases in dependence of the temperature and carbon content. Note that the figure is simplified and not all constituents are labelled. Adapted from Merkel and Thomas [10].

behaviour of austenitic stainless steels [15]. The subject of stacking fault energy will be discussed more in detail in Chapters 3.1.3.1 and 3.1.3.2. However, ab initio calculations by Jiang *et al.* indicate that C atoms can be incorporated into dissociated dislocations and, thus, locally increase the stacking fault energy [16].

The strengthening effect of carbon is not continuous: It diminishes when reaching a carbon concentration in the steel of 0.6%.

Higher amounts of carbon will reduce weldability, surface quality and resistance against intergranular corrosion [13, 17, 18]. The latter is mainly due to the formation of brittle carbides along the grain boundaries and the concomitant depletion of alloying elements like chromium.

**Nitrogen:** Like carbon, nitrogen is a strong austenite stabiliser. In fact, it is considered as the strongest FCC stabilising element [14, 18, 19]. Similar to carbon it is known that nitrogen decreases the stacking fault energy in austenitic steels [15]. However, there is also evidence that it increases it (locally). According to De Cooman, a concentration of 0.4% N promotes twin formation in ASS [16].

Besides the positive effect on strength and hardness as well as weldability and machinability, ductility and toughness may suffer from the addition of more than  $\approx 1\%$  of nitrogen [14, 18].

Since carbon leads to sensitisation of steels, nitrogen is often the preferred interstitial alloying element [6].

In combination with molybdenum, nitrogen increases the resistance against localised corrosion [20].

**Nickel:** Nickel is undoubtedly an extremely effective and important alloying element in ASS because of its strong FCC stabilising impact. Furthermore, it lowers the critical cooling rate and  $M_s$ -temperature for martensite formation during quenching of hardenable steels [13, 16, 17, 21].

Nickel increases the stacking fault energy of ASS up to a percentage of about 12% strongly. Higher concentrations provide only a moderate additional enhancement [15].

It is well-known from Charpy tests on austenitic grades that nickel increases low-temperature strength and ductility and moderates the ductile-to-brittle transition. Highly nickel-alloyed steels show ductile fracture behaviour even at extremely low temperatures. Precipitation hardening steels benefit from formation of intermetallic compounds of nickel increasing their strength [14, 20].

In addition to that, nickel increases the stacking fault energy and decreases the corrosion rate in the active state, especially in acidic environments [20].

In Fe-Cr-Ni steels, the nickel level has to be properly adjusted to the chromium content, to adjust the desired phase composition. The effect of nickel depends furthermore on the Cr concentration [15].

**Chromium:** It is not exaggerated that chromium is the name giver of austenitic *stainless* steels. Through the formation of a dense, nanometres thick layer of  $\text{Cr}_2\text{O}_3$  at the surface of the steel, it effectively enhances the resistance against general and pitting corrosion and moreover

the high-temperature oxidation resistance [18, 20]. Steels are considered stainless when they contain more than 11-12% Cr [13].

Due to its high reactivity with carbon, this can be a disadvantage too, because it tends to form  $\text{Cr}_{23}\text{C}_6$ . These brittle precipitates reduce the corrosion resistance of the grain boundaries. Furthermore, when increasing the chromium content of steels, the probability to form brittle  $\sigma$ -phase increases as well.

Chromium improves the hardenability and strength of steels. This is due to the mismatch caused by its difference in size increasing the local energy around this substitutional atom. In addition to that, dislocation motion is hampered [13].

The stacking fault energy decreases with concentration of chromium of up to 10-15%. This effect becomes weaker at higher levels [15].

**Manganese:** Manganese is the most important alloying element in so-called TWIP steels. It is known to reduce the stacking fault energy and thus to suppress the formation of  $\epsilon$ -martensite [16]. This effect is not linear. Although the SFE diminishes by the addition of manganese, at concentration higher than 15%, a sharp increase can be observed [15]. However, contrasting information about a general enhancement of the SFE by manganese can be found in the literature, as well [21].

Although it increases the stability of the austenite phase at low temperatures, it stabilises the  $\alpha$  phase at higher ones [20]. Its  $\gamma$  preserving effect is only half as potent as that of nickel [6]. Still, because of the high costs of nickel, Mn is used for its substitution [18].

In addition of stabilising the  $\gamma$  matrix, Mn contributes also to strength and hardness but decreases the resistance against pitting corrosion. Together with sulphur, it forms MnS inclusions, which ameliorate the machinability during cutting [14].

Higher amounts of Mn in the alloy will enhance the solubility for nitrogen [18, 20].

**Molybdenum:** Molybdenum is a ferrite forming element and carbide former. At amounts lower than  $\approx 4\%$ , it increases the material's resistance against crevice, pitting and uniform corrosion in sour environments [13, 20]. At amounts higher than this, 475°C-embrittlement and the formation of secondary phases like the brittle  $\sigma$  are possible [18].

In low-alloyed steels, molybdenum retards austenite-to-pearlite-transformation upon cooling. A positive effect on hardenability, high-temperature strength and creep resistance is also accredited to the element.

**Silicon:** Silicon acts as a strong solid solution strengthener [16]. Martin *et al.* investigated its influence on TWIP steels and found out that the addition of up to 2% Si contributes to hardness and strength [20]. This is due to the introduction of vacancy defects, hampering dislocation movement [21]. Si furthermore decreases the stacking fault energy [15].

Silicon is known to increase the corrosive resistance by facilitating the formation of the  $\text{Cr}_2\text{O}_3$  passive layer but can promote the formation of the brittle  $\sigma$  phase [18].

Because it reduces the stacking fault energy in the system, it fosters the martensitic transformation in austenitic stainless steels and promotes ferritic structure [20, 22].

**Aluminium:** A contrary effect can be observed when adding aluminium to the material: The stacking fault energy increases and by that martensitic formation is suppressed [22, 23].

Since it inhibits the austenite grain growth during manufacturing, aluminium is an effective means to control the grain size of the alloy. This will increase the strength according the *Hall-Petch* relation [14].

Aluminium is known to increase the oxidation resistance when added in substantial amounts [20].

The above described positive effect of some elements on the  $\gamma$  phase stability can result in the enlargement of the  $\gamma$ -area in the iron-carbon diagram with a simultaneous decrease of the  $A_1$  (P-K-line) and  $A_3$  (G-S-line) temperature. Figure 3.2 visualises schematically the very left side of the Fe-C diagram with an open and a closed  $\gamma$ -area.

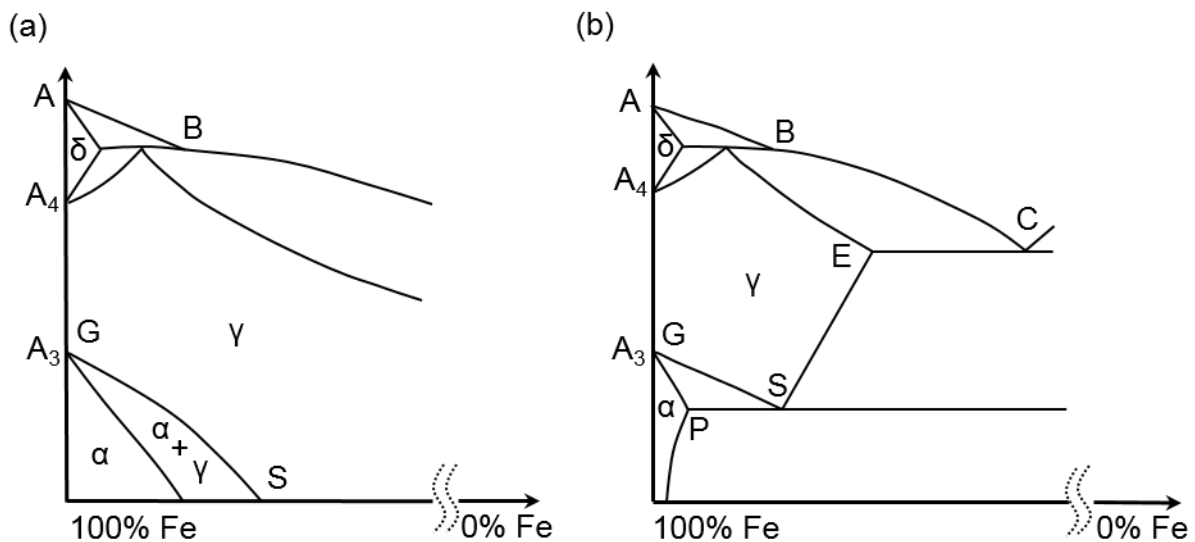


Figure 3.2: The extract of the left side of the Fe-C diagram shows (a) an enlarged, open  $\gamma$ -area and (b) an extended, closed  $\gamma$ -region, bordered by secondary phases. Figure according to Merkel and Thomas [10].

The isothermal ternary phase diagram of iron, nickel and chromium at 1100°C is plotted in Figure 3.3. It clarifies the influence of the alloying elements Cr and Ni on the phase formation of the widely used austenitic steel Fe-Cr-Ni-18-8 (AISI 304 or EN 1.4301). By adding chromium, the alloy leaves the  $\gamma$ -area and forms a certain extend of  $\alpha$ -iron.

Phase diagrams are thus able to *depict* the structural composition of an alloy with a given chemical composition. A means to *predict* the structure is the *Schaeffler* diagram. Here, the so-called nickel-equivalent  $Ni_{eq}$  is plotted against the chromium-equivalent  $Cr_{eq}$ .  $Ni_{eq}$  is a measure of the stability of austenitic steels against martensitic transformation. Post *et al.* [24] announced already in the 1940s, the following expression:



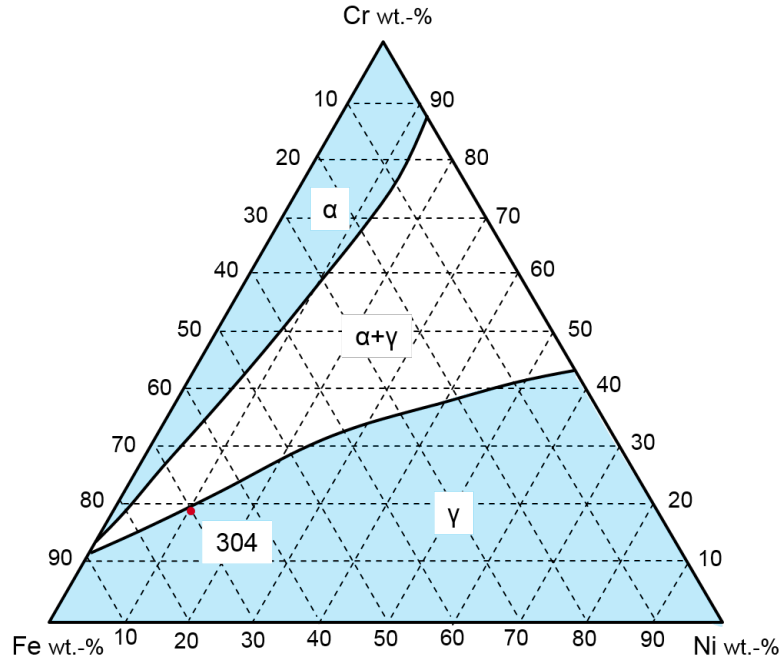


Figure 3.3: Isothermal section of Fe-Cr-Ni phase diagram at 1100°C with the composition of the AISI 304 alloy marked. Figure according to Verhoeven [13].

$$Ni_{eq} = \%Ni + 0.65\%Cr + 0.98\%Mo + 1.05\%Mn + 0.35\%Si + 12.6\%C \quad (1)$$

This equation has been adapted and modified numerous times, to take the effect of more alloying elements into account. The probably most recent stems from Takaki *et al.* and Takemoto *et al.*, respectively [24, 25].

In the present manuscript, the Ni-equivalent proposed by Weiß *et al.* shall be utilised hereafter: [26]

$$Ni_{eq} = \%Ni + 30\%C + 18\%N + 0.5\%Mn + 0.3\%Co + 0.2\%Cu - 0.2\%Al \quad (2)$$

In contrast, the  $Cr_{eq}$  gives information about the impact of ferrite stabilisers:

$$Cr_{eq} = \%Cr + \%Mo + 1.5\%Si + 0.5\%W + 0.9\%Nb + 1.5\%V + 0.9 \quad (3)$$

Another way of predicting the microstructure of ASS is the WRC diagram of the *Welding Research Council*. Kotecki and Siewert introduced the WRC-1992 diagram to overcome the shortcomings of the Schaeffler diagram. It therefore does not make predictions based directly on the ferrite content but rather on the more precise magnetically based ferrite number (FN) [27].

### 3.1.2. Classification

Stainless steels are grouped into ferritic, martensitic, austenitic and duplex stainless steels [20].

The family of austenitic stainless steels is, according to the *American Iron and Steel Institute*, labelled AISI 300 series. An overview of the different grades in that group are shown in Figure 3.4.

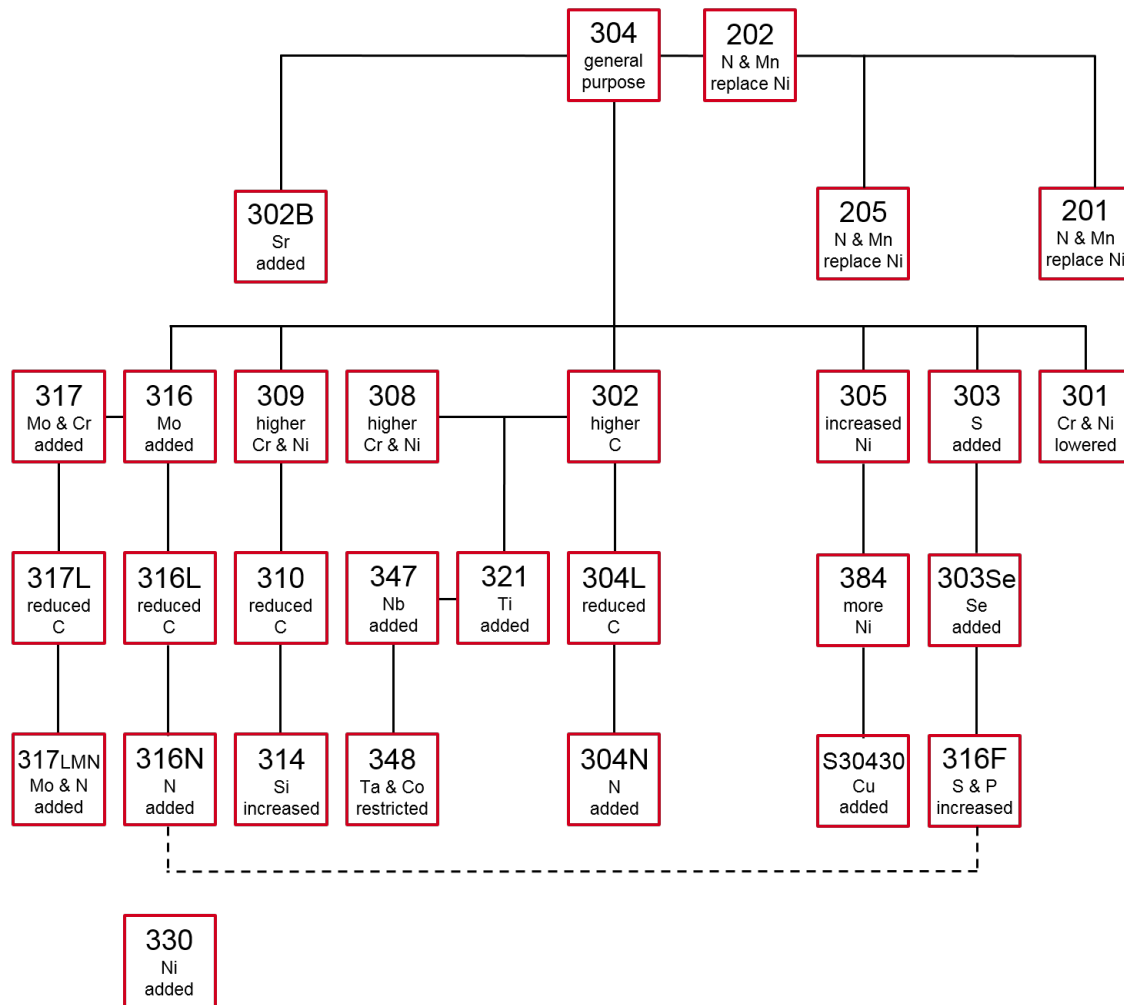


Figure 3.4: Classification of austenitic stainless steels regarding their chemical composition according to the American Society for Metals [28].

The main alloying elements of the 304 grade on top of the scheme are 18.0-20.0% chromium and 8.0-10.5% nickel as well as  $\leq 2\%$  manganese and  $\leq 1\%$  silicon. The carbon content is with 0.08% very low [14].

Austenitic stainless steels are again subdivided into *stable* and *metastable* austenitic stainless steels based on the phase and chemical composition, the austenite stability and thus hardening behaviour. Figure 3.5 classifies different alloys into three groups of metastable alloys. Although they do not necessarily consist of only one, austenitic phase, they are called metastable austenitic steels.

### 3.1.3. Hardening behaviour in metastable steels

Metastable austenitic steels possess the outstanding capability to increase their strength and ductility when subjected to external, mechanical loads. First reports on this date back to the

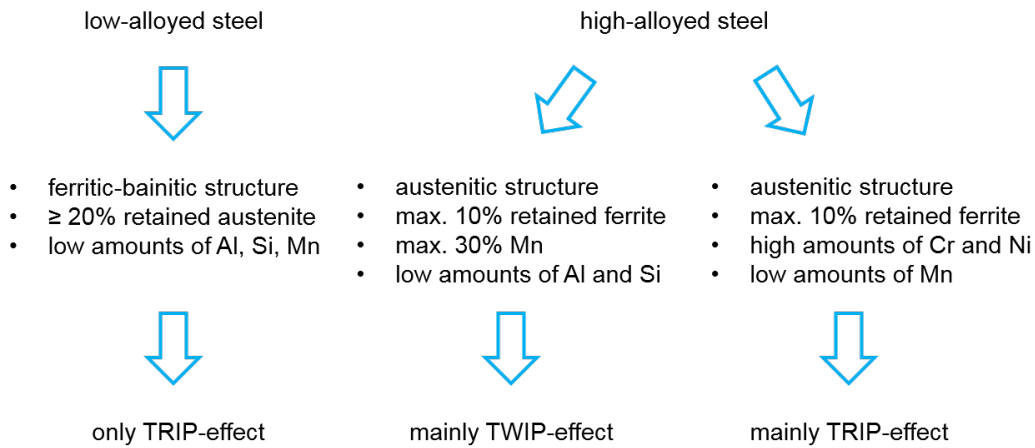


Figure 3.5: Classification of metastable austenitic steels regarding the chemical composition and their resulting deformation behaviour.

late 19<sup>th</sup> and early 20<sup>th</sup> century, with the development of the V2A steel in Germany and the high-manganese steels in England. Nowadays, these grades are known as AISI 304 or EN 1.4301 and Hadfield steel, respectively [13].

The capacity to increase strength and ductility at the same time can be assigned to either a *transformation* of the crystal structure from the original austenite into martensite in so-called TRIP (**t**ransformation-**i**nduced **p**lasticity) steels or excessive *twin formation* in TWIP (**t**winning-**i**nduced **p**lasticity) steels. A comparison of these two differing behaviours with a steel without strengthening effect is shown schematically in Figure 3.6.

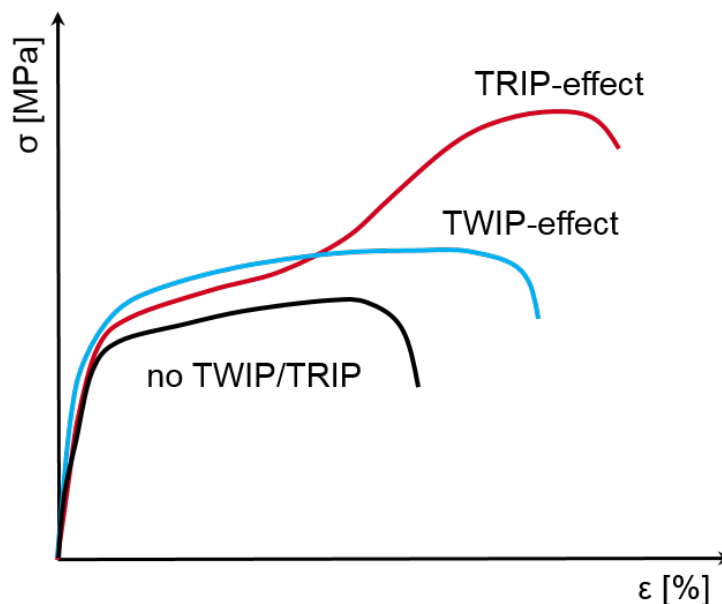


Figure 3.6: Schematic stress-strain-curves of a TWIP, a TRIP and a steel without these hardening behaviours.

The strengthening effect is reflected in the formation of dislocations and the inhibition of their free movement by obstacles like twin boundaries and martensite interfaces. The increased density of newly formed interfaces, thus, represents an effective means to prevent dislocations, the carrier of plastic deformation, to glide through the metallic lattice [22, 29]. Kim *et al.* emphasise that deformation twinning increases also the strain-hardening rate due to the creation of twin boundaries. This is called the *dynamic Hall-Petch* effect [30].

In comparison to dislocation tangling, which positive contribution saturates during mechanical loading, martensite and twins form also in the high-strain region. Due to this progressive formation of new obstacles, they are a more efficient hardening mechanism [31].

Linderov *et al.* investigated the deformation mechanisms in different TRIP and TWIP steels with *in-situ* acoustic emission experiments during tensile tests. They found that dislocation glide, formation of stacking faults, mechanical twinning and martensitic phase transformation are simultaneous mechanisms with dislocation glide as the least important in contributing to the increase in strength [32].

**3.1.3.1. Underlying processes** Without knowing about the underlying processes of *athermal* martensite formation, the craft of hardening steels has been known for centuries. Crucial steps include here the heating above the austenite-start-temperature  $A_S$  ( $A_4$  temperature in the Fe-C diagram) for austenitising the structure. The alloy is cooled down below the martensite-start temperature  $M_S$ , determined mainly by the chemical composition. This supplies the necessary *chemical driving force*  $\Delta G_{chem}$  for martensite nucleation. By reaching the  $M_S$ -temperature, the free energy difference  $\Delta G_{\gamma \rightarrow \alpha'}$  between the austenite and martensite is below the critical driving force  $\Delta G_{crit}$  needed. Figure 3.7 schematically plots this process [33].

Martensite is the result of a cooperative, diffusionless shear movement in the austenite lattice. Between  $M_S$  and  $M_d$ , the chemical driving force is too low and, thus, the critical value  $\Delta G_{crit}$  can not be achieved. Nonetheless, martensite can still be formed if the material is subjected to external mechanical load  $W_{mech}$ , providing the necessary energy difference as the driving force. The  $M_d$ -temperature limits the regime where *deformation*-induced martensite can be build [11, 33–38].

Two kinds of deformation-induced martensite formation can be identified, depending on the degree of external load. Wendler *et al.* refer to this as *stress*-induced and *strain*-induced martensite formation [39]. This is shown in Figure 3.8.

In the elastic deformation regime, stress-induced martensite can be formed below the  $M_S^g$ -temperature. It is distinguished by an increase in strength with only a negligible additional elongation in the  $\sigma$ - $\epsilon$ -curve. Strain-induced martensite formation takes place between  $M_S^g$  and  $M_d$  when subjected to higher loads. Only this process is called TRIP-effect [39]. Stress-assisted martensite nucleates on the same sites as athermal martensite such as intersections of shear bands, twins and grain boundaries. It forms even below the yield strength. Strain-induced  $\alpha'$ -martensite, in contrast, forms at defects which the plastic deformation produces [41]. Dislocation that are produced after passing the yield strength, thus, promote martensite formation [42].

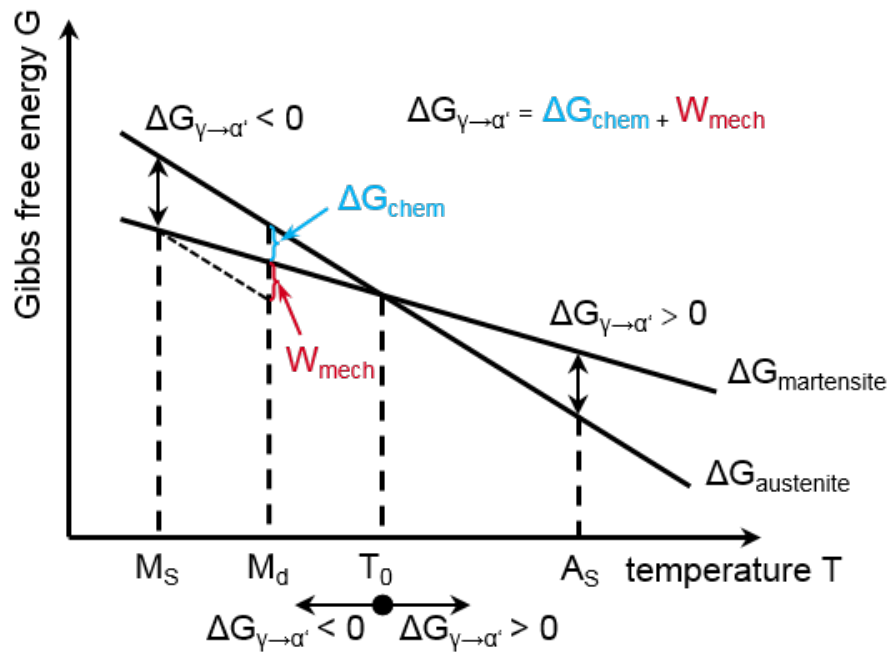


Figure 3.7: Schematic depiction of the temperature profile of Gibbs free energy as the main driving force for martensitic transformation.

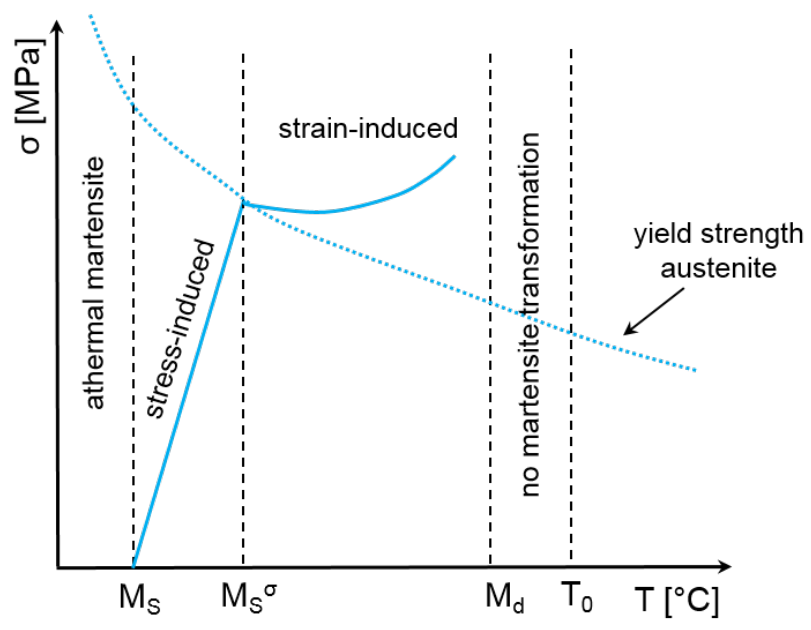


Figure 3.8: Schematic depiction of the temperature regimes for athermal, stress-induced and strain-induced martensite formation, according to Wendler et al. [40].

Another important parameter is the  $M_{d30}$ -temperature. It represents the temperature at which 50% of the austenite is transformed into martensite at a plastic strain of 30%. Therefore it is a valuable estimation of the interaction between temperature and mechanical load and the phase stability of the material.

Already in 1975 Olson and Cohen in their groundbreaking work proposed the deformation-induced martensitic transformation to take place in deformation bands [43]. By means of *in-situ* SEM investigations during tensile tests, Weidner *et al.* were able to prove this [39]. By increasing the plastic deformation from 3.6 to 15%, they found that strain localisation took place in these deformation bands, while the strain in the surrounding austenite remained unchanged.

In these bands, to which Biermann *et al.* referred to as slip bands with highest *Schmid factor*, first stacking faults of high density and with ongoing load  $\epsilon$ -martensite was built up [26]. This happened due to shear along  $\langle 112 \rangle$ -direction [44]. Differences in the magnitude of shear, led to the formation of  $\alpha'$  islands within the bands. Grains with a primary slip system on the  $\{111\}$ -planes exhibited with 0.48 the highest Schmid factor. Both researcher groups found the same behaviour.

The phase distribution maps of EBSD observations Chun *et al.* conducted on a Fe-15Mn-2Cr-0.6C alloy revealed the formation of  $\alpha'$ -martensite within the previously existing  $\epsilon$ -areas [45].

By means of fatigue tests on the austenitic steel 316LN and subsequent transmission electron microscopy TEM investigations, Kruml *et al.* were also able to prove the presence of the hexagonal  $\epsilon$ -phase within the austenitic base material. By means of diffraction patterns in the TEM, they observed the plate-like arrangement of this structure solely on  $\{111\}$ -planes of the matrix [46]. In addition to that, at almost every intersection of these platelets  $\alpha'$ -martensite was detected. This confirmed what Lecroisey and Pineau as well as Olson and Cohen postulated already in the early 1970s [43, 47].

The formation of martensite during uni-axial deformation of 301 and 304 grades was also observed by Talonen *et al.*. Their subsequent SEM measurements confirmed the evolution of the  $\alpha'$ -phase on deformation bands. Together with X-ray diffraction XRD measurements and calculations, the group revealed different structures of the shear bands, as well. Depending on temperature, mechanical load and chemical composition, the stacking faults forming these bands, can overlap either in successive  $\{111\}$ -planes or on every second plane [11]. Their width and distance influence directly if either the TRIP or TWIP behaviour prevails.

According to Olson and Cohen, the critical thickness of a  $\alpha'$ -martensite embryo is 13.5 atomic planes [43]. Staudhammer *et al.* estimated this to be even 27, meaning that a significant number of stacking faults are necessary for martensite nucleation [11].

Kim *et al.* analysed nine TWIP steels with varying manganese and silicon contents after tensile tests at room temperature by EBSD and TEM. Not only did they confirm the formation of martensite in shear bands but were also able to depict two types of stacking faults as pre-stages of it [30]. The analyses of the outer fringes enabled them to distinguish between *intrinsic* and *extrinsic* stacking faults.

This formation is caused by the dissociation of dislocations into *Shockley* and *Frank* partial dislocations, respectively, with the material between them faulted. In the area spanned by these partial dislocations, stacking faults can emerge [28, 48].

According to De Cooman *et al.*, stacking faults in FCC alloys are assumed to be mostly intrinsic, which is also due to the fact that extrinsic SFs have not been observed too often [16]. Taking the sphere model as basis, an intrinsic SF forms by shifting the topmost layer of a FCC crystal by  $\frac{a}{6} \langle \bar{2}11 \rangle$  on a  $\{111\}$ -plane. The repetition on a neighbouring plane results in an extrinsic SF as it is sketched in Figure 3.9.

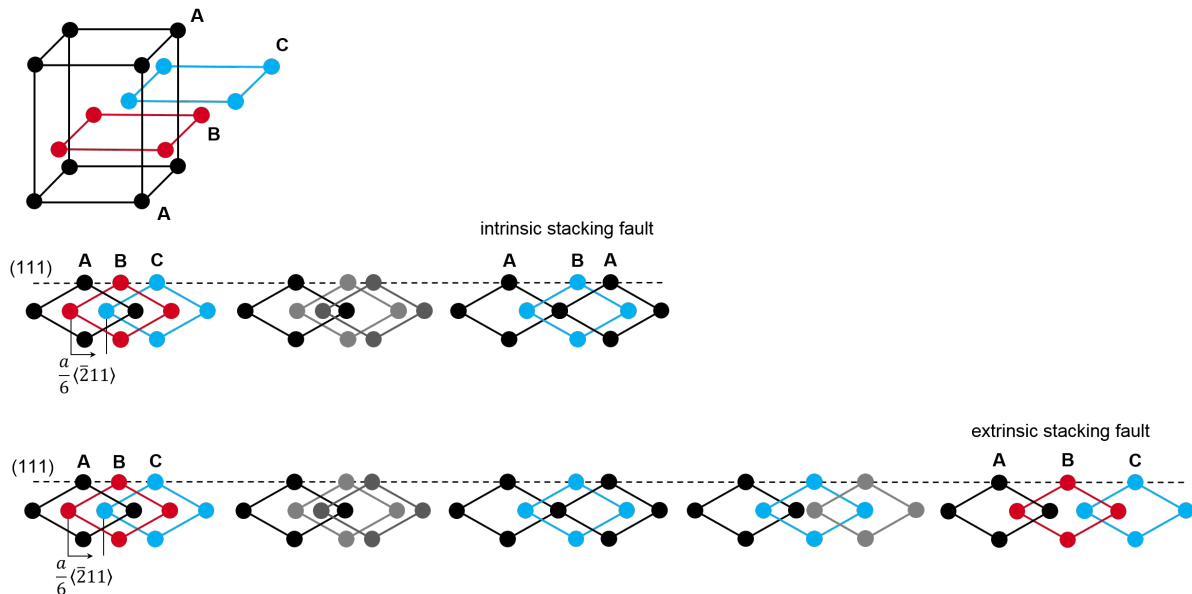
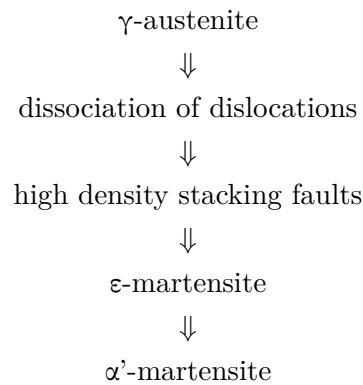


Figure 3.9: Sequence of the formation of intrinsic and extrinsic stacking faults in FCC materials according to De Cooman *et al.* [16].

Stacking faults are the basis of both  $\epsilon$ -martensite and twins. Intrinsic SFs, arranged on every second  $\{111\}$ -plane of the FCC lattice, lead to an ABABAB stacking sequence and therefore  $\epsilon$ -martensite. Three overlapping SFs on successive planes are referred to as mechanical twin [11, 48, 49].

The positive, i.e. hardening, effect of twin formation starts, when stacking faults are generated in abundance. An increased work-hardening rate is the result when those SF can not slip past each other and pile-up [28].

In conclusion, the already in 1970 by Mongonon *et al.* proposed sequence of martensitic transformation has to be extended [50]:



Taking the FCC austenite from which it evolves as the basis, the formation of BCC martensite can be described as illustrated in Figure 3.10. Since the formation of martensite takes place by shear of atomic planes, a mismatch develops resulting in a tetragonally distorted BCC cell. This is often assigned to as body-centred tetragonal BCT. Thus, Figure 3.10 reflects only an ideal status without mismatch.

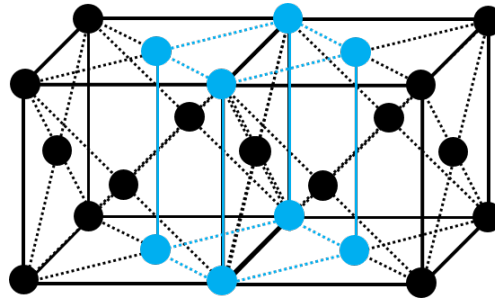


Figure 3.10: Description of BCC martensite (blue) within the FCC structure (black) in the ideal, undistorted unit cell.

To fully describe the  $\gamma \rightarrow \alpha'$ -transformation on the crystallographic scale, models were developed by Bain, Pitch, Nishiyama-Wassermann and Kurdjumov-Sachs. Figure 3.11 depicts them and shows the corresponding orientation relations between the initial FCC and the tetragonal BCC [51].

The lattice distortion is described differently in every model, so that different formations of grains and  $\gamma/\alpha'$ -phase boundary for every case are assumed. That is why the unit cells are slightly tilted against each other [51]. Because this tilt is very small, material scientists and crystallographers concluded that the movement of atoms during phase transformation is rather small as well.

### 3.1.3.2. Influencing factors on the strain-hardening behaviour

If and to which extent a metastable austenitic steel exhibits the TRIP and/or the TWIP effect, depends on various factors such as strain rate, stacking fault energy, chemical composition, temperature, pre-treatment and stress state. That is why in the following these factors shall be discussed briefly.



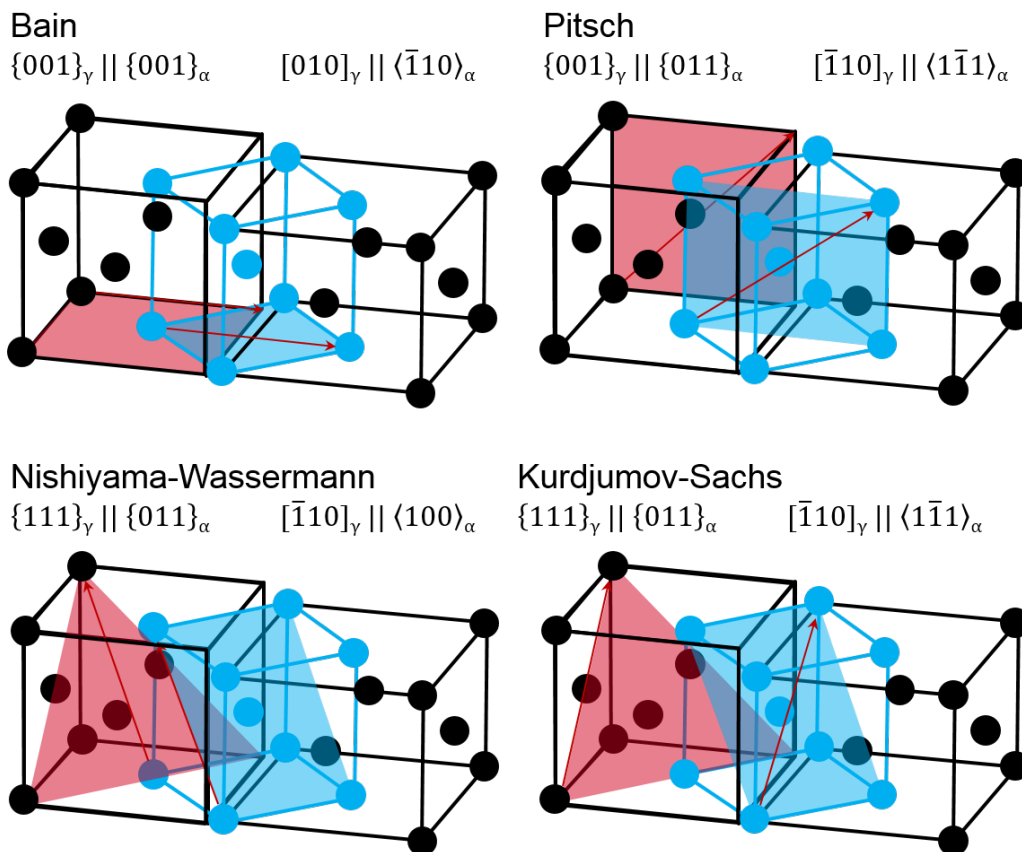


Figure 3.11: Description of BCC martensite (blue) within the FCC structure (black) considering the movement of atomic planes and the resulting orientation relationships during martensitic transformation according to Bain, Pitsch, Nishiyama-Wassermann and Kurdjumov-Sachs. Note that the models possess more than the one given symmetry-equivalent variant.

### Stacking fault energy

Hirth *et al.* defined the stacking fault energy as a yardstick to assess the probability of screw dislocations to split into partial dislocations [52]. A low SFE indicates a higher tendency of perfect dislocations to dissociate and move away from each other [35].

The stacking fault energy plays a crucial role for the deformation mechanism of metastable austenitic steels [30]. Although there are discussions about precise values, it is commonly accepted that steels exhibiting a low SFE tend to the formation of  $\epsilon$ - or  $\alpha'$ -martensite while higher SFE facilitates mechanical twinning [11, 28, 35, 53, 54].

A non-exhaustive overview of the stacking fault energies calculated by different researchers and their implication on the deformation mechanism are given in Table 6.4.

Table 3.2: *Stacking fault energies in metastable austenitic steels and their influence on the deformation behaviour.*

Mechanism	SFE [ $\text{mJ}/\text{m}^2$ ]	Reference
<b>martensite formation</b>	$\leq 15$	[30]
	$\leq 18-20$	[40, 44]
	$\leq 20$	[22, 49, 55]
	$\leq 18$	[56]
<b>twin formation</b>	$15 \leq \text{SFE} \leq 45$	[30]
	$\geq 20$	[22, 55]
	$18 \leq \text{SFE} \leq 35$	[56]
	$15 \leq \text{SFE} \leq 30$	[49]

As discussed previously, stacking faults are the basis for both martensite and twin formation. Li *et al.* conducted tensile tests together with EBSD investigations on different types of metastable high entropy alloys. In alloys with lower SFE, gliding partial dislocations of  $\frac{1}{6}\langle 111 \rangle$  Burgers vector formed stacking faults. The HCP plates acted as nuclei for  $\epsilon$ - and  $\alpha'$ -martensite, proving stacking faults to be central for the hardening behaviour of the alloys. In accordance to Głowacka *et al.*, the researchers claim that a larger amount of SFs was needed to initiate the TRIP effect. Only in grades with low SFE, enough dislocations split up and form SFs with high density.

By means of TEM observations, the separation distance of partial dislocations, representing a stacking fault, can be estimated. Byun *et al.* suggested a separation distance of about 10 nm [55]. When applying mechanical load, this span increases. The SF between the partials can not be overcome by cross-slip, thus contributing to strain hardening.

Talonen *et al.* conducted tensile tests on the austenitic grades 304 and 301LN. Together with SEM results, the XRD-based calculations of the stacking fault energy suggested that the SFE strongly affects the fault width and number of overlapping SFs. The overlapping of SFs become more irregular at higher temperatures [11].

The researchers further concluded that the influence of the SFE on the phase stability of austenite is even stronger than the free energy difference  $\Delta G_{\gamma \rightarrow \alpha'}$ . Upon cooling the grade 301LN

from 80 to  $-40^{\circ}\text{C}$ , the calculated SFE dropped from 20.3 to only  $8.3\text{ mJ/m}^2$ , thus making the martensitic transformation more likely [36, 53].

This is in accordance to preceding results of Pontini and Hermida [57]. With the help of X-ray diffraction and subsequent calculations, the researchers were able to determine the stacking fault energy of cold-rolled AISI 304 grade at  $-196$ ,  $-67$  and  $20^{\circ}\text{C}$ . The results showed a significant increase with higher temperature from 19.5 to 25.7 and  $30.4\text{ mJ/m}^2$ , respectively.

Extended martensite and twin formation under similar loading conditions but decreasing temperature was observed by several researchers [31, 33, 55, 58–61]. Because of the changing stacking fault energy and austenite stability, a transition from dislocation glide to twinning and martensite formation with lower test temperature becomes obvious. Byun *et al.* demonstrated this for the grade AISI 304, depicted in Figure 3.12.

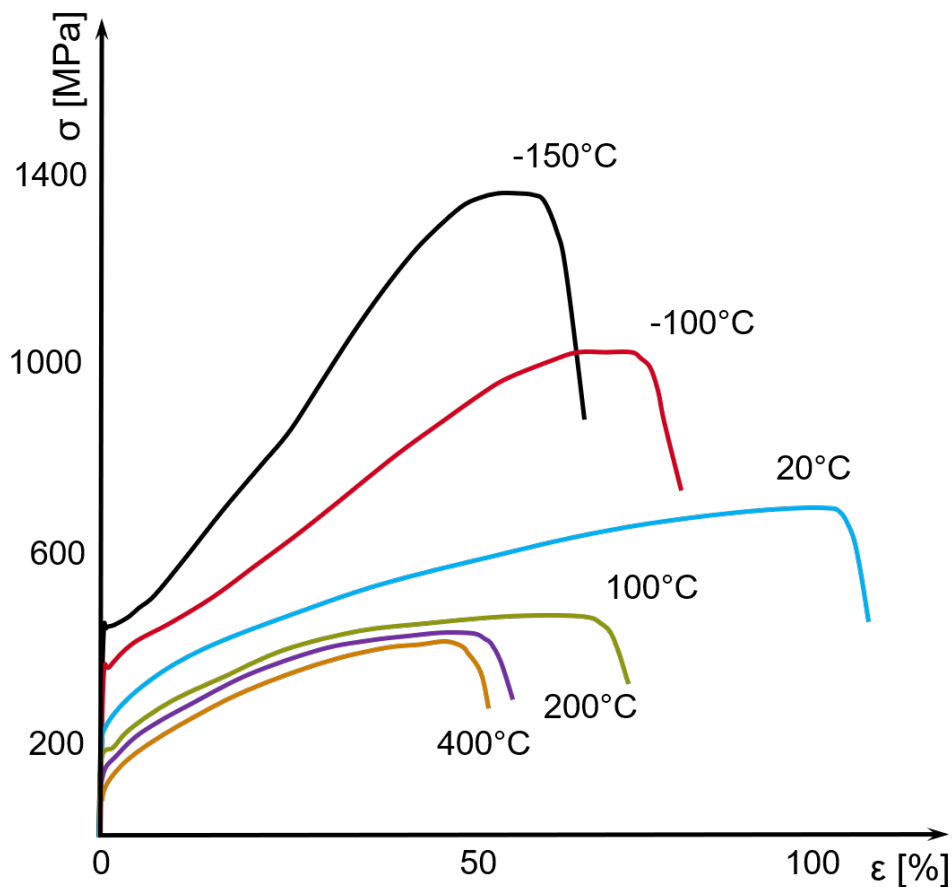


Figure 3.12: Stress-strain curves of AISI 304 alloys after tensile tests at different temperatures. The dependence of the strain-hardening behaviour is obvious. According to Byun *et al.* [55].

At  $-150$  and  $-100^{\circ}\text{C}$  the material showed a very pronounced TRIP behaviour, reaching ultimate tensile strength of  $\approx 1400$  and  $\approx 1000\text{ MPa}$ , respectively. Much lower strength, but an increased ductility of about 100%, was achieved at room temperature. Here, besides mechanical twins martensite was still formed, which is most likely due to a stacking fault energy in the range of  $18\text{--}20\text{ mJ/m}^2$  where both mechanisms overlap. The existence of such a domain was proven by

Gussev *et al.* by tensile and indentation tests and subsequent EBSD analyses. They found that in a Ni-rich 304 grade, tested at room temperature, twins and martensite existed [62].

Further ascending the test temperature lead to diminishing of both ultimate tensile strength and elongation, as illustrated in Figure 3.12.

How the stacking fault energy influences the dislocation structure in austenite was illustrated by Hannula *et al.* with TEM images of hydrogen-charged, tensile-tested AISI 304 samples. The material exhibited a planar dislocation structure and planar slip behaviour. This was accounted to the low SFE, which was further reduced by the presence of hydrogen [19].

A similar approach was pursued by Kim *et al.* when they conducted TEM observations of Fe-Mn alloys with different carbon and aluminium contents. Both the thickness of strain-induced twins and the ultimate tensile stress increased with decreasing SFE [30].

A comprehensive study on the strain-hardening of TRIP and TWIP steels was provided by Huang *et al.* [38]. Due to its dominating effect on the formation of martensite and twins, the model was determined by the stacking fault energy. By that, the kinematic model was able to precisely predict the hardening behaviour of seven different steels, incorporating dislocation glide, martensite formation and twinning.

The results clearly validated theory and previous findings of other groups that martensite formation diminishes in favour of twinning, when the SFE increases, e.g. by lowering the carbon concentration.

### **Pre-treatment and materials condition**

The grain size is an important factor not only for the strain-hardening behaviour but for the hardness, strength and ductility, in general. For the low temperature regime this is described by the *Hall-Petch* relation.

Samek *et al.* investigated the impact of the austenite particle size on the transformation behaviour in several TRIP steels and observed a considerable decrease of the  $M_s^g$  temperature [63]. In other words the austenite stability increased when the austenitic grains were smaller.

In accordance to these findings are results of Li *et al.* [53]. They conducted tensile tests on dual-phase high-entropy alloys with 4.5 and 45  $\mu\text{m}$  grain size, respectively. Not only did the alloy with smaller grains possess a higher strength and strain hardening rate, but achieved this with forming 10-20% less martensite than its counterpart.

Weidner *et al.* adjusted the initial grain size of  $\approx 500 \mu\text{m}$  of a fully austenitic Cr-Mn-Ni steel through thermo-mechanical treatment [64]. Depending on the treatment, the specimen had a mean grain size of 0.51 to 2.55  $\mu\text{m}$  afterwards. During the subsequent tensile tests all samples achieved similar ultimate tensile stress of  $\approx 1200 \text{ MPa}$ , although the ductility decreased significantly with reducing grain size.

Not only the grain size but also their orientation changes the hardening behaviour of metastable austenites. According to Gussev *et al.*, in the investigated Ni-rich 304 grade twinning occurred only in the  $\{111\}$  grains, but not in  $\{001\}$  and  $\{101\}$ . Furthermore twinning was observed to happen preferably under tensile load other than during indentation tests [62].

Deliberate adjustment of the grain orientation can therefore have positive contribution to the hardening behaviour.

The influence of heat treatment on a X80Mn16 TWIP steel was examined by Mesquita *et al.* [65]. Upon austenitisation, specimens were quenched to defined holding temperatures. Isothermal holding was followed by quenching to room temperature. By means of XRD and TEM observations, the researchers were able to identify  $\epsilon$ -martensite after cooling in samples treated at 500°C for 100 h. Specimens tempered for shorter times were still fully austenitic.

With longer holding times, cementite formed within the austenite. As a consequence, the matrix was depleted from carbon, reducing the stability of the austenitic phase. This in turn allowed martensite to form during quenching and shows that even stable austenitic stainless steels will form martensite when treated improperly.

Talonen and Hänninen emphasised the importance of the stored energy in the austenite that is introduced during production and material treatment. They claimed that it acts as an additional driving force for the transformation [36].

### Strain rate

The influence of the strain rate on the mechanical response of steels was investigated by Hecker *et al.* on an AISI 304 alloy. Uni- and biaxial tension tests with strain rates of  $\dot{\epsilon} = 10^{-3}$  and  $10^3 \text{ s}^{-1}$  pointed out that the deformation-induced martensite formation diminished dramatically. This effect was even more pronounced at higher strains and amounts to a reduction of about 25% at 40% strain [34].

Subsequent TEM investigations challenged these findings when they revealed a higher number of deformation bands and intersections. As previously discussed in Chapter 3.1.3.1, these are nucleation sites for martensite and twins. A higher number should therefore result in a higher twin and martensite fraction. From this the researchers derived a decreased driving force  $\Delta G_{\gamma \rightarrow \alpha'}$  [34].

Meyers *et al.* subjected a 304 alloy to shear deformation with a strain rate of  $10^4 \text{ s}^{-1}$ . The high strain rates lead to a considerable suppression of martensitic transformation due to local heating of the specimen. The researches stated that high strain rates applied on the material constrained the heat transfer within the sample, leading to *adiabatic* heating [62].

The influence of the strain rate on the stress-strain behaviour of the austenitic grades AISI 304L and 309 was investigated by Lichtenfeld *et al.* by means of tensile tests at varying strain rates [66]. Subsequent XRD and microscopical examinations revealed  $\alpha'$ -martensite fractions of 68.8% at 30% strain in the metastable 304L steel, when tested at  $1.25 \cdot 10^{-4} \text{ s}^{-1}$  in comparison to 19.9% at  $400 \text{ s}^{-1}$ . This was also reflected in an increased work-hardening rate. In contrast, the stable 309 grade did not transform and showed only slight changes in work hardening.

Yet another disparity of both alloys is the evolution of the ultimate tensile stress. Due to the (partial) prevention of the  $\gamma \rightarrow \alpha'$  transformation in the 304L steel with higher strain rates, the total strength decreased. In contrast, the ultimate tensile strength of the 309 steel steadily

increased. Piling-up of dislocations at grain boundaries and other obstacles was the reason for that.

Talonen and Hänninen investigated the energetics of plastic deformation of seven austenitic stainless steels [11]. They measured temperature increase, mechanical energy and formation of  $\alpha'$ -martensite during tensile tests at  $\dot{\epsilon}=10^{-3}\text{ s}^{-1}$ . According to the authors, this strain rate was high enough to consider the experiment adiabatic. Depending on the material the specimen temperature increased about 60-80 K at a logarithmic plastic strain of 0.35, thus raising the stacking fault energy.

Currently, there is agreement of how the strain rate affects the hardening behaviour of metastable austenites. Due to an adiabatic temperature increase in the material, both austenite stability and stacking fault energy increase, reducing the number and density of stacking faults, slip bands and intersections. Together with the decreasing free energy  $\Delta G_{\gamma\rightarrow\alpha'}$  as the chemical driving force, martensitic transformation becomes less favourable.

#### 3.1.4. Applications

Practically everywhere to be found, austenitic stainless steels play an important role in many applications.

Due to their excellent energy absorption capacity and strength-weight ratio, crash-related parts in automobiles are manufactured from steels exhibiting TRIP and TWIP effect [22, 30, 44, 67–70]. Moreover the grade AISI 304 is used for tanks, handrails, housings for catalytic converters and exhausts [71].

As the most common austenitic stainless steel, AISI 304 can be encountered also in paper production, food processing industries, transportation, architecture and design and in everyday life in the form of kitchenware, handrails and many more [20, 72].

According to Garion *et al.*, Fe-Cr-Ni austenitic steels are also commonly used as components in superconducting magnets and cryogenic transfer lines. This is not only due to their ductility even at extremely low temperatures, but because they are not susceptible to the strong magnetic fields present [29].

Within the framework of the current thesis, two applications have to be considered in particular: The storage and transport of chemicals, petrochemicals and hydrogen in the energy sector and the use of austenitic stainless steels as structural components in aggressive (sour) media.

To avoid corrosion in pipes or hulls, cathodic protection is operating. This indeed lowers or even eliminates the corrosive attack, but leads to the generation of hydrogen from the medium.

Hydrogen is regarded as a promising source of power for the future's carbon-lean energy mix. The establishment of a reliable infrastructure for producing, storing and transporting hydrogen is of crucial importance in this. Austenitic stainless steels have been identified as potential materials for tubes, pipes and tanks in this infrastructure [23, 73–75].

A successful use of ASS as valves, springs and linings of pressure vessels in fuel cells was reported already several years ago [76, 77].

In both cases hydrogen atoms might enter the metallic matrix causing severe damages to the material. The safe use of parts and components subjected to hydrogen bears challenges and arises new questions concerning processing, treatment and selection of proper materials. They are formulated as follows.

### 3.2. Fundamentals of hydrogen-assisted damage

#### 3.2.1. Sources of hydrogen and its uptake

In order to unfold its deteriorative impact on structural materials, hydrogen has first to enter the metallic matrix. This can take place already during production and manufacturing, e.g. due to heat treatment or welding, or during application. In the latter case, hydrogen is not already present in the metallic matrix of the component but enters it while its in use. For different cases, this is illustrated in Figure 3.13.

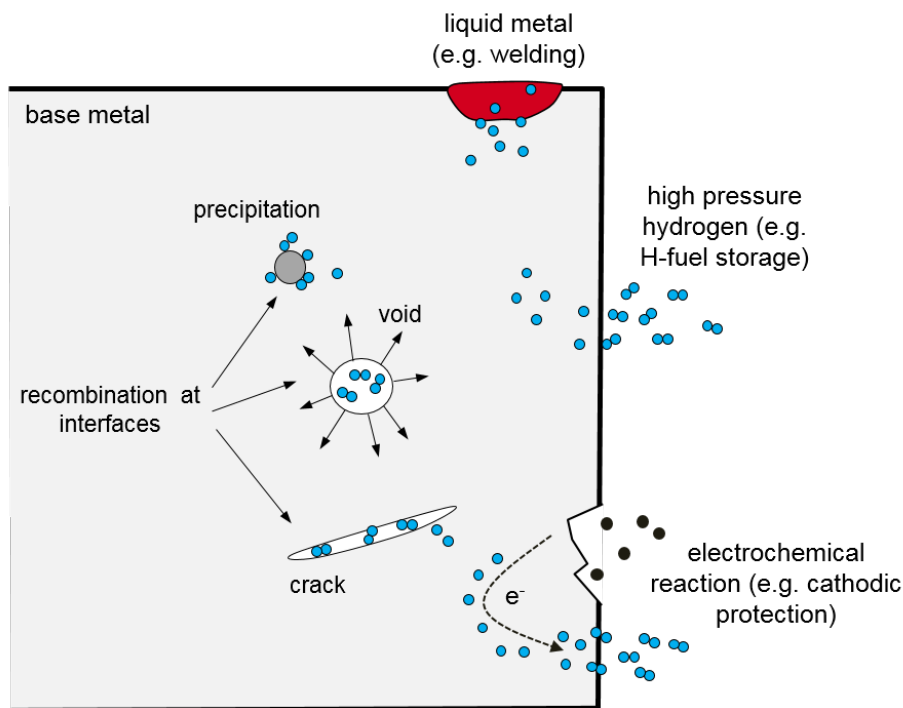


Figure 3.13: Possible sources for the ingress of hydrogen atoms into the material and their possible recombination at internal interfaces. Figure following Böllinghaus [78].

#### Corrosion and cathodic protection

Austenitic stainless steels are frequently subjected to aggressive media like chemicals, petrochemicals or saltwater, from which hydrogen can be absorbed. Due to its character, it is also called *electrochemical absorption* [78].

In acidic media, hydrogen is transported to the metallic surface as hydronium ions where it discharges into water molecules and atomic hydrogen. In alkaline solutions neutral water

is reduced to hydroxide ions and atomic hydrogen. Both reflect the cathodic reaction of the electrochemical process. The so formed atoms can be adsorbed *at* the surface and either recombine to molecules (i) or absorbed *into* the matrix, that is the bulk, (ii). It is noteworthy that only atomic hydrogen can be taken up from the liquid phase. Figure 3.14 schematically depicts both cases which are known as *Volmer-Heyrovsky-Tafel*-mechanism [6].

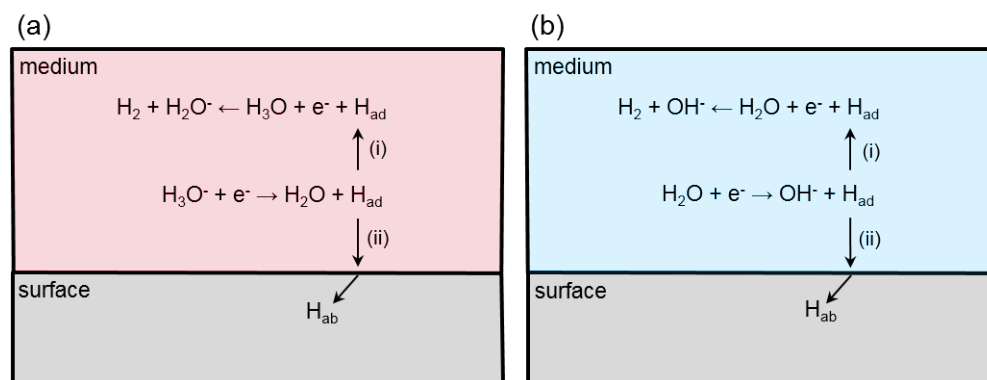


Figure 3.14: Schematic depiction of the adsorption and absorption process of hydrogen in acidic (a) and alkaline solutions (b).

The equations in Figure 3.14 do of course not fully outline the complex process of hydrogen uptake. Formation of a capacitive electrochemical double-layer or diffusion and trapping of hydrogen atoms at energetically favourable sites are not taken into consideration here [79].

Certain chemical elements which naturally occur in aggressive media in which austenitic stainless steel are used hamper the recombination of hydrogen and thus increase the number of adsorbed and absorbed atoms. Typical promoters are phosphorus, arsenate, selenium and sulphur [80]. In research, this effect is taken advantage of: electrolytes for introducing hydrogen artificially into the metallic matrix often contain these so-called *recombination poisons*.

### High-pressure hydrogen

The uptake of hydrogen from the gas phase is different from liquids, because the required step to dissociate hydrogen molecules in the liquid electrolyte is omitted. Possible scenarios are the storage and transportation of hydrogen as fuel and its dispersion from station to vehicle.

In order to bring gaseous hydrogen into the metallic matrix, a certain *dissociation* and *adsorption energy* needs to be provided [78]. To break the molecular bond between two hydrogen atoms, the hydrogen-metal bonds must supply an energy larger than the energy cost of simple moving chemisorbed hydrogen atoms along the surface [81]. Temperature and gas pressure are the main influencing factors of hydrogen adsorption and absorption [82]. They are described by *Sievert's law*, given in Equation 4.

$$c_H = \sqrt{p_{H_2}} * e^{-\left(\frac{\Delta G}{RT}\right)} \quad (4)$$



The soluble concentration of hydrogen in the metal  $c_H$  depends on the partial pressure  $p_{H_2}$ , the reaction enthalpy  $\Delta G$ , the absolute temperature  $T$  and the ideal gas constant  $R$ . The reaction enthalpy is made up of the dissociation energy  $\Delta G_{diss}$  and adsorption energy  $\Delta G_{ad}$ .

Accordingly, high temperature and high pressure facilitate the adsorption of hydrogen into the metal surface. This was pointed out e.g. by Harris and becomes obvious from Equation 4: The dissociation probability increases exponentially with rising temperature  $T$  [81]. The dissociation and adsorption of hydrogen at room temperature is less probable. This is mainly because of the very high free dissociation energy that needs to be provided. As a rule of thumb, Böllinghaus gives values of 200°C and 200 bar to introduce considerable amounts of hydrogen into the surface. However, due to a lower diffusion coefficient, the subsequent absorption can be hampered for instance by oxide layers on the metal surface [78]. Mechanical (plastic) deformation on the other side might enhance this process. This will be discussed in Chapter 3.2.2.2.

### 3.2.2. Transport of hydrogen

Regardless of whether the uptake of hydrogen took place from the gaseous or the liquid phase, the transport into the material can take place in general by diffusion and dislocation-aided.

#### 3.2.2.1. Diffusion-assisted transport

Lattice diffusion is the most common way of hydrogen to move through a metallic matrix. It is the equalisation of differences in concentration by particle movement along the concentration gradient based on the so-called *random walk*. The relation between the hydrogen concentration  $c_H$ , diffusion coefficient  $D$  and the atom flux  $j$  can be expressed by *Fick's laws*. For the steady-state condition the Fick's *first law* is expressed as

$$j = -D \nabla c_H = -D \left( \frac{\partial c_H}{\partial x} + \frac{\partial c_H}{\partial y} + \frac{\partial c_H}{\partial z} \right) \quad (5)$$

A simplified approach, considering only one-dimensional diffusion is given with

$$j_x = -D * \frac{\partial c_H}{\partial x} \quad (6)$$

Both equations are only valid under the assumption of a constant concentration gradient and continuous adsorption and absorption process, the steady-state condition.

Fick's *second law* takes changes in diffusion with time  $t$  into account, i.e. addresses the non-steady-state:

$$\frac{\partial c_H}{\partial t} = D \nabla^2 c_H * \left( \frac{\partial^2 c_H}{\partial x^2} + \frac{\partial^2 c_H}{\partial y^2} + \frac{\partial^2 c_H}{\partial z^2} \right) \quad (7)$$

A one-dimensional expression results in

$$\frac{\partial c_H}{\partial t} = D * \frac{\partial^2 c_H}{\partial x^2} \quad (8)$$

A solution of Fick's second law was given, among many others, by Yamabe *et al.* [83]:

$$c_H(x, t) = c_0 \left[ 1 - \operatorname{erf} \left( \frac{x}{2\sqrt{D_H t}} \right) \right] \quad (9)$$

An even more simplified approach to estimate the *diffusion length* or *penetration depth* of hydrogen into the material is given with Equation 10. Although it regards diffusion as one-dimensional movement and neglects important processes like adsorption or changes in diffusivity, it is used as a rule of thumb in several publications [84–88].

$$x = 4\sqrt{D_H t} \quad (10)$$

The diffusion coefficient of hydrogen in FCC materials such as austenitic stainless steels was determined based on the aforementioned equations. It is in the order of  $D_H = 10^{-16} \frac{m^2}{s}$  [89]. According to Owczarek and Zakroczyński, it is  $\approx 1.4 \cdot 10^{-16} \frac{m^2}{s}$  in the austenite phase of a H25N5M duplex stainless steel [90]. While Li gives a diffusion coefficient of  $2.24 \cdot 10^{-16} \frac{m^2}{s}$  for an AISI 304L grade, permeation experiments of Katsuta and Furukawa yield values of  $4.06\text{--}6.38 \cdot 10^{-16} \frac{m^2}{s}$  in the 304 steel [91, 92].

Böllinghaus *et al.* conducted an extensive literature study to collect hydrogen diffusion coefficients  $D$  of various steel grades [93]. Based on that, the authors plotted *scatterbands* showing the evolution of  $D$  with temperature. The minimal and maximal value at room temperature  $D_{min} = 3.932 \cdot 10^{-17} \frac{m^2}{s}$  and  $D_{max} = 3.659 \cdot 10^{-15} \frac{m^2}{s}$ , respectively, are in perfect agreement with the aforementioned numbers and, thus, underpin them.

A special form of hydrogen movement inside metal lattices is the so-called *Gorsky effect*. It describes a strain- and stress-assisted diffusion towards energetically favourable regions. Tensile stresses offer more space for hydrogen because they enlarge the crystal lattice. Compressive stresses, on the other hand, compress the matrix. Regions of highest tensile stress are therefore the most favourable sites. A diffusion current from compressed regions towards regions under tensile load evolves [94, 95].

### 3.2.2.2. Dislocation-assisted transport

Dislocations are one dimensional defects of the crystal, their origin and movement is the basis of plastic deformation in metals. Like other deviances from the ideal crystal, dislocations change the diffusivity of hydrogen within the metallic matrix. They offer pathways for hydrogen, a phenomenon called pipe diffusion, and bind hydrogen.

Bastien and Azou investigated the strain, strain rate and temperature dependence of hydrogen embrittlement in steel alloys. Concluding from the results, they suggested the concept of hydrogen transport in form of *Cottrell atmospheres*, first published in 1951 [96].

Hydrogen is attached and bond as "cloud" to moving dislocations, wanders through the material and can thus reach higher transport rates in comparison to lattice diffusion. When reaching and surpassing grain boundaries, inclusions or other imperfections, hydrogen may be stripped of the dislocation and attached at the respective obstacle, like sketched in Figure 3.15.

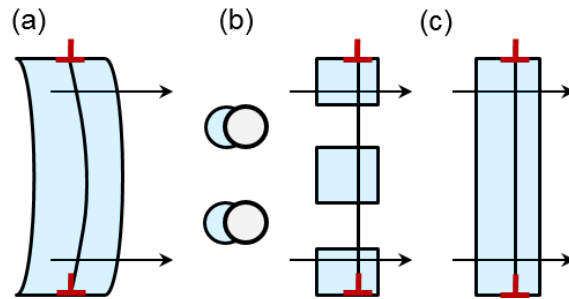


Figure 3.15: A moving hydrogen-decorated dislocation (a) passes two obstacles (b) where part of the hydrogen cloud is stripped off. Pipe diffusion along the dislocation restores the atmosphere as dislocation moves further (c). According to Tien *et al.* [96].

Another indication for dislocation-assisted transport of hydrogen was delivered by Brass *et al.* They compared the desorption flux of the hydrogen isotope tritium ( $^3\text{H}/\text{T}$ ) from strained and un-strained 316L alloy. Samples that were subjected to mechanical load degassed stronger than their non-strained reference. These results allow to draw the conclusion of dislocations transporting hydrogen/tritium to the surface of the specimen [85].

Slow-strain-rate tests (SSRT) on a high-manganese TWIP-steel conducted by Lee *et al.* point to the same direction. In connection with supplementary thermal-desorption analyses (TDA) as well as SEM and XRD measurements, it was obvious that hydrogen was transported deeper into the samples that were mechanically tested [97].

The aforementioned process takes place, if the binding energy  $E_B$  between hydrogen and obstacles is greater than the one between hydrogen and dislocations, which is estimated to be in the order of 0.1-0.5 eV. Not only the transfer from dislocation to trapping sites was identified as a possible scenario for dislocations "loosing" their hydrogen atmosphere. Tien *et al.* stated that beyond a certain velocity of a dislocation, it will be stripped-off the hydrogen cloud.

This phenomenon was observed indirectly in science and industrial applications alike. Hydrogen pre-charged samples were mechanically tested under various strain rates excessively in the past [30, 66, 67, 73, 98–102]. The results were consistent in revealing a reduced strength and ductility of steels with lower strain rate. In these cases, dislocations moved too slowly through the matrix, dragging hydrogen with them. Thus, it unfolded its deteriorative impact.

Pre-strained samples further showed higher total concentrations of hydrogen and greater penetration depth than un-strained ones, whether charged before or during mechanical straining. This can be ascribed to the higher dislocation density  $\rho_d$  in pre-strained materials [103].

### 3.2.3. Trapping

Although hydrogen can diffuse through the metallic matrix, it might cease its movement to occupy several sites of the host lattice. Due to its extremely small size it is able to be incorporated in the interstitial lattice sites of the crystal. The two main crystal structures of steels, body-centred cubic BCC and face-centred cubic FCC, offer different lattice vacancies. Figure 3.16 compares these based on the simple sphere model.

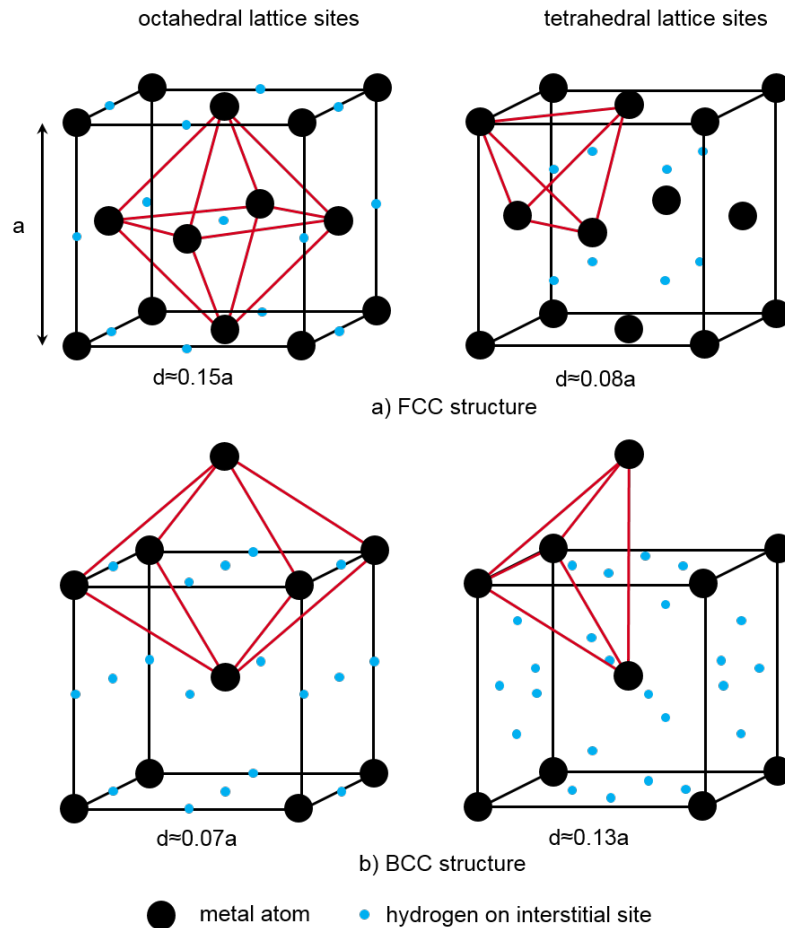


Figure 3.16: Octahedral and tetrahedral lattice sites in (a) FCC and (b) BCC structures of steels. The size of the respective interstices  $d$  is given for every site. Figure according to Grong [104].

In FCC materials like nickel and austenitic steel, hydrogen is preferably solute in the octahedral sites, while it is obvious that hydrogen prefers the larger tetrahedral sites in BCC structures. Rietveld analyses of neutron diffraction data, gathered by Hoelzel *et al.* on the AISI 304 and 310 grades, confirmed this. After charging the materials gaseously, the group revealed that hydrogen was exclusively located on the octahedral sites [105].

From the characteristics of the different structures follows that the BCC phase has a high diffusion rate and a low solubility for hydrogen, which is due to the low packing factor in comparison to FCC. FCC materials are characterised by a lower diffusion rate and a higher solubility due to their close-packed lattice [6].

Interstitial lattice sites are not the only location where hydrogen can be physically stored in the material. Inhomogeneities like phase and grain boundaries, voids, inclusions and dislocations are present in every alloy and can act as traps as well. An overview of these gives Figure 3.17.

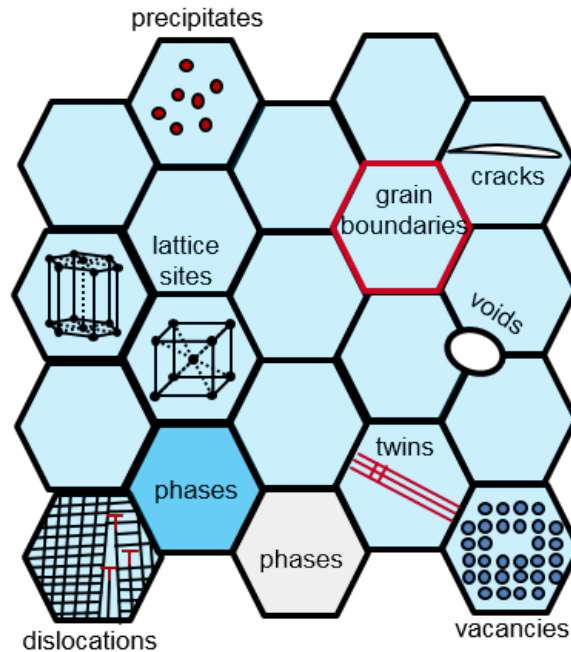


Figure 3.17: Overview of different trapping sites in the microstructure of metals. Figure follows Koyama et al. [23].

The release of hydrogen from these traps, commonly called *de-trapping*, takes place when a higher energy than the binding energy  $E_A$  is provided to the system. Depending on the magnitude of this energy, material science distinguishes *reversible* and *irreversible* traps. Table 3.3 gives a brief overview of different trapping sites and their binding energies, determined by different research groups.

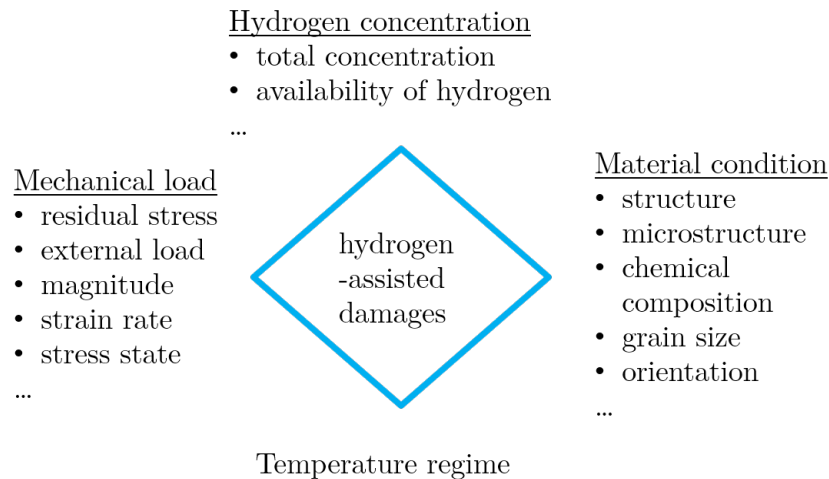
### 3.2.4. Effects of hydrogen on steels

The deteriorative impact of movable hydrogen in the matrix of metallic alloys and, in the frame of the present work, especially austenitic stainless steels, has many characteristics. Hydrogen-assisted damages are influenced by several factors of which the most important ones are the (critical) hydrogen concentration, the material's condition and the mechanical load. The temperature regime plays a vital role too. The scheme in Figure 3.18 illustrates these factors.

Extensive research has been carried out in the past and is still ongoing to describe and explain the complex phenomena of hydrogen-assisted damages. This is also due to the various manifestations these deteriorations have. A reduced mechanical strength, ductility and toughness are the most prominent implications. Metallic alloys might lose their surface integrity by the ingress of hydrogen as well. The next chapter is dedicated to these damages.

Table 3.3: *Trapping sites for hydrogen in metallic alloys and the respective activation energy needed for de-trapping.*

Trapping site	Activation energy $E_A$ [kJ/mol]	Reference
<b>dislocations</b>	29±5	[106]
	26	[107]
	25 (screw)	[108]
	20 (edge)	[108]
<b>vacancies</b>	38±5	[106]
	38-48	[109]
	55	[108]
<b>voids</b>	38±5	[106]
<b>interfaces</b>	87 (TiC-H)	[107]
	94.6 (TiC-H)	[52]
	22 ( $\gamma/\epsilon$ )	[97]
<b>grain boundaries</b>	58.6±5	[52]

Figure 3.18: *Important factors that influence hydrogen-assisted damages.*

### 3.2.4.1. Degradation of mechanical properties

The probably best described deteriorative impact of hydrogen on steels is the reduction of mechanical properties such as strength, ductility and toughness. Several studies and reviews on this topic can be found in the literature [78, 110–113].

In summary it can be said that hydrogen reduces tensile strength and ductility of the tested specimen, whereby high-strength steels are more prone to degradation. Furthermore, research is in agreement about the strain rate influencing the ramifications of hydrogen. High strain rates reduce the deteriorative impact of hydrogen, lower increase it. This is mainly due to the dislocation-drag, described in Chapter 3.2.2.2.

Koyama *et al.*, for instance, conducted tensile tests on charged and non-charged TWIP steel Fe-18Mn-1.2C [114]. Their results vicariously show the negative influence of hydrogen on metals in general and austenitic stainless steels in particular.

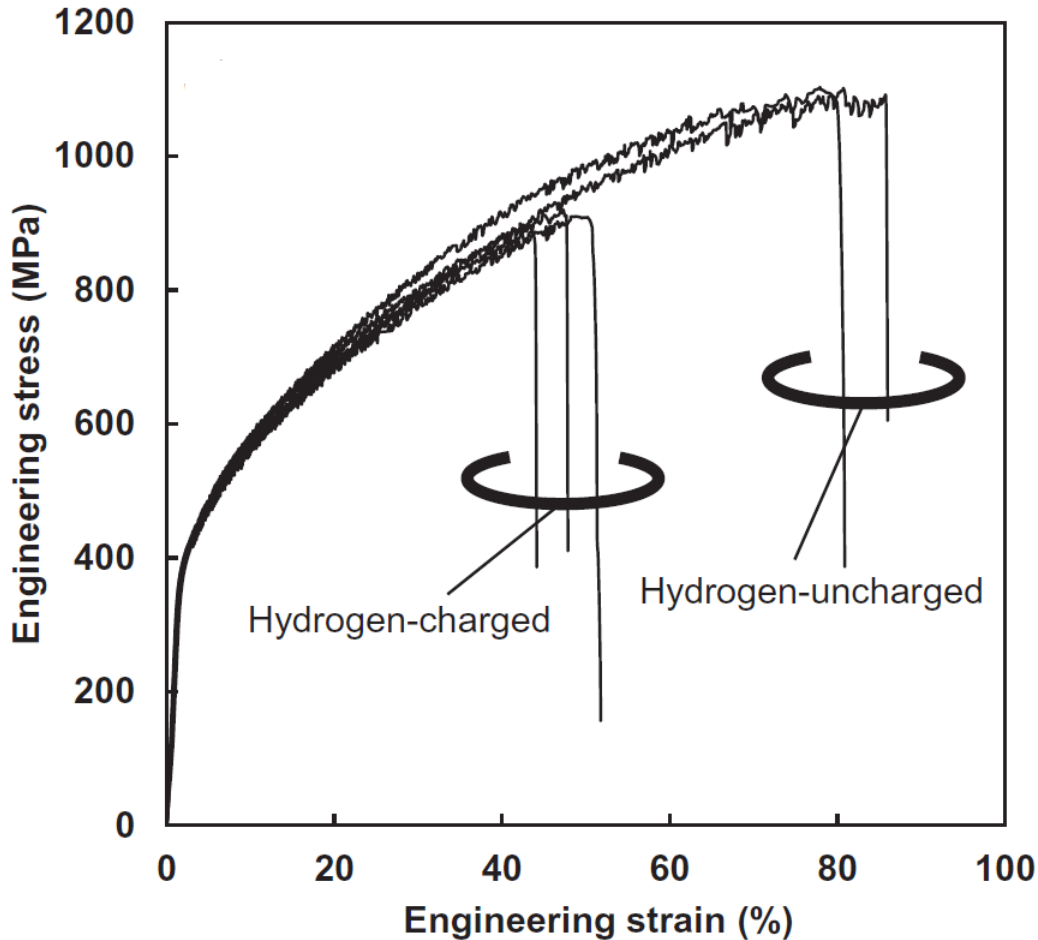


Figure 3.19: Reduction of mechanical tensile strength and ductility of the steel Fe-18Mn-1.2C in the presence of hydrogen [114].

Concomitant to a loss of ductility is the transition from ductile-to-brittle crack behaviour under mechanical load [115, 116]. This can be explained by an interaction of different mechanisms, further described in Chapter 3.2.5.

It is well known that hydrogen not only reduces the maximum strength and ductility during linear (tensile) load. It curtails the fatigue strength and fatigue limit and changes the behaviour of fatigue crack propagation [77, 117–122].

Among many other researchers, Matsunaga *et al.* electrochemically charged the steel grade AISI 304 with hydrogen and subsequently conducted tensile-compression-fatigue tests [77]. They found that the crack growth rate of hydrogen pre-charged samples was higher than in the comparison specimen. An explanation for this was the formation of slip bands acting as pathway

for hydrogen. Transferred to a component in its later application, a faster crack propagation is equivalent to a reduced lifetime.

The work-hardening behaviour of austenitic stainless steels is affected by hydrogen, as well. As it was mentioned before, the stacking fault energy describes the behaviour of steels under plastic deformation, i.e. work-hardening. Austenitic steels with a low SFE tend to form martensite, whereas SFEs higher than  $\approx 18\text{-}20\text{ mJ/m}^2$  foster twinning [40]. Whiteman and Troiano claimed that hydrogen lowers the SFE already 50 years ago [123]. This was underpinned by XRD and TEM analyses e.g. by Pontini and Hermida [57].

A hydrogen-decreased stacking fault energy will therefore influence not only the ultimate tensile strength of a material but its ductility and fatigue strength. A lower SFE promotes the formation of  $\alpha'$ -martensite which is not only more brittle than the native austenite but offers a faster pathway for hydrogen into the material (cf. Chapter 3.2.2).

### 3.2.4.2. Loss of surface integrity

Hydrogen diffusion and accumulation in metallic lattices alters the surface microscopically. Among others, the formation of blisters and cracks is one manifestation.

Laureys *et al.* charged ultra-low carbon steel samples, differently treated for different times with hydrogen [124]. The observed number and geometry of blisters strongly depended on the pre-treatment of the material. Cold-deformed specimens showed severe blistering, while recrystallised samples suffered much less from this damage. From that, the authors concluded that deformation-induced defects, such as micro-cracks and dislocations, hampered diffusion of hydrogen into the material and caused its accumulation underneath the surface. This led to bulging of the surface and eventually to cracks.

Zhang *et al.* investigated pipe-line steel API X80 und cathodic protection [4]. With higher current density during charging, simulating cathodic overprotection of the pipe-line during service, the amount and size of blisters increased as well.

The occurrence of blisters in highly alloyed steels was proven e.g. by Sobol *et al.* on a duplex stainless steel (DSS) 2205 [125]. It was shown that blistering occurred solely in the ferrite. Cross-sectioning blisters allowed following conclusion: Due to the high diffusivity of hydrogen in BCC phases, high amounts of hydrogen entered ferritic grains. Subsequently it was trapped at the interface to the austenitic grains lying underneath where it accumulated. A primary crack was formed. After reaching a certain concentration of hydrogen-induced mechanical strain and caused secondary cracks that damaged the surface.

Among others, Yang *et al.*, Tiegel *et al.*, Rozenak *et al.* and Saleh *et al.* demonstrated the formation of blisters and surface cracks due to hydrogen charging, as well [126–129].

It has to be emphasised that cracking and blistering are hydrogen-induced phenomena that can take place even in the absence of external stress and strain.

The described hydrogen-assisted damages will only occur under certain conditions, as it was indicated by the scheme in Figure 3.18. For instance austenitic stainless steels are less prone to "hydrogen embrittlement" than ultra-high-strength martensitic steels (UHSS). ASS can absorb



much higher amounts of hydrogen into their lattice before the critical concentration to initiate the deteriorative effect of hydrogen is reached. Hydrogen-assisted cracking and degradation of metals is always a result of synergies of the surrounding conditions.

### 3.2.5. Mechanisms of hydrogen-assisted damage

As diverse as hydrogen may degrade steels, leading to failure of parts and components, as diverse theories were developed describing their origin and underlying processes.

#### 3.2.5.1. Hydrogen-Enhanced Localised Plasticity - HELP

The *HELP*-mechanism describes the phenomenon of *hydrogen-enhanced localised plasticity* in steels. Tavares *et al.*, for instance, defined it as enhanced mobility of dislocations in preferred crystallographic planes in high-strained regions such as crack tips. Along these planes cracking occurs by microvoid coalescence. Small dimples next to cleavage regions at the fractured surface of tensile samples are typical features for that [101].

Although it was known before, Beachem delivered the first interpretation of this phenomenon in 1972, laying the basis for the description of hydrogen-enhanced dislocation movement later delivered by Birnbaum and Sofronis [130, 131].

Part of their concept is the perception that hydrogen segregates to dislocations (and other obstacles) and concomitantly alters the stress field around them. The movement of dislocations through the lattice and across obstacles requires a certain energy. This amount of energy is reduced when the elastic stress field is decreased. Hence, they can move more easily in the presence of hydrogen. Due to the promoted dislocation slip, the material's yield strength decreases.

An increased mobility of these hydrogen-decorated dislocations will further lead to an accelerated transport of hydrogen into the material, accelerating also hydrogen-assisted cracking.

Experimental as well as application-oriented studies proved that hydrogen facilitates dislocation movement as was done by nano-indentation tests, mechanical testing on bulk specimens, where softening and strain localisation could be observed, and TEM observations [132].

The first direct experimental prove was delivered by Bond *et al.* and Lee *et al.* [133, 134]. By means of a TEM with a custom-built objective pole-piece that could be flooded with hydrogen gas, the researchers were able to strain steel samples during observation. These sophisticated experiments proved the dislocation movement, and thus localised plasticity, triggered by hydrogen. It could also be shown that the distance between piled-up dislocations and the cross-slip is decreased.

In contrast to this softening effect is the hardening effect that can be ascribed to hydrogen atmospheres around dislocations, pinning dislocations. However, this effect is only of importance in temperature and strain rate regimes, in which hydrogen cannot keep up with dislocations [132].

### 3.2.5.2. Hydrogen-Enhanced Decohesion - HEDE

High localised hydrogen concentrations weaken the metallic bonds of the host lattice and may lead to the separation of atoms. This process is called *hydrogen-enhanced decohesion*. Furthermore, hydrogen atoms lower the surface energy of atomic planes and grain boundaries and therefore promote cleavage-like fractures [116].

Sufficiently high hydrogen concentrations occur if very high elastic stresses prevail. The weakening of metallic bonds results from a decrease in the electron-charge density between metal-metal atoms due to the presence of hydrogen. According to Lynch, this can happen, for example, in the vicinity of sharp crack tips, in regions of high hydrostatic stress fields in the distance of about twice the crack-tip-opening displacement, particle-matrix interfaces or specifically built grain boundaries [132].

Macroscopically, the decohesion of the lattice is revealed by a quasi-cleavage fracture surface due to localised brittle material behaviour. Typical features are (quasi-)cleavage and intergranular fractures [101]. Among many other groups, Pan *et al.* investigated the austenitic grade AISI 304L by means of SSRT and SEM of pre-charged samples. In connection to measurements of the hydrogen concentration within the specimen, the group was able to trace the ductile-to-brittle transition with increasing amount of hydrogen, leading to a decreased stress intensity factor [115].

Based on ab-initio density functional theory calculations, Dadfarnia *et al.* showed that the HEDE mechanism does not take place only by physical stretching and breaking of atomic bonds but by an electron/charge transfer [135]. Figure 3.20 stems from this simulation.

Figure 3.20a) shows that electrons are removed from iron atoms adjacent to the grain boundary and also from the hydrogen within the GB. These electrons are transferred to Fe atoms within the grain boundary, leading to decohesion, because less electrons participate in the Fe-Fe bonds. Figure 3.20b) shows that surface hydrogen is more favourable than the one at grain boundaries. A reduction of bonding is caused by a charge loss of a hydrogen atom. Adjacent sub-surface Fe atoms increase their charge and therefore strengthen bonding [135].

### 3.2.5.3. Adsorption-Induced Dislocation Emission - AIDE

While HELP is a model describing the enhanced mobility of dislocations due to *internal* hydrogen, AIDE delivers an interpretation for the enhanced formation and emission of dislocations evoked by *external* hydrogen. In its essence, the *adsorption-induced dislocation emission* takes place due to hydrogen decreasing the formation energy of dislocations in the vicinity of crack tips and the reduction of the nucleation energy of kink pairs [101, 136, 137]. The mechanism of AIDE can be seen as a part of the *DEFECTANT* concept developed by Kirchheim that describes the reduction of the formation energy of different kinds of defects by solute segregation. The higher the chemical potential and concentration of the respective solute atom, the greater the decrease [138].

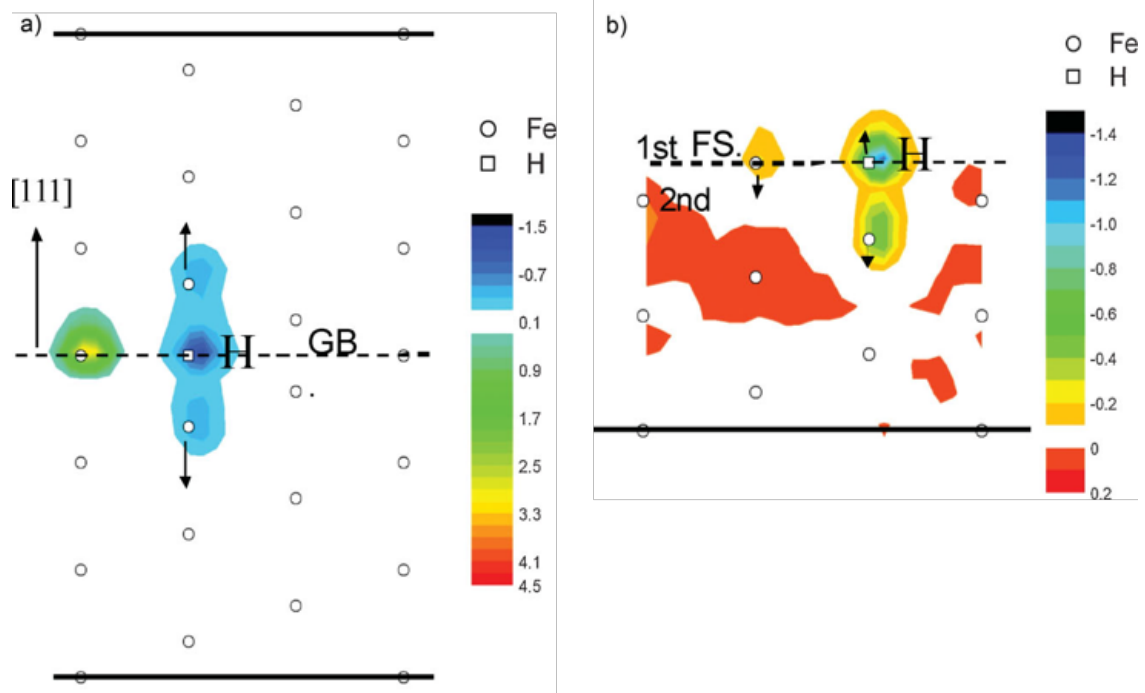


Figure 3.20: *Electronic charge-density-difference contours for (a) a  $\Sigma 3$  grain boundary (GB) and (b) the free surface (FS) in BCC iron. Blue colour indicates an electron deficit, red contours an excess of electrons. Figure taken from [135].*

In fact, the AIDE mechanism shares similarities with both aforementioned models. It "combines" the weakening of interatomic bonds as for HEDE with crack growth accompanied by localised slip like in HELP theory [132].

When Lynch first proposed the AIDE concept, he pointed out that even though the formation of dislocations is facilitated locally, the consequence still is the embrittlement of the material [132].

In the absence of a critical concentration of hydrogen, ductile crack propagation proceeds by coalescence of micro-voids ahead of the crack. This is connected to the formation and emission of dislocation from the plastic zone *ahead* of the crack tip. Because only a few dislocations are emitted directly from the crack tip and converge it, blunting takes place. Therefore crack propagation requires large strains.

With hydrogen present in the surrounding media and *adsorbed* into the first atomic layers, dislocations are not only formed more easily but may also allow alternate slip on both sides of the crack. The necessary strain for coalescence with voids is decreased by that. A facilitated crack propagation with reduced dimple size is the result [132].

Robertson *et al.* yielded information about this effect with in-situ TEM experiments on a nickel alloy [139]. In addition to hydrogen-induced changes in the dislocation mobility and cracking behaviour, dislocations were emitted from the crack tip and the grain boundary ahead of the crack.

Calculations of Barnoush *et al.* showed that the free energy  $G$  in hydrogen-charged samples is increased with respect to non-charged materials. The difference between these curves is the

driving force  $\Delta G_H^*$  for dislocation emission. It increases up to a certain dislocation loop size  $r^*$  [136]. Additionally, their nano-indentation measurements clearly revealed that the so-called pop-in load is lower in hydrogen-charged specimen. From their results a hydrogen-induced reduction of the activation energy for homogeneous dislocation nucleation can be concluded.

It is obvious that none of the above mentioned processes takes place separately from each other. For example, Djukic *et al.* gave a comprehensive review of the synergistic impact of localized plasticity and decohesion in different metals [140].

#### 3.2.5.4. Phase transformations

As discussed in Chapter 3.1.3.1, austenitic stainless steels may transform to martensite when subjected to mechanical load or low temperature. Not mentioned above is the influence of hydrogen on these materials and its capability to trigger martensite formation.

Already in 1982, Tanino *et al.* reported the formation of HCP platelets on the  $\{111\}$  planes in AISI 304 after cathodic charging [141]. Other researchers observed  $\gamma \rightarrow \epsilon$ - and  $\gamma \rightarrow \alpha'$ -transformation as well.

Because of the high complexity and the interplay of different effects hydrogen can have on (austenitic) steels, there is not only one mechanism causing structural changes in the material. Khatak *et al.*, Głowacka *et al.*, Koyama *et al.* and Pontini *et al.* have e.g. stated that hydrogen lowers the stacking fault energy of austenitic stainless steels [57, 114, 142, 143]. As Chapter 3.1.3.2 described, a SFE lower than  $\approx 20 \text{ mJ/m}^2$  support the dissociation of dislocations and the formation of martensite.

Beside this "chemical influence", hydrogen exerts mechanical force on the metallic lattice it is dissolved in. Based on that is the *internal pressure theory* developed by Zapffe and Sims that explains hydrogen-induced void and crack growth in metals [144]. Several researchers questioned this theory though [52]. One point of criticism is the high amount of hydrogen necessary to obtain high pressure within the material. This can be only delivered by high-fugacity charging, irrelevant for industrial applications.

A transformation of the FCC phase into BCT phase has different implications. Macroscopically, it is especially connected to an increased strength and a reduced ductility. As Garion *et al.* stated, structural transformation would have severe consequences on the performance of joints in particle accelerators. This is due to the transition from para- to ferro-magnetism [29].

Also the higher diffusivity of hydrogen in the newly developed martensite (cf. Chapter 3.2.3) is critical because it accelerates the ingress of hydrogen into the material (under load) and, thus, accelerates hydrogen-assisted damage.

### 3.3. Approaches to evaluate hydrogen-assisted damage

#### 3.3.1. Mechanical characterisation

Relatively easy and simple methods to assess the deteriorative impact of hydrogen on metallic alloys are given by mechanical testing methods. Among those are tensile, pressure, flexural tests,

nano-indentation measurements and Charpy impact tests. As different as the experiments and the resulting mechanical parameters are, they deliver valuable information on strength, ductility, hardness and toughness.

Numerous researchers conducted tensile tests on different alloys and compared the materials behaviour in the absence and in the presence of hydrogen [31, 59, 66, 102, 114, 145–150]. Summarising it can be said that hydrogen lowers the ultimate tensile strength, yield strength and elongation of the tested specimen.

The resistance of steel against fatigue crack growth was investigated e.g. by Tsay *et al.* [147, 151–154], Kawamoto *et al.* [155], Bahrami *et al.* [156] and Saintier *et al.* [121]. Valuable information about the durability of parts and components for industrial applications could be drawn from the results. Samples that were tested in gaseous hydrogen atmospheres can therefore reflect components for the still to be established hydrogen infrastructure. In dependence of the applied pressure hydrogen enhanced the crack propagation rate of the material and also decreased the fracture toughness.

The influence of hydrogen on the nucleation of dislocations was, e.g., investigated by Barnoush *et al.* by means of nano-indentations [157]. Their measurements, performed on a cathodically polarised Fe-3wt.% Si alloy, revealed lower pop-in loads with higher hydrogen content. From that, a facilitated dislocation nucleation was concluded.

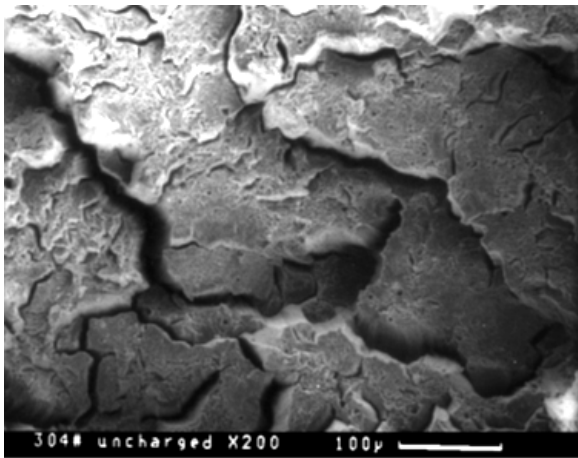
Although mechanical tests can describe the impact of hydrogen on the materials properties, the main drawback of these methods is the lack of information about the localisation of hydrogen. The results, thus, do not allow to draw conclusions about the underlying mechanism leading to the materials degradation.

### 3.3.2. Microscopic analyses

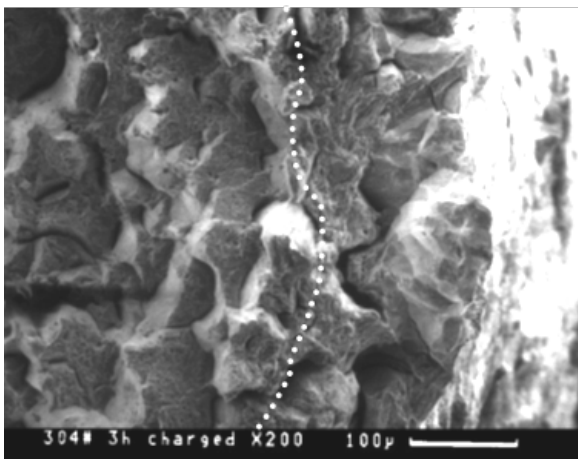
In combination with mechanical characterisation techniques, microscopic examinations can deliver useful information of how the degradation of macroscopic features like strength and ductility is reflected on the microscopic scale. For this reason, a great number of researches conducted SEM analyses of the fracture surface of previously tested specimens [19, 76, 114, 130, 142, 158–173]. It was found that a transition of the cracking mode from transcrystalline to intercrystalline, from ductile to brittle, can take place in samples charged with or tested in hydrogen (atmosphere).

Au studied the influence of hydrogen and tritium on the cracking behaviour of the grade AISI 304. Some of these results are shown in Figure 3.21.

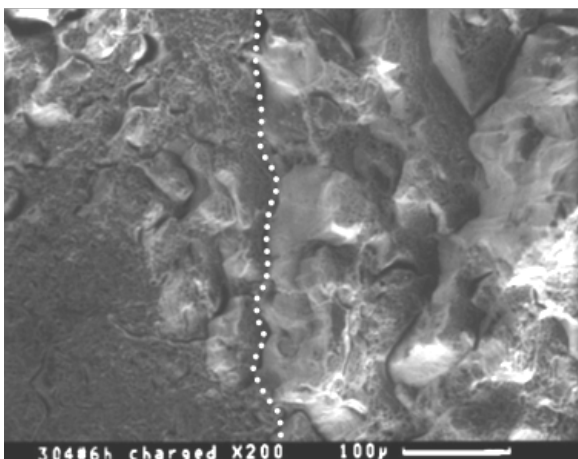
The evolution of hydrogen-induced brittle fracture within an otherwise ductile material is clearly revealed by the SEM images. Higher amounts of hydrogen caused a stronger decrease of the mechanical properties as well as larger fractions of intergranular, brittle cracks. The reason for the ductile-to-brittle transition is due to hydrogen lowering the cohesive force of the lattice, explained by the HEDE mechanism. According to Rhode, it can be summarised as follows [174]:



Transgranular cracking of the **uncharged** specimen made from AISI 304.

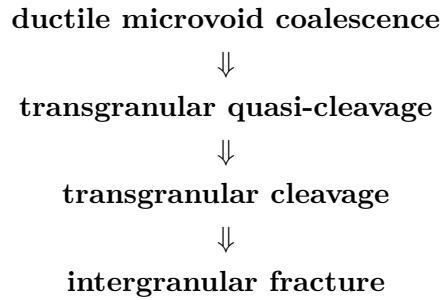


Brittle fractured outer part ("crown") of a specimen containing **25 ppm** of hydrogen.  
Reduction of strength: 10%  
Reduction of ductility: 20%



Brittle and ductile features in the central area of a specimen with **45 ppm** of hydrogen.  
Reduction of strength: 16%  
Reduction of ductility: 23%

Figure 3.21: Fracture surfaces of tensile specimen from AISI 304 steel with different hydrogen contents. A ductile-to-brittle transition occurs with higher amounts of hydrogen. Adapted from Au et al. [168].



The combination of complementary mechanical and microscopical examination methods gives only indirect clues of how hydrogen influences the material but provides no information of *where* hydrogen is located in the microstructure.

### 3.3.3. Hydrogen mapping techniques

Hydrogen mapping techniques fill this gap by visualising directly or indirectly the distribution of hydrogen in the material. Table 3.4 gives a brief overview of the different techniques.

#### 3.3.3.1. Secondary ion mass spectrometry

Secondary ion mass spectrometry is a highly versatile tool for the characterisation of solid materials. Its principle is based on the acceleration of primary particles, their impact on the sample and the subsequent detection of the sputtered secondary particles from the target surface. From that very simplified point-of-view, its functioning is comparable to instruments like secondary electron microscopes, where primary electrons lead to the emission of secondary electrons.

Viehböck pioneered the development of SIMS with a prototype, where he placed a gas discharge tube slightly above a specimen. Already away in 1949, the feasibility of this approach was demonstrated first [180, 181]. 40 years later, secondary ion mass spectrometry was an established, well-proven analytical technique. A rough classification of SIMS instruments can be done by the flux of primary ions impinging upon the specimen. SIMS working with ion doses smaller than  $10^{12}$  ions/cm<sup>2</sup>, the so-called *static limit*, are regarded as *static*. Even though SIMS is a destructive analysis, this ensures that secondary ions are released from quasi-unaltered areas. In contrast to that, *dynamic* SIMS operates with higher primary ion fluxes. This allows a deeper and faster penetration into the material and the analyses of layers deep-seated in the sample. The detection of trace elements is enabled by the high erosion rate and the larger amount of sputtered secondary ions in comparison to the static case.

When a solid sample is sputtered by primary ions of a few keV energy, a fraction of the particles emitted from the target is ionized. Secondary Ion Mass Spectrometry consists of analysing these secondary ions with a mass spectrometer. Secondary ion emission by a solid surface under ion bombardment supplies information about the elemental, isotopic and molecular composition of its uppermost atomic layers. The secondary ion yields will vary greatly according to the chemical environment and the sputtering conditions (ion, energy, angle). This can add complexity to

Table 3.4: Overview of hydrogen mapping techniques [175–179].

mapping technique	function
Silver decoration/ hydrogen microprint technique (HMT)	Immersion of the sample with a reactive emulsion (e.g. $KAg(CN)_2$ ). The absorbed hydrogen reduces Ag ions to metallic silver. These clusters are localised by an SEM and reflect the H distribution. Lateral resolution: sub-micron (depending on Ag cluster size and SEM resolution).
Electron-stimulated desorption technique (ESD)	An electron beam excites the bonding state between adsorbed hydrogen and the surface. Due to the bombardment, ions leave the surface and are gathered by a two-dimensional pulse counting system in dependence of the ion energy. From that a 2D map can be reconstructed. Lateral resolution: tens of micrometers.
Scanning Kelvin probe force microscopy (SKPFM)	An oscillating nm-sized tip with a defined potential scans the specimen surface and records either the electrostatic force interaction or the surface topography. Both data give information about the evolution of the hydrogen in the surface, reflected in changes in contact potential and topography. Lateral resolution: tens of nanometres.
Neutron tomography NT	Bombardment of a rotating specimen with neutrons which interact much stronger with the hydrogen's protons than with the cores of the alloying elements. A scintillator transforms the signal of the transmitted neutrons into visible light which is detected by a camera. Thus, a 3D mapping is possible. Lateral resolution: 20-30 $\mu\text{m}$ .
Atom probe tomography (APT)	By applying high voltages on the sample (few nm tip), atoms are ionised and leave the sample. The position of these evaporated atoms is determined, allowing a 3D reconstruction of the atomic distribution. Lateral resolution: several nanometres down to lattice parameter resolution.
Secondary ion mass spectrometry (SIMS)	The bombardment of the specimen with primary ions sputters secondary particles from the surface. The ionised particles hit the channel plate and can be distinguished according to their flight time. A 2-dimensional image showing the local distribution of ions results. Lateral resolution: several ten to few hundred nanometres; mass resolution $> 10000$ .



the quantitative aspect of the technique. SIMS is nevertheless recognized as the most sensitive elemental and isotopic surface analysis technique.

### The sputter process

In the course of machine development, several primary ion sources, such as Nielsen, hollow cathode or duo-plasmatron ion source, have been tested. Dynamic SIMS operates often with caesium and oxygen sources, while static SIMS uses bismuth, gallium or gold, as well as argon or carbon cluster ions.

Primary particles are accelerated and focused by a complex lens system that is illustrated schematically in Figure 3.22.

When the primary ions (PI) hit the surface a so-called *collision cascade* starts. This leads to the emission of mono- and polyatomic secondary particles, backscattered ions, electrons and photons. Only about 1% of these particles are ions that can be used for analyses in standard ToF-SIMS instrumentations. Using e.g. laser post-ionisation or cluster signals normalised to the sputter ion signal, increases this number and thus the information content [182, 183].

The sputter yield, i.e. the number of sputtered atoms per incident particle, is highly dependent on the (crystal) structure, orientation, mass and temperature of the sample and further also on mass, energy and incidence angle of the primary ion beam. It increases up to a certain angle and increasing ion mass, acceleration energy and current up to a specific maximum and then decreases again. In contrast to that, the excited volume which determines the regime of the collision cascade, decreases with increasing primary ion mass. The single collision regime results from the bombardment with relatively light ions (e.g. He) at low acceleration voltages (e.g. 1 keV). The linear cascade regime occurs when ions of medium or higher masses and energies of about  $1 \leq U \leq 10$  keV hit the sample. It is characterised by a relatively long mean free path of the colliding ions. The use of highly accelerated, high mass ions leads to the spike regime. Not only does it induce the biggest damage in the surface, but furthermore localised heating of the sample [184, 185].

As mentioned above, the sputter yield depends on the constitution of the specimen. The electronic state of the matrix atoms is of crucial importance for the ionisation probability during ion bombardment. Reactive ions like caesium and oxygen enhance this probability [187].

Differences in the sputter yield can lead to *preferential* sputtering when analysing multi-component materials with SIMS. The unequal erosion rate of the various constituents of the sample result not only in a surface relief, but further in the change of the surface composition as compared to the bulk. This *altered layer* is enriched with the component of the lowest sputter yield [184].

Within the altered layer, the implantation of primary ions has to be considered as another factor that influences the outcome of SIMS measurements. The depth of implantation depends on the acceleration energy and mass of the sputter ion and is about 1-10 nm. Ion implantation thus alters the stoichiometric composition of the surface layers.

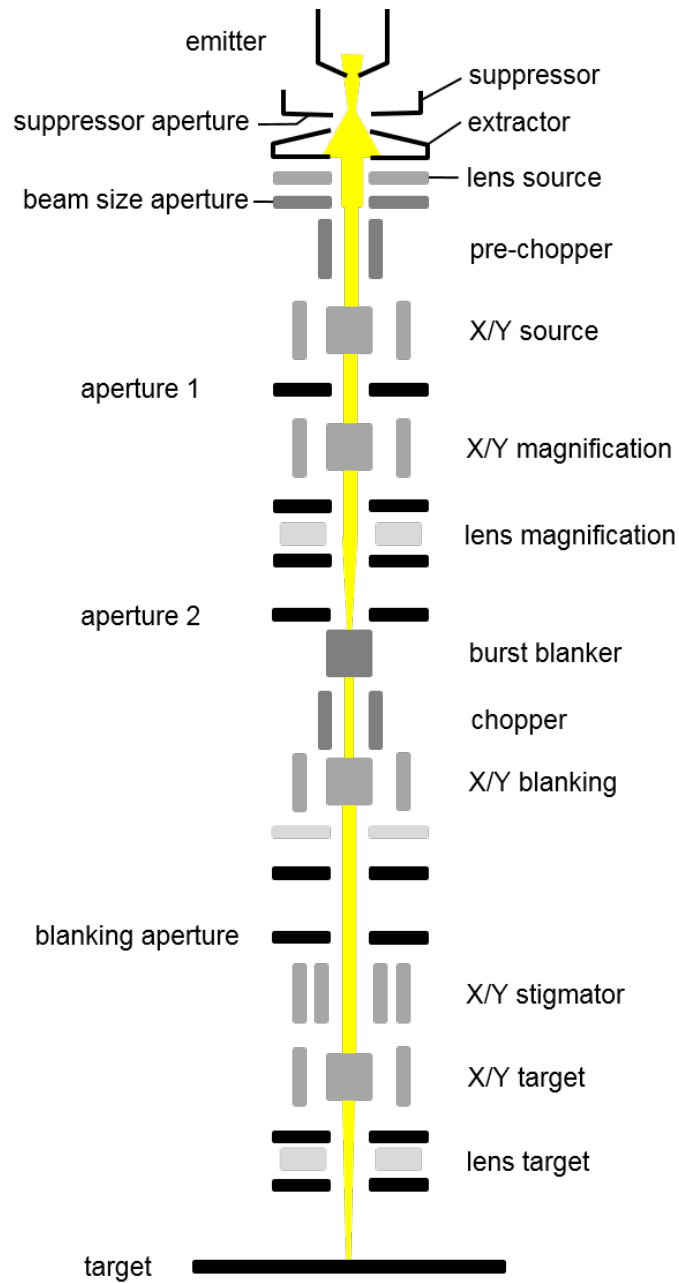


Figure 3.22: Schematic depiction of the liquid metal ion gun (LMIG) to generate, accelerate and focus a bismuth ion beam for analysis, adapted from IONTOF GmbH.

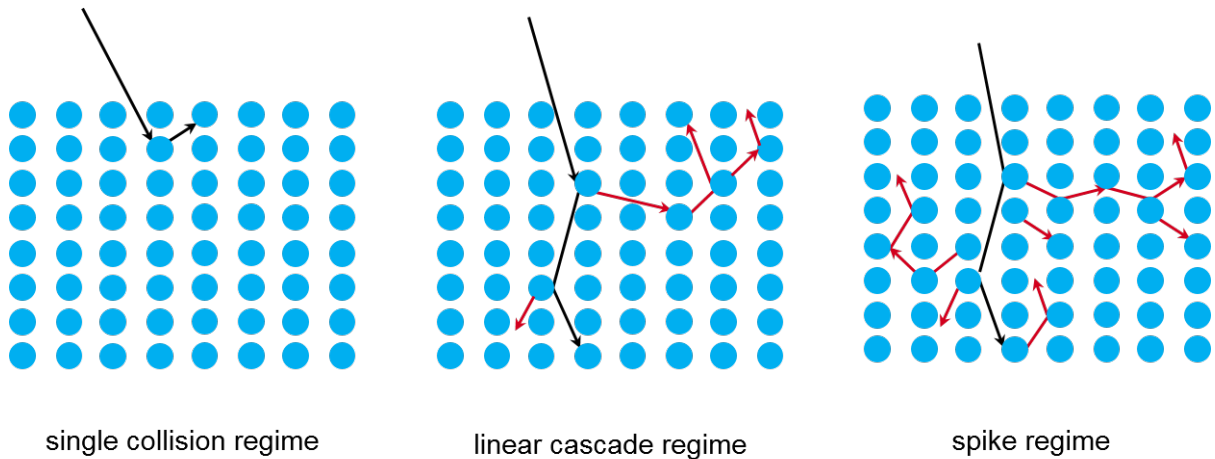


Figure 3.23: Schematic depiction of the different sputter regimes depending on the mass and kinetic energy of the primary ion. Scheme following Sigmund [186].

### Time-of-Flight Secondary Ion Mass Spectrometry

Various different detectors have been developed to analyse the secondary particles emitted from the surface. Among those are quadrupole, magnetic sector field detector, ion cyclotron resonance mass analysers and ion trap mass analysers [188]. Because it would go beyond the scope of the present work, only the time-of-flight (ToF) detector will be explained here.

After secondary particles are sputtered from the specimen surface, the ionised fraction is accelerated by an electric field towards the ToF analyser. Before reaching this, they drift through a field-free zone that is called flight tube. Since every ion acquires the same kinetic energy, their mass determines the velocity with which they travel through the flight tube. From the time-of-flight  $t$  that can be measured, the mass-to-charge ratio  $\frac{m}{q}$  can be obtained with the help of Equation 11:

$$t = L * \sqrt{\frac{m}{2qU_e}} \quad (11)$$

Here,  $L$  is the length of the flight tube and  $U_e$  reflects the acceleration voltage. From this it also becomes clear that light elements will reach the detector faster than heavier elements which allows their separation.

The operation principle is schematised in Figure 3.24.

Big advantages of ToF-SIMS instruments are a practically unlimited mass range from 1 (hydrogen) to extremely large molecules in the range of hundreds of kilo Dalton and a high sensitivity [188].

A drawback in the use of time-of-flight mass spectrometers used to be the poor mass resolution. In order to increase this, the length of the ion formation pulse (time distribution), the size of the volume where the ions are formed (space distribution) and the variation of the initial kinetic energy of the ions (kinetic energy distribution) need to be optimised. Longer flight paths increase

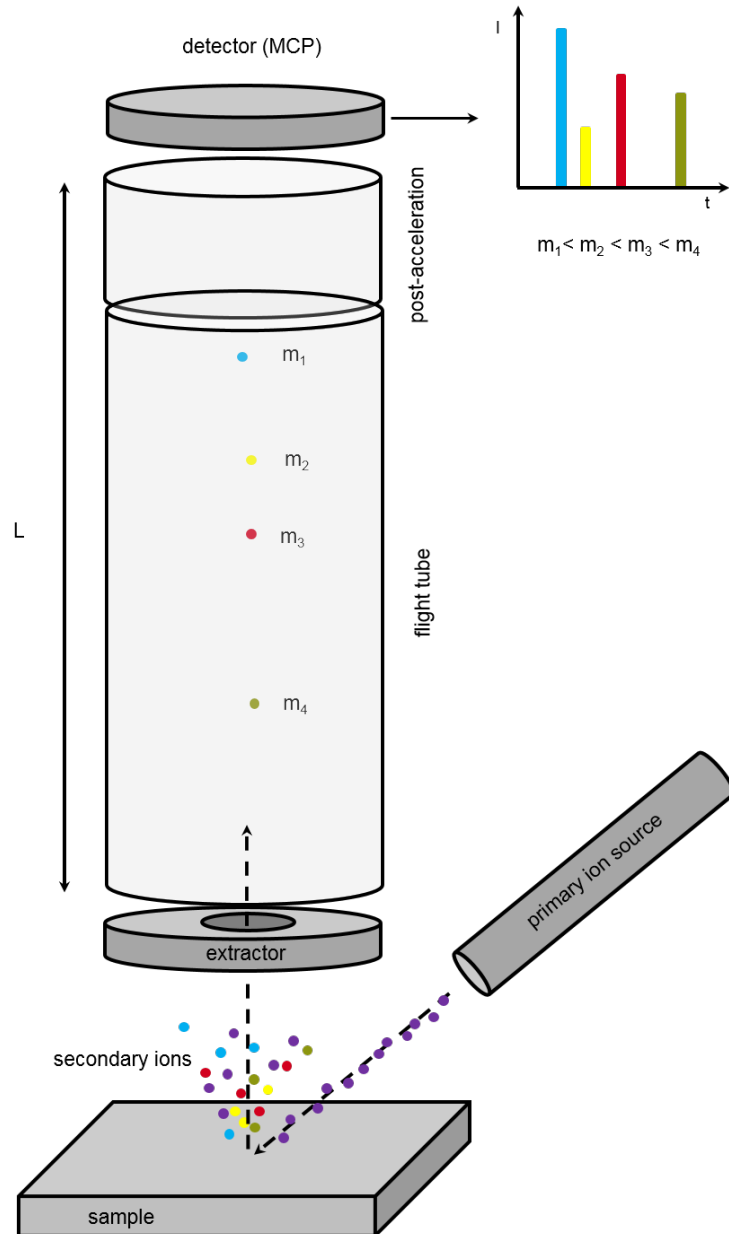


Figure 3.24: Schematic depiction of the function of a time-of-flight detector. Primary ions hit the surface and sputter secondary ions with the masses  $m_1 < m_2 < m_3 < m_4$  from the surface. They are extracted, pass the flight tube and hit the detector with a time offset that indicates their mass.

the mass resolution as well [188]. When two ions hit the detector at the same time, their masses might be mistakenly summed up and counted as one heavier element. The differentiation between ionic molecules with the same mass-to-charge ratio is also not trivial.

For some applications, the low sputter rates in comparison to dynamic SIMS can be another disadvantage.

### Secondary Ion Mass Spectrometry in Hydrogen Research

(ToF-)SIMS is a well-established and often used method especially in biology, chemistry and microelectronics or as a means for quality control [175, 189–194]. The analysis of hydrogen in metallic alloys is a rather exotic application. Nonetheless, several groups proved its feasibility and value for hydrogen research.

Frank *et al.* conducted perhaps one of the first SIMS studies to gain knowledge about the diffusion and trapping behaviour of the AISI 302 grade [195]. They made depth profiles with a dynamic SIMS on electrochemically charged specimen of which half was plastically strained before analyses. The results clearly showed a deeper penetration into the matrix in the strained specimen, caused by enhanced diffusion.

In 1994, Gao *et al.* and Oltra *et al.* analysed the hydrogen distribution around crack tips in strained and pre-charged ferritic and duplex stainless steel, respectively [196, 197]. Both groups observed a hydrogen re-distribution in the vicinity of the crack and a transition in the cracking mode.

Takai *et al.* identified grain boundaries and segregation bands in high-strength steel as possible trapping sites for hydrogen after conducting tensile tests in a deuterated, aqueous solution [198].

The influence of hydrogen on the plasticity of austenitic stainless steels was investigated by Brass *et al.* in 2006. Different charging conditions were tested for the introduction of hydrogen and deuterium in AISI 316L coupons to study the diverging influence on subsequent tensile tests [85].

Kawamoto *et al.* investigated the local hydrogen distribution around fatigue crack tips in AISI 304 austenitic steel with secondary ion mass spectrometry and hydrogen microprint technique [155]. They pointed out that SIMS detected hydrogen in the plastic zone near the crack tip, but that the HMT was not able and ascribed this to difficulties for hydrogen to effuse from the sample. Furthermore, the researchers described the problem of a false detection of hydrogen due to edge effects. Nevertheless, since the group did not take the hydrogen signal from the background into consideration, the results are questionable.

Based on the work of Straub *et al.*, Sobol *et al.* used a ToF-SIMS to successfully map the varying deuterium distribution in the ferritic and austenitic phases in duplex steels and to show the detrimental effects of the hydrogen isotope on the materials (micro-)structure [125, 199–202].

Similar results were obtained by Tanaka *et al.* as they analysed DSS and Fe-30% Ni alloys with a Ga-FIB-ToF-SIMS [203]. They were also able to observe grain boundaries providing fast diffusion paths in the nickel alloy.

Only recently, MnS inclusions as trapping sites for hydrogen were identified with a dynamic NanoSIMS by Al-Aboura *et al.*. For this, the authors charged commercial AISI 303 alloys (cf. Figure 3.4) with deuterium [204].

McMahon *et al.* investigated the distribution and behaviour of deuterium in compact tension specimens after fatigue testing [205]. The samples were gaseously pre-charged AISI 316L grades. The researchers were able to visualise localised deuterium enrichment within dislocation clusters, strongly supporting the HELP mechanism.

### 3.3.4. Quantitative examination methods

The aforementioned techniques are able to measure the (negative) effect of hydrogen on the material (cf. Chapter 3.3.1) or to portray the distribution (cf. Chapter 3.3.3), they do not yield the exact concentration within the lattice. For this, techniques like carrier gas hot extraction (CGHE) and thermal desorption spectroscopy (TDS) are deployed. With the help of these techniques, not only the overall amount of hydrogen can be measured. They allow also the determination of diffusion coefficients for a constant temperature [174, 206] and the assignment of effusing hydrogen to different trapping sites like precipitates, grain boundaries or interfaces [70, 207–209]. Basic principle for both is the exposure of a hydrogen-charged specimen to a controlled temperature-time regime and the simultaneous detection of releasing hydrogen. This can be done e.g. by a quadrupole mass spectrometer or thermal conductivity detector.

In order to activate the diffusion of trapped hydrogen from the sample, it is typically heated to a distinct temperature to provide the necessary energy. However, there were also successful cryo-TDS investigations in which austenitic steels were cooled down. This was done to study the hydrogen desorption during  $\gamma \rightarrow \alpha'$ -phase transformation [75, 89].

The hydrogen content in a metallic specimen may be determined through quantitative methods but it can not deliver information on the impact of this specific concentration. This of course holds true for all the other methods discussed in this chapter. It is therefore inevitable to combine different techniques to be able to draw a full picture of the interplay between *hydrogen concentration*, *material* and its (micro-)structure and the *stress state*.

## 4. Objectives of the present investigations

According to the state of the art presented in the previous chapters, several conclusions can be drawn. Austenitic stainless steels are steels that contain high amounts of alloying elements such as chromium and nickel. As a result, this class of steel possesses a face-centred cubic crystal structure even at room temperature and below. This provides ASS with a high ductility and toughness. Because of that and a high corrosion resistance, these alloys find various applications for instance in the automotive production, the pulp and paper industry, the food sector and in medical applications.

By applying an external mechanical load or by cooling below the so-called  $M_S$ -temperature, the FCC austenite might transform into BCC martensite via an intermediate hexagonal phase. Connected to that is a dramatic change of the mechanical properties such as strength, ductility and fatigue behaviour. Moreover, an altered crystal structure leads to enhanced diffusivity for hydrogen. This is of high relevance for other branches, such as the chemical and petrochemical industry and the renewable energy sector, where ASS are commonly used. Parts and components that are used in these applications encounter aggressive, hydrogen containing media or even pure highly-pressurised hydrogen gas. An external load might cause the austenite-to-martensite-transformation promoting the uptake of hydrogen into the material. Together with the load, this might induce hydrogen-assisted cracking, further deterioration of the mechanical properties and additional phase transformation too. A safe and reliable use of the structural element is, under this condition, not given any more.

Although extensive research was done during the last 100+ years and several mechanisms underlying hydrogen-assisted damages were identified, many ambiguities remain. More information about the behaviour of the (micro-)structure of ASS in the presence of hydrogen, the precise localisation of hydrogen within the matrix and the interaction with external mechanical load are still needed.

The objectives of the following study are therefore:

- Identification of hydrogen-assisted damages of the microstructure by scanning electron microscopy.
- Evaluation of hydrogen-assisted changes of the crystal structure in due consideration of
- the visualisation of the distribution of deuterium within the material as a tracer for hydrogen.
- Observation of the behaviour of deuterium in the material when subjected to external mechanical load.

The four main objectives are interconnected and none of the features will be examined detached from the others. Two austenitic stainless steels, the grades AISI 304L and AISI 316L, are the subjects of the present work.

## 5. Experimental

### 5.1. Materials and sample preparation

#### 5.1.1. Alloys

The two most widely used austenitic stainless steels were investigated in the present study. According to the *American Iron and Steel Institute*, they are designated AISI 304L and 316L, respectively. The European denotations are EN 1.4307 and 1.4404, respectively.

Like discussed in Chapter 3.1.4, their mechanical properties and corrosion resistance qualifies them for many applications where hydrogen-related damages frequently occur.

Table 5.1 shows the chemical composition of both materials, given from the supplier and determined with an optical emission spectrometer from *SPECTRO Analytical Instruments GmbH* (Kleve, Germany).

Table 5.1: Chemical composition of the investigated materials according to the supplier and measured by an optical emission spectrometer (OES). All values are given in wt.-%.

Material	source	C	N	Cr	Ni	Mn	Mo	Si	P	S	Fe
<b>304L</b>	supplier	0.022	0.053	18.25	8.05	1.53	negl.	0.38	0.033	0.002	bal.
	OES	0.027	≤0.1	18.38	8.21	1.54	negl.	0.48	0.029	0.004	bal.
<b>316L</b>	supplier	0.017	0.05	16.9	10.1	1.23	2.02	0.46	0.031	0.001	bal.
	OES	0.02	0.056	17.14	10.32	1.22	1.95	0.45	0.023	0.002	bal.

*ThyssenKrupp Schulte GmbH* (Dortmund, Germany) delivered the alloy grade 304L that was cold-rolled, annealed at  $\approx 1000^\circ\text{C}$ , pickled and finally soft rolled to 0.5 mm thickness by the supplier. This is the most commonly applied treatment for steels to ensure corrosion resistance and evenness.

The grade 316L was purchased from *Outokumpu PSC Germany GmbH* (Heidenheim, Germany) as warm-rolled, solution-annealed and quenched 20 mm sheets. Subsequently the surface was pickled as well. Optical micrographs for both steels gives Figure 5.1.

It has to be pointed out that the ferritic and martensitic fractions inside the austenite, shown in Figure 5.1, already formed during production and treatment of the material by the suppliers.

Information about the phase composition in dependence of the chemical composition (cf. Table 5.1) gives the *Schaeffler-diagram* [210]. As discussed in Chapter 3.1.1, alloying elements have different effects on the stability of the materials structure. The Schaeffler-diagram plots the *chromium-equivalent* as a measure of BCC stabilisers against the *nickel-equivalent* that summarises different FCC stabilising elements.

Calculating the Cr- and Ni-equivalent for both materials and marking them in Figure 5.2 shows that AISI 304L consists mainly of austenite with up to  $\approx 10\%$  ferrite, while AISI 316L should contain only  $\approx 5\%$ . This is due to a higher nickel concentration that stabilises the FCC phase. However, the exact amount of  $\delta$ -ferrite in the alloys was not determined ahead of the experiments. It can be assessed e.g. by a magnetic scale that measures the magnetic moment of the phases. The Feritscope MMS-PC2 by *Helmut Fischer GmbH*, Sindelfingen, Germany was



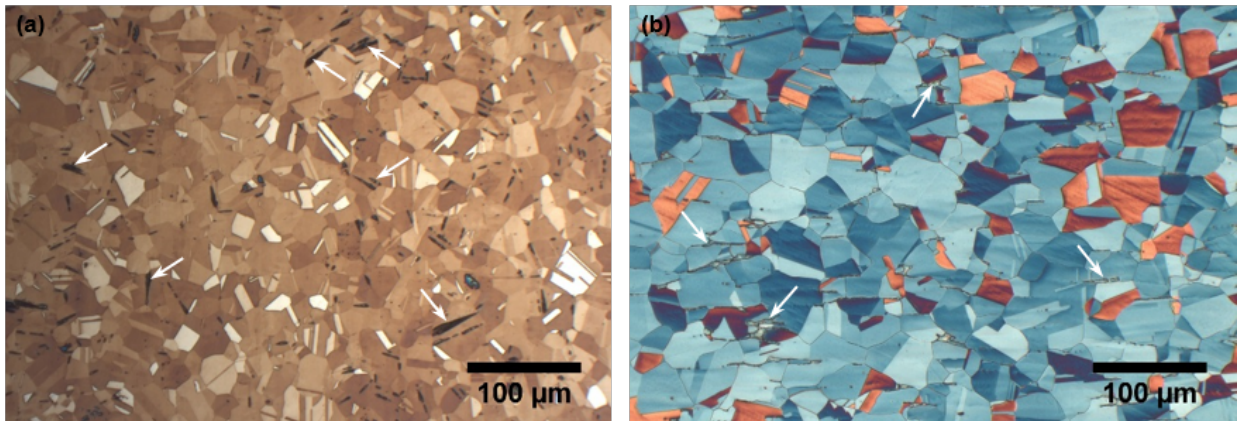


Figure 5.1: Optical micrographs of the investigated grades AISI 304L (a) and AISI 316L (b) after etching with Beraha II. White arrows mark ferritic and martensitic fractions that stem from the production process. They are not distinguishable from each other with the means of optical microscopy.

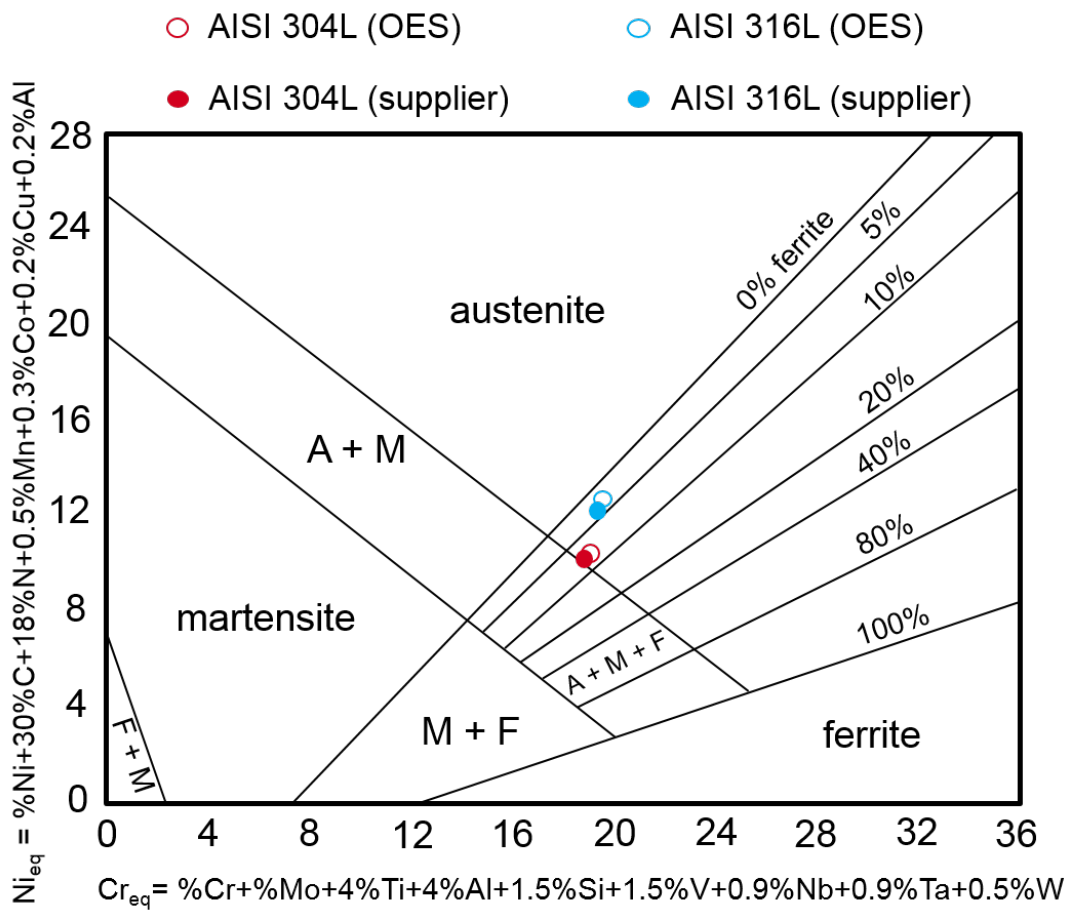


Figure 5.2: The Schaeffler-diagram plots the expected phases of steels depending on their nickel- and chromium-equivalent. The locations of the investigated materials are marked by dots. Figure according to Kotecki et al. [27].

used in the present study. It is able to determine the fraction of ferrite by magnetic induction method, based on the different magnetic properties of BCC and FCC structures.

However, evaluation of the ferrite content was not successful. Two reasons for this can be adduced. One is the small thickness of the AISI 304L sheet material falling below the minimal sample thickness of the instrument. The other is the omnipresence of residual  $\alpha'$ -martensite on the surface of both materials. Its origin was rolling of the steel sheets. A reliable determination of  $\delta$ -ferrite was therefore not possible, due to similar magnetic properties of these both BCC phases.

### 5.1.2. Sample preparation

To thoroughly study hydrogen-induced material degradation in the different steel grades, two types of samples were prepared. Simple square-shaped specimen for *ex-situ* experiments and notched bending samples for *in-situ* experiments, which were mechanically strained *during* ToF-SIMS measurements. A sketch of both types is depicted in Figure 5.3

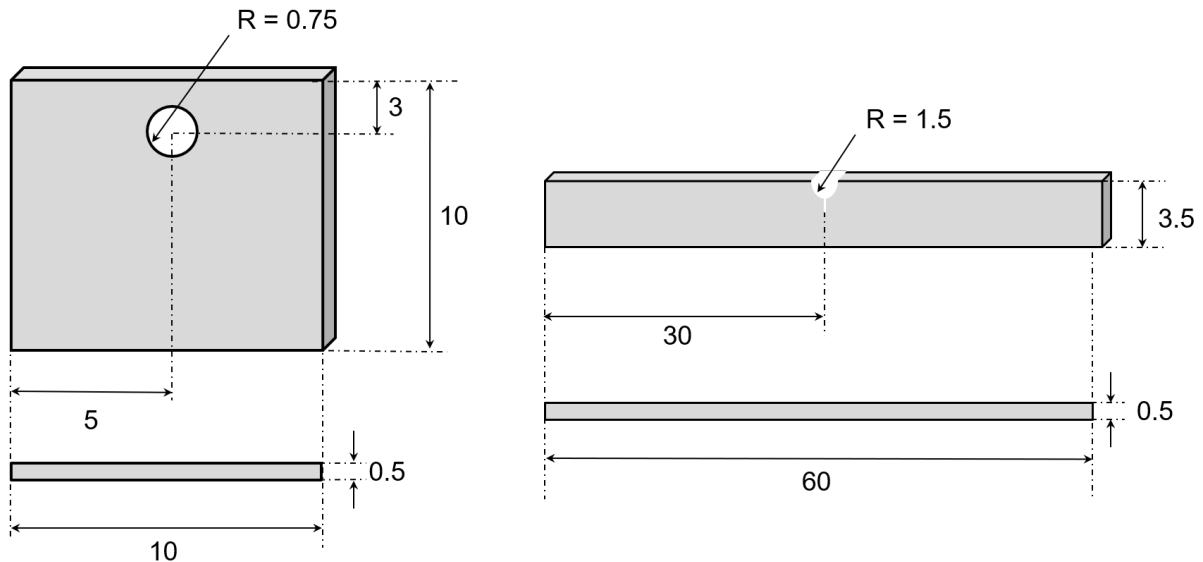


Figure 5.3: Sample dimensions for *ex-situ* (a) and *in-situ* experiments (b) in millimetres.

In the course of the present study, different techniques for specimen preparation were carried out. This was partly to optimise the outcome of the later experiments and partly necessary due to preparation-induced artefacts.

To reach the best results, a combination of treatments was chosen. Thus, at first samples were ground and polished mechanically and subsequently polished electrolytically for 5 s, which Figure 5.4 shows. Because this experience was gained only during the progress of the present work, the *ex-situ* samples were not polished electrolytically.

Table 5.2: Juxtaposition of the different sample preparation techniques that were tested in the scope of the present work.

mechanical preparation	electrochemical polishing	ion polishing
grinding from 800 to 4000 grit; polishing from 3 to 0.25 $\mu\text{m}$ with colloidal silica; complete removal of the production-induced martensite from the surface not possible	electrolytic polishing with the A2 solution purchased from <i>Struers GmbH (Berlin, Germany)</i> for different times; etching times longer than 20 s led to a wavy, uneven surface, not suitable for SIMS analyses	broad beam argon bombardment with a PECS instrument of <i>Gatan GmbH (Munich, Germany)</i> ; polishing times of >4 h necessary to remove martensite from the surface

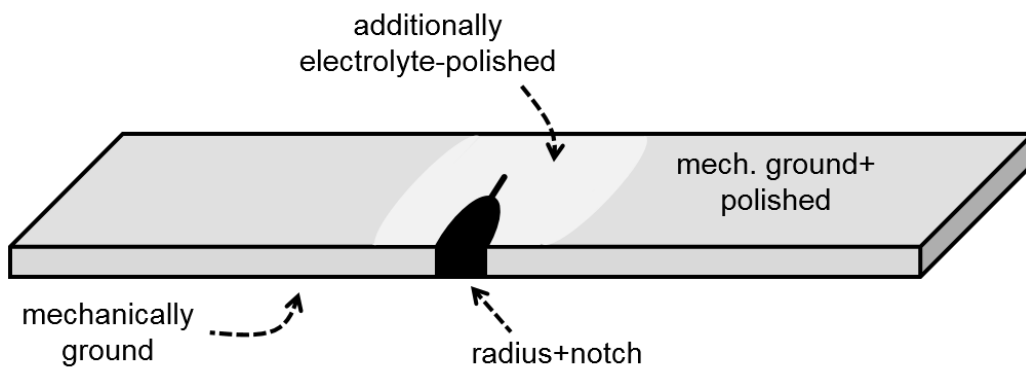


Figure 5.4: Schematic depiction of the sample preparation of the in-situ samples.

### 5.1.3. Electrochemical charging

The introduction of hydrogen into the metallic matrix of a specimen can be realised by several methods. A relatively easy and widely used approach is the electrochemical charging process [19, 77, 125, 126, 207, 211–216]. In this galvanic process, the hydrogen source was the electrolyte from which it formed at the sample surface. The platinum counter electrode acted as the anode, whereas the specimen was cathodically polarised. To keep the electrolyte oxygen free, it was constantly bubbled with pure inert gas through a PTFE hose.

A schematic drawing of the electrochemical charging facility is shown in Figure 5.5, the parameters applied and materials used are listed in Table 5.3.

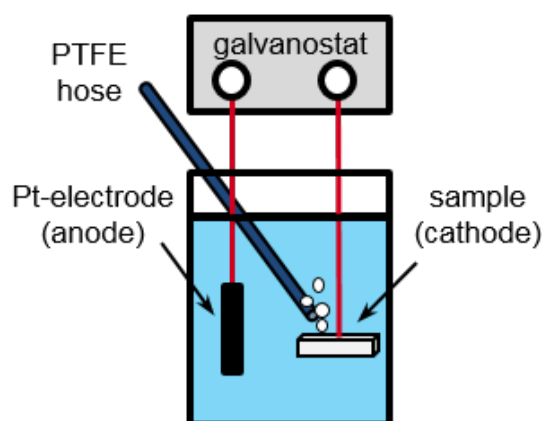


Figure 5.5: Schematic drawing of the facility for the electrochemical charging of the material with hydrogen and deuterium, respectively.

Table 5.3: Parameters of the electrochemical charging processes.

experiment	solution	current density	duration	scavenging gas
ToF-SIMS	0.05M D <sub>2</sub> SO <sub>4</sub> +0.01M NaAsO <sub>2</sub>	5 mA/cm <sup>2</sup>	24/48/72 h	nitrogen
ToF-SIMS	0.05M D <sub>2</sub> SO <sub>4</sub>		24/48/72/120 h	nitrogen
CGHE	0.05M H <sub>2</sub> SO <sub>4</sub>			argon

A necessary requirement for successfully analysing hydrogen with ToF-SIMS is the use of an appropriate tracer. This can either be its isotope deuterium (<sup>2</sup>H/D) or tritium (<sup>3</sup>H/T). Due to certain risks and difficulties in the application of tritium, deuterium was used in the present study. The necessity stems from the natural abundance of hydrogen and the high sensitivity of the ToF-detector. A differentiation between artificially charged hydrogen and that in the rest gas in the analysis chamber of the instrument is otherwise extremely difficult.

Yamabe *et al.* developed a method to eliminate the interfering background signal of hydrogen that is omnipresent even in high-vacuum instruments [83, 217]. Due to the great experimental effort of their approach, it was not applied in the present study.

To impede the recombination of atomic hydrogen/deuterium at the specimen surface, first charging procedures were done with the addition of 0.01M NaAsO<sub>2</sub> as a recombination poison. This will be discussed further in Chapter 6.1.

## 5.2. Scanning electron microscopy

In order to characterise the microstructure before and after charging with deuterium, the specimens were analysed with the scanning electron microscope Zeiss Supra 40 of *Carl Zeiss GmbH (Oberkochen, Germany)*

A Schottky field emitter emitted primary electrons which are accelerated with 20 kV and focused on the samples. Due to that, a number of interaction products were generated and emitted from the so-called *excited volume*. Among these are different kinds of secondary electrons, backscatter electrons, X-rays, Auger electrons and cathodoluminescence. The attached Everhart-Thornley detector gathered and detected the secondary electrons.

## 5.3. Electron backscatter diffraction

In contrast to the use of secondary electrons, carrying information about the morphology of the substrate, backscatter electrons deliver a material contrast. That means elements and phases can be distinguished concerning their atomic mass (Z-contrast). Further, the crystal structure can be determined.

In the present work, EBSD investigation were carried out with a LEO Gemini 1530 VP SEM, manufactured by *Carl Zeiss GmbH (Oberkochen, Germany)*. The attached e<sup>-</sup>flash<sup>HR</sup> system from *Bruker Nano GmbH (Berlin, Germany)* acquired the diffraction patterns. Additionally, it was equipped with back- and foreshattered electron detectors (ARGUS). All the experiments were carried out with an acceleration voltage of 20 kV. The gathered data itself was processed by the software CrystAlign *Bruker Nano GmbH (Berlin, Germany)*.

To enhancing the backscatter coefficient and the electron yield, specimens have to be tilted in EBSD measurements. The higher this tilt is, the higher the backscatter coefficient  $\eta$  is, resulting in an increased signal intensity because more electrons are scattered. This enhances the signal-to-noise ratio and increases the contrast of the backscatter Kikuchi diffraction pattern (BKDP), since EBSD raw signal is the sum of inelastically and elastically scattered and diffracted electrons, i.e. background *and* BKDP. A sample tilt of 70° is the standard positioning in many EBSD systems, although it leads to a strong intensity gradient in the EBSD patterns.

When the electron beam hits the surface of the sample, it interacts with the matter so that a variety of interaction products evolve. Additionally, electrons are elastically and inelastically diffracted at the atomic planes. The Bragg equation gives for this process the basic relations:

$$n\lambda = 2d_{hkl}\sin\Theta_{hkl} \quad (12)$$

with  $\lambda$  as the wavelength,  $d_{hkl}$  the inter-planar distance and  $\Theta$  the angle between electron beam and plane.

A part of the backscattered electrons hits the phosphorus screen of the detector. Because of its high luminescence, the electrons induce Kikuchi bands, i.e. diffractions patterns on this screen. It is important to note that only elastically scattered electrons form the BKD pattern. Figure 5.6 exemplary shows the arrangement of the phosphorous screen in the centre together with fore- and backscattered electron detectors above and below the phosphorous screen.

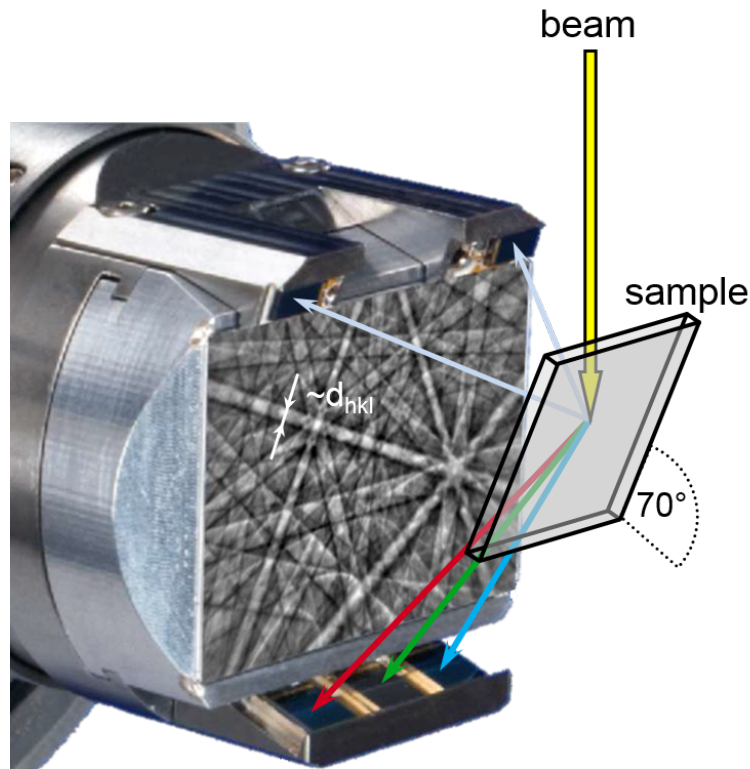


Figure 5.6: Detector unit of Bruker with the FSE detectors above and BSE detectors below. At the centre is the  $e^-$  flash<sup>HR</sup> system with the Kikuchi patterns schematised. Based on [218].

The width of the bands results from the planar spacing  $d$ . Together with the angles between them, the crystal's symmetry can be derived. For bands get broader and angles vary towards the edges of the screen, a complex mathematical correction of the raised data is required. The reason for this is mainly due to the *gnomonic projection* of three-dimensional information on a two-dimensional plane. Only one single point on the screen with the shortest distance to the sample, the *pattern centre*, is non-distorted.

In anisotropic materials and so in the analysed steel grades, the grains do not possess a specific orientation; a circumstance illustrated by Figure 5.7. However, it is important to be able to describe the direction and location of the unit cell forming the grains. This can be done by so-called *inverse pole figures (IPF)* in x-, y- and z-direction. EBSD technique provides this information, thus enabling statements about (hydrogen) charging- and (mechanical) loading-induced features.

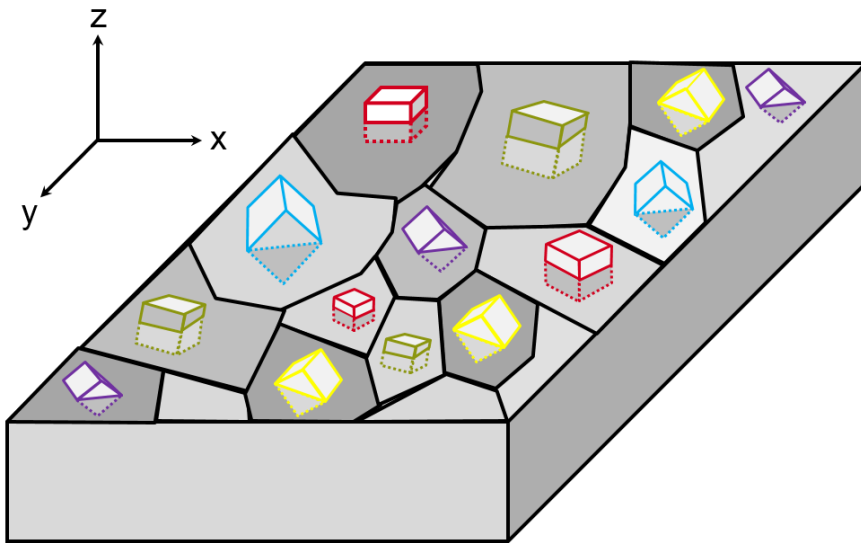


Figure 5.7: Sketch of the orientation distribution of the grains in a polycrystalline material and how to interpret inverse pole figures. The IPF-Z maps show the grain orientation parallel to the normal direction  $z$  of the material's surface.

#### 5.4. Time-of-flight secondary ion mass spectrometry

Analyses of steel samples with ToF-SIMS were done with the non-standard collimated burst alignment mode (CBA) developed by Holzlechner *et al.* [219] and Kubicek *et al.* [220] on a TOFSIMSIV manufactured by *IONTOF GmbH (Münster, Germany)*. With this mode, a lateral resolution down to 100 nm is achievable. However, it delivers a poor mass resolution  $\frac{m}{\Delta m}$  of only about 200. Only in the burst mode, i.e. by "cutting" the ion beam into smaller packages, a mass resolution of up to 6000 can be reached. From this follows that a reliable distinction between charged deuterium (D) and abundant hydrogen molecules ( $H_2$ ) is not possible in the CBA mode. The spectrometry, or high current bunched (HCBU), mode has to be applied for this purpose. With a mass resolution of 11000-13000, it is able to distinguish between these species.

Ahead of every single experiment, the respective measurement mode has to be aligned to achieve the optimal performance. Because of device restrictions, only one mode at a time can be used during analysis. The calibration procedure can not be done on the self-developed sample holder so that switching to another mode is not advisable. Thus, confirmation of the presence of deuterium with the help of the HCBU mode was done only once and not for every experiment. The validity of this was shown by Sobol [6] and Straub [200].

Bismuth ions ( $Bi_1^+$ ) were shot onto the specimen with an energy of 25keV and a current of  $\approx 200$  pA. The region of interest (ROI) with  $100 \times 100$ ,  $150 \times 150$  or  $200 \times 200$  [ $\mu m$ ], respectively, was rastered in "random mode" with  $512 \times 512$  pixels and one shot per pixel. This ensured a sufficient image resolution. Other than e.g. the "sawtooth mode", the random mode further does not lead to accumulation of primary ions on adjacent areas of the ROI.

Since the ion yield of negatively charged hydrogen ions and its isotope deuterium is much higher, all the experiments were conducted in the negative polarity. That means the extractor (cf. Fig. 3.24) extracted only negatively charged ions.

The analysis with bismuth preceded a sputter cycle with caesium ions ( $\text{Cs}^+$ ). Thus, remaining contaminants were removed and the sputter yield of deuterium increased [125, 187]. The particles had an acceleration energy of 1 and 3keV, respectively. In the course of the present work the negative impact of this sputter cycle on the investigated steels was discovered. This effect was, to the best of the authors knowledge, not described in the literature so far and will be discussed in Chapter 6.1. Considering the energy and mass of the ions, the sputter process is supposedly a combination of linear cascade and spike regime.

For diffusion of hydrogen in steels strongly depends on the temperature, samples were cooled down during the experiments. Thus, effusion could be hampered. As shown and discussed in Chapter 5.1.2, two types of experiments were conducted: in-situ and ex-situ. Two different sample holder had to be used for this purpose. Due to their different construction, the sample holder for in-situ test allowed only cooling to  $\approx -75^\circ\text{C} \pm 5^\circ\text{C}$ , whereas the other allowed further cooling down to  $\approx -130^\circ\text{C} \pm 5^\circ\text{C}$ . Due to the metastability especially of the 304L grade, this should of course be avoided.

### 5.5. Combination of four-point-bending test and ToF-SIMS

Figure 5.8 shows the build-up of the in-situ sample holder developed by Sobol [6]. Two piezo-actuators from *piezosystem jena GmbH (Jena, Germany)* are mounted on a sample holder from IONTOF that was further equipped with two counter bearings. This arrangement applied a mechanical force on four points of the sample, whereas a constant bending moment between the two inner bearings deploys. The piezo-translators themselves consist of a stack of ceramic plates with a thickness of 0.5 mm each. Applying a voltage to this stack results in the expansion of the material. This is called the *inverse piezo-electric effect*. A maximum deflection of  $50 \mu\text{m}$  can be thus realised.

With the help of EDM, a slit of 0.2 mm thickness was milled into the specimen, beginning in the notch root. Therefore, the highest stress/strain is predetermined to occur there. Figure 5.9 outlines the geometry of the 4PB sample and the force transmission points.

When the mechanical force is applied to the specimen, tensile stress ( $\sigma+$ ) deploys at the upper part of the sample, whereas compression stress ( $\sigma-$ ) prevails in the lower part. The notch acts as stress concentration site. Under sufficient load a *plastic zone* develops underneath this notch. Figure 5.9 illustrates the characteristic kidney-shape of the plastic zone in red.

It is of course important to be able to assess the magnitude of stress and strain on the material during load. This was done with the software *ANSYS* by a co-worker. The results in Figure 5.10 give an impression of the distribution and dimension of stress and strain around the notch root. Since mechanical tests were not part of the present work, material data was taken from the literature [221–224] as the basis for *Ramberg-Osgood curves* reflecting the stress-strain curves during bending [225].

As Figure 5.10(a) visualises, the highest strain (symbolised as red colour) of  $\approx 0.66\%$  occurs in the notch root. Assuming that plastic deformation starts at a strain of 0.2%, the distance from the notch in y-direction, in which the material is still under plastic strain, is  $\approx 65 \mu\text{m}$ . This is



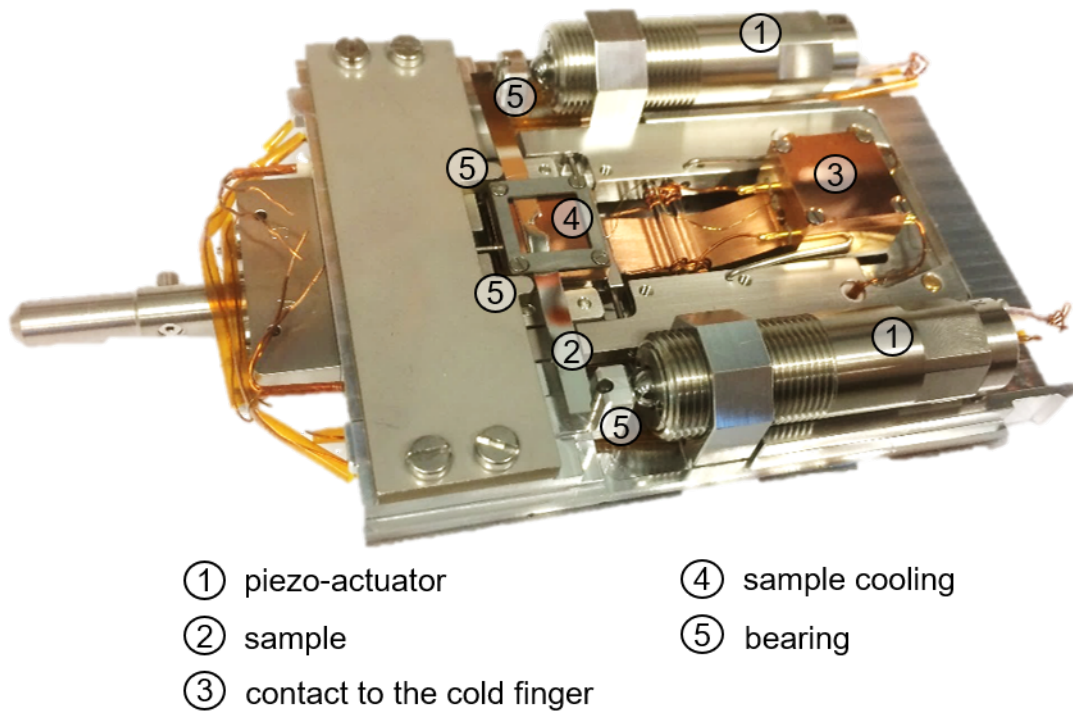


Figure 5.8: Depiction of the four-point-bending device used for the *in-situ* experiments in the ToF-SIMS, developed by Sobol [6].

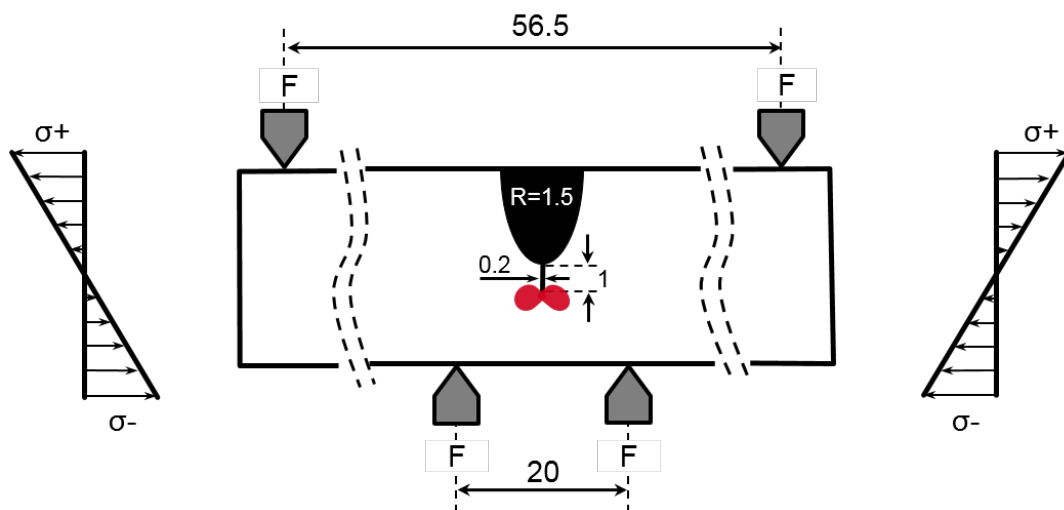


Figure 5.9: Schematic depiction of the points of load transmission into the specimen. The plastic zone that might deploy under sufficient load is illustrated in red directly beneath the notch. Further, the directions of tensile ( $\sigma+$ ) and compressive ( $\sigma-$ ) stress within the *in-situ* specimen under load are shown. Dimensions are given in millimetres.

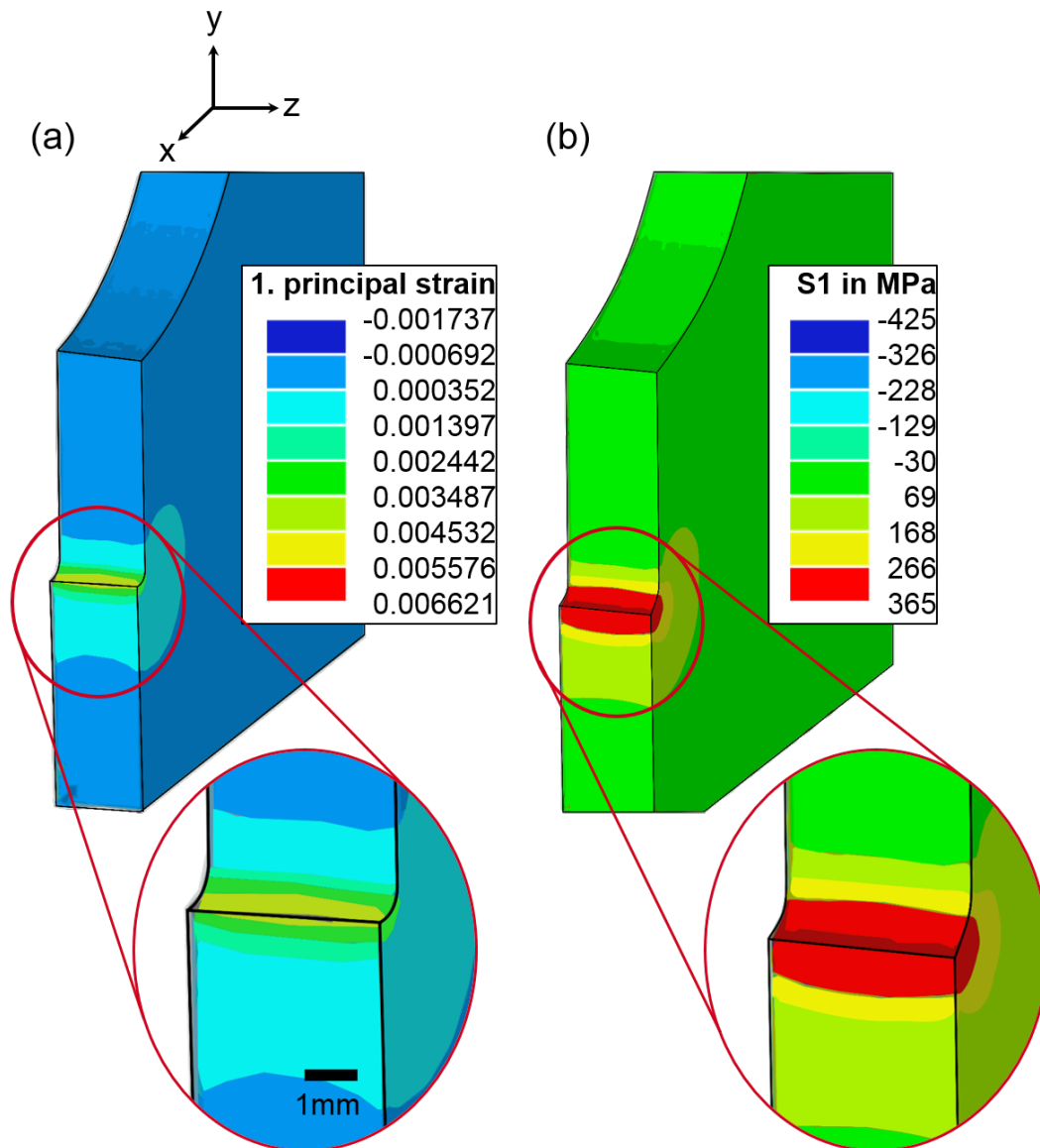


Figure 5.10: *Reproduction of the results of the finite element analysis of the grade AISI 304L under mechanical load with the software Inkscape. (a) shows the first principal strain and (b) the first principal stress S1 that reflect the highest strain and stress, respectively. These occur in x-direction, i.e. normal to the notch, when the specimen is bended. The original simulation was done by Dr. Tobias Mente with ANSYS [226].*

coloured in green. For both materials, AISI 304L and 316L, these numbers are similar and vary only slightly.

### 5.6. Data treatment

Analysing steel surfaces with accelerated particles like ions (ToF-SIMS) or electrons (SEM) faces researchers with several difficulties. Since the yield strongly depends on topography, incident angle and also the atomic number of the material, the results can easily be misinterpreted. This made data processing of the gathered SIMS data inevitable.

Firstly, temperature and device instabilities during the measurements were compensated by shift correction of the raw image data with the on-board software *SurfaceLab* of the SIMS instrument. Afterwards, a method of multivariate data analysis (MVA), the so-called principal component analysis (PCA), was applied on the acquired SIMS image data to consider covariant features, such as deuterium fragments bound to oxygen. One can imagine PCA as reduction of dimensionality of the data, i.e. the original variables, to a lower number of orthogonal variables. This was done with *ImageLab* by *Epina Softwareentwicklungs- und Vertriebs-GmbH* (Retz, Austria)

PCA looks at the total variance within a data set and is thus able to consider those features. The information content can be increased significantly so that the chemical components and differences within the sample can be identified [227, 228]. By scaling the data ahead of the PCA, the noise level is reduced so that variances of the signals became visible and peaks comparable. A normalisation removes differences in the data that are due to charging, edge effects and instrument variations.

Although only one sample at a time is being processed, principal component analysis is still applicable. In case of the acquired ToF-SIMS data, every measurement point within the ROI reflects one spectrum, whereas the intensities of individual masses give the variables [228]. This data can be depicted as a covariance matrix forming the basis of PCA. This MVA method reduces the complexity/dimensionality of that data matrix considerably and creates new data matrices containing *scores*, *loadings* and *residuals*.

Finally, the obtained principal components (PC) that reflect specific features of the SIMS data and the SEM image can be fused. This was also done with *ImageLab*. Lohninger and Ofner recognised the trend towards multi-method and thus multi-sensor material analysis from which the necessity to combine the different information stems [229].

Further information on multivariate data analysis can be found e.g. in [230–233] and in particular for steels in [125, 201, 202, 234].

### 5.7. Determination of the hydrogen content

In order to determine the content of hydrogen within the charged specimen, carrier gas hot extraction (CGHE) was employed. The hydrogen analyser G8 Galileo from *Bruker AXS GmbH* (*Karlsruhe, Germany*), equipped with the quadrupole mass spectrometer (MS) ESD 1000 from

*InProcess Instruments Gesellschaft für Prozessanalytik mbH (Bremen, Germany)*. With this, a resolution of 10 ppb per 1 g of specimen weight can be achieved [174].

During CGHE, samples were heated up to 400 and 900°C to not only accelerate but to ensure the effusion of deeply trapped hydrogen as well (cf. Chapter 3.2.3).

Figure 5.11 illustrates the procedure of the CGHE measurements with the respective temperature regimes.

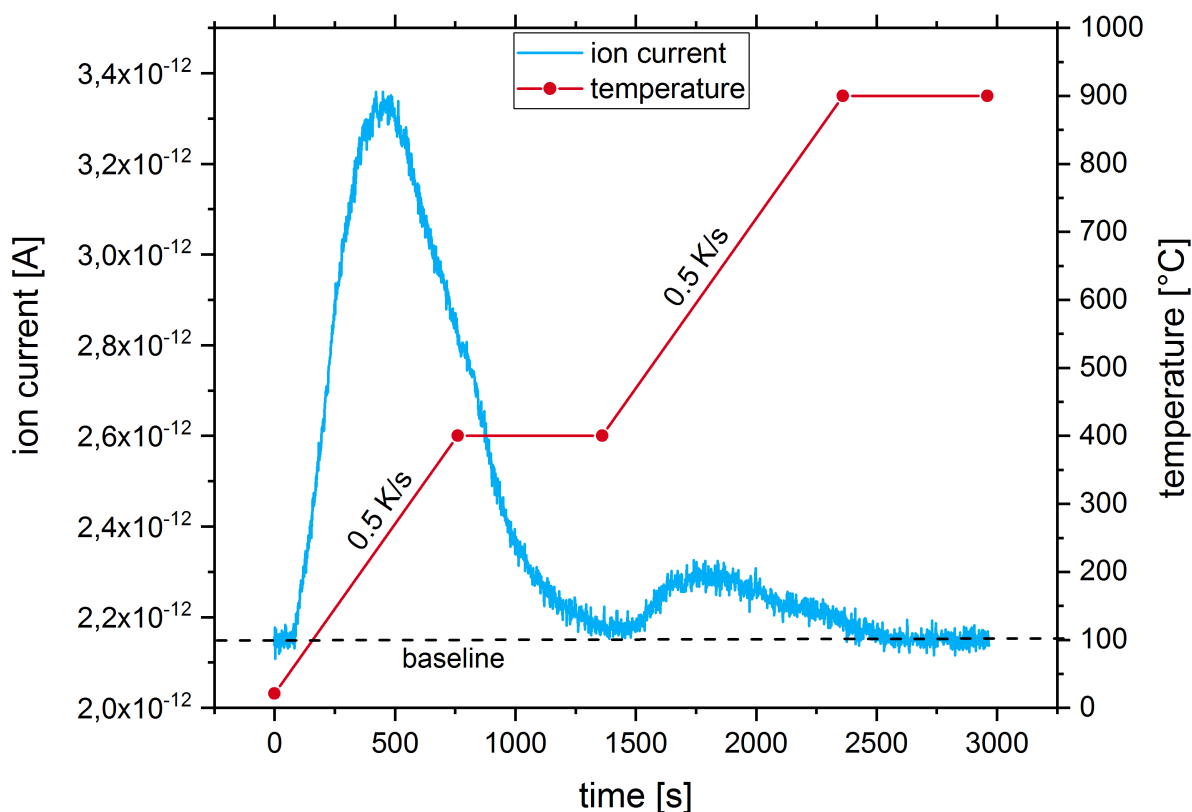


Figure 5.11: Temperature profile for the CGHE measurements (red line) and the evolution of the ion current (blue line) representing hydrogen ions effusing from the sample.

A constant flow of high purity nitrogen gas transported the released hydrogen to the mass spectrometer, where they were accelerated along the longitudinal axis between the four bars of the quadrupole MS, as shown in Figure 5.12.

The opposing electrodes have the same polarity, so that they form two anodes and two cathodes with a constant direct current (DC). A high frequency alternating current (AC) is superimposed. The variation of current, frequency and AC amplitude allows the separation of ions concerning their ion mass and valence ratio. Only ions with a specific ratio are forced on stable sinus-shaped flight path and therefore able to reach detector that measures the ion current. Other species will move on unstable trajectories and leave the quadrupole [174, 235].

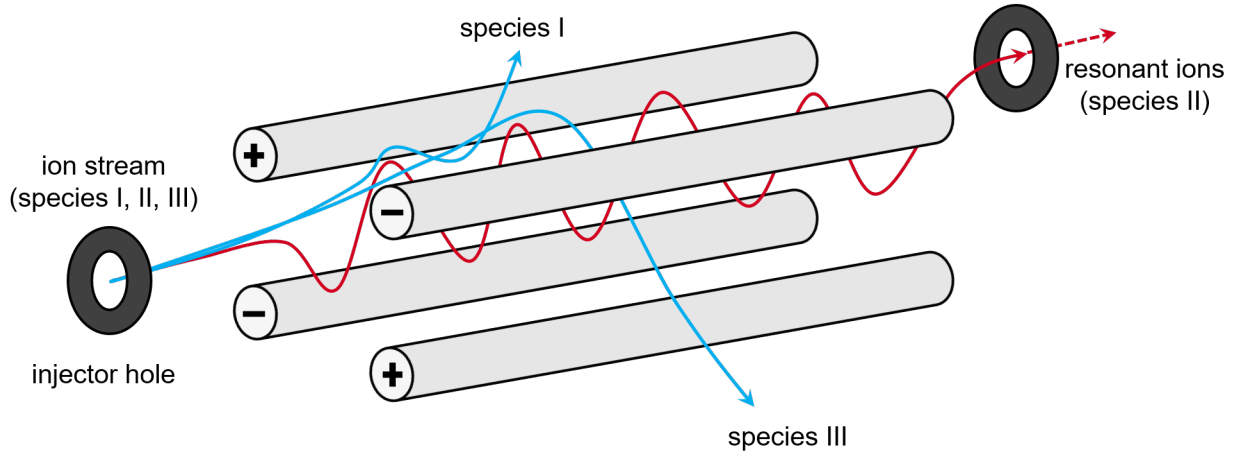


Figure 5.12: Schematic depiction of a quadrupole mass spectrometer according to Salmi et al. [235].

Solubility and diffusivity of hydrogen and deuterium isotopes in steel are in the same order of magnitude [113]. However, the difference in size and behaviour must be taken into account when extrapolating the amount of deuterium based on data derived from CGHE. Based on the mass isotope effect and diffusion coefficients, it is assumed that the relationship between diffusivity of hydrogen and deuterium is [236]:

$$\frac{D_H}{D_D} = \sqrt{\frac{m_D}{m_H}} \Rightarrow D_H = \sqrt{2}D_D, \quad (13)$$

where  $D_H$  and  $D_D$  are the diffusion coefficients of hydrogen and deuterium and  $m_H$  and  $m_D$  the masses of the isotopes

Katsuta and Furukawa investigated permeability, diffusivity and solubility of deuterium and hydrogen in AISI 304 grades comparatively [92]. According to them, the ratio of permeability of hydrogen and deuterium  $\frac{\Phi_H}{\Phi_D} = 1.4$  and the ratio of diffusion coefficients  $\frac{D_H}{D_D} = 1.2$ . The difference in the solubility is with  $\frac{S_H}{S_D} = 1.1$  even smaller. These results imply that during electrochemical charging less deuterium enters the metal lattice as compared to hydrogen. However, the bigger size and, thus, stronger impact of deuterium on the matrix quite likely compensates this. It is important for the present thesis, for hydrogen-induced damages will be assessed based on the influence of deuterium on the austenitic grades.

Following this, the concentration of deuterium was derived from the measured amount of hydrogen with:

$$x_D = \frac{x_H}{\sqrt{2}}, \quad (14)$$

where  $x_D$  and  $x_H$  are the amount of deuterium and hydrogen, respectively (cf. Chapter 6.1).

Applying Equation 14 on the diffusion length introduced as Equation 10, the maximum depth from which deuterium effused during hot extraction can be estimated. The following diagram is based diffusion coefficients from the literature. It is important to mention that the curves do not reflect the actual behaviour of deuterium since it considers only bulk diffusion in an ideal FCC

lattice. Relevant features like dislocations, grain and twin boundaries, voids or other interfaces are not considered. Furthermore, processes such as adsorption, absorption or phase transformation are neglected as well. The so-called *skin-effect*, only recently proposed by Polyanskiy *et al.*, is not taken into account either [237]. It describes the shielding effect hydrogen-saturated layers exhibit on newly arriving hydrogen. By that further uptake of hydrogen by electrochemical charging is slowed down or even inhibited. However, as a first approximation Figure 5.13 is useful. It shows a large variation in the diffusion depth of deuterium, dependent on the coefficient the calculation is based on. It varies from  $\approx 26 \mu\text{m}$  to about  $\approx 55 \mu\text{m}$ .

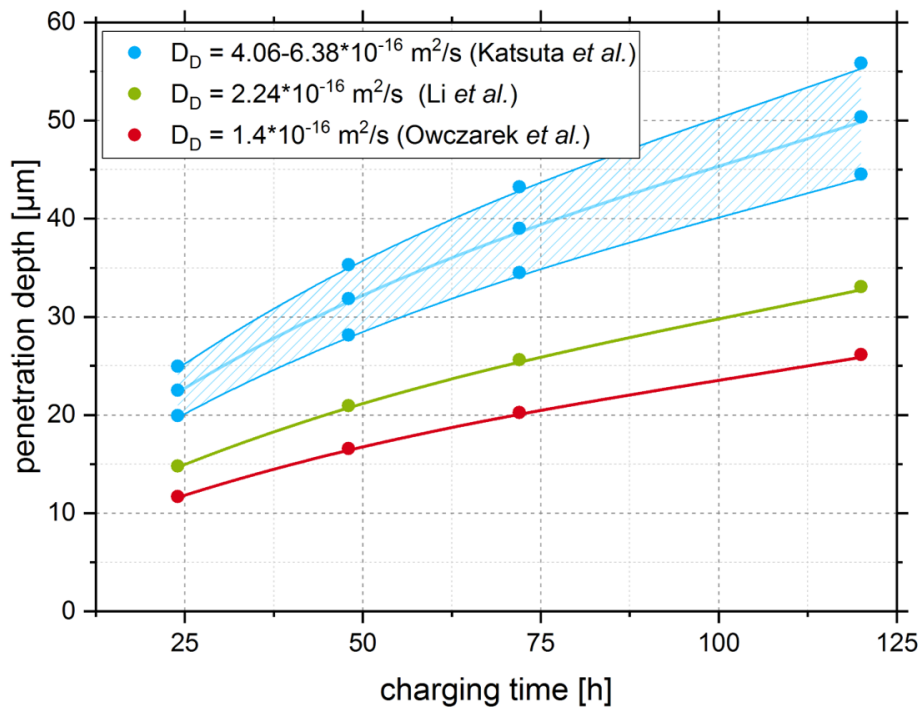


Figure 5.13: Penetration depth (*i.e.* diffusion length) of deuterium during electrochemical charging for different charging times (*cf.* Chapter 3.2.2). The diffusion coefficients were taken from [90–92].

## 6. Results and discussion

### 6.1. Experimental challenges and drawbacks

#### 6.1.1. Influence of recombination poison on the surface and the deuterium uptake

A large number of publications described the use of recombination poison in the electrochemical charging process [30, 85, 88, 115, 125, 126, 142, 212, 214, 238–246]. It is said, that these substances hamper the recombination of atomic hydrogen/deuterium and, thus, increase its uptake into the metallic matrix. However, the underlying mechanisms remained commonly undiscussed and the positive effect was unquestioned.

In the present work, the commonly used recombination poison sodium arsenite was used during the first charging procedure on AISI 304L samples. Some of the results are shown in Figure 6.1.

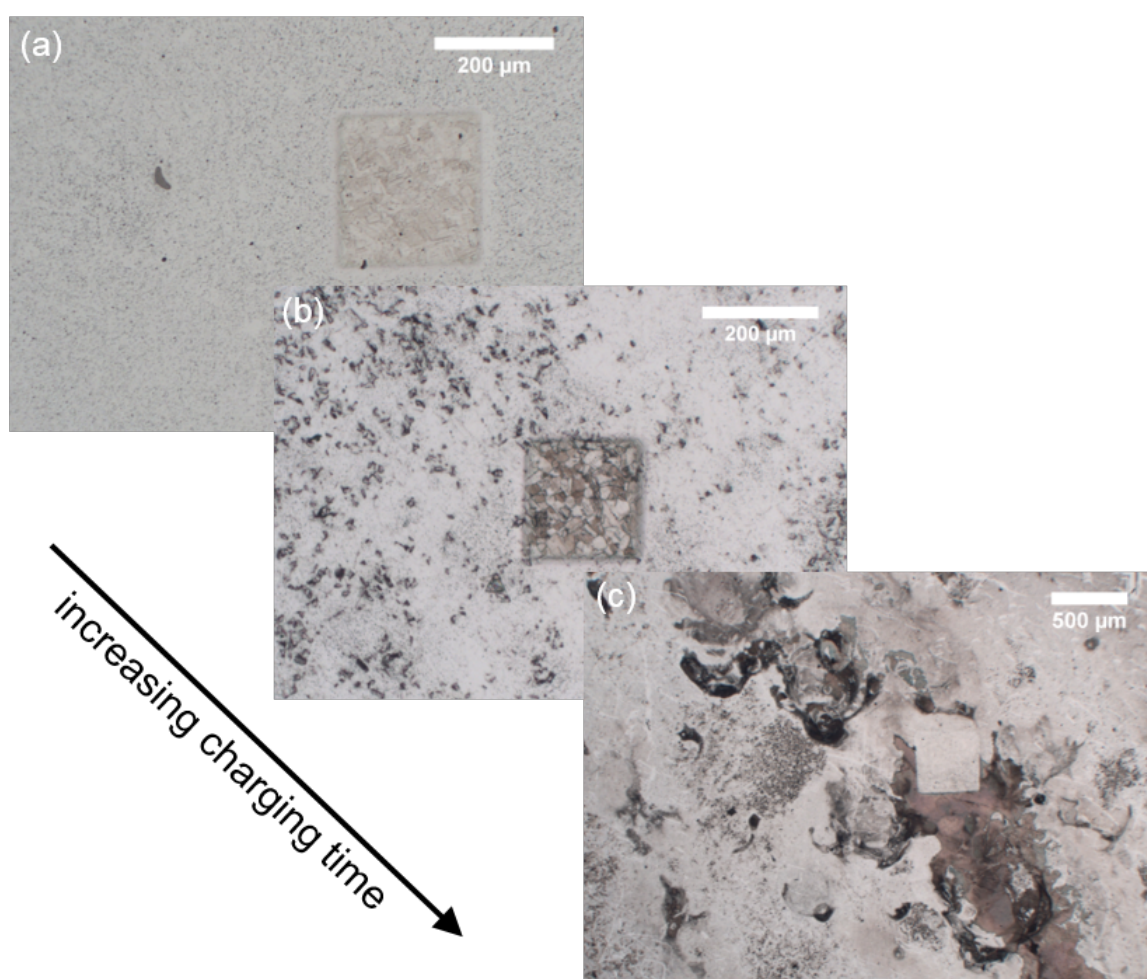


Figure 6.1: Optical micrographs of samples made from AISI 304L charged for (a) 24, (b) 48 and (c) 72 h with 0.05M  $D_2SO_4$  and 0.01M  $NaAsO_2$  as recombination poison. The sputter crater of the ToF-SIMS examinations is visible as a square in every image.

It is obvious that a brown/black surface layer formed during charging. Furthermore, the electrolyte was coloured dark. ToF-SIMS investigations revealed arsenic, oxygen, iron, nickel,



carbon, nitrogen and sulphur on the surface. Benchmark tests of samples from the same material charged *without* sodium arsenite did not exhibit these surface precipitates.

In which way NaAsO<sub>2</sub> affected the uptake of hydrogen was analysed by CGHE. The results are summarised in Table 6.1.

Table 6.1: *Calculated amount of hydrogen from the CGHE measurements in AISI 304L after charging for 24 and 48 h, respectively. All values are given in ppm.*

		with NaAsO <sub>2</sub>	without NaAsO <sub>2</sub>
24 h	peak 1	13.3	31.8
	peak 2	3.1	3.4
	total	16.4	35.2
48 h	peak 1	62.1	84.3
	peak 2	1.4	1.8
	total	64.0	86.1

The combined results indicate that the recombination poison led to chemical reactions on the steel surface. The evolving precipitates hampered the absorption of hydrogen into the matrix, which was proven by quantitative hot extraction. Yet, the exact stoichiometric composition and structure of the precipitations was not investigated. Table 6.1 shows that larger amount of hydrogen was taken up by the sample charged in a solution without the recombination poison. In addition to that, charging with NaAsO<sub>2</sub> complicated SIMS measurements. Long sputter times of up to  $\leq 15$  min were necessary until an adequate deuterium signal was detected. However, high energy sputtering for longer times can harm the materials surface condition and cause the so-called *mixing* effect, i.e. the implantation of primary ions into the first  $\approx 1$ -10 nm of the surface. This reduces not only the depth resolution but leads to an altered chemical composition of the surface. How serious the influence of the Cs<sup>+</sup>-beam can be, is discussed in the next chapter. Main conclusion from the first preliminary results was the omission of NaAsO<sub>2</sub> during the cathodic charging procedure.

### 6.1.2. Sputter-induced artefacts

EBSD analyses after the first *in-situ* experiments in the ToF-SIMS, delivered remarkable results of which Figure 6.2 shows two. Comparing the phase distribution maps of before and after charging and SIMS analysis revealed  $\gamma \rightarrow \alpha'$ -phase transformation in some locations of the surface. These locations have sharp edges and are quadratic. The caesium sputter beam in the ToF-SIMS rastered the surface with in square shape with exactly the same dimensions as measured in the EBSD phase maps. It can, thus, be assumed that caesium sputtering caused the transformation. The depicted craters in Figure 3.14 are marked by a white dotted line.

Although the samples were analysed after charging, no deuterium could be detected. This was most likely due to maladjustments of the galvanostat that applies and keeps a constant current density at the sample. To prevent the diffusion of deuterium in and from the sample, every SIMS measurement was done at low temperatures. In this case, it was  $-80^\circ\text{C} \leq T \leq -60^\circ\text{C}$ . This is



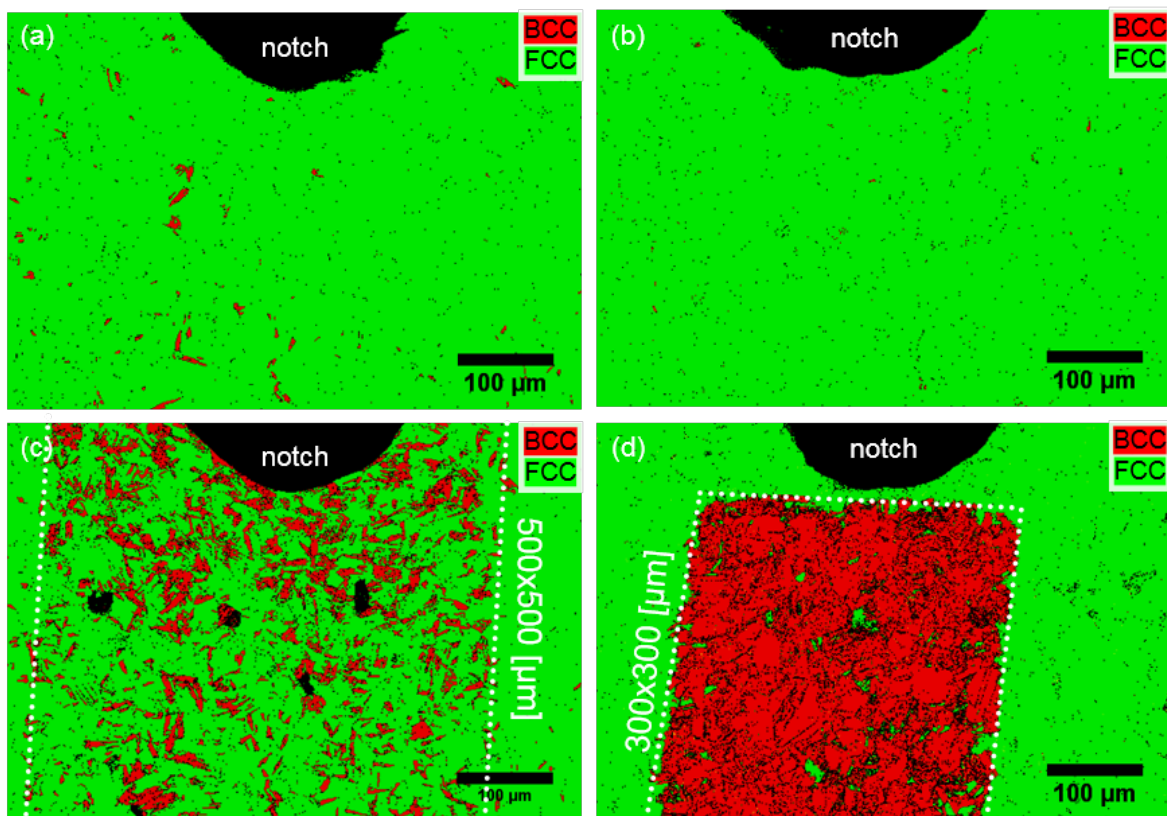


Figure 6.2: Phase maps of AISI 304L before (a)+(b) sputtering and after sputtering with a 3keV  $Cs^+$ -beam for 3 min (c) and 3.5 min (d), respectively. The dotted line margins the sputtered area. Black regions refer to areas where Kikuchi pattern (i.e. the diffraction patterns) could not be indexed.

apparently below the  $M_d$  temperature, outlined in Figure 3.7. From this it can be concluded that the  $\gamma \rightarrow \alpha'$ -phase transformation was triggered by the ion bombardment and supported by the low temperature reducing the austenite stability. It needs to be emphasised that no external mechanical bending was applied on these samples.

Differences in the amount of transformed austenite were not only due to the longer sputter time in Figure 6.2(d) in comparison to 6.2(c), but to the different sizes of the sputtered area. The  $\text{Cs}^+$ -beam scanned the surface with an energy of 3 keV and a current of 35-40 nA. Therefore a similar current, distributed on an area of  $300 \times 300$  (in (d)), resulted in a higher current density than on  $500 \times 500 \mu\text{m}^2$  (in (c)). This is synonymous to a more intense ion bombardment, introducing more (plastic) deformation into the surface layer. It can be concluded that the combined effect of higher current density and longer sputter time caused more extensive phase transformation in Figure 6.2(d).

Sputter-induced phase transformation was also observed in a sample shown in Figure 6.3. The figure juxtaposes the pristine surface of the sample before and after electrochemical charging for 48 h and SIMS measurements. The sputtered area is well distinguishable in the phase distribution and IPFZ maps in Figure 6.3(c) and (d). Outside the crater only small amounts of residual martensite from the production are visible ( $<1\%$ ), whereas the fraction of  $\alpha'$ -martensite inside the crater amounts to  $\approx 65\%$ . By comparing the inverse pole figures in (b) and (d) altered orientation relation become obvious. A large fraction of the randomly oriented grains changed to the [111] direction normal to the surface or close to it. Not all of the former austenite grains changed their orientation, but those that did, are solely oriented in [111]. In order to compensate the deformation energy of the ion beam, the austenite lattice accommodated by shear.

The formation of  $\alpha'$ -martensite due to sputtering is an artefact. It changed the structure of the material in the surface layers. As it was discussed before (cf. Chapter 3.2.3) this led to an altered diffusion behaviour of hydrogen/deuterium and trapping capabilities of the material. For the aim of the present work is to analyse hydrogen- and deuterium-assisted damages, a sputter-induced  $\gamma \rightarrow \alpha'$ -formation strongly counteracts this goal. Effects that result from the ingress and accumulation of H/D would necessarily be overestimated if the influence of the  $\text{Cs}^+$ -beam will not be excluded or at least minimised within the experiments. Therefore, the following investigation was carried out.

## 6.2. Systematic analyses of sputter-induced martensite formation

To successfully exclude the  $\text{Cs}^+$ -beam as an artefact within the ToF-SIMS measurements and to better understand the sputter-induced formation of martensite, sputter tests on both steel grades, AISI 304L and 316L, were performed. Different sputter times and beam energies were chosen to determine the range in which a "safe" sputtering is possible. Table 6.2 shows the details of these experiments.

Not only the "sputter side" has to be considered but the "materials side" as well. The assessment of the stability of the austenitic phase under plastic deformation is often done by the  $M_{d30}$  – temperature. It is defined as the temperature at which 50% of the austenite transformed

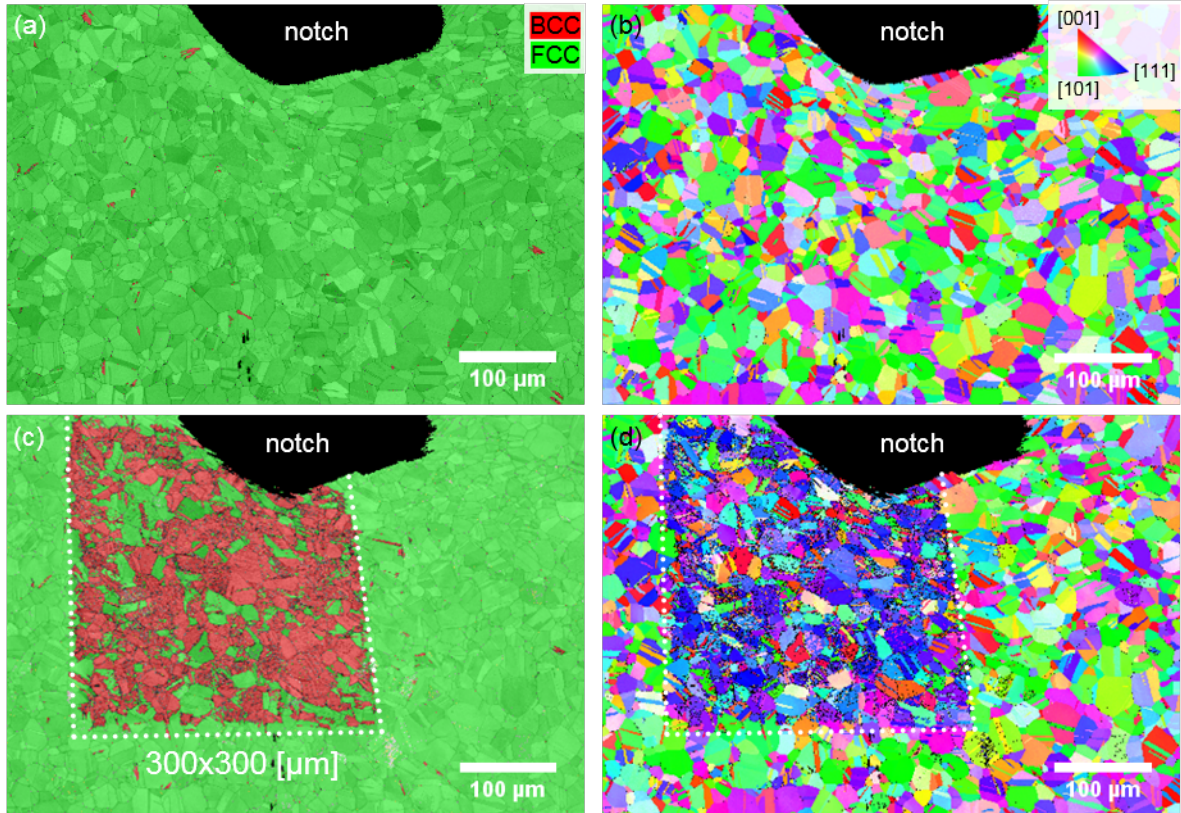


Figure 6.3: Overlay of phase and pattern quality maps of AISI 304L before (a) and after electrochemical charging for 48 h and SIMS analyses (c). The respective inverses pole figures in  $z$ -direction are given in (b) and (d). The surface of the specimen was sputtered with a 3keV  $Cs^+$ -beam for 3 min before SIMS analyses. A white dotted frame margins the sputtered area.

Table 6.2: Details of the sputter tests on the grades AISI 304L and 316L. Both procedures were done at room temperature and  $-80^\circ C$ , respectively.

current [nA]	energy [keV]	time [s]	crater size [ $\mu m^2$ ]
$\approx 30$	3	10, 30, 60, 120, 210, 300	250 $\times$ 250
$\approx 13$	1		

into martensite during a (tensile) deformation of 30% [247]. According to Talonen and Hänninen [11] it is given as:

$$M_{d30} = 551 - 462 * wt.\%(C + N) - 9.2 * wt.\%Si - 8.1 * wt.\%Ni - 13.7 * wt.\%Cr - 29 * wt.\%(Ni + Cu) - 18.5 * wt.\%Mo - 68 * wt.\%Nb - 1.42(ASM\ grain\ size - 8) \quad (15)$$

Equation 15 correctly takes the grain size of the alloy as an influencing factor into consideration. For this reason, the ASTM grain size number was determined by the linear intercepts method. It is plotted together with the calculated  $M_{d30}$ -temperature for both steel grades in Table 6.3.

Table 6.3: Calculated  $M_{d30}$ -temperatures and determined ASTM grain size numbers of the AISI 304L and 316L steel grades, respectively. For the calculation both the chemical composition given by the supplier and the composition determined by OES were used.

		$M_{d30}$ -temperature [°C]	ASTM grain size
<b>304L</b>	supplier	16.6	8.3
	OES	8.2	
<b>316L</b>	supplier	-54.7	7.1
	OES	-67	

Another benchmark that indicates the tendency of metastable austenitic steels to form martensite is the aforementioned stacking fault energy (cf. Chapter 3.1.3.2). It was calculated with different semi-empirical equations taken from [40] and [48] and plotted in Table 6.4.

$$SFE1 = 39 + 1.5\%Ni - 1.34\%Mn + (0.06\%Mn)^2 - 1.75\%Cr + (0.01\%Cr)^2 + 15.21\%Mo - 5.59\%Si + 26.27(\%C + 1.2\%N) * (\%Cr + \%Mn + \%Mo)^{0.5} + 0.61(\%Ni(\%Cr + \%Mn))^{0.5} - 60.69(\%C + 1.2\%N)^{0.5} \quad (16)$$

$$SFE2 = -53 + 6.2\%Ni + 0.7\%Cr + 3.2\%Mn + 9.3\%Mo \quad (17)$$

$$SFE3 = 16.7 + 2.1\%Ni - 0.9\%Cr + 26\%C \quad (18)$$

Table 6.4: Stacking fault energies of the AISI 304L and 316L steel grades, respectively. For the calculation both the chemical composition given by the supplier and the composition determined by OES were used. The underlying equations were taken from [40, 48].

		SFE [mJ/m <sup>2</sup> ]		
		Eq. 16	Eq. 17	Eq. 18
<b>304L</b>	supplier	17.47	14.58	17.75
	OES	18.76	15.7	18.1
<b>316L</b>	supplier	53.26	44.17	23.14
	OES	53.63	45.02	23.47

Of course not only the chemical composition and the grain size affect the strain- and stress-induced  $\gamma \rightarrow \alpha'$ -transformation. Internal stress, resulting from production or (heat) treatment, acts as a driving force as well. Furthermore, a reliable estimation of the SFE strongly depends on the equation it is based on. The results for the grade 316L in Table 6.4 vary dramatically, especially between Equation 16 and Equation 17 on the one and Equation 18 on the other side. This is due to the influence of molybdenum that is not recognised in Equation 18. Since alloy 304L does not contain molybdenum (to a considerable amount), the equations yield similar results.

However, stacking fault energy and  $M_{d30}$ -temperature give a first indication of the expected behaviour of the investigated alloys when subjected to external mechanical load. Consequently, phase transformation is supposed to take place increasingly in the grade AISI 304L during similar ion bombardment as compared to the grade 316L. This is due to the higher stability of the austenite phase of the latter, as discussed in Chapter 3.1.1.

Phase distribution maps of the sputtered surfaces under the above mentioned conditions are shown in Appendix A.1. They provide the basis for the determination of the austenite and martensite fraction before and after sputtering. It is noteworthy that  $\epsilon$ -martensite was not detected in any of the phase maps. Furthermore, the inverse pole figure clearly show that sputter-induced  $\alpha'$ -martensite predominantly evolved in grains orientated in  $[111]$  direction or close to it. Deformation by the  $\text{Cs}^+$ -beam, that hit the sample in an angle  $30^\circ$  to the normal, took place by the creation and slip of dislocations in preferred  $\{111\}$  planes [248].

The amount of martensite formed during sputtering was concluded from the austenite fraction determined with *ImageJ*. Since it was not always possible to differentiate between newly formed martensite and primordial martensite and damages on the surface, the following diagrams depict the evolution of the austenitic fraction in the course of sputtering. This phase could be determined reliably by converting the original image from the RGB (red-green-blue) colour spectrum into the HSB scale (hue-saturation-brightness). Creating a stack within this colour range split the three HSB channels and, thus, segmented the phases. Thresholding finally yielded the fraction of austenite in percent of the total area of the EBSD image.

Figure 6.4 plots the evolution of the FCC phase sputtered with a 1 keV  $\text{Cs}^+$ -beam in dependence of the sputter time and temperature. Figure 6.5 summarises the results of the sputter tests in which a beam energy of 3 keV was chosen. All the graphs were fitted with a polynomial function to emphasise the progress.

In Figure 6.4, the shape of the curve for the steel AISI 304L sputtered at  $-80^\circ\text{C}$  is sinusoidal. This is due to the data points for 10 and 30 s of sputtering, respectively. By comparing these measurement points with its associated EBSD images in Figure A.6, it becomes obvious that this is a misleading result. The unusual low fractions of austenite ( $\approx 70$  and  $75\%$ , resp.) is not due to an extensive martensite formation, but to the presence of scratches on the surface. They stem from sample handling or transport. Apart from these two "outliers", the results show that with longer sputtering time, the austenite-to-martensite ratio decreases. It is obvious that longer sputter times led to a higher energy input and, thus, plastic deformation.

The evolution of the austenite fraction in the course of sputtering at 20°C is represented as unfilled red circles and a dotted line. Due to a decrease in the chemical driving force, i.e. Gibbs free energy  $\Delta G_{\gamma \rightarrow \alpha'}$ , a smaller amount of austenite transformed into martensite. Consequently, the dotted line (*304L RT*) lies above the dashed line (*304L -80°C*). Figure 3.7 illustrates the behaviour of the chemical driving forces in dependence of the temperature already.

Comparing the results of the sputter tests conducted on the steel AISI 316L at -80 and 20°C shows only slight differences in the materials behaviour. Only the inset in Figure 6.4 reveals small variations of  $\approx 1\%$ . Both curves converge towards higher sputter times. The differences are due to residuals of martensite, i.e. centre line segregations, within the material, but not to sputter-induced phase transformation. As the lower  $M_{d30}$ -temperature and the greater SFE indicated, the alloy AISI 316L possesses a higher stability of the FCC phase. It is more sluggish towards strain-induced  $\gamma$ - $\alpha'$ -transformation. Therefore, sputter times of 300 s at 1 keV were not sufficient to produce martensite.

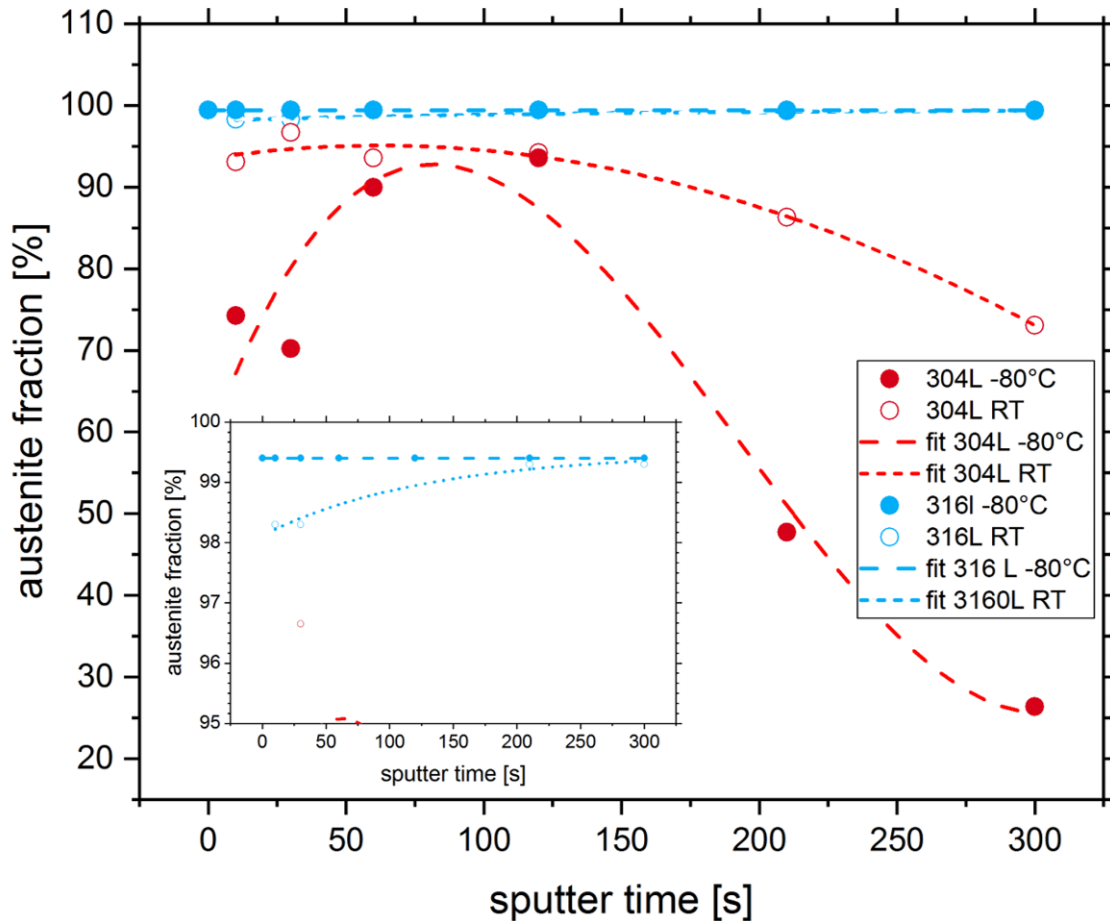


Figure 6.4: Evolution of the austenite fraction in dependence of the sputter time and the temperature regime. Every measurement spot was sputtered once to not accumulate damages. The sputter beam energy was **1 keV**. The inset is a magnification of the graphs showing the alloy 316L sputtered at room temperature and -80°C.



Figure 6.5 presents the determined fraction of austenite in AISI 304L and 316L after sputtering with the 3 keV Cs<sup>+</sup>-beam. Some inconsistencies are apparent within the data. The values of the austenite fraction for 60 and 120 s at -80°C of the steel 304L are  $\approx 10\%$  higher than those of the grade 316L. Moreover, the 304L grade exhibited a higher austenite fraction after 120 s of sputtering at -80°C than at room temperature. These findings contradict previous findings and literature, e.g. [36, 53, 55]. Temperature variations or deviations of the Cs<sup>+</sup>-beam current in the ToF-SIMS could account for those findings. Brief fluctuations of the beam current would result in a lower current density and, thus, a lower accumulated energy introduced into the surface. Local variations of the internal stress state in the different locations of the samples could also have altered the  $\gamma \rightarrow \alpha'$ -transformation behaviour.

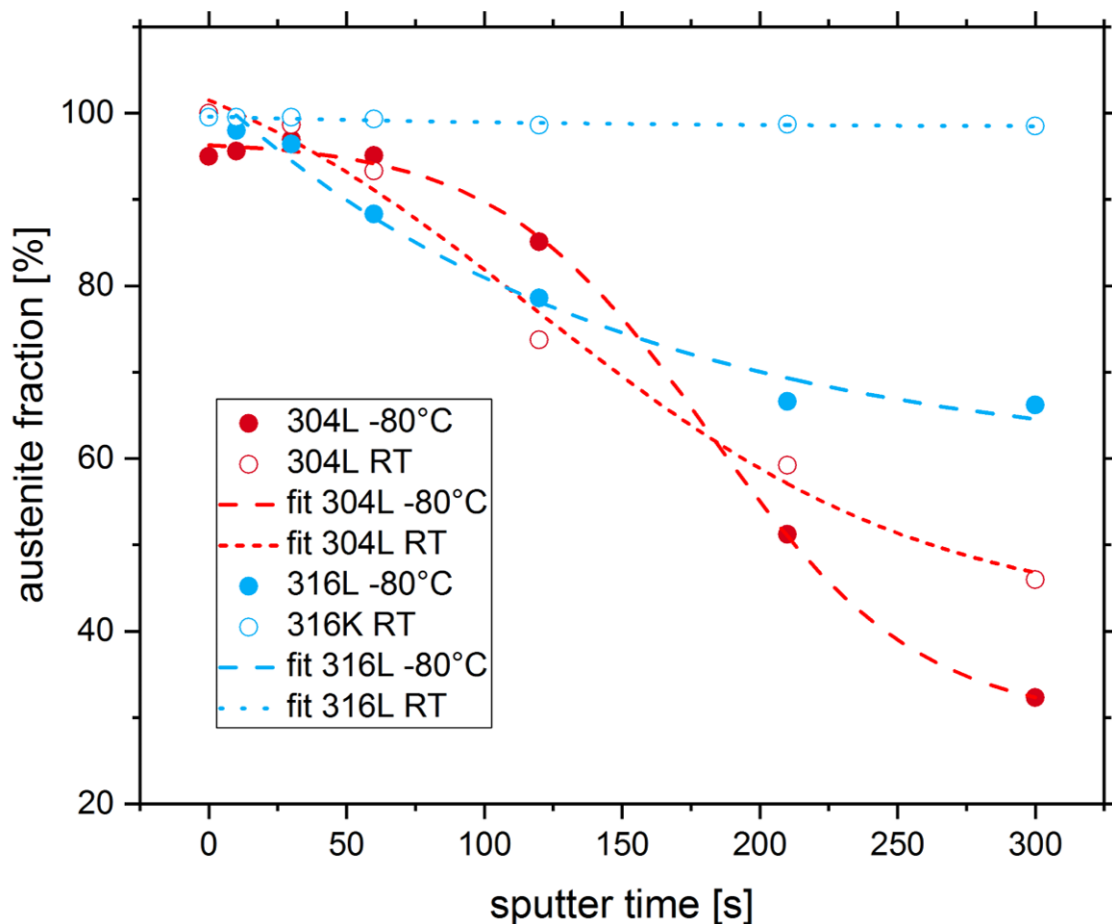


Figure 6.5: Evolution of the austenite fraction in dependence of the sputter time and the temperature regime. Every measurement spot was sputtered once to not accumulate damages. The sputter beam energy was 3 keV.

However, Figure 6.5 shows that towards sputter times longer than 120 s, the distribution of the curves follows again the expected trend. The largest amount of transformed austenite is found in the alloy grade AISI 304L sputtered at -80°C, followed by the sample from the same material tested at 20°C. Only about 30% of the former FCC phase transformed into BCC at -80°C in

the sample made from AISI 316L. Sputtering the same material at room temperature did not generate martensite.

The phenomenon of adiabatic heating and its influence on the transformation behaviour in (austenitic) stainless steels was recognised long ago, e.g. by Olson and Cohen [43] and Hecker *et al.* [34], and since then described in the literature, e.g. in [11, 22, 33, 36, 63, 249]. Lichtenfeld *et al.* investigated the influence of varying strain rates on the alloy grades AISI 304 and 309 by means of tensile tests [66]. By determining the fraction of transformed austenite and calculations, the group found that adiabatic conditions were already fulfilled at strain rates of  $\dot{\epsilon} \geq 0.125 \text{ s}^{-1}$ . Much higher strain rates were expected in the present study, since the impact velocity of the caesium beam  $v$  represents the strain rate. It can be calculated with the equation of the *kinetic energy*  $E_{kin}$ :

$$E_{kin} = \frac{1}{2} * m * v^2 \quad (19)$$

Reorganised it leads to:

$$v = \sqrt{\frac{2 * E_{kin}}{m}} \quad (20)$$

The kinetic energy equals the acceleration voltage of 1 and 3 keV, respectively. The relative atomic mass of a caesium atom  $m$  is  $\approx 2.21 * 10^{-25} \text{ kg}$  and was derived from the atomic mass of  $\approx 132.91 \text{ u}$  multiplied by the atomic mass unit of  $1.66 * 10^{-27} \text{ kg}$ .<sup>1</sup> This calculation led to an impact velocity of  $v_{Cs1keV} \approx 3.8084 * 10^4 \frac{\text{m}}{\text{s}}$  of the 1 keV beam and  $v_{Cs3keV} \approx 6.595 * 10^4 \frac{\text{m}}{\text{s}}$  of the 3 keV beam. These can be understood as the respective strain rates the sample was exposed to. Adiabatic heating did therefore most likely occur in the vicinity of the impact crater of the Cs<sup>+</sup>-beam. How much this hampered  $\gamma \rightarrow \alpha'$ -transformation is difficult to assess and the present work can not deliver this. The magnitude of the volume that heated up is unknown too. However, the influence of adiabatic heating with regard to its effect on the (chemical) driving force for  $\gamma \rightarrow \alpha'$ -transformation should be less significant, especially for the case of the low temperature sputter tests.

Yet, the temperature rise in the volume beneath the sputtered area causes another effect that needs to be considered. Due to the high strain rate of the ion beam and the rather poor thermal conductivity of the investigated steels of about  $16.2 \text{ W/mK}$ , a thermal gradient  $k$  between the topmost, i.e. influenced, layers and the layers below evolves.<sup>2</sup> It is well known from the literature that thermal gradients can lead to damages of the material. For instance Virkkunen conducted extensive research on the thermal fatigue of austenitic and duplex stainless steels [250]. Even though thermal fatigue did not occur in the present case, the underlying mechanism is similar. It can be described as follows: Sputter-induced temperature increase in the surface layers led to localised thermal expansion. For the investigated steel grades, the (linear) coefficient of thermal

<sup>1</sup>The mass of the missing electron of the Cs<sup>+</sup> ion was neglected.

<sup>2</sup>As a comparison, pure copper has a thermal conductivity of  $k \approx 400 \text{ W/mK}$ .



expansion is in the range of  $16 \leq \alpha \leq 17.2 \mu\text{m}/\text{mK}$ . Because expansion was largely constraint by the surrounding "cold" material, thermal stress  $\sigma_{th}$  developed. It was reported that depending on the extend of the temperature gradient, the magnitude of resulting mechanical stress can reach the yield limit [250].

Although, the magnitude of sputter-induced thermal stress is unknown in the scope of this work, it might have contributed a driving force in the same line as external mechanical load  $W_{mech}$  (cf. Chapter 3.1.3.1). Summarising, all possible factors that influence the  $\gamma \rightarrow \alpha'$ -transformation during sputtering are given in Equation 21. A promoting factor of martensite formation is assigned positively and a hampering factor negatively.

$$\begin{aligned} \text{net driving force} = & \text{sample cooling} + \text{thermal stress } \sigma_{th} + \text{sputtering} \\ & \Delta G_{\gamma \rightarrow \alpha'} \uparrow \quad W_{mech} \uparrow \quad W_{mech} \uparrow \\ & - \text{adiabatic heating} \\ & \Delta G_{\gamma \rightarrow \alpha'} \downarrow \end{aligned} \quad (21)$$

Table 6.5 lists critical sputter times in dependence of the applied energy and temperature for both alloy grades. These can act as a guideline for further measurements. All sputter tests were conducted on *uncharged* samples. For this reason, the transferability towards real experiments on deuterium-charged samples has to be questioned. This is because hydrogen/deuterium affects the material physically by stressing the lattice and chemically by increasing the austenite stability. Additionally, remains of martensite that existed before analyses and scratches that incurred after sputtering complicated the evaluation. More experiments need to be conducted to fully depict the influence of sputtering on (austenitic stainless) steels.

Table 6.5: *Critical values of sputter times, energies and temperatures that can act as guideline for further experiments.*

	maximum sputter time 304L		maximum sputter time 316L	
	at RT	at -80°C	at RT	at -80°C
<b>1keV</b>	<210s	<120	$\geq 300\text{s}$	$\geq 300\text{s}$
<b>3keV</b>	<60	<120	$\geq 300\text{s}$	<120s

The main conclusion of the sputter tests is of course that a sputter-induced  $\gamma \rightarrow \alpha'$ -transformation in the grades AISI 304L and 316L is not only possible but under certain circumstances inevitable. It is remarkably that high-density stacking faults and  $\epsilon$ -martensite were not observed in any of the analysed sputter craters. From that it can be concluded that the deformation energy introduced into the material locally reached values high enough to pass through the whole formation cascade that was presented in Chapter 3.1.3.1.

Finally, the experiment had to be adjusted to the investigated materials. Thenceforward the 1 keV  $\text{Cs}^+$ -beam was applied instead of the 3 keV beam to clean the surface of the *in-situ* specimen before analyses. Due to this lack of knowledge prior to the *ex-situ* experiments, they have been carried out using an acceleration voltage of 3 keV of the  $\text{Cs}^+$ -beam. This has always to be taken into consideration in the following chapter.

### 6.3. Ex-situ experiments

#### 6.3.1. Deuterium-induced (micro-)structural changes

Figures 6.6 and 6.7 show SEM images and EBSD maps of the same areas for samples before and after deuterium charging without the addition of  $\text{NaAsO}_2$  for 24 and 48 h, respectively.

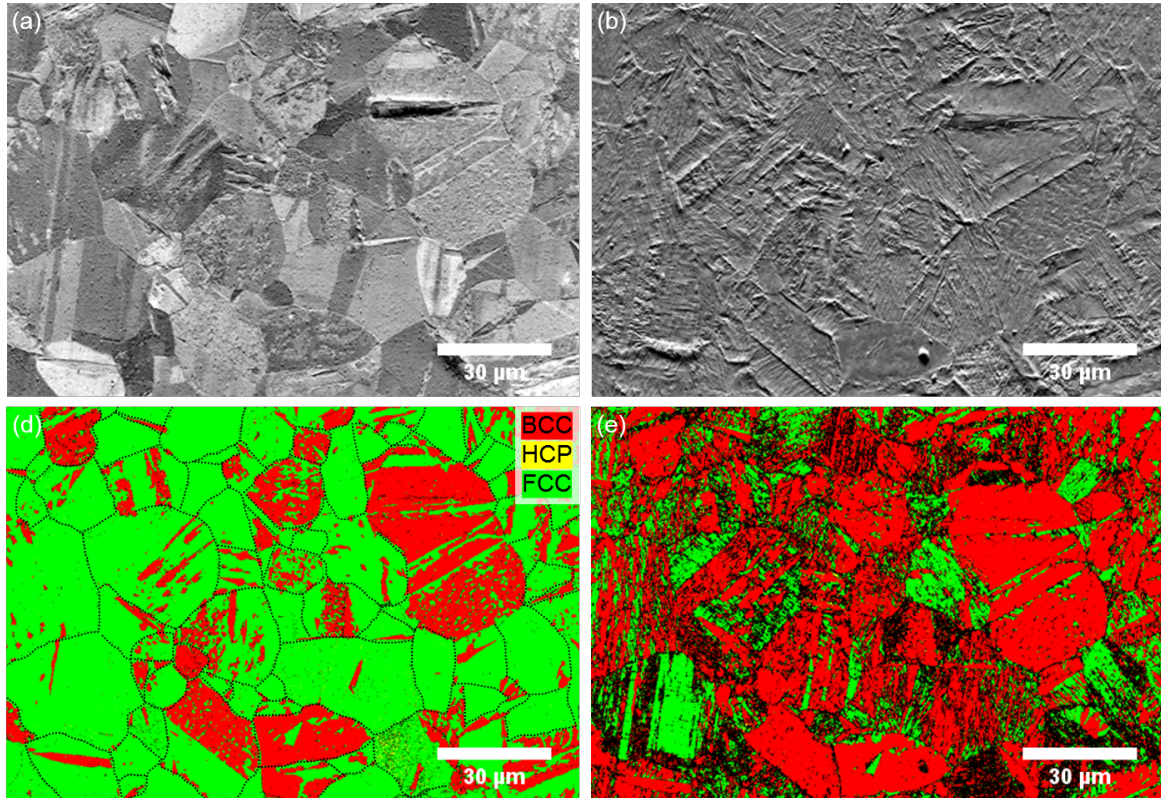


Figure 6.6: SEM images of the microstructure of the investigated steel AISI 304L (a) before and (b) after electrochemical charging for 24 h. The respective phase distribution maps are displayed in (c) and (d). Red colour represents BCC-like phases ( $\delta$ -ferrite, martensite), while green-coloured areas indicate FCC phase. Black pixels refer to measurement positions with no solutions. The dotted lines in (c) highlight some grain and twin boundaries.

The specimen surfaces in Figure 6.6(a) and (c) has been polished to mirror level with  $0.25\mu\text{m}$  colloidal silica as the last step. Within certain grains, twins are visible as parallel lines. This is due to local channeling-in behaviour of the primary electron beam during scanning. After charging, the same areas exhibit a much higher roughness owing to the ingress of deuterium (cf. Figures 6.6(b) and 6.7(b)). This is true except for a few grains which are smoother. In comparison to the phase maps in Fig. 6.6(c) and 6.7(c), it becomes clear that these areas have a BCC/BCT structure which existed already before charging and refers to  $\alpha'$ -martensite. Although sample preparation by mechanical grinding and polishing was done with great care, martensitic transformation on the surface apparently occurred to a certain extent. In some cases entire austenite grains transformed into martensite.

The increased roughness of the surface can be explained by the formation of  $\alpha'$ -martensite. This strain-induced transformation of austenite into martensite is characterised by a volume

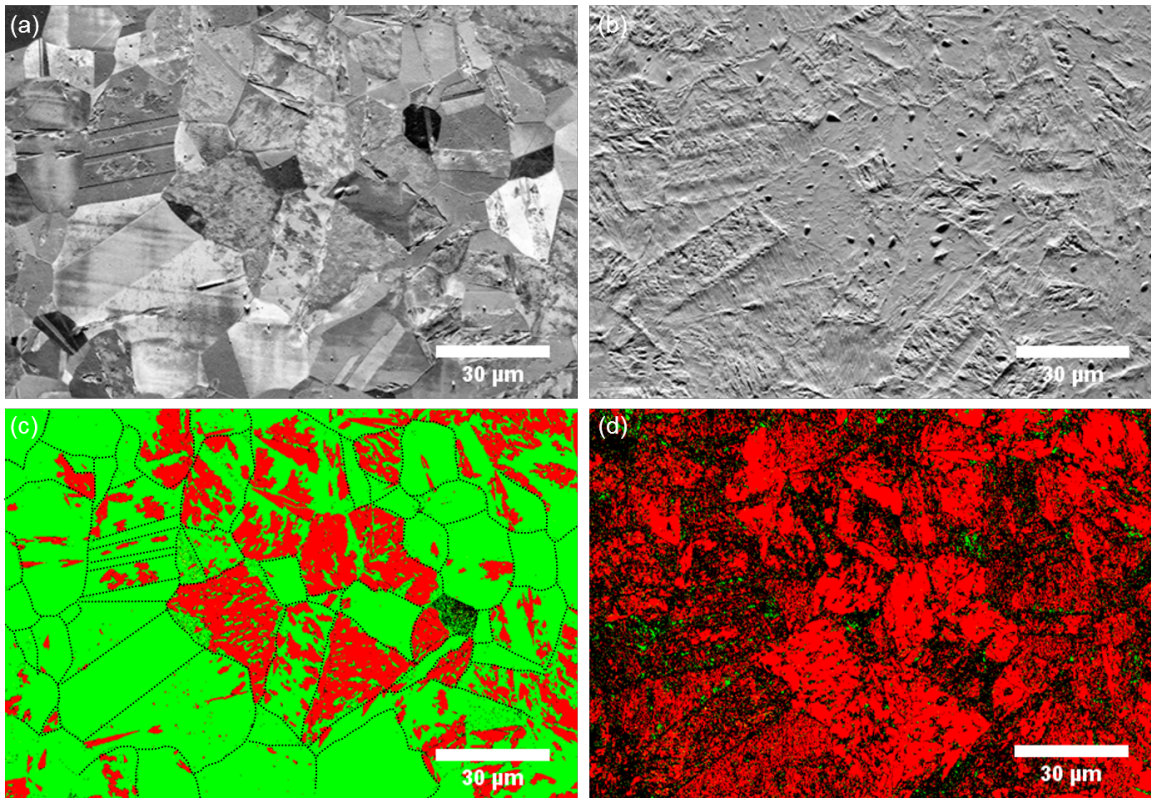


Figure 6.7: SEM images of microstructure of the investigated steel AISI 304L (a) before and (b) after electrochemical charging for 48 h. (c) and (d) display the respective phase distribution maps collected by EBSD. Red colour represents BCC-like phases ( $\delta$ -ferrite, martensite), while green-coloured areas indicate FCC phase. Black pixels refer to measurement positions with no solutions. The dotted lines in (c) highlight some grain and twin boundaries.

increase and shift of the orientation relations of the unit cell which led to a distortion of larger areas of the matrix [51, 86]. According to Martin et al., the volumetric expansion is about 2.7% [48]. Calculations by Yang et al. yielded values of 1.5-3.5% [126].

Bullough *et al.* ascribed the surface relief to a shape deformation. Martensite evolves at the expense of the austenitic parent lattice surrounding it. The shear movement of atomic planes, concomitant with altered orientation relationships of the unit cells and the induced movement of dislocations result in this relief formation [251].

The uptake of atomic deuterium and its accumulation increases the mean lattice plane spacing. Rozenak et al. proved this by XRD measurements on austenitic steel AISI 304, observing peak shifts to smaller Bragg angles, i.e. bigger lattice plane spacing. They derived an increase of 5.8% for  $\gamma$  and 5.5% for  $\epsilon$  [37, 128, 213].

Sobol *et al.* investigated deuterium-induced effects in duplex stainless steels. SEM and EBSD investigations revealed that blistering exclusively occurred in the ferritic phase [125, 202, 234]. Similar features are visible in Figure 6.6(b) and 6.7(b) when compared to the phase maps shown in 6.6(c) and 6.7(c). The material's surface shows blisters in the BCT martensitic phase, whereby the sample charged for 48 h has a greater number. As reason for blistering an accelerated diffusion of deuterium in martensite combined with a slower diffusion in an austenite grain beneath is assumed. Thus, accumulation of deuterium at the martensite-austenite interface is expected.

According to Wendler et al. [40], austenitic stainless steels with a stacking fault energy less than 18-20 mJ/m<sup>2</sup> tend to martensitic transformation under mechanical load. The calculation of the SFE for the investigated steels yields values of 15.7 to 18.1 mJ/m<sup>2</sup>, depending on the equation used [48]. By such similar SFEs, it can not be excluded that a charging-induced  $\gamma \rightarrow \epsilon \rightarrow \alpha'$  transformation can take place.

The phase distribution maps in Figure 6.6(d) and 6.7(d) prove the assumed transformation from austenite to  $\alpha'$ -martensite. No  $\epsilon$ -martensite was detected. The comparison between Figure 6.6(d) and 6.7(d) indicates that a higher fraction of austenite in the sample charged for 48 h transformed into martensite which is consecutive since more deuterium can enter the matrix and induce more strain [198, 252, 253]. The accumulation and assumed recombination to D<sub>2</sub> molecules at voids, cracks and other defects induced mechanical pressure. This mechanical force  $W_{mech}$  supplied the driving force for the strain-induced  $\gamma \rightarrow \alpha'$ -transformation (cf. Chapter 3.1.3.1).

### 6.3.2. Distribution of deuterium

The results of the principal component analysis (PCA) and the data fusion of ToF-SIMS and SEM images are shown in Figure 6.8.

It can clearly be seen that deuterium is distributed in the matrix heterogeneously so that different accumulation sites were identified. Ferrite and martensite grains with relatively low deuterium concentration are marked with (i). The low concentration is due to the low solubility and high diffusivity of deuterium in this phase. Thus, atoms could easily diffuse into the grains but were not trapped deeply. It is assumed that after charging stopped, deuterium was effusing



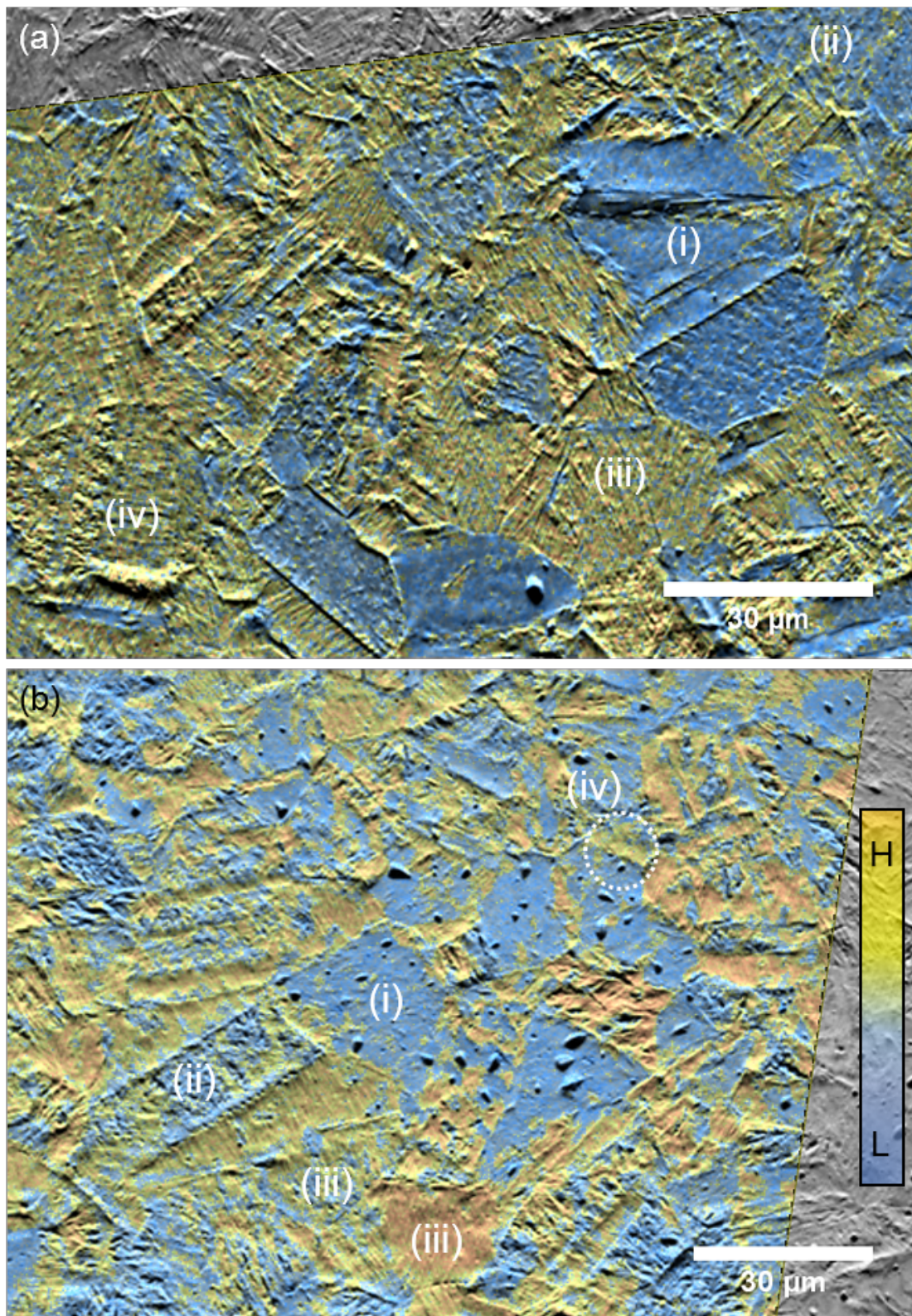


Figure 6.8: Fusion of ToF-SIMS data and SEM images of the sample charged for (a) 24 and (b) 48 h, respectively. Depicted is the distribution of deuterium and its co-covariants as the principal component two (PC2). The colour bar represents the intensity of the deuterium signal, whereas orange means a relatively high and blue a relatively low intensity.

from the matrix rapidly. Phase distribution maps in Figures 6.6 and 6.7, illustrate that these phases were existing already before electrochemical charging.

Labelling (ii) also shows regions with a relatively low amount of deuterium. In comparison to Figure 6.6 and 6.7, it becomes clear that these grains were former austenite which transformed to martensite. The conversion of the lattice structure from FCC to BCT was accompanied by the decrease of solubility and the increase of diffusivity [211, 234]. As a consequence, most of the trapped deuterium was released from the grains.

In contrast to this are grains exemplarily marked with (iii). These former austenitic grains transformed into martensite as well but exhibited considerably higher deuterium concentrations.  $\alpha'$ -martensite contains many defects like dislocations or stacking faults, which can act as traps for hydrogen/deuterium [211, 242]. It is possible that the trapped deuterium, being released during the transformation, was re-trapped at these defects.

As mentioned before, the  $\text{Cs}^+$  sputter cycle preceding the analysis had to be considered as another influential factor for phase transformation. For this reason, it can not be excluded here that phase transformation took place mainly due to the sputter beam and not due to charging as was already discussed in Chapter 6.2. Phase distribution maps in the Chapter A.1 prove this. The absence of the intermediate  $\varepsilon$ -phase can be another indication for the impact of the  $\text{C}^+$ -beam. Following the formation sequence chapter 3.1.3.1 introduced, HCP martensite is the precursor of BCT martensite. Because the combination of sputtering and deuterium introduced enough energy in terms of plastic strain, austenite went through the whole  $\gamma \rightarrow \alpha'$ -sequence and  $\varepsilon$  was not detectable by EBSD.

The necessary energy of the  $\gamma \rightarrow \alpha'$ -transformation can not only be provided by the Gibbs free energy  $G_{\gamma \rightarrow \alpha'}$  but also by mechanical load  $W_{mech}$  applied on the material as shown in Figures 3.7 and 3.8. Cooling of metastable austenitic steels increases the Gibbs free energy, but decreases austenite stability and stacking fault energy [26]. Therefore, it is anticipated that cooling down the samples in the ToF-SIMS after charging was not sufficient to start the nucleation of martensite. However, the deuterium-induced mechanical strains that were supported by  $\text{Cs}^+$  sputtering provided the necessary mechanical driving force for this process. Because of the reduced diffusivity of deuterium at lower temperatures, its effusion from the newly formed  $\alpha'$  regions was retarded, thus allowing it to be detected by SIMS.

Following this, it is assumed that grains marked by (ii) transformed *during* charging, whereas newly formed martensite labelled with (iii) transformed *after* charging.

The comparison of Figure 6.8 with the phase maps in Figures 6.6 and 6.7 reveals grains with FCC structure enriched with deuterium, marked with (iv). As discussed before, austenite has a high solubility for hydrogen in comparison to BCC/BCT phases. That explains the relatively high amount of deuterium in these grains. However, it is possible that the orientation of the grain was unfavourable for the transformation from FCC to BCT structure.

## 6.4. In-situ experiments

### 6.4.1. Deuterium-induced cracking of the surface

The formation of cracks and slip lines during and after electrochemical charging, i.e. due to the ingress, accumulation and effusion of deuterium was already described in the literature [4, 124, 126, 127, 234, 254]. Deuterium entered the lattice during electrochemical charging and caused its expansion. This was demonstrated e.g. by XRD measurements in [213, 255, 256]. One result of the supersaturation of the surface layers with deuterium were differences in the stress states of the surface and inner layers [257]. In the hydrogenated, i.e. the deuterium-charged layers, compressive stress evolved. By that a stress gradient similar to the one described in Chapter 6.2 is caused. Figure 6.9 illustrates the evolution of the deuterium-induced internal stress state in the (sub-)surface layers.

According to Mathias *et al.*, deuterium rearrangement begins in the moment the cathodic potential is removed from the specimen and charging stops [258]. According to the authors, this is the critical stage of crack formation, because the deuterium-expanded lattice contracts in the course of desorption of deuterium. Compressive stresses shift into tensile stresses inside the surface [259]. The distribution of deuterium was heterogeneous in the present case. That implies that the resulting tensile stresses were inhomogeneous, as well. These tensile stresses were the origin of cracking. Preferred cracking along grain boundaries and twins occurred due to the orientation differences between the grains, leading to increased stress applied on them. The higher the misorientation and tilt between two grains or grain and twin, the higher the arising stress. Consequently, cracks shown in the micrographs in Figure 6.10 should be running along highly tilted twin and grain boundaries.

Desorption of deuterium preserved the tensile stress at the crack tip of cracks that nucleated shortly after electrochemical charging stopped. That is why those fractures kept growing during the continuous release of deuterium from the surface [259].

It is assumed that the concomitant deuterium-induced decrease in cohesive strength of the lattice facilitates this process [254]. An effect described by the HEDE mechanism [135]. Figure 6.10 illustrates these features by an example. Here, the micrographs of both grades electrochemically charged for five days are shown. Cracks formed predominately along grain boundaries, i.e. intergranular and along twin boundaries and along slip bands, i.e. transgranular. They run straight and parallel to each other. Some of the twin boundary cracks branch out into short sub-cracks that grow along the slip lines. Crack density and crack length seem to increase with longer charging time. A compilation of SEM micrographs for different charging times can be found in the Appendix (cf. A.2).

Among others, Koyama *et al.* [114] and Bal *et al.* [73] investigated the susceptibility to hydrogen embrittlement of the metastable austenitic alloys Fe-18Mn-1.2C and Fe-23Mn-0.5C, respectively. Tensile specimens tested in hydrogen-containing atmosphere exhibited an altered fracture behaviour in comparison to non-charged samples. Based on these results, the authors developed a model to explain the observed phenomenon. A scheme of this model is depicted in Figure 6.11.



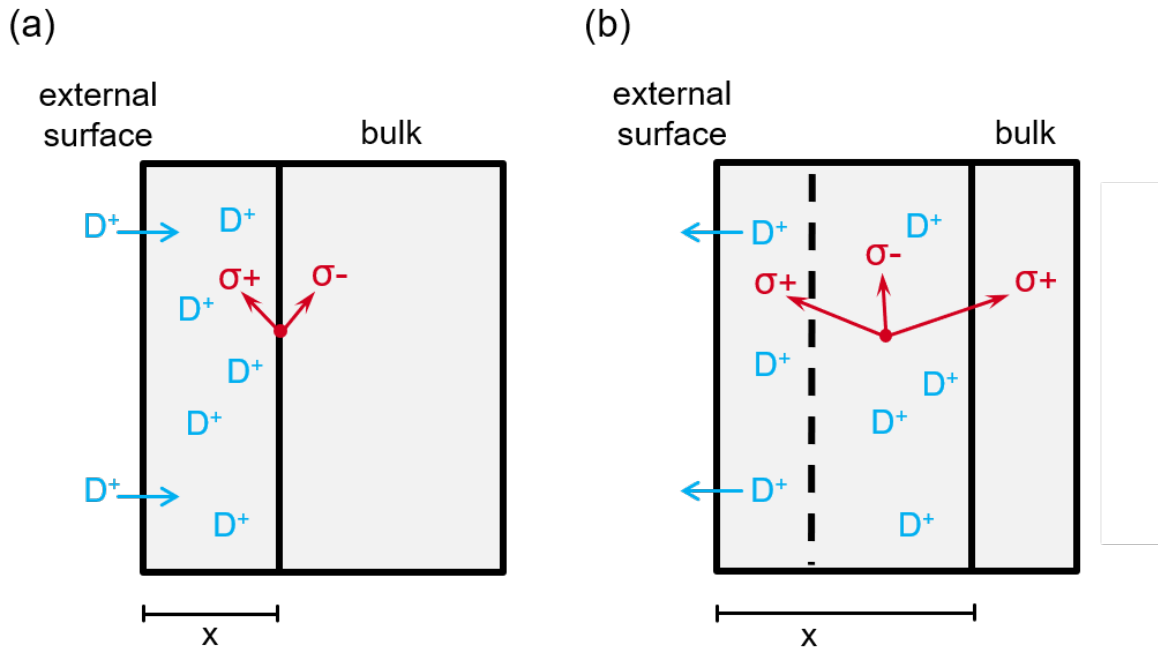


Figure 6.9: Evolution of internal mechanical stresses during electrochemical charging (a) and during outgassing (b). According to Mathias et al. [259]

In contrast to the high manganese TWIP steels investigated by Koyama *et al.* and Bal *et al.*, the alloys investigated in the present study tend to form martensite during mechanical loading (i.e. hydrogen charging) and only to a smaller extent mechanical twins. In addition to that, no tensile tests were conducted here. This is why the model of crack formation developed in [114] can not be applied altogether. However, the model can be adapted to the current observations by comparing it with results obtained e.g. by Yang *et al.* [126]. The group investigated the effects of electrochemical charging of the austenitic grade AISI 304 with regard to martensite formation, surface cracking and anodic dissolution behaviour. After electrochemical charging of their samples, the authors found similar features as shown in Figure 6.10. Cracks along grain boundaries and parallel cracking of twin boundaries were visible. Furthermore, some of the cracks grew through charging-induced epsilon martensite and along the  $\epsilon/\gamma$ -interfaces. Accordingly, sub-cracks branching out from larger cracks in Figure 6.10, can be interpreted as cracks running through newly formed martensite. Also shown in Figure 6.10(a) are cracks that initiated at the intersections of martensite and slip bands and twin boundaries, respectively.

The proposed crack formation can be described accordingly like this:

1. Formation of slip bands
2. Formation of 1.  $\epsilon$ - and 2.  $\alpha'$ -martensite
3. Cracking of  $\gamma$ - $\alpha'$ -interfaces
4. Formation of cracks on intersections of slip bands and martensite



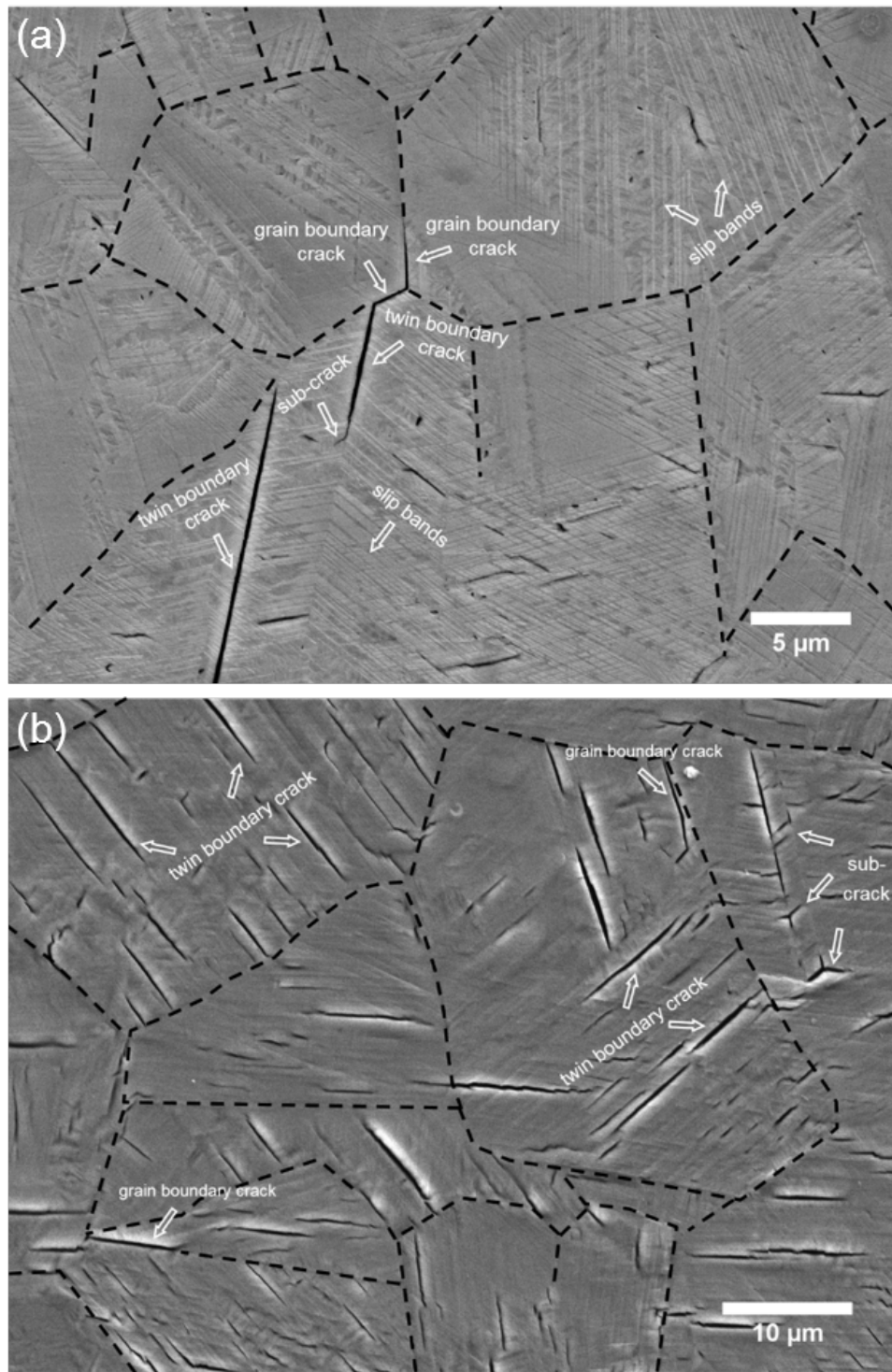


Figure 6.10: SEM micrographs of the surface of grades AISI 304L (a) and 316L (b) after electrochemical charging for 120 h. The dashed lines mark some grain boundaries and twin boundaries. Microscopic features such as cracks and slip bands are marked by arrows.

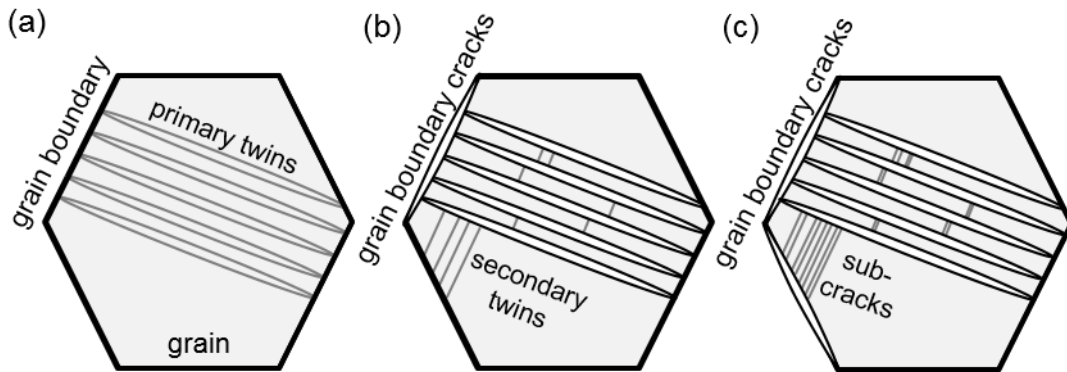


Figure 6.11: *Sequence of hydrogen-assisted cracking in steels can be described by the formation of primary twins (a), the formation of grain boundary cracks due to loss of cohesive strength with concomitant cracking of primary twins and the formation of secondary twins (b) and finally the evolution of sub-cracks (c). Adapted from Koyama et al. [114].*

The task of the following chapter is therefore not only to validate deuterium-induced phase transformation, but to discuss the process of crack formation. Electron backscatter diffraction was applied to proof this.

The depth of the cracks was not determined in the current work. However, they correlate with the penetration depth of deuterium plotted in Figure 5.13. Conservatively estimated, their depth was about  $26\ \mu\text{m}$ .

#### 6.4.2. Deuterium-induced phase transformation

Deuterium-induced phase transformation was already discussed in Chapter 6.3.1. However, due to the influence of the  $3\ \text{keV}\ \text{Cs}^+$  sputter beam, these results can not deliver an undistorted characterisation of the actual impact of deuterium charging on the investigated alloys. Furthermore, the above-presented sequence of crack formation shall be analysed with the help of the phase distribution maps. Samples from both steel grades have been electrochemically charged for different times and subsequently analysed by EBSD. The results are depicted and compared in the following.

Figure 6.12 shows the pristine condition of a sample made from AISI 316L. Apart from about 2.5% BCC phase, which can be attributed to the centre line segregations, the surface is fully austenitic. These segregations are due to flowing segregated molten steel in between the dendrites. It is caused by the steel's shrinkage during solidification or bulging [260].

Figure 6.12(a) and (b) were taken directly below the notch, whereas (c) and (d) in a distance of  $\approx 500\ \mu\text{m}$  from it. This enabled the separation between sputtered and un-sputtered regions on the surface.

The surface condition after electrochemical charging for 24 h and ToF-SIMS analysis is shown in Figure 6.13. A white dotted line margins the area sputtered with the  $1\ \text{keV}\ \text{Cs}^+$ -beam. The higher number of unsolved patterns within the sputter crater indicates a higher damage in this region. However, by taking the orientation maps in Figure 6.13(b) and (d) into consideration, it becomes obvious that no preferred grain orientation evolved during sputtering as it was observed

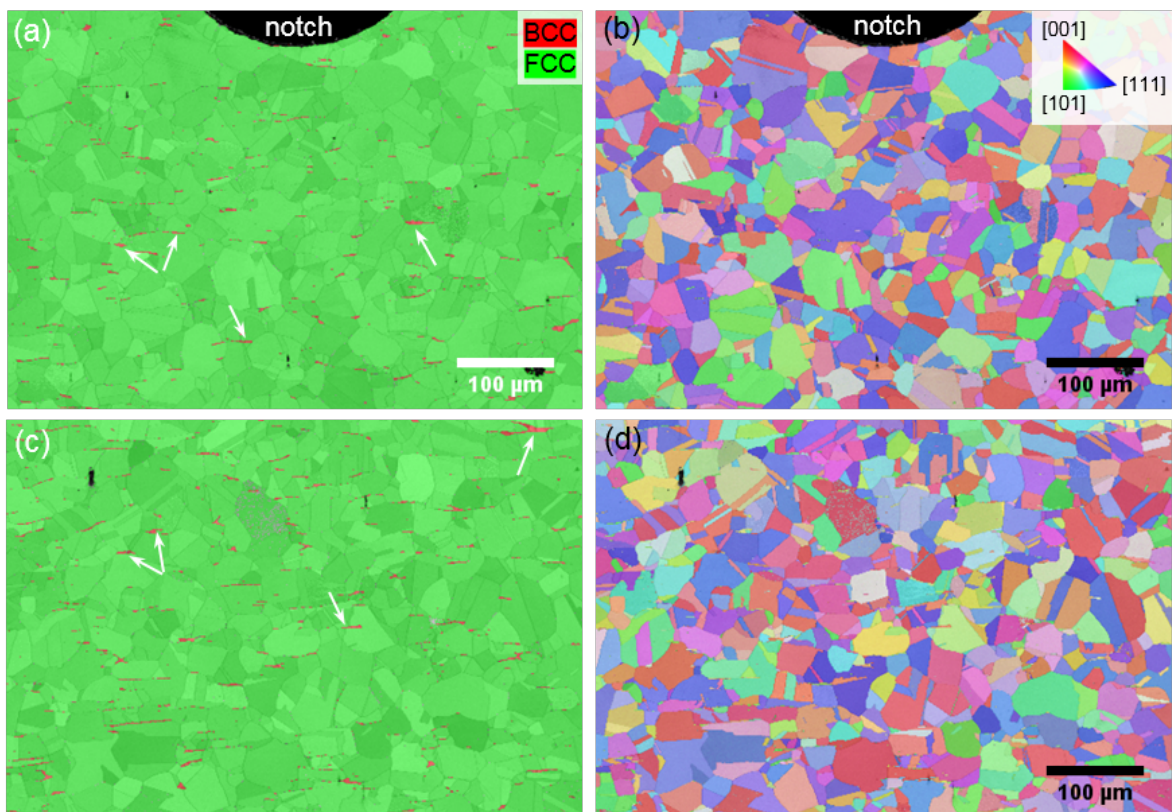


Figure 6.12: Phase and pattern quality maps of AISI 316L after preparation directly below the notch (a) and further away from it (c). The corresponding inverse pole figures in z-direction (IPF-Z) are given in (b) and (d). White arrows mark some of the centre line segregations that developed during solidification after the continuous casting process.



for the sputter tests (cf. A.1). About 88% of the sample surface outside the sputtered area consists of austenite, i.e. that  $\approx 10\%$  transformed into  $\epsilon$ - and to a smaller extent  $\alpha'$ -martensite. In contrast to that, few locations of the hexagonal phase are visible within the sputter crater.

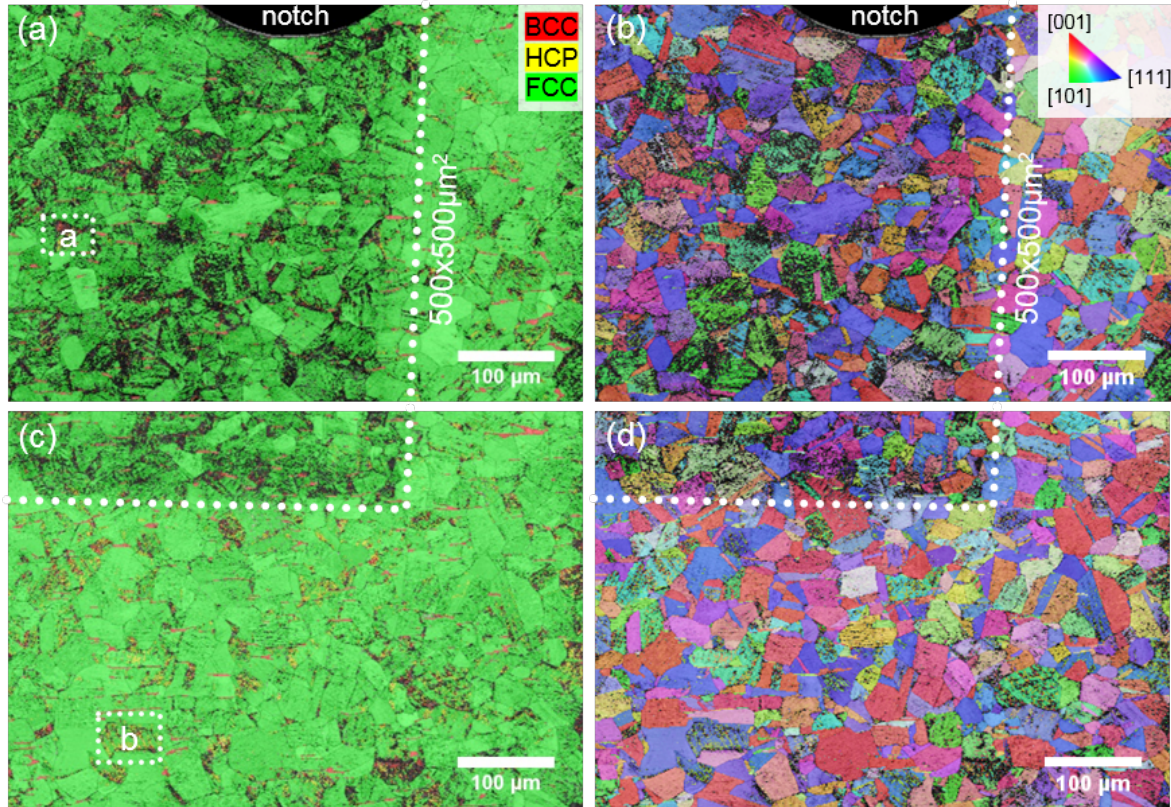


Figure 6.13: Phase and pattern quality maps of AISI 316L after electrochemical charging for 24 h and ToF-SIMS analysis in (a) and (c). The corresponding inverse pole figures in  $z$ -direction (IPF-Z) are given in (b) and (d). White squares labelled [a] and [b] mark positions where high-resolution images were taken from. These images are depicted in Figure 6.14. The white dotted line margins the region that was influenced by the sputter beam in the ToF-SIMS.

Higher magnified images of the locations labelled  $a$  and  $b$  in Figure 6.13 are shown in the next figure. Figure 6.14(a) gives the phase distribution map *within* and (b) *outside* the sputter crater. The higher magnification enables the identification of slip bands and thin lines of  $\epsilon$ - and  $\alpha'$ -martensite. Single strips of martensite vary in thickness between  $\approx 100$  nm to  $\approx 600$  nm. On closer examination, it becomes apparent that the BCC martensite exists as islands within the hexagonal  $\epsilon$ -martensite. Almost all intersections of slip bands contain  $\alpha'$ -martensite. This is consistent with the literature, as grain boundaries,  $\epsilon$ -martensite and intersections of slip bands were reported to be preferred nucleation sites for  $\alpha'$ -martensite [41, 62, 261, 262].

Not only strips of  $\epsilon$  and  $\alpha'$ , but also block-like martensite with thickness up to  $1 \mu\text{m}$  prevails. These locations can be assigned to intersections of slip bands with grain boundaries where localised high stresses made it energetically favourable to accommodate through shear and, thus, phase transformation.

It is important highlight again that the materials surface shown in Figure 6.14(b) was *neither* sputtered at any point during SIMS analysis *nor* did it contain pre-existing martensite

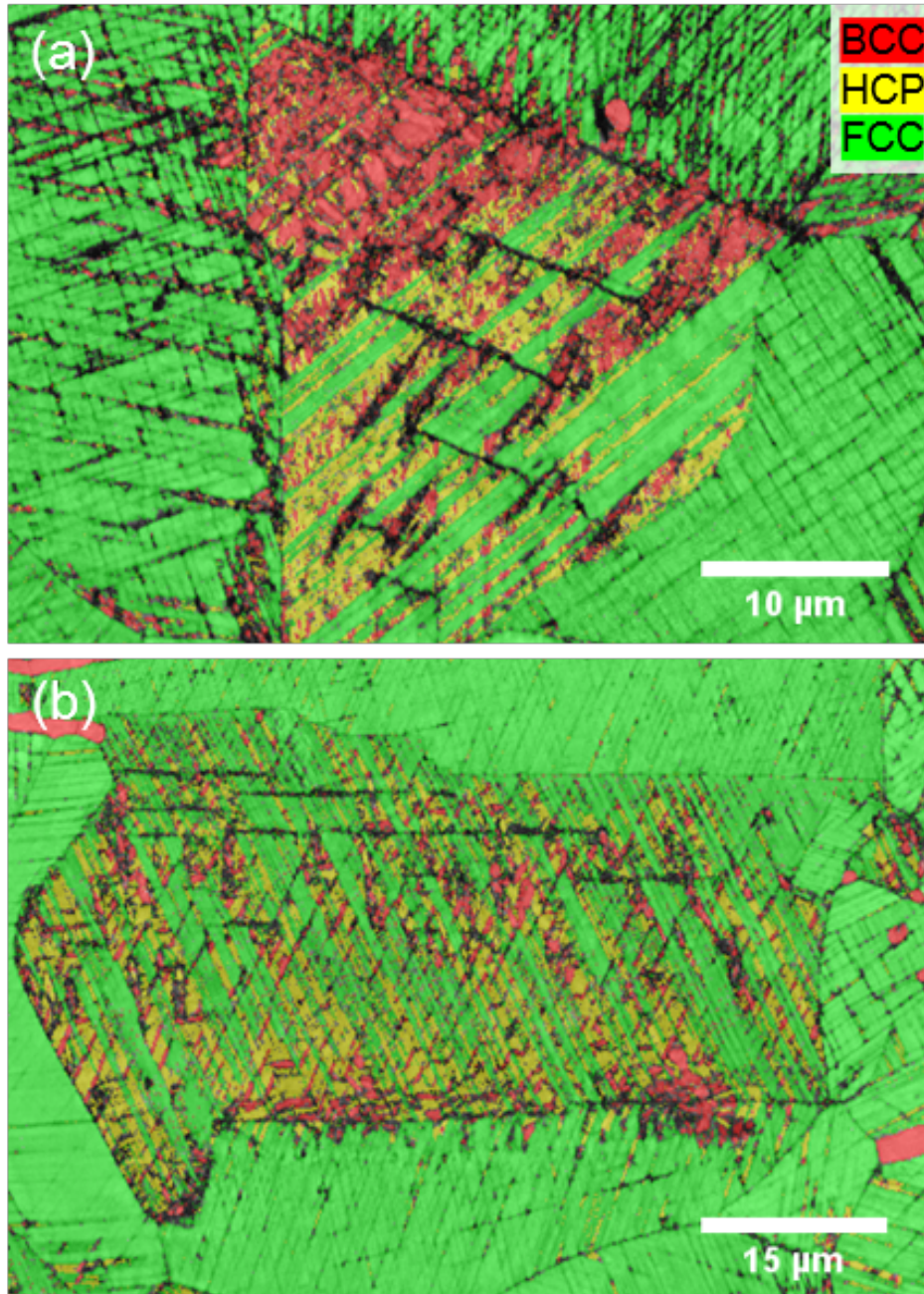


Figure 6.14: Phase and pattern quality maps of AISI 316L after electrochemical charging for 24 h and ToF-SIMS analysis. The images were taken from a sputtered (a) and a non-sputtered area (b) that are shown in Figure 6.13(a) and (c), respectively.



before charging. Deuterium can therefore be assumed to be the major cause of the  $\gamma \rightarrow \varepsilon \rightarrow \alpha'$ -transformation.

Figure 6.15 presents the initial phase distribution in alloy AISI 304L before (a) and after charging with deuterium for 48 h (c). The respective inverse pole figures are displayed in (b) and (d). This sample was *not* polished electrolytically before charging. That is why about 47% of the analysed surface consists of residual  $\alpha'$ -martensite from the production. Structural changes that developed in this phase due to charging are mainly reflected by zero solutions in the EBSD data. Some of the formerly well-indexable BCC grains were strongly distorted so that no Kikuchi patterns could be indexed. The amount of martensite and highly damaged phase after charging and ToF-SIMS adds up to  $\approx 65\%$ . It has to be pointed out that no sputter craters or the observed and above-mentioned typical [111]-orientation that resulted from  $\text{Cs}^+$  sputtering are visible in Figure 6.15(c) and (d). This was described in Chapter 6.2.

Austenite grains which were affected by the ingress of deuterium exhibit an increased surface roughness and increased number of damages. Black pixels, i.e. unsolved patterns, express that. Additionally, the formation of slip bands and martensite can be observed. White arrows in Figure 6.15(a) and (c) indicate some of these features.

It is well known that the BCC phase has a lower solubility but higher diffusivity for hydrogen and deuterium than FCC materials. The uptake and trapping of deuterium during charging should have been low in the martensite and dissolved deuterium would have diffused out from the grains quickly after charging. Eventually, more severe damages and phase transformations were expected to take place in the austenitic grains than in the martensitic grains. However, the opposite behaviour was observed. An explanation for this is the delivery condition of the sheet material. Cold rolling produced martensite and a high amount of lattice defects, such as dislocations, within the first layers of the material. As it was pointed out in Chapter 3.2.2.2, dislocations can support the transport of hydrogen atoms into the material as they are attached to the stress field of the dislocations. A behaviour observed by many researchers by the comparison of pre-strained and un-strained specimen [30, 88, 173].

A recent study by Claeys *et al.* supports this. The authors investigated the influence of hydrogen on the formation of martensite during straining in DSS 2205 [263]. They found that dislocations migrate into the material upon straining in hydrogen atmosphere. Hydrogen was, thus, delivered into deeper layers of the material. In addition to that, new dislocations evolved due to a reduced shear modulus.

However, this might not be the reason in the present case since no external plastic deformation, connected to the formation of dislocations, took place during the cathodic charging. The increased number of damages after charging is most likely due to the ability of dislocations to trap hydrogen. Deuterium entered the (BCC) grains during charging. Instead of diffusing further into deeper layers of the material, it was trapped by the dislocations. Deuterium accumulated in the following and damaged the material. Insufficiently indexable Kikuchi patterns resulted from that.

The following figures depict the influence of 72 h electrochemical charging with deuterium on the steel grade AISI 304L. For this purpose, Figure 6.16 shows the phase distribution and grain

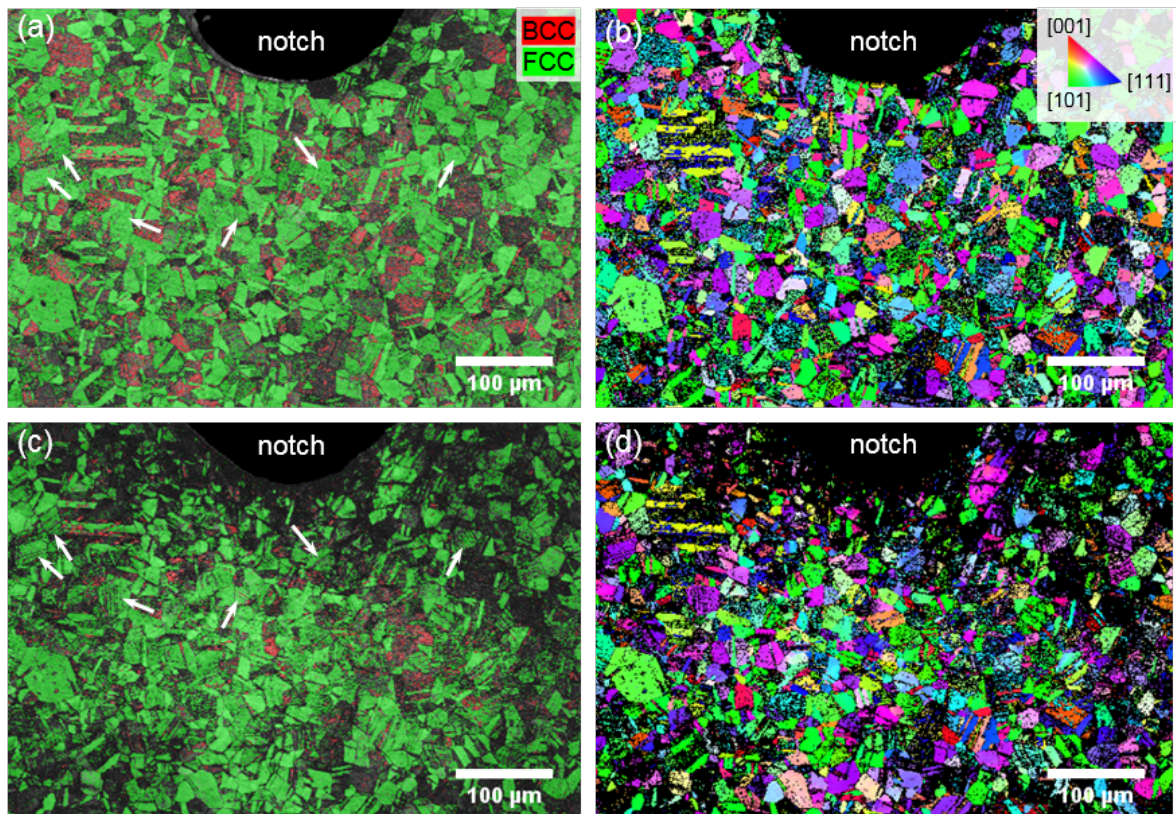


Figure 6.15: Phase and pattern quality maps of AISI 304L before (a) and after electrochemical charging for 48 h (c) and the corresponding inverse pole figures in z-direction (IPF-Z) in (b) and (d), respectively. Note that the sample was not polished electrochemically. The martensite fraction remained from the production process and was not fully removed by mechanical grinding.

orientation *before* charging, whereas Figures 6.17 and 6.18 illustrate the changes that occurred due to charging.

In the pristine condition only about 1% of BCC phase remained on the surface. The rest was successfully removed by mechanical and subsequent electrolytic sample preparation.

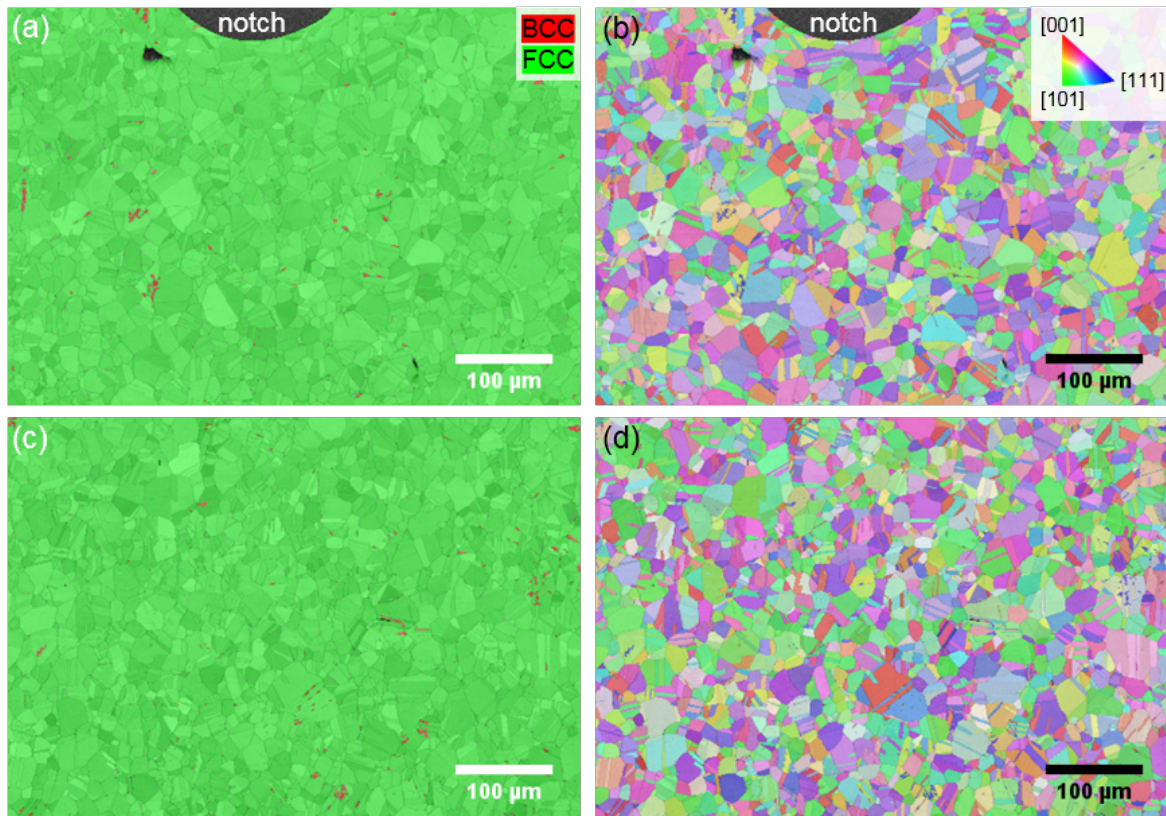


Figure 6.16: Phase and pattern quality maps of AISI 304L after electrochemical polishing in (a) and (c) and the corresponding inverse pole figures in  $z$ -direction (IPF-Z) in (b) and (d). Black pixels refer to measurement positions where none of the pre-defined phases could be indexed.

Figure 6.17(a), (c) and (d) show the phase distribution within the material surface after electrochemical charging. The higher magnified images in (c) and (d) stem from *within* the sputter crater that exhibits a high density of defects in the form of unsolved patterns. Only about 29% of the ROI was identified as austenite, as compared to 41% in the un-sputtered area in Figure 6.18(a). Both of these overviews, directly below the notch and distant from it, were acquired with a step size of 119 nm. This can be interpreted as the step width of the electron beam rastering the surface. A smaller pixel size of 99 nm and a smaller ROI, as it was chosen for the higher magnified micrographs, increased the hit rate. That means the number of zero-solution pixels decreased. This is due to a higher precision in beam positioning on smaller surfaces and a better ratio of pixel and step size. The minimal step size in EBSD analyses is limited by the information/excited volume, the elemental number of the investigated material and the acceleration voltage.<sup>3</sup> Examining the higher magnified phase maps in Figure 6.17(c) and

<sup>3</sup>It should be mentioned as side note that the terms "high resolution" and "high magnification" are not identical and should not be confused. The first refers to the size of the electron beam, whereas the latter describes the feasibility of beam positioning.



(d) and Figure 6.18, thus, shows that the number of un-indexed pixels is somehow overestimated in the overviews.

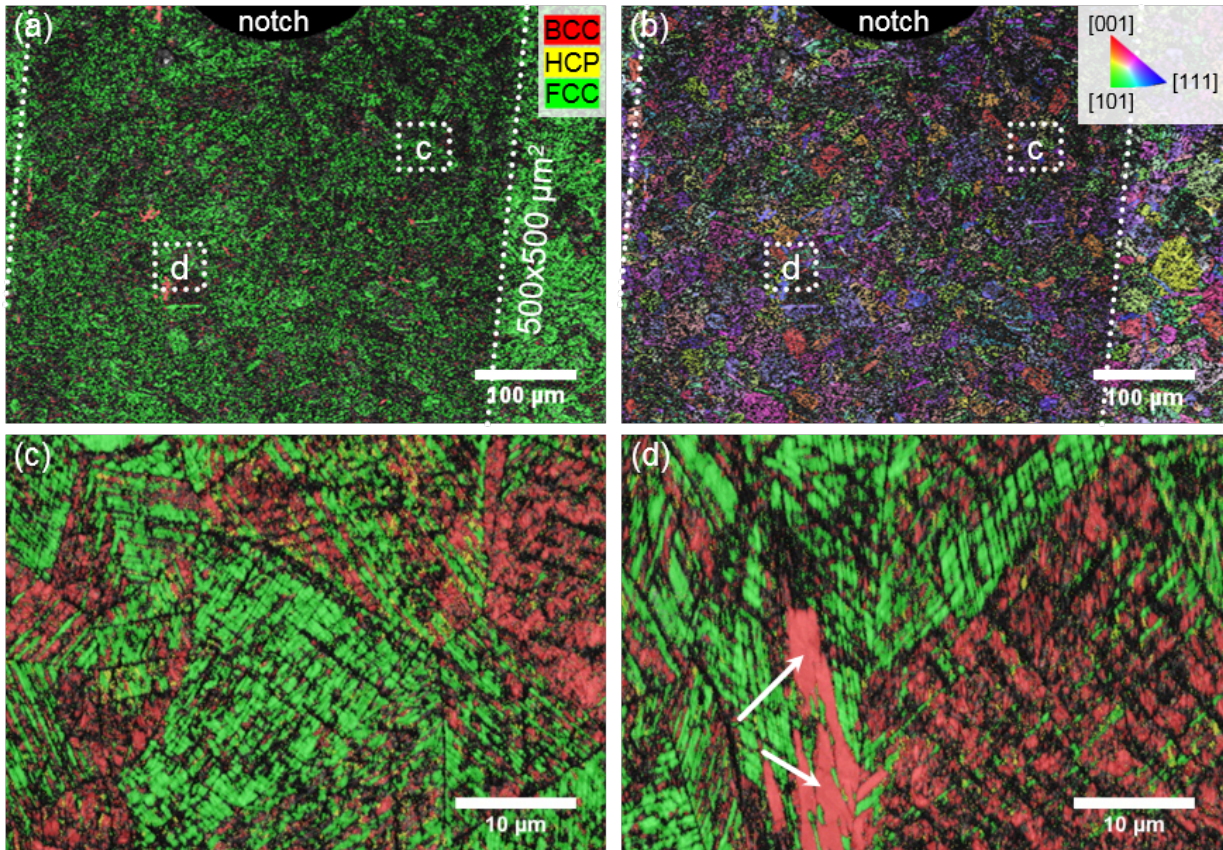


Figure 6.17: Phase and pattern quality maps of AISI 304L after electrochemical charging for 72 h and ToF-SIMS analysis (a) and the corresponding inverse pole figure in z-direction (IPF-Z) in (b). The higher magnified ROIs, marked by dotted squares, are shown in (c) and (d). White arrows mark BCC phase that existed already before charging.

A comparison of the phase distribution maps in Figure 6.17(c) and (d) and Figure 6.18(b) reveals a lower fraction of  $\epsilon$ -martensite in the sputtered surface than in the un-sputter crater. This is most likely due to the additional mechanical energy introduced by the  $\text{Cs}^+$ -beam. Deuterium-charging introduced mechanical stress into the material and induced a shear movement of atomic planes. Stacking faults and  $\epsilon$ -martensite formed on slip bands as they represent energetically favoured sites. The formation stopped during or after charging as the surface condition in Figure 6.18(b) reflects. Additional energy caused by sputtering in the ToF-SIMS carried the martensitic transformation forward (cf. Figure 6.17(c)+(d)). Another sample of the grade AISI 304L was charged and analysed under the very same conditions. The respective phase maps, which are plotted in the Appendix as Figure A.20 and A.21, verify this finding.

Comparing the EBSD results in Figure 6.17 and Figure 6.18 (304L) with those in Figure 6.19 (316L) qualitatively, a larger fraction of martensite and a higher amount of defects at the surface of the grade AISI 304L is evident. This difference is more pronounced in the respective phase maps in the vicinity to the notch: The sputter craters are clearly visible in both alloy grades, but

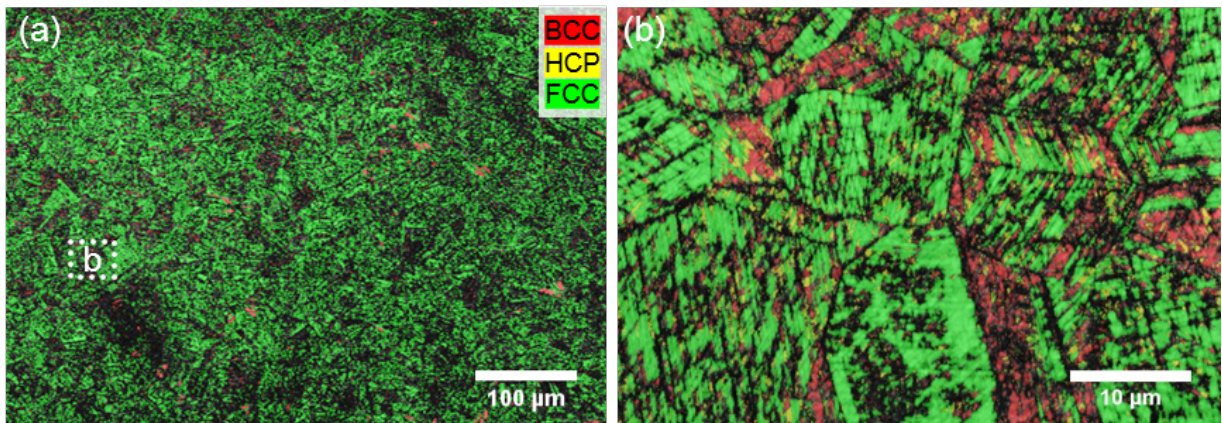


Figure 6.18: Image (a) shows the phase and pattern quality map of an un-sputtered area distant from the notch of the same sample shown in Figure 6.17. The white square indicates the location of the higher-magnified region in (b).

a larger amount of un-solved pattern is obvious in steel AISI 304L. This clearly shows that the impact of the caesium beam on the integrity of AISI 304L, like it was discussed in Chapter 6.2, is higher as compared to the AISI 316L grade. The higher amount of defects and martensite in 304L as compared to 316L can clearly be assigned to the higher stability of the austenite phase of the latter. A higher content of nickel as FCC stabilising element together with a lower amount of the BCC stabiliser chromium makes grade 316L less prone to  $\gamma \rightarrow \alpha'$ -phase transformation (cf. Chapters 3.1.1 and 6.2).

It has to be pointed out that in both grades the larger proportion of the surfaces was affected by the ingress of deuterium in a way that delivered only poor EBSD signals which were not interpretable. Thus, they were assigned to as zero-solution instead of BCT phase. However, on several spots within the investigated ROI martensite shines through the non-indexed areas, proving that the  $\gamma \rightarrow \alpha'$ -conversion took place. Analyses with a higher magnification and a pixel size smaller than the applied 119 nm per pixel can overcome this problem to a certain degree.

Higher magnified images of the surface of the grade AISI 316L are shown in Figure 6.19(e) and (f). Comparing these with its counterpart AISI 304L in Figure 6.17(c) and (d) and Figure 6.18(b) reveals another difference between the steels. Slip bands in which  $\epsilon$ - and consequently  $\alpha'$ -martensite formed seem finer and distinct from each in the alloy grade 316L. Even in grains that almost completely transformed from FCC to HCP and BCT, individual martensite bands can be identified and distinguished. In contrast to that is the more broad and block-like shape of the martensite in steel AISI 304L.

Martensite-formation taking place on preferred slip bands where the highest shear stress occurs was already described in the present work several times. Thickness of these bands, amount and shape of martensite and the  $\epsilon/\alpha'$ -ratio vary, for instance, with the chemical composition and, thus, stacking fault energy of the alloy. A thorough study on the behaviour of martensite-formation in Fe-Cr-Ni in dependence of external load, stacking fault energy, grain orientation and temperature was delivered by Tian *et al.* [264]. Figure 6.20 is based on these observations. It was extended and adapted to the investigated alloys in order to be able to apply it in the present work.



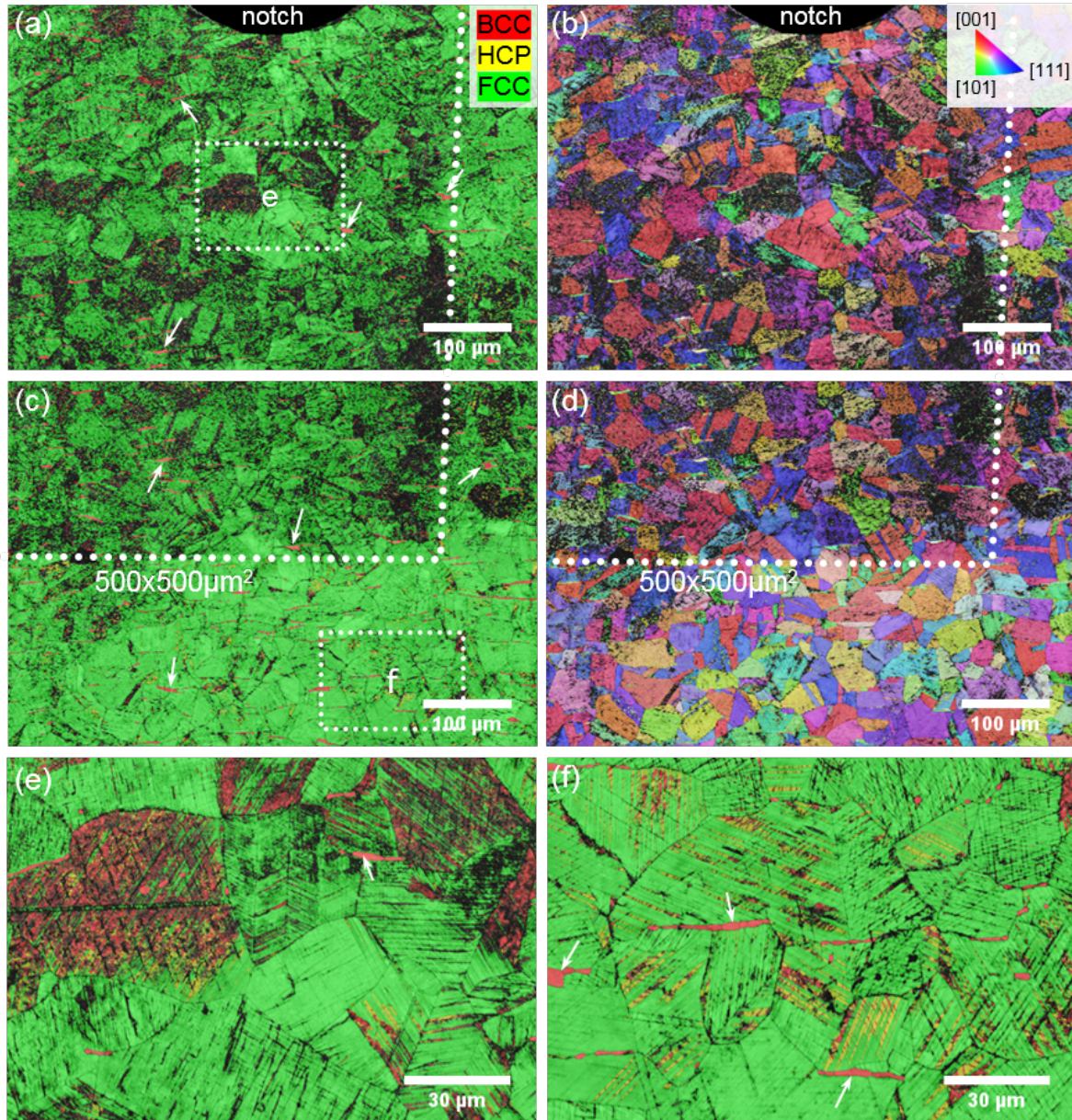


Figure 6.19: Phase and pattern quality maps of AISI 316L after electrochemical charging with deuterium for 72 h and ToF-SIMS analysis in (a) and (c). The corresponding inverse pole figures in  $z$ -direction (IPF-Z) are given in (b) and (d), respectively. White squares in (a) and (c) mark positions where high-resolution images were taken. These magnifications of a sputtered and un-sputtered area are shown in (e) and (f), respectively. White arrows indicate exemplary the centre line segregations. Black pixels refer to measurement positions where none of the pre-defined phases could be indexed.

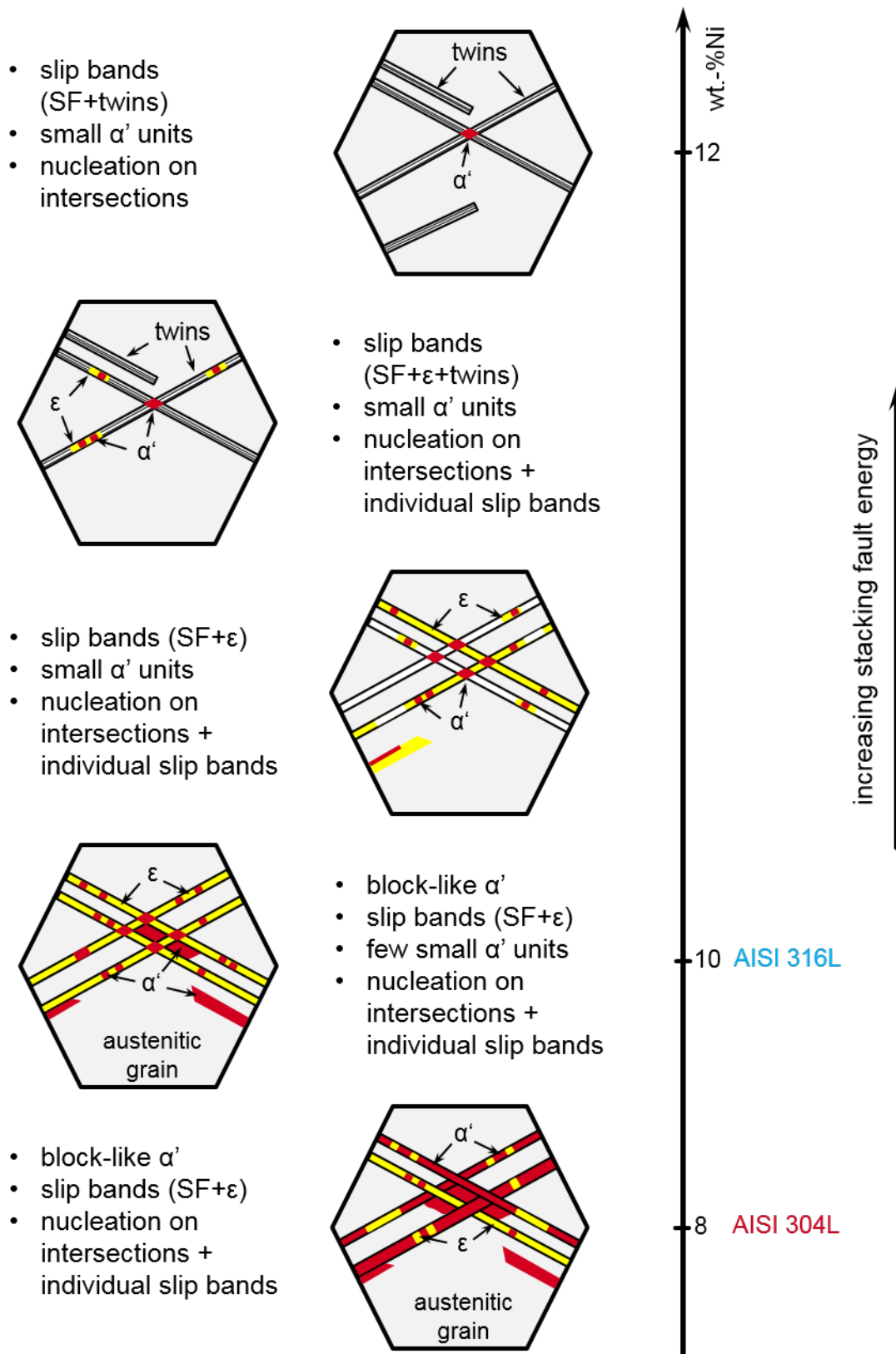


Figure 6.20: Formation of deformation-induced martensite and mechanical twins in austenitic stainless steel in dependence of the nickel concentration and, thus, stacking fault energy. Adapted and extended from Tian et al. [264].

Figure 6.20 depicts the influence of the stacking fault energy on the transformation behaviour in austenitic stainless steels. Every image is an idealised representation of real conditions after a certain degree of plastic deformation. In this example, the ordinate shows the nickel concentration of the respective alloy. Higher concentrations of nickel increase the stacking fault energy and, thus, facilitate deformation-induced twinning. Lower amounts of nickel, as in the investigated alloys AISI 304L and AISI 316L, will foster  $\gamma \rightarrow \epsilon \rightarrow \alpha'$ -phase transformation.

Rather thick block-like  $\alpha'$  structures with only few remaining  $\epsilon$ -martensite form on slip bands and their intersections in 304L grades. After the same degree of plastic deformation, 316L grades will ideally form less  $\alpha'$ -martensite that is shaped partially block-like and partially slender and more fine. This was observed in the phase maps in Figures 6.14, 6.18, 6.19, 6.22 and A.21.

Figure 6.20 is only able to describe the phenomena of twinning and phase transformation for a very limited scope of alloys. It does not take other factors like temperature into account. The amount of transformed austenite of course depends also strongly from the extent of mechanical deformation. In addition to that does not only nickel increase the stacking fault energy. It was discussed in Chapters 3.1.1 and 3.1.3.1 that the so-called TWIP steels contain high concentrations of manganese and potentially considerable amounts of nitrogen. Both elements are strong austenite stabilisers and will promote twinning and suppress martensite formation.

The following image shows the phase distribution maps and inverse pole figures of a sample made from grade 304L before and after electrochemical charging for 120 h. The sputter crater is again visible in the overview in Figure 6.21(c) and (d). The percentage of martensite and un-solved patterns inside the crater amount to  $\approx 86\%$ . With  $\approx 82\%$  in the image of the un-sputtered area, it is only slightly lower. White squares marked with *a-d* in Figure 6.21(c) and (d), respectively, indicate locations where higher magnified micrographs were taken.

It becomes obvious in Figure 6.22 that the number of pixels with zero solution was again overestimated in the large area overviews. By reducing the step size from 119 nm in Figure 6.21 to 99 nm in Figure 6.22(b)-(d) or even 74 nm in (a), the precision for the pattern recognition increased greatly.

As it was already discussed, martensite formed on slip bands. Shear on those bands introduced stacking faults in each second close-packed  $(111)_\gamma$  plane of the structure, referred to as hexagonal  $\epsilon$ -martensite. Even though this phase prevailed and is visible in the micrographs in yellow colour, the larger fraction transformed further into the BCC/BCT phase. Grain boundaries of the initial austenite acted as obstacles for the slip or shear bands. In this context Martin *et al.* utilised the term *deformation band* rather than shear band [48], because shear bands perpetuate through high-angle grain boundaries (HAGBs). Applying this information on the phase maps depicted in Figure 6.22 but also in Figures 6.14, 6.19 and 6.25 allows the assumption that grain boundaries at which deformation bands are stopped are most likely high-angle grain boundaries with a misorientation angle greater than  $15^\circ$  [265].

Another characteristic is highlighted in Figure 6.22 by white arrows. The indicated BCC phase does, in contrast to the newly formed  $\epsilon$ - and  $\alpha'$ -martensite, not contain higher roughness or defect density reflected as zero-solutions in the EBSD images. This phase is caused by production of



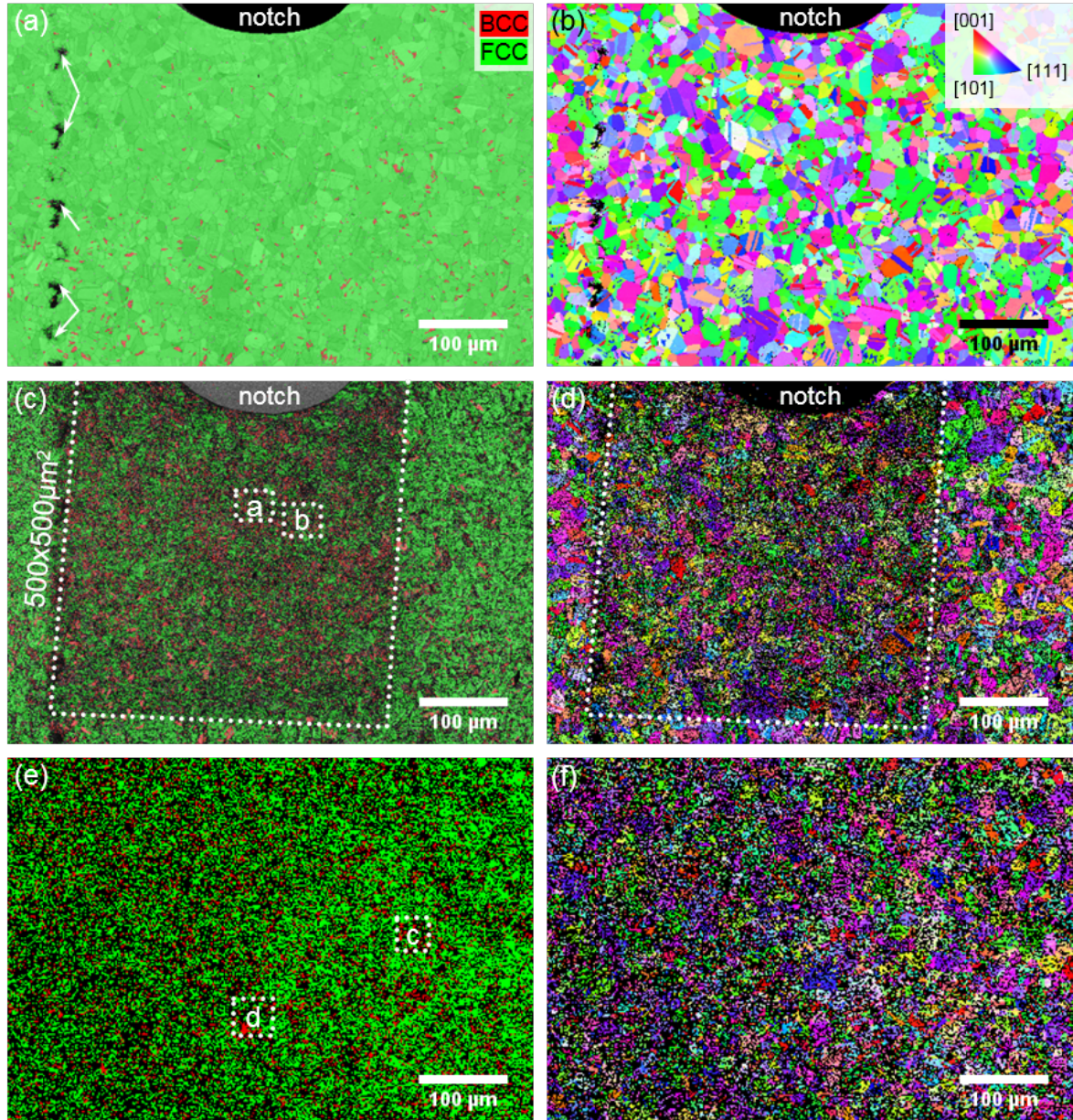


Figure 6.21: Phase and pattern quality maps of AISI 304L before (a) and after electrochemical charging with deuterium for 120 h and ToF-SIMS analysis in (c) and (e). The corresponding inverse pole figures in z-direction (IPF-Z) are given in (b), (d) and (f). Higher magnified images of locations labelled with a-d are given in Figure 6.22. The white arrows indicate contaminations or damages on the surface that are due to sample preparation. Black pixels refer to measurement positions where none of the pre-defined phases could be indexed.



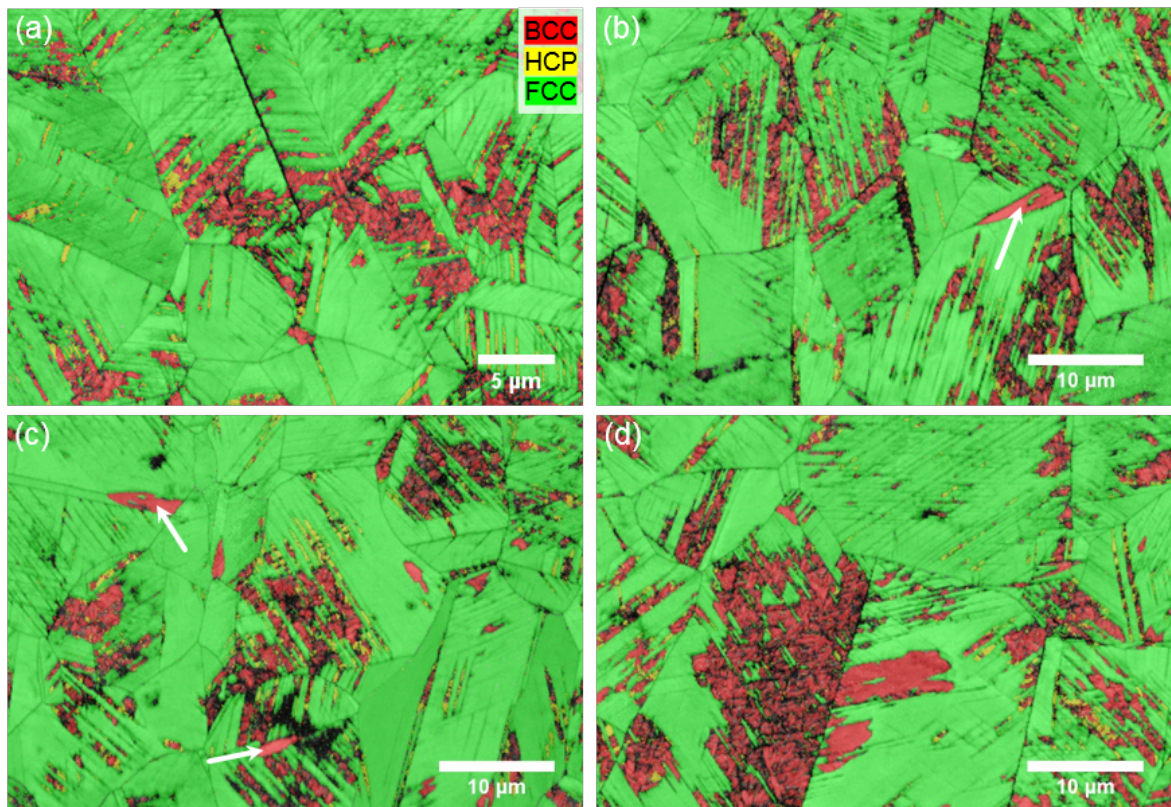


Figure 6.22: Higher magnification micrographs of selected areas in the phase maps shown in Figure 6.21 (c) and (e), respectively. ROIs (a) and (b) lie within the sputter crater, while (c) and (d) stem from the non-sputtered surface. White arrows indicate martensite or  $\delta$ -ferrite that existed already before charging.

grade AISI 304L. Unlike the rolling-induced martensite that was shown above (cf. Figure 6.15), it can be  $\delta$ -ferrite. According to the Schaeffler diagram presented in Chapter 5.1, this is an intrinsic part of the investigated alloy. It originates during solidification and depends strongly on the chemical composition of the material [266].

The reason why these residuals seem to be not affected by electrochemical charging lies in its high diffusivity and concomitant low solubility for hydrogen, as it was mentioned above (cf. Chapter 6.3.1). In contrast to the surrounding austenite with a diffusion coefficient in the order of magnitude of  $D \approx 10^{-16} \frac{m^2}{s}$ , these martensite islands have a diffusion coefficient  $D \approx 10^{-10}$  to  $10^{-11} \frac{m^2}{s}$  [90, 174].

Due to a lower packing density of the unit cell, the BCC phase offers faster diffusion pathways for hydrogen. As a result a lower absolute amount of deuterium entered the martensite, and was not trapped deeply. During sample transport and ToF-SIMS analyses after charging ceased, it most likely effused from the lattice.

Figures 6.23, 6.24 and 6.25 depict the surface of steel AISI 316L after cathodic charging for 120 h. Figure 6.23 gives an overview of the deuterium-inflicted surface, while Figure 6.24 depicts higher magnified ROIs from *within* the sputter crater and Figure 6.25 from several *un-sputtered* regions.

In both,  $Cs^+$ -sputtered and un-sputtered areas, extensive cracking of the surface can be observed. Fractures are visible as straight black lines and correspond to un-indexed regions. This is obvious for these fractures did not contain indexable material. Grains with a higher fraction of newly formed martensite exhibit more cracks.

The following higher-magnified phase distribution maps serve the purpose to verify the scenario of deuterium-induced crack formation along twins, interfaces and grain boundaries that was proposed in Chapter 6.4.1. The images were therefore taken with a step size of 110, 95 and 59 nm, respectively.

White arrows in Figure 6.24(d) emphasise primary cracks that are located on slip bands and branch out into sub-cracks. They are deflected at the junction with an intersecting slip band and change direction to propagate further on that "second" band. Martensite is present on each intersection of these deformation bands. The angle between these pairings is about  $60^\circ$ . Around 100 angles between slip bands were determined in other EBSD and SEM images to confirm this. In total four angles between the deformation bands were found, which are in almost perfect agreement to the ideal angles between lattice planes and directions, respectively. Table 6.6 gives exemplary the family of all directions together with the ideal and measured angles. A "||"-symbol indicates that also parallel directions are included because of their equivalence. The same holds true for lattice planes between which the very same angles prevail. This is due to the translation symmetry in the cubic crystal lattice. The angles between two slip bands that reflect the trace of a slip plane therefore allow to identify the crystallographic planes involved.

Cracking of the  $\gamma/\varepsilon$ - and  $\gamma/\alpha'$ -interfaces are highlighted by white arrows in Figure 6.25(e) and (f). A small rim of FCC phase is visible at the flank of these cracks, indicating that these cracking sites are most probably interfaces. It can, thus, be concluded that interfaces between



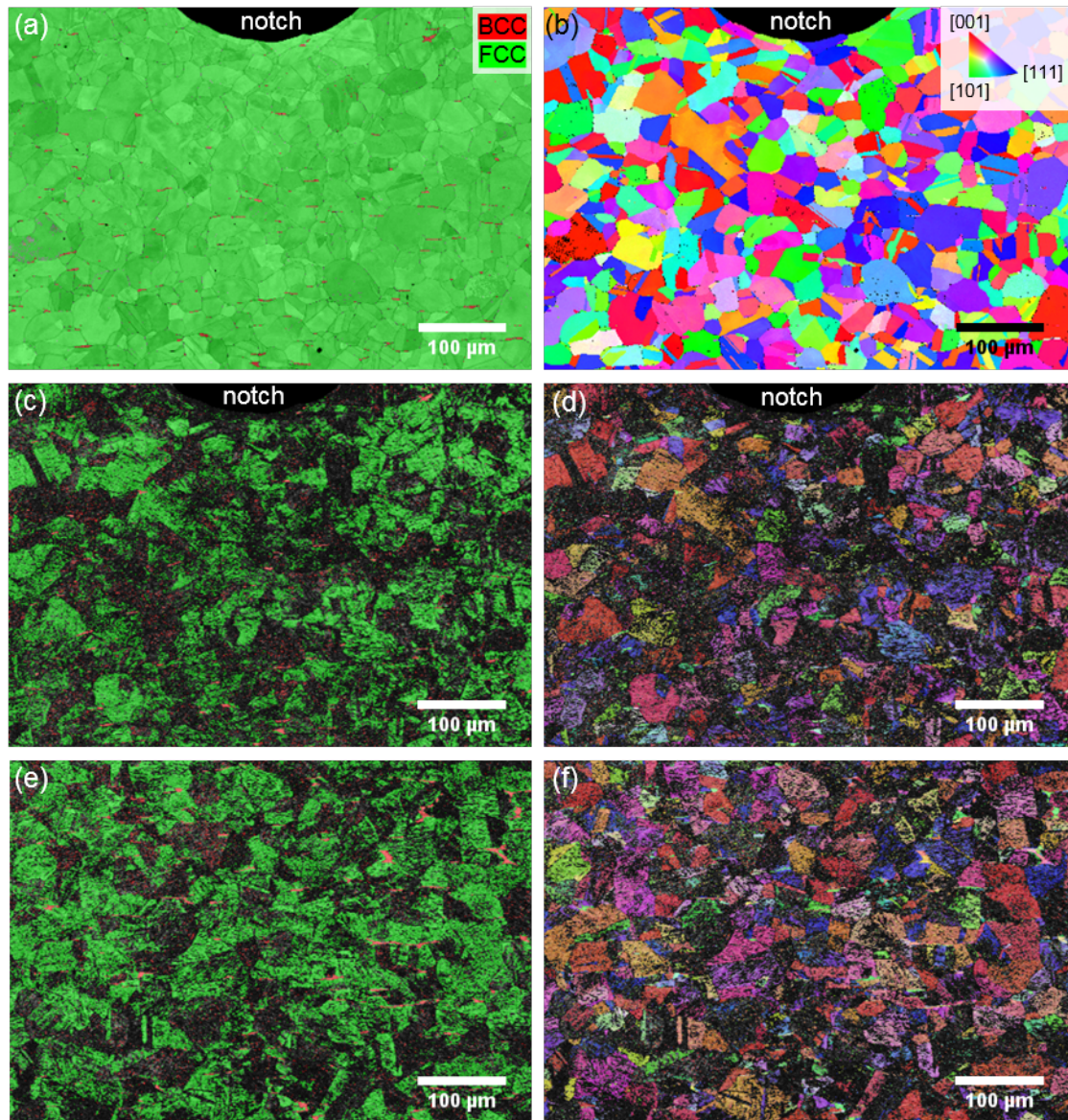


Figure 6.23: Phase and pattern quality maps of AISI 316L before (a) and after electrochemical charging with deuterium for 120 h and ToF-SIMS analysis in (c) and (e). The corresponding inverse pole figures in z-direction (IPF-Z) are given in (b), (d) and (f). The white arrows indicate exemplary the centre segregations. Black pixels refer to measurement positions where none of the pre-defined phases could be indexed.



austenite and martensite, but also between martensite and martensite are preferred cracking sites, as it was mentioned before. The same is of course true for grain boundaries as an interface between grains of different orientation.

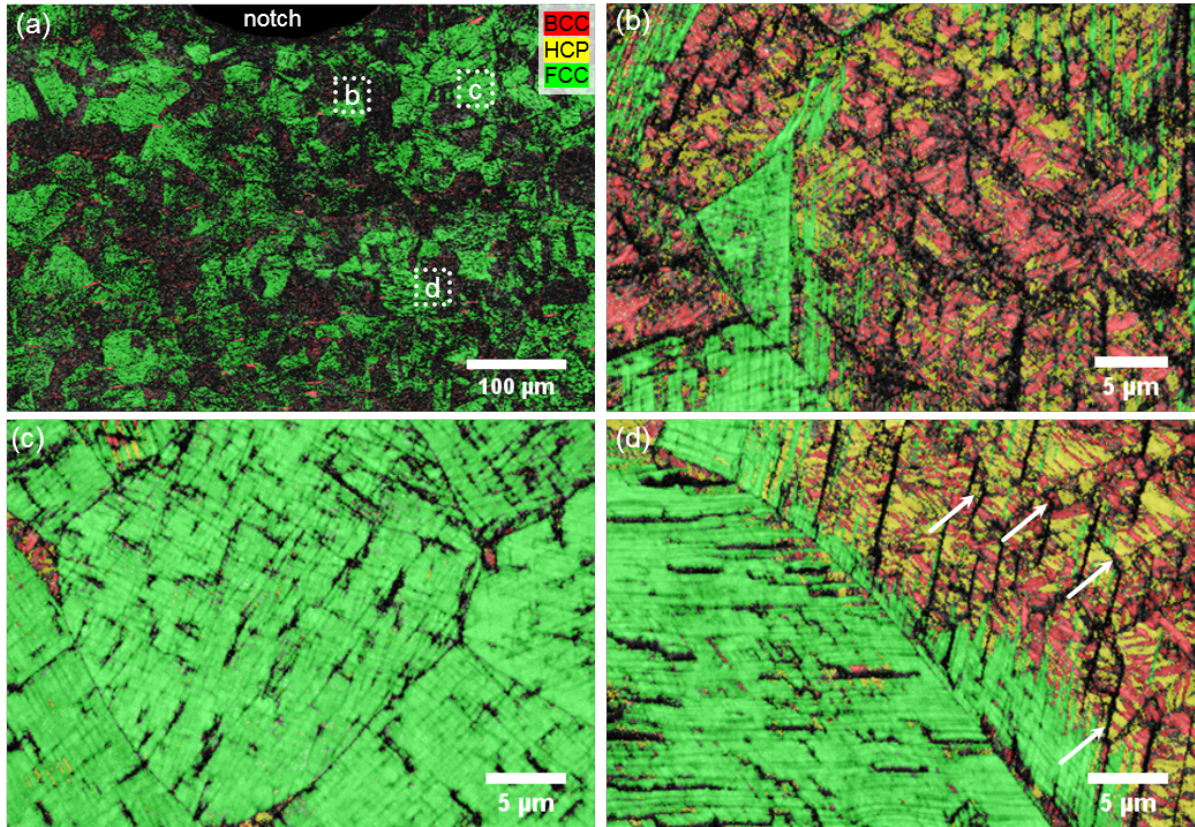


Figure 6.24: Phase and pattern quality maps of the same sample as in Figure 6.23 in (a). Positions where high-resolution micrographs were taken are marked by white squares and shown in (b), (c) and (d). White arrows in (d) emphasise primary cracks that are located on slip bands and branch out into sub-cracks. Black pixels refer to measurement positions where none of the pre-defined phases could be indexed.

Table 6.6: Angles between planes and directions in cubic crystal systems.

family of directions	ideal angles	measured angles
$\  \langle 111 \rangle \  \langle 001 \rangle$	$54.74^\circ$	$52.47^\circ$
$\  \langle 111 \rangle \  \langle 101 \rangle$	$35.26^\circ$	$34.46^\circ$
$\  \langle 001 \rangle \  \langle 101 \rangle$	$45^\circ$	$44.2^\circ$
$\  \langle 101 \rangle \  \langle 101 \rangle$	$60^\circ$	$60.67^\circ$

The phase distribution maps and the corresponding inverse pole figures in Figures 6.12 to 6.23 display another interesting feature. From these figures, it becomes obvious that the areas with the highest density of defects and transformed austenite are grains in  $[111]$  and  $[101]$  direction normal to the surface. Grains in the  $[001]$  direction seem to be less affected. A comparison of the IPFZ maps in Figure 6.23 and the phase maps in 6.24 clarify this particularly. All of the



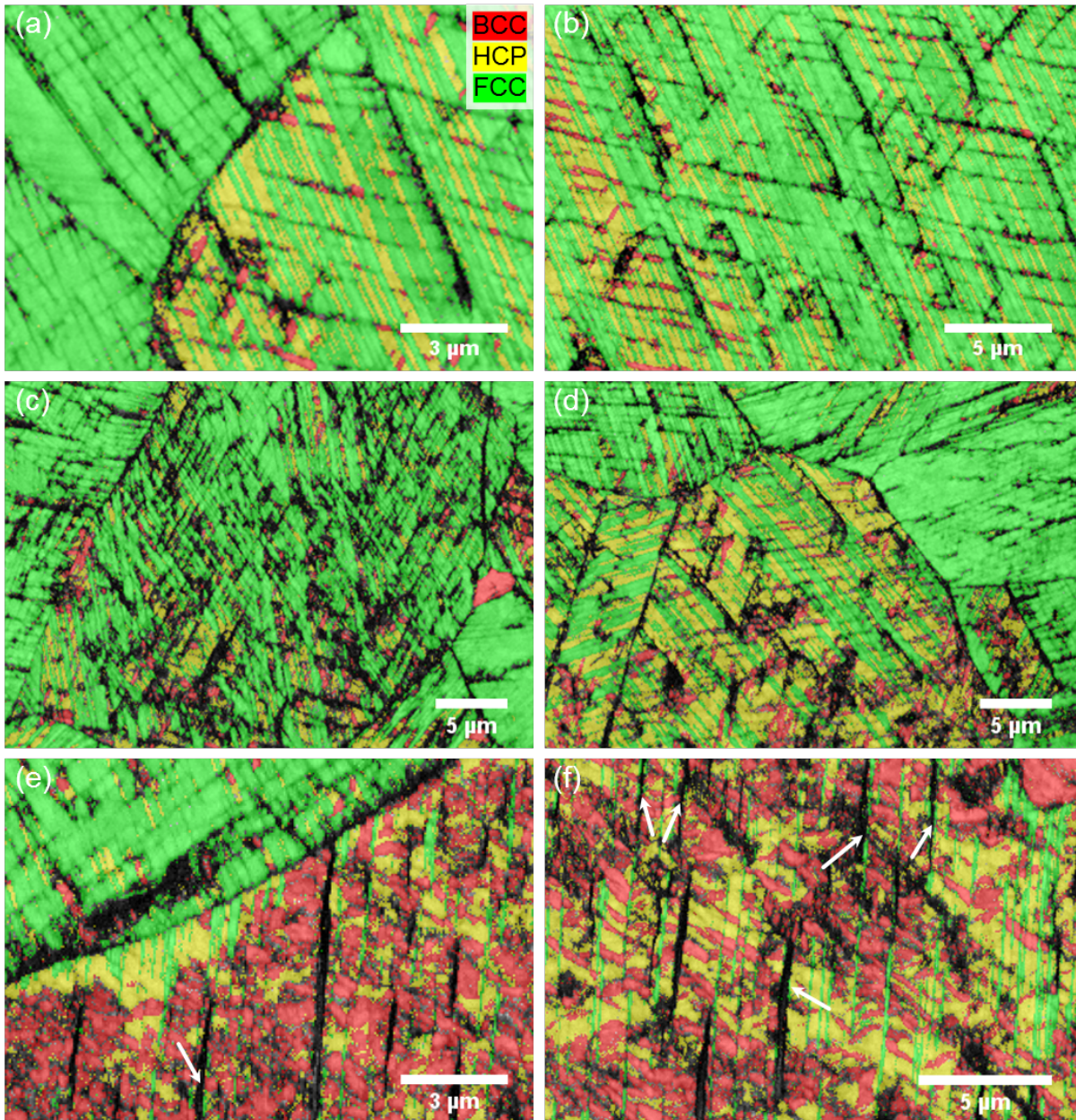


Figure 6.25: High resolution phase distribution and phase quality maps of AISI 316L after electrochemical charging with deuterium for 120 h and ToF-SIMS analysis. The micrographs stem from regions outside the areas shown in the overview in Figure 6.23 and therefore reflect un-sputtered material. Black pixels refer to measurement positions where none of the pre-defined phases could be indexed. White arrows indicate cracks rimmed by a small strip of austenite.

un-transformed austenite grains depicted in these micrographs have a [001] orientation normal to the surface. This phenomenon was observed in both steel grades.

Cao *et al.* investigated the effect of texture on the diffusion behaviour of hydrogen in nickel [267]. They found that the adsorption energy for hydrogen in the (111) planes is the lowest while in (001) it is the highest. As consequence hydrogen can be taken up more easily in grains with this orientation. Figure 6.26 illustrates this.

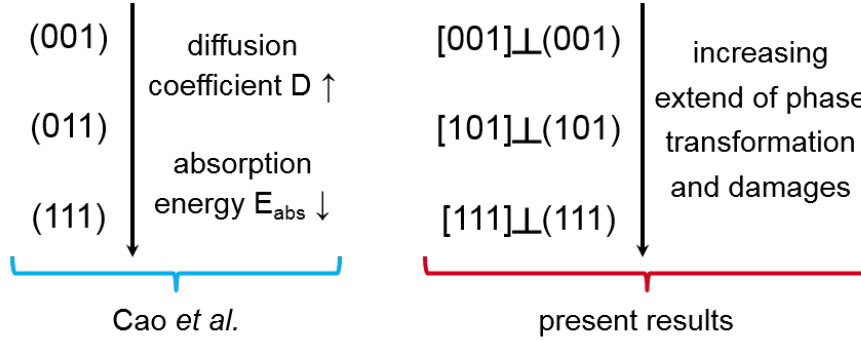


Figure 6.26: According to Cao *et al.* [267], absorption and diffusion of hydrogen in FCC materials is anisotropic. The present findings are in agreement with those findings.

Considering the orientation relations in crystal structures and specifically in cubic lattices (cf. Figure 3.11), it becomes clear that the [001] direction is perpendicular to the (001) plane. According to Cao *et al.*, these planes have the highest absorption energy and lowest diffusion coefficient for hydrogen, as well. From this it follows that during charging less deuterium entered those grains, damaging the material less severely.

Mechanical transformation and phase transformation in FCC materials take place on specific *slip systems* that are defined by a slip plane and a direction. *Schmid's law* describes the resulting shear stress on a specific slip system when the material is under tensile stress:

$$\tau_{res} = \underbrace{\cos\phi * \cos\lambda}_{\text{Schmid factor } m} * \sigma \quad (22)$$

As it was mentioned before in Chapter 6.4.1 and illustrated by Figure 6.9, entrance of deuterium into the metal lattice leads to its expansion and the evolution of compressive stress. After electrochemical charging stopped, deuterium effused from the matrix. The concomitant contraction caused tensile stress. Schmid's law is valid for single crystals under tensile stress. Because a single grain is defined as volumetric unit with homogeneous properties, it can be regarded as a single crystal. For this reason, it is assumed that Schmid's law is, in principle, applicable.

Following it, the highest resulting shear stress  $\tau_{res}$  developed on the  $(111)_\gamma$  and  $(101)_\gamma$  planes, whereas the resulting stress on  $(001)_\gamma$  planes must have been lower. These planes are perpendicular to the [001] direction which is reflected by the IPF-Z as to be parallel to the surface. Thus, a lower resulting shear stress develops in this slip system. Figure 6.27 illustrates Schmid's law and the slip systems. Furthermore, mechanical slip occurs on densely packed planes. In FCC

structures this corresponds to the (111) planes. The [001] direction is not a viable direction for this process, because the family of systems  $\langle 001 \rangle \{111\}$  does not exist.

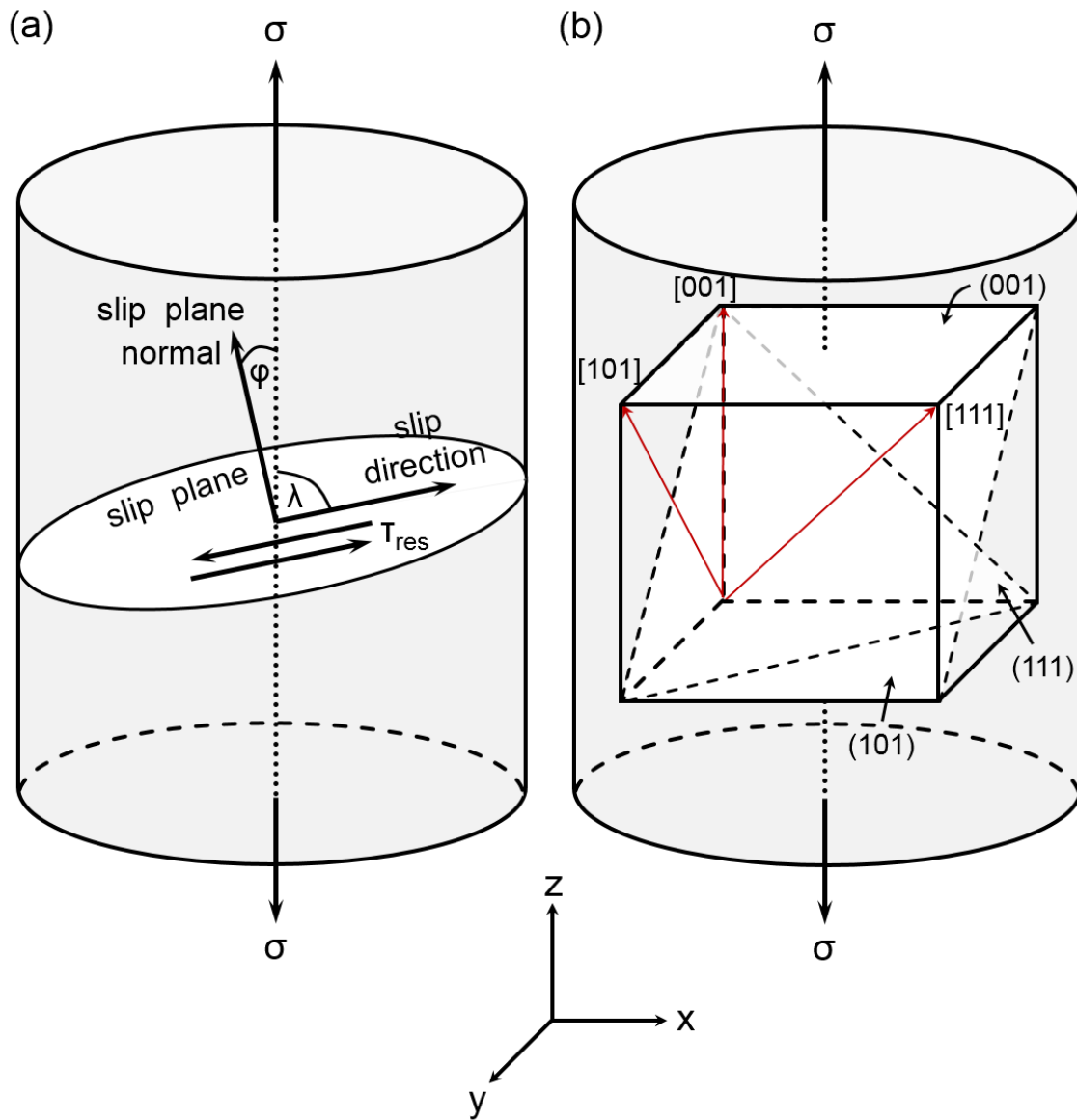


Figure 6.27: Schmid's law (a), visualised by a cylinder model, describes the resulting shear stress when a tensile stress is applied. Some slip planes and directions in FCC structures are outlined in (b). Due to the translation symmetry of the cubic system, these are sufficient to describe the major slip systems.

Considering Equation 22 and Figure 6.27, it becomes clear that shear stress along the  $(111)_\gamma$  and  $(101)_\gamma$  planes is higher than on  $(001)_\gamma$  planes. Consequently, a higher (external) mechanical load is necessary to induce phase transformation in grains with a [001] orientation normal to the surface. Following this, it should be theoretically possible to control  $\gamma \rightarrow \alpha'$ -phase transformation and to specifically induce it only in certain grains. Adjusting the duration of electrochemical charging can be a means to achieve this. Relatively short times should lead to a phase transformation only in [111] grains and longer charging time would additionally cause [101] grains to transform.

Extending the duration to even longer times should finally provoke martensite formation in grains oriented in [001], as well.

Anisotropic deformation behaviour in austenitic stainless steels was also observed e.g. by Gussev *et al.* [62]. The researchers investigated a nickel-enriched AISI 304 steel by means of indentation and tensile tests and subsequent EBSD measurements. A focus was thereby on the morphology of newly-formed martensite and the effect of grain orientation on the transformation structure. Their results showed that deformation twins and their intersections acted as the precursor for martensite in the tensile tests. In contrast, martensite formed mainly in the vicinity of grain boundaries during indentation. However, EBSD measurements for both indicated that  $\gamma \rightarrow \alpha'$ -transformation did not occur in the grains close to [001] orientation. Gey *et al.* observed a similar behaviour of a AISI 304 steel grade after tensile tests [248]. Although Gussev *et al.* as well as Gey *et al.* investigated merely the anisotropic behaviour of the steel grades AISI 304 and *not* the influence of hydrogen, their results can provide useful indication that hydrogen can effect austenitic stainless steel in a similar way like external mechanical deformation does. It was also proven by numerous researchers e.g. by XRD measurements that the ingress and accumulation of hydrogen into the metal lattice causes internal mechanical stress sufficiently high to evoke  $\gamma \rightarrow \alpha'$ -transformation [57, 212, 213, 256, 258, 259, 268] .

Mathias *et al.* conducted XRD and Mössbauer transmission spectroscopy measurements and tensile tests on charged and hydrogen-free samples from the steel grades AISI 304L, 316L and 310 [269]. The authors emphasised the similarity of the structure and orientation of hydrogen-induced martensite and deformation-induced martensite. Even though more research needs to be done to clarify the impact of hydrogen on the structure of (austenitic stainless) steels, the present results and the aforementioned references strongly indicate that hydrogen causes compression stress during ingress and tensile stress during egress that can trigger  $\gamma \rightarrow \varepsilon \rightarrow \alpha'$ -transformation.

Another observation has to be mentioned to close the gap between the analyses of sputter-induced martensite, discussed in Chapter 6.2, and the present findings of deuterium-assisted martensite formation. The evaluation of the results of the sputter tests revealed that the transformed areas systematically showed a [111] orientation normal to the surface. Several samples of the two investigated alloys were electrochemically charged for different times. The analyses of numerous IPFZ maps did not exhibit the same feature. Although the sputter crater was usually visible in the phase and IPFZ maps and exhibited a higher number of damages, an exclusive [111] direction did not manifest. From this, it can be concluded that sputtering with a 1 keV  $\text{Cs}^+$ -beam did not induce additional  $\gamma \rightarrow \alpha'$ -phase transformation. The present findings therefore deliver significant evidence that the transformation has been initiated by deuterium. Comparing high magnification EBSD images from within and from outside the sputter crater underpin this.



### Further considerations

A comparison of the fraction of transformed austenite between the two investigated materials and the different charging times reveals differences in their extend. However, by comparing the phase distribution maps in Chapter 6.4.2 and the Appendix A.3, some inconsistencies can be recognised. That is why Figure 6.28 exemplary plots three samples from AISI 316L. Even though these samples were prepared in the same manner and each charged for 72 h under the same conditions, differences in the surface condition are obvious. Identical charging parameter did not lead to the same amount of martensite and damages on the analysed surface. For such reason, a direct relation of the fraction of transformed austenite and the charging time does not seem to exist. This further means that the extend of transformed austenite can not be quantified reliably by selecting various charging times.

First of all, the size of the analysed ROIs have to be questioned. Phase distribution maps presenting an overview have a size of approximately  $600 \times 450 \mu\text{m}$ . Considering the dimensions of a bending specimen of  $60 \times 3.5 \text{ mm}$ , this reflects only about 0.13% of the total specimen surface. EBSD images are for this reason not fully representative.

Following reasons that prohibit a direct correlation between charging time, absorption of deuterium and  $\gamma \rightarrow \alpha'$ -formation were identified and will be discussed in the following. The respective impact is assessed and marked accordingly with  $\zeta$  for *less significant*,  $\zeta\zeta$  for *important* and  $\zeta\zeta\zeta$  for *critical*.

- $\zeta$  Sample preparation: Variations in the process of electrolytic polishing were inevitable. The temperature of the solution influences the removal of material from the surface. Because the laboratory in which this treatment was done is not temperature-controlled, the outcome of the polishing process is somehow influenced by the ambient temperature. In the progress of the present work, an optimal combination of mechanical and five-second electrolytic polishing was found. Due to turbulences of the liquid solution and selective erosion, the surface became wavy towards longer times. Although timing was careful, small variations may have occurred.
- $\zeta$  EBSD analyses are affected by many factors. The yield of backscattered electrons strongly depends on the angle in which the specimen is tilted towards the beam and the surface condition of the sample. The distance between electron source and sample (working distance) and especially between sample and detector is crucial too. Due to the polishing process, every sample differs slightly from the others. Those minor differences in the surface quality might cause small variations in the outcome of the EBSD analyses. The same applies for the detector-sample and the working distance. However, these factors would have influenced the results of the phase determination as a whole and not specifically the identification of, e.g., the BCC phase.
- $\zeta$  Current fluctuations in the electricity grid that were not fully compensated by the galvanostat might also affect the cathodic charging process. No information about the probability

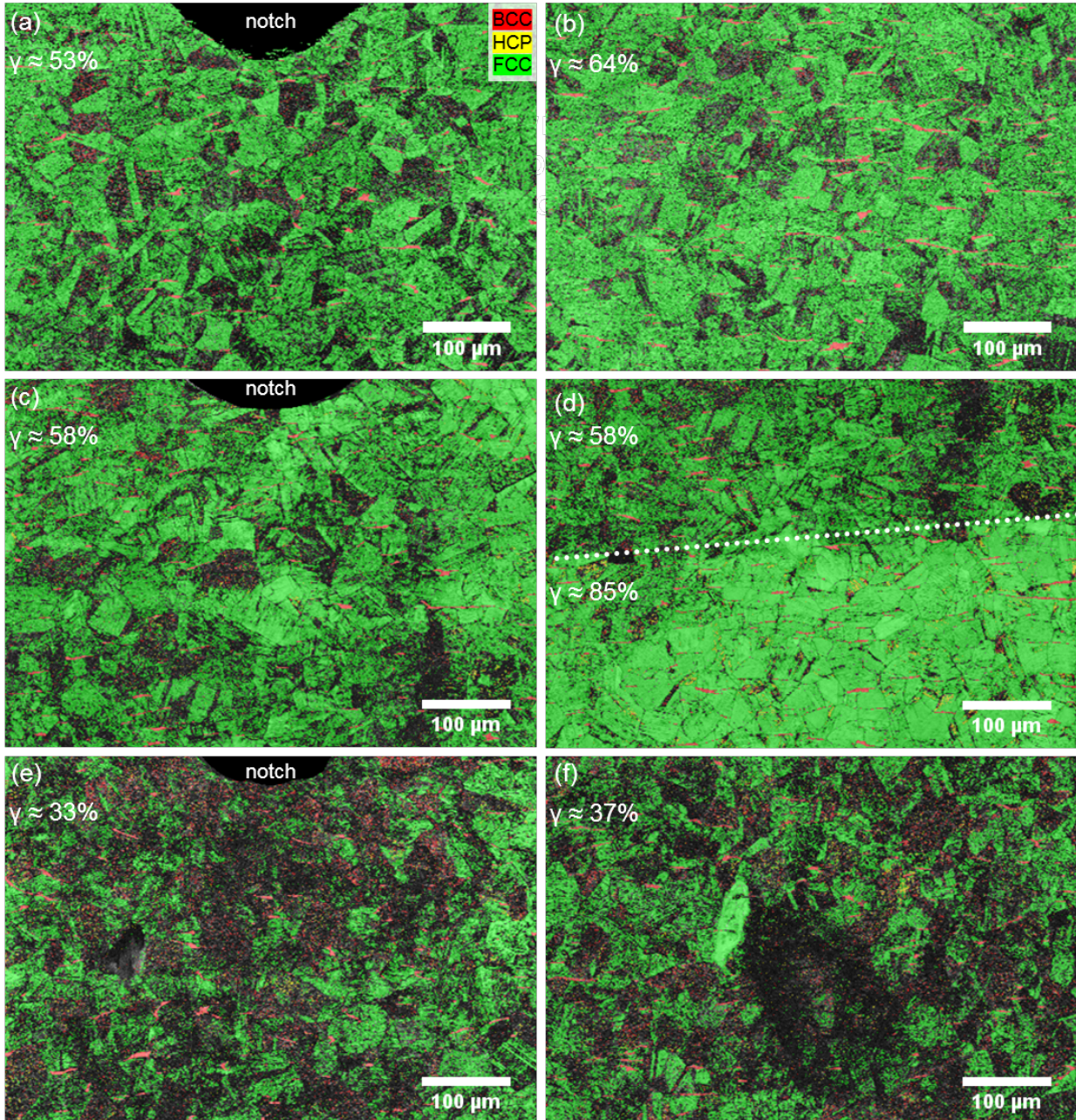


Figure 6.28: Phase distribution maps of three samples made from AISI 316L after electrochemical charging for 72h. Micrographs (a), (c) and (e) show ROIs directly underneath the notch that were sputtered, while (b), (d) and (f) show un-sputtered ROIs below. The white dotted line in (d) separates the image into a sputtered (above) and an un-sputtered region (below). The numbers give the fraction of austenite within the respective image.



and the extent of those current variations are known. However, it is assumed that the device was reliable and a negative influence negligible.

- ⚡ Another element to consider is the storage time of the specimen before electrochemical charging. Chromium was introduced in Chapter 3.1.1 as the element that provides austenitic stainless steel's corrosion resistance by forming a thin, dense layer of  $\text{Cr}_2\text{O}_3$  on the surface. This protective layer is an effective barrier against the penetration of hydrogen and deuterium [270, 271]. A sample that was cathodically charged shortly after polishing might have taken up more deuterium than a sample that was charged only after several weeks of storage. Nonetheless, this oxide layer can form relatively quickly after electrolytic polishing. For this reason it is assumed that the absorption of deuterium into the surface of a sample stored for one day was most likely not much higher than the absorption of deuterium of a sample stored e.g. for two weeks.
- ⚡ Electrochemical charging was done with great care. However, a variety of error sources exist in this process. The same current density  $J$  of  $5 \text{ mA/cm}^2$  was applied. It was calculated with the applied current  $I$  and the surface of the sample  $A$ . Already minor differences of the thickness of the specimens, caused by sample preparation, has a major effect on the current density. Due to its small size, an exact determination of the thickness of the specimen was not possible. The available calliper used for this was not precise enough to measure differences below  $100 \mu\text{m}$ . Therefore, a thickness of  $400 \mu\text{m}$  was assumed for all specimens. That is why the current density was perhaps above  $5 \text{ mA/cm}^2$  for some samples and below for others. However, the difference in the current density between a sample thickness of  $400 \mu\text{m}$  and e.g.  $300 \mu\text{m}$  amounts to  $J_{400-300}=0.139 \text{ mA/cm}^2$ . Even though this reflects a deviation of less than 3% and should not be a crucial factor, it must not be neglected.
- ⚡ A factor that strongly influences the electrochemical charging process is the concentration of the electrolyte. A higher concentration of  $\text{D}_2\text{SO}_4$  in the solution increases the availability of deuterium that may enter the metal. A concentration of  $0.05\text{M}$   $\text{D}_2\text{SO}_4$  was chosen in the present study. Several samples were charged with one batch of the electrolyte before it was renewed. Even though the charging cell was covered during the process, evaporation was inevitable. That led to the concentration of the solution over time and might have increased the uptake of deuterium of subsequent specimens.
- ⚡ All of the samples depicted in Figure 6.28 were analysed before and after charging and ToF-SIMS measurements. The time period between the end of electrochemical charging and the moment the sample reached its final temperature of  $\approx -75^\circ\text{C} \pm 5^\circ\text{C}$  in the SIMS is an important aspect. Deuterium effuses from the sample during this time. Even though desorption and diffusion were not fully stopped during the measurement, the low temperature hampered these processes significantly. Hydrogen-induced surface cracking and phase transformation take place not only during charging but perhaps mainly during desorption [76, 126, 272]. That is why the delay time is considered as an important factor.

Sample transport and mounting to the sample holder took only few minutes, whereas cooling down in the SIMS about 45 min. This time span is subjected to variations due to troubles with the pre-cooling in the airlock of the device. Some samples were sufficiently cooled for transfer into the main chamber after 35 min, others only after 50 min. A longer time at a "higher" temperature causes more deuterium to effuse and, thus, more damages.

### 6.4.3. Accumulation of hydrogen at grain boundaries

As it was discussed before, grain boundaries can both effectively trap hydrogen *and* enhance its diffusion (cf. Chapter 3.2.3). Trapping reduces the amount of diffusible hydrogen and by that increases the materials resistance against hydrogen-assisted cracking. However, as it was discussed in Chapter 3.3.1, this in turn can lead to a transition from transgranular to intergranular cracking along the grain boundaries. This is due to the loss of cohesive strength. Which type of grain boundaries are able to trap hydrogen and which offer a faster pathway is still under debate [241, 273–275]. Zamanzade *et al.* e.g. investigated the susceptibility of different grain boundaries towards hydrogen-induced blistering in nickel and found different diffusivities depending on the misorientation angle [275]. So-called *random* grain boundaries with a misorientation of 30-40° offer fast pathways for hydrogen diffusion. Low angle GBs and random grain boundaries with a misorientation below 25° are less sensitive to hydrogen segregation and blistering.

Molecular-dynamic simulations conducted by Teus and Gavriljuk on  $\alpha$ -iron partially confirmed this: Diffusivity for hydrogen varied depending on the misorientation angle  $\Theta$  of the respective grain boundary [276]. Yet, their calculations revealed distinctly higher activation energies for grain boundary diffusion in comparison to the bulk diffusion. This can be interpreted as trapping at the high-angle *special*  $\Sigma 5$ ,  $\Sigma 17$  and  $\Sigma 25$  grain boundaries. Preferred trapping at  $\Sigma 5$  grain boundaries was confirmed by Kulkova *et al.* with first-principle calculations [277].

Figure 6.29 displays the fused SEM micrograph of steel AISI 316L with SIMS data after deuterium charging for 72 h. It shows the signal of mass 43 that can be assigned to the fragments of  $CNOH^-$ . It reveals the accumulation of *hydrogen* at the grain boundaries of the material.

To make sure that the above shown is not only due to the presence of carbon, nitrogen and oxygen, the signal of the masses 26 ( $CN^-$ ), 27 ( $CNH^-$ ), and 42 ( $CNO^-$ ) were also considered. A higher signal intensity at the grain boundaries was only observed in mass 27, whereas it was not visible in masses 26 and 42. The dendrogram after hierarchical cluster analysis (HCA) underlines this finding. It is able to find and depict clusters within the dataset, i.e. the spectrum. These clusters form the branches of the dendrogram and represent signals that are connected [234]. It showed that the masses 26 and 42 are part of a different sub-cluster than 27 and 43. This is shown in Figure A.28 in the Appendix.

To further verify whether hydrogen was trapped at the grain boundaries as shown in Figure 6.29 and did not stem from moisture or rest gas in the chamber of the ToF-SIMS, the signal of the masses 27 and 43 were checked against the signals of 1 ( $H^-$ ), 16 ( $O^-$ ), 17 ( $OH^-$ ) and 33 ( $O_2H^-$ ). Unlike  $CNH^-$  and  $CNOH^-$ , these signals showed a homogeneous distribution and were grouped in a different cluster of the dendrogram. From these findings, it can be concluded that hydrogen

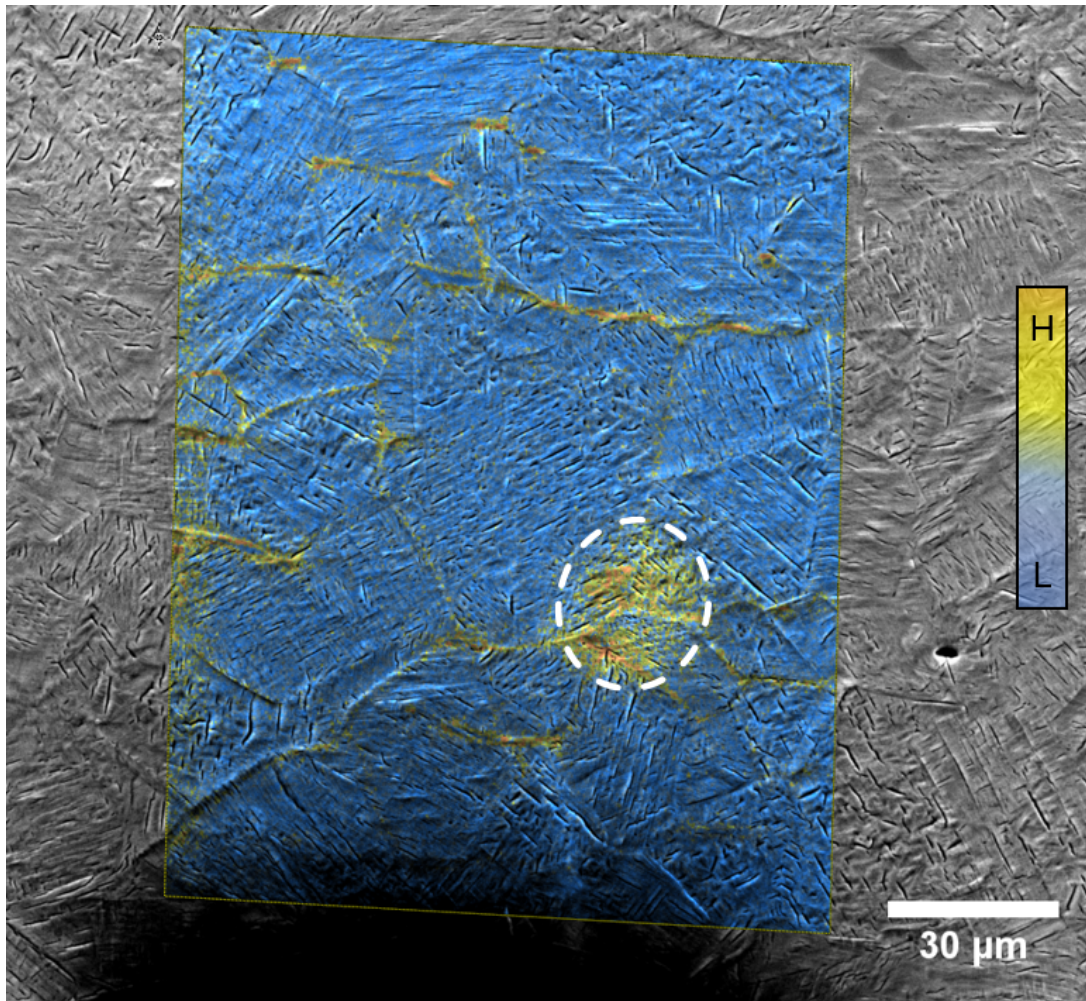


Figure 6.29: Data fusion of a SEM micrograph and the signal of  $\text{CNOH}^-$  in AISI 316L after 72 h of charging. The white circle indicates a region with the high intensity that is partially due to contaminations on the surface. The notch is visible in black at the bottom of the image.

was indeed trapped along the grain boundaries. This happened most likely during the steel production process because the sample was *not* charged with hydrogen but with deuterium.

Even though steel AISI 316L was solution annealed after rolling to homogeneously distribute alloying elements in the material, segregations of carbon, nitrogen and hydrogen at the grain boundaries can prevail. This is due to the amorphous structure of grain boundaries.

A H/D exchange, as it was described by Sobol *et al.*, has to be considered as an explanation, as well [234]. The authors charged samples from DSS electrochemically with deuterium. Subsequent ToF-SIMS measurements revealed both accumulations of deuterium *and* hydrogen around cracks. Since the used solution in their study did not contain hydrogen, its origin was explained to be sample cleaning and transfer to the SIMS chamber. This exchange of deuterium by hydrogen must not be understood as a chemical reaction, but rather as physisorption of hydrogen.

It is crucial to emphasise that an accumulation of hydrogen was *not* observed in alloy grade AISI 304L. This is as an indication of hydrogen being trapped at grain boundaries during manufacturing of steel 316L rather than a H/D exchange during sample handling. The ability of nitrogen and carbon to trap hydrogen and deuterium at the grain boundaries of a duplex steel DSS 2205 was observed by Sobol *et al.* by means of ToF-SIMS investigations [201]. Nitrogen and carbon probably segregated towards the grain boundaries during heat treatment and trapped hydrogen there. The SIMS instrument operated in the present study has an extreme high surface sensitivity with a detection limit in the lower ppm regime [189, 190]. Although it delivers only qualitative information, its ability to detect small traces of elements is unrivalled. This is why already very low amounts of hydrogen within the steel were sufficient to be visualised. Figure A.29 in the Appendix exemplary shows another specimen from the steel grade 316L where hydrogen accumulation was found.

Following the above-described argumentation of Teus and Gavriljuk and Kulkova *et al.*, the grain boundaries at which a higher signal intensity of hydrogen was detected are supposed to be *special* GBs with a certain misorientation angle. However, these angles were not determined in the present study.

#### 6.4.4. Accumulation of deuterium at interfaces and sputter-induced martensite

Interfaces between different phases like austenite and martensite can act as trapping sites for hydrogen and thus, deuterium (cf. Chapter 3.2.3). Figure 6.30 displays both the distribution of deuterium imaged by ToF-SIMS and the EBSD phase maps of the same ROI after electrochemical charging for 48 h. It is obvious that deuterium is distributed heterogeneously and that the overall signal intensity is rather low. This is owed to complication during the SIMS measurements. Problems with the scaffold in which the sample was mounted occurred after introduction into the main chamber. In order to solve these issues, the specimen had to be removed from the sample holder and was stored for  $\geq 1$  h in a deep freezer. In addition to that it could not be cooled during the transfer out from and back into the SIMS. As a result diffusible deuterium effused from the sample while deeply trapped deuterium prevailed. That is why the signal of deuterium in Figure 6.30(a) can be regarded as the signal of predominantly deeply trapped deuterium.

A white arrow in Figure 6.30(b) shows deuterium-induced slip bands that partially turned into stripes of  $\alpha'$ -martensite. These features are well visible as elevated parallel lines in (a). The superimposed SIMS data clearly show deuterium around the lines.

Pu and Ooi studied the dislocation-mediated transport of hydrogen in the austenitic stainless steel AISI 304 by means of hydrogen microprint technique and scanning electron microscopy [108]. The researchers electrochemically charged samples with hydrogen, conducted compression tests and applied the microprint technique afterwards (cf. Table 3.4). They found accumulations of hydrogen at newly formed slip bands at the surface. An explanation for this observation is the trapping and movement of hydrogen in form of Cottrell atmospheres around dislocations. Under compression, these dislocations migrate towards the surface and leave the sites for preferred silver deposition alongside the slip bands.

Considering their findings, it can be concluded from the present observations that deuterium entered the grain and induced mechanical compressive stress high enough to induce shear of atomic planes and to some extent trigger phase transformation. The newly formed  $\gamma$ - $\alpha'$ -interfaces trapped deuterium so that it did not effuse during storage of the sample in the deep freezer. Connected to that was the formation of dislocations as additional traps for deuterium (cf. Table 3.3). As additional mechanical strain acted the  $\text{Cs}^+$ -beam. As it was discussed before, it did not induce phase transformation. However, it deformed the topmost layers of the material.

It was discussed previously that deuterium can not only be trapped at interfaces, but also directly *within* the martensite phase. This subject was raised already in Chapter 6.3.2 and shall be discussed further here. Figure 6.31(a) shows the phase maps and (b) the distribution of deuterium in the same ROI of a sample made from the steel AISI 304L after charging for 48 h. Some of the austenite grains transformed into martensite during the SIMS measurement due to sputtering. This is apparent from the phase distribution map in Figure 6.31(a) and was shown already in Figure 6.3 (cf. Chapter 6.1.2). Inverse pole figure represent the orientation of the grains in  $z$ -direction, i.e. normal to the sample surface. The comparison of both the IPFs in Figure 6.3 (b) and (d) clearly reveal changes in the orientation of grains due to martensite formation. The orientation of the grains was heterogeneous without any preferred direction before charging and SIMS investigation. In the course of caesium bombardment atoms changed their position and martensite formed. This of course led to changing orientation relations within the distorted matrix (cf. Figure 3.11), reflected in a  $[111]$  direction solely in the sputtered region.

The fusion of SIMS and SEM data in Figure 6.31(b) shows a heterogeneous distribution of deuterium and its covariants, condensed in PC2, in the matrix. Areas with a relatively high, moderately high and a relatively low intensity can be distinguished. Because of the higher solubility in austenite in comparison to martensite, it was expected that the untransformed austenite grains are enriched with deuterium. However, the related phase map in Figure 6.31(a) makes clear that the opposite is the case.

Koyama *et al.* electrochemically charged several austenitic steel grades and conducted cryogenic thermal desorption spectroscopy [75, 89]. Their reversal approach of not heating but cooling specimens enabled the researchers to study the release of hydrogen during martensite formation. The martensitic fraction within the samples increased the desorption capability of the investigated



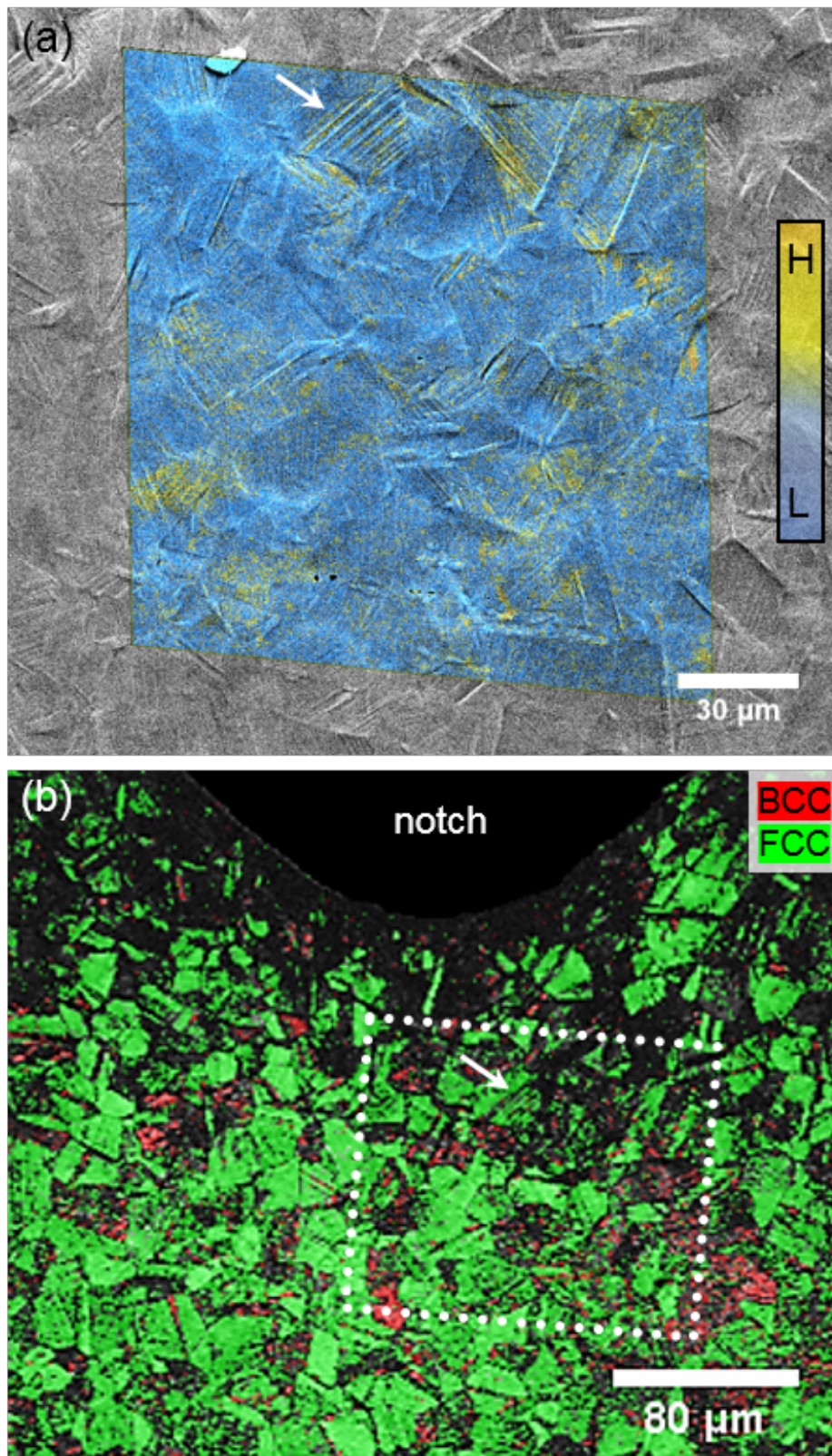


Figure 6.30: Fusion of a SEM image and ToF-SIMS data (a) and phase and pattern quality maps (b) of AISI 304L after electrochemical charging for 48 h. The colour scale in (a) refers to the signal intensity of the  $D^-$  and  $OD^-$  fragments after PCA. A white square in (b) indicates the location of ROI analysed by SIMS; the arrow highlights slip bands and newly formed martensite.

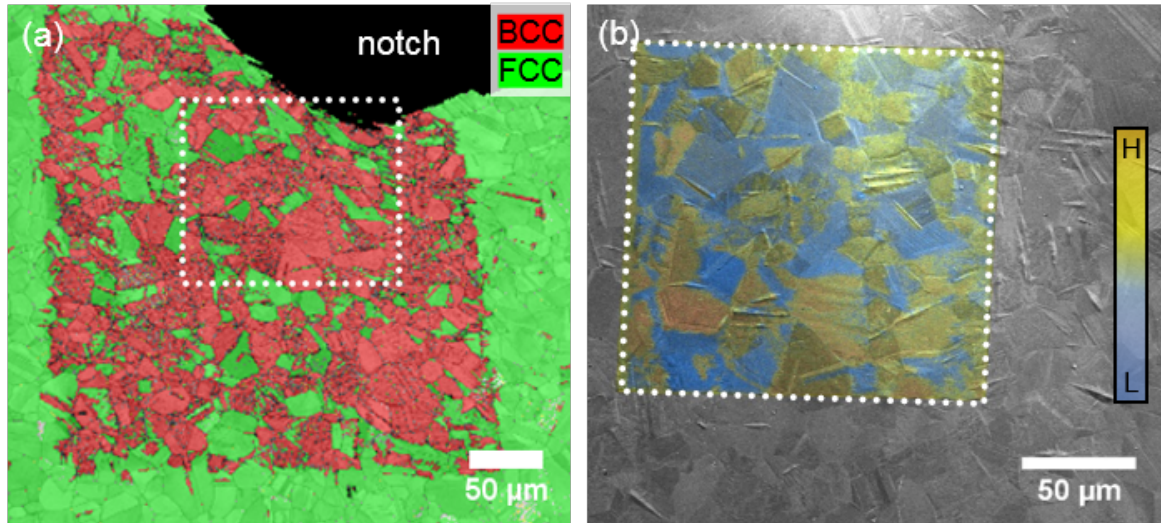


Figure 6.31: Phase and pattern quality maps of the sputtered area below the notch of AISI 304L after electrochemical charging for 48 h (a) and fusion of a SEM image and ToF-SIMS data of the same ROI (b). It was sputtered for 2.5 min with a 3 keV  $Cs^+$ -beam. A white square in (a) and (b) indicates the location of ROI analysed by SIMS. The colour scale in (b) refers to the signal intensity of the  $D^-$  and  $OD^-$  fragments after PCA.

steels by considerably increasing the mobility of hydrogen. This can be called *de-trapping*. Concluding from this, de-trapping of hydrogen in the course of  $\gamma \rightarrow \alpha'$ -transformation was the expected result. However, this was not observed in the present findings.

Martensite contains a high density of defects such as dislocations [108]. It is composed of blocks divided into sub-blocks that consist of laths. According to Morsdorf *et al.*, austenite transforms into lathy martensite in between parallel interfaces with the  $\{110\}$  habit plane upon quenching [278]. Austenite can prevail in between these laths. Both the residual austenite and the  $\gamma$ - $\alpha'$ -interfaces can trap hydrogen effectively [107, 252, 279, 280]. Bérès *et al.* showed experimentally that these martensite laths accumulate hydrogen and thus act as crack nucleation sites, especially when intersecting prior austenite grain boundaries [281].

Tian *et al.* studied Fe-Cr-Ni alloys with varying  $\gamma$ -stability both after quenching to different temperatures and 10% cold rolling to answer the question whether built-up and properties of *athermal* martensite (AM), i.e. martensite that forms upon quenching, resemble those of *deformation-induced* martensite (DIM) [282, 283]. Regardless of its origin,  $\alpha'$ -martensite formed in shear bands with a high density of stacking faults or  $\epsilon$ -martensite. So-called *blocky* structures, on the other hand, were only observed upon quenching and in the investigated steels with the lowest austenite stability. The authors found also that the width of  $\epsilon$ -bands after cold deformation was smaller in comparison to the quenched counterparts and explained this with the limited thickness of shear bands as preferred nucleation sites for  $\epsilon$ .

The conclusion that DIM possesses a similar structure like athermal martensite is of high importance for the present work. It allows to conclude from this insight to a similar trapping and diffusion behaviour of hydrogen in the BCT phase formed during charging or the experiment.

Following this, Figure 6.31 implies that deuterium entered certain austenite grains during charging. The subsequent sputtering in the ToF-SIMS caused *only* those austenitic grains to transform into martensite that were already pre-stressed by the dissolved deuterium. Thus, phase transformation took place due to the combination of both internal (deuterium) *and* external (sputtering) load. The low temperature of about  $-70^{\circ}\text{C}$  hampered deuterium effusion. Additionally, deuterium was probably *re-trapped* at transformation-induced defects and the  $\gamma$ - $\alpha'$ -interfaces. Images of higher lateral resolution EBSD could furthermore deliver information of the exact structure of martensite and possible retained austenite within it. Higher resolution SIMS maps could then provide a more accurate distribution map of deuterium.

Deuterium penetrated the surface of the material during charging randomly. The question of why it entered some grains and some not can not be answered. It is well-known that pre-strained material is able to take up higher amounts of hydrogen/deuterium in a shorter time than pristine material. This effect is mainly due to the higher amount of dislocations acting as diffusion paths for hydrogen (cf. Chapter 3.2.2.2), but also due to a certain amount of stored deformation energy from rolling. However, the sample was mechanically ground and polished and in addition electrochemically polished before analyses to remove highly distorted and defect-rich material from the surface. Accordingly, it is assumed that the enhancement of deuterium diffusion by dislocations is negligible here.

Hua *et al.* studied the influence of crystallographic orientation on hydrogen diffusion in grade AISI 304. They found that hydrogen effusion from charged samples was faster from (001) and (101) grains than from (111) grains [284]. The pristine material depicted in Figure 6.31 (a) and (b) does not show a preferred crystallographic orientation. Only after sputtering, the predominant orientation of the newly formed martensite was [111]. Following the argumentation of Hua *et al.*, the effusion of deuterium during sample transfer from charging facility to the chamber and during analysis was slower in these grains because of the changed orientation due to martensite formation. Thus, re-trapping at newly-formed defects, such as dislocations, and orientation-dependent slowed-down diffusion are supposedly the reasons for the detection of deuterium almost solely in the martensitic phase.

To sum up, it can be said that the present findings together with the above-cited literature indicate the following:

- Deformation-induced and quenching-induced martensite possess a similar structure with a high amount of lattice defects.
- Deuterium can be deeply trapped by these defects and the interfaces of newly-formed martensite and residual austenite.
- Martensite can form due to *internal* mechanical load (deuterium-induced) and *external* mechanical load (deformation-induced). Both have a similar structure and trapping properties for deuterium and, thus, hydrogen.



- Even though the critical concentration of deuterium for  $\gamma \rightarrow \varepsilon \rightarrow \alpha'$ -transformation might not be reached during cathodic charging,  $\text{Cs}^+$ -sputtering can provide the missing energy to initiate this process.

#### 6.4.5. Distribution of deuterium in the material

Due to the insufficient sample preparation of the *ex-situ* samples in contrast to the *in-situ* specimens, the distribution of deuterium in the material shall be analysed in the following chapter again. The negative effects of the sputter beam can not be excluded completely, but its impact was minimised by the selection of a shorter sputter cycle and a lower acceleration voltage and beam current. Figures 6.32 and 6.34 present the distribution of deuterium after electrochemical charging for 72 h in steel grade AISI 304L and 316L, respectively. Phase maps are included in the depictions to enable the identification of deuterium-induced structural changes and possible trapping sites.

It was already discussed previously that grain boundaries and twins can act as potential trapping sites for hydrogen (cf. i.a. Figure 6.29). White arrows in Figure 6.32(a) now highlight locations of relatively high concentration of deuterium around these features. The fusion with the underlying SEM image shows cracks running along the slip bands and partially along the grain boundary. A higher intensity of the deuterium signal around those cracks is indicated by brighter colour. It allows the conclusion that accumulation of deuterium at these interfaces caused this fissures. Since deuterium was detected at these features, the above-mentioned formation of cracks during its effusion was probably of less importance here. The reason why the twins and twin boundaries do not appear to be damaged can be a lower mismatch as compared to the grain boundaries or highly distorted slip bands surrounded by "pristine" austenite. A higher mismatch would have caused higher mechanical load on these interfaces, leading to preferred cracking.

Selective deuterium-induced damages and phase transformation was already discussed in the previous chapter. Figure 6.32 highlights this feature in the phase maps and fused SEM/ToF-SIMS image. The dashed white line in the lower right corner margins a grain with an orientation of [101]-[111] normal to the surface. It is labelled with (i). Two bands/twins with a [001] orientation lie inside the grain. The respective IPFZ map can be found here in 6.33 and in the appendix as separated Figures A.19 and A.20.

The [101]-[111] parent grain transformed almost completely into martensite, whereas the [001]-units are less affected by deuterium. Although some damages are visible, the original FCC structure remained in these two bands (cf. Fig. 6.32(b)). By comparing SIMS and EBSD data, a higher intensity of the deuterium signal inside the newly formed  $\alpha'$ -martensite inside of grain (i) becomes apparent. It explains the less severe damage in the [001] twins, too. As compared to the rest of the grain, the concentration of deuterium is lower here. It is noteworthy that the part of the twin exhibiting more damages shows a higher intensity of deuterium, as well.

This observation supports the considerations made in Chapter 6.4.2 that electrochemical charging can trigger  $\gamma \rightarrow \varepsilon \rightarrow \alpha'$ -phase transformation preferably in [111] and [101] grains. This process started already after a relatively short duration as the phase maps and inverse pole figures

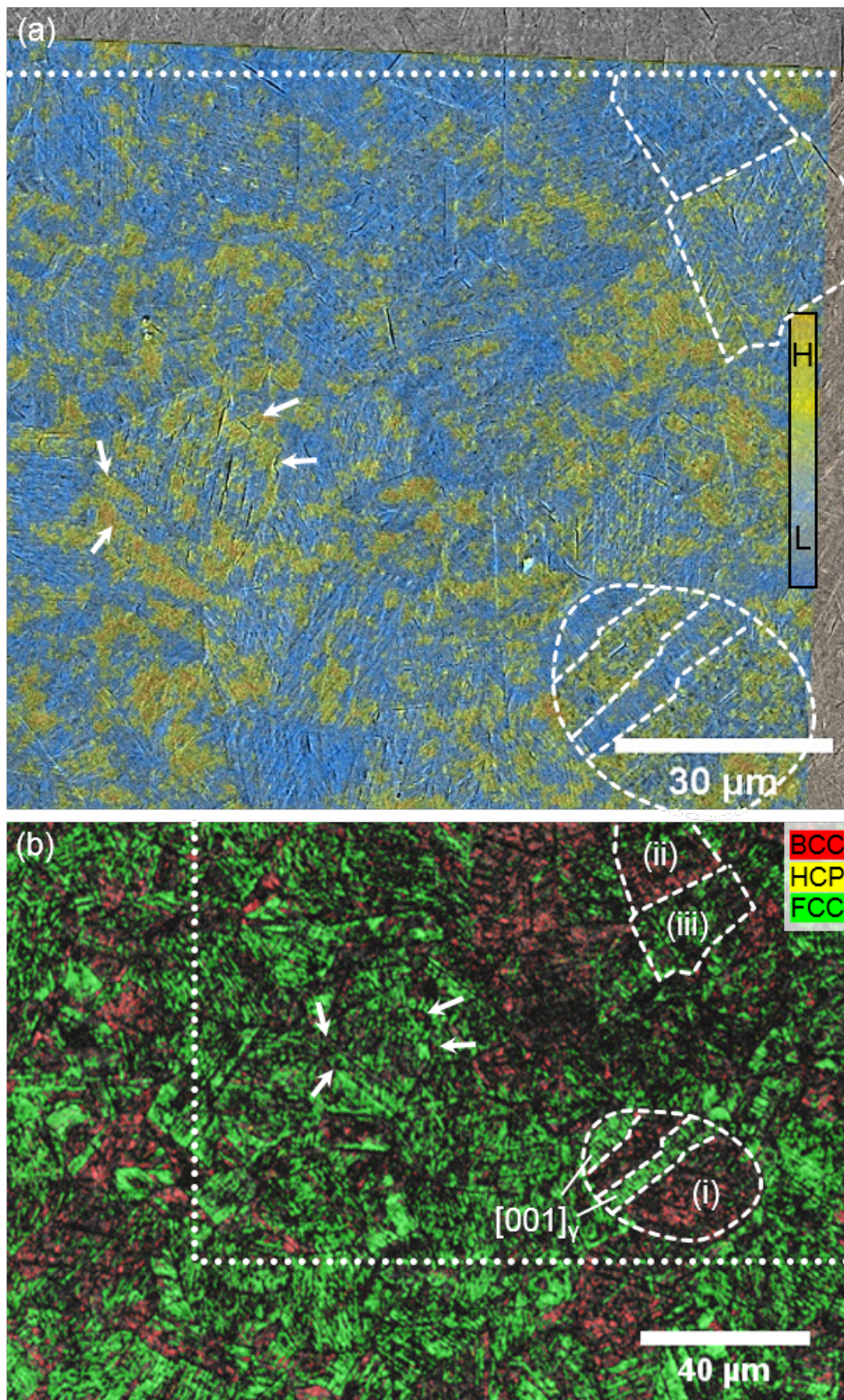


Figure 6.32: Data fusion of a SEM micrograph and ToF-SIMS data of a 304L steel sample charged for 72 h. The distribution of deuterium is reflected by PC2. The dotted line in (a) and (b) indicates the edges of SIMS and EBSD image. Dashed lines highlight special features such as grain and twin/sub-grain boundaries inside it. White arrows highlight accumulation of deuterium at grain and twin boundaries.



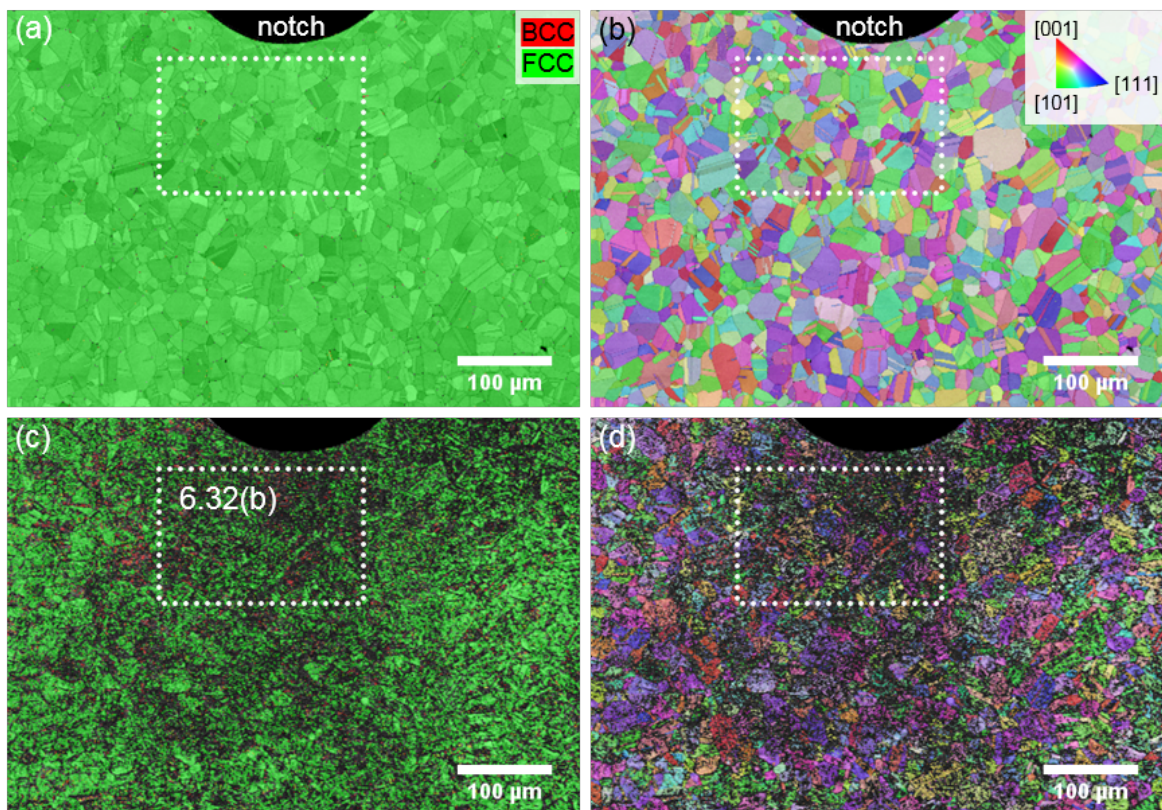


Figure 6.33: Phase distribution and corresponding inverse pole figure maps of AISI 304L before (a) and (b), respectively and after charging for 72h and ToF-SIMS investigation in (c) and (d), respectively. The dotted square indicate the location of higher magnified micrographs in Figure 6.32(b).

after charging for 24 h proof (cf. Fig. 6.12 and 6.13). The damaging effect of deuterium could only begin to unfold in [001] grains after cathodic charging for 72 h, though. It can therefore be assumed that charging for a longer time would have damaged the highlighted [001] twin in Figure 6.32(a) further. Phase maps and IPFZ maps of a sample also made from AISI 304L alloy and charged for 120 h, shown in Figure 6.21, underpin this.

In contrast to grain (i) are two grains in the upper right corner of Figure 6.32(a) and (b). Grain (ii) is almost completely transformed from FCC to BCT structure. The SEM micrograph reveals a jagged surface with high surface roughness, the fused SIMS data shows a low intensity of deuterium. Its neighbouring grain (iii) is damaged too but mainly kept its austenitic structure. Figure 6.32(a) shows that the concentration of deuterium is relatively higher here. Partially fractured slip lines are visible, as well. However, a correlation between the orientation of the grains, transformation behaviour and the distribution of deuterium is not apparent.

Figure 6.34(a) shows the fusion of SIMS data and a SEM image and (b) the respective EBSD phase maps of steel grade 316L. The specimen was electrochemically charged for 72 h, as well. Other than in the case of the aforementioned sample made from AISI 304L,  $\epsilon$ -martensite is visible in the phase distribution maps. It mostly lies as remains within the surrounding  $\alpha'$ -phase. White arrows mark some of these locations. Considering the identical sample treatment and charging conditions, this can be an implication for the higher stability of the austenite phase in AISI 316L. Locally increased deuterium concentrations were detected independent of the structure. Therefore both austenite and martensite are able to bind deuterium. It is solute (mainly in the octahedral interstitial sites) in the FCC lattice [18, 285] and trapped at interfaces, voids and dislocations in the newly formed DIM (cf. Chapter 6.4.4).

Park *et al.* argue that retained austenite in steel weldings acts as a reservoir for hydrogen [107]. According to them, solute hydrogen is released from the  $\gamma$ -grains during phase transformation. The now available hydrogen is supplied to the surrounding material. Olden *et al.* dispute this phenomenon and claim that it will be trapped at phase boundaries and lattice defects [86]. The findings documented in the literature are consistent with the results found and illustrated e.g. in Figures 6.32 and 6.34. It was not only proven that deuterium causes a phase transformation in ASS but also that deuterium might be trapped in such transformed grains.

This can be interesting and relevant for industrial applications. Even though it is known since the 1970s, the effect of hydrogen-induced phase transformation is still under debate. During this phase transformation, the properties of the alloy change dramatically. The FCC austenite possesses a high mechanical ductility and high solubility but low diffusivity for hydrogen, whereas the newly formed BCT martensite is more brittle and has a lower solubility and higher diffusivity for hydrogen as compared to its parent lattice [173, 211]. These altered diffusion properties are believed to facilitate hydrogen uptake that, in consequence, can induce more phase transformation. An unfavourable cycle may begin, accelerating the materials degradation. This idea can be at least partially confuted by the present findings. Martensite was shown as an effective trap for deuterium and, thus, hydrogen. It is therefore questionable if the diffusivity of deuterium in deformation-induced martensite is in the same order of magnitude as the velocity of diffusion in original BCC materials.



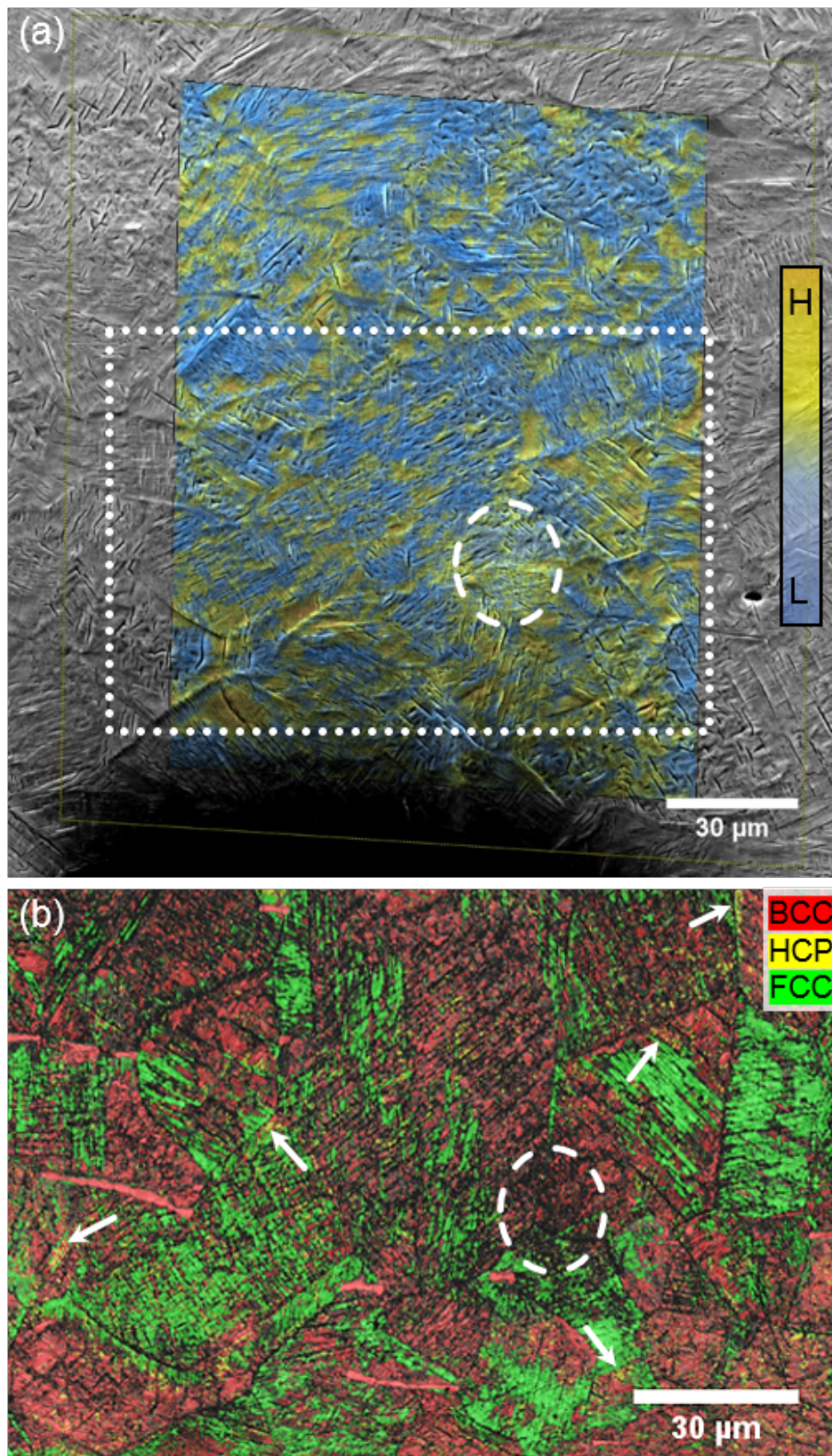


Figure 6.34: Data fusion of a SEM micrograph and ToF-SIMS data of a sample charged for 72h (a) and the phase distribution map in (b). The distribution of deuterium and its covariants is given as the PC3. The notch is visible as a black shadow at the bottom of (a). The white frame margins the location where the EBSD image stems from, white arrows indicate remains of  $\epsilon$ -martensite.

#### 6.4.6. Behaviour of deuterium during mechanical load

##### AISI 304L

The already partly shown results of the EBSD analyses before and after electrochemical charging for five days are shown in Figure 6.35 as a reminder.

Figure 6.35(a) shows the materials condition after sample preparation. After five days of electrochemical charging and ToF-SIMS analyses, the surface underwent changes. EBSD is able to illustrate the transformation of the original FCC phase into BCC martensite (cf. Figure 6.35(b)) by analysing the same ROI as before charging. Due to the impact of the  $\text{Cs}^+$ -beam, used for removing contaminants from the surface, the sputtered region is visible. It was damaged more severely and contained a larger fraction of martensite as compared to the un-sputtered surface. This is due to the additional energy input in terms of mechanical deformation. Areas where no diffraction bands could be indexed, i.e. measurement points with zero solution for the *Kikuchi patterns*, are indicated in black colour in the phase maps. The high number of these locally unsolved patterns is due to the higher thickness and density of the damaged surface.

The results show that the influence of the sputter beam must not be neglected in the discussion of the ToF-SIMS results. For other methods, such as dynamic SIMS, where the energy and flux of the primary ion beam are much higher, this is particularly important.

Figure 6.35(c) shows the pattern quality and phase maps that are marked by the white dashed square in Figure 6.35(b). It has a higher magnification and was taken with a smaller step size of the rastering electron beam. This significantly improved the image quality and its information content. A reduced step size thus leads to slower but more precise measurements. This is why the non-indexed measurement points in (b) are reduced dramatically. Figure 6.35(c), thus, shows that the influence of the sputter beam is overestimated in the phase distribution map in (a). Furthermore, Figure 6.35(c) not only displays the BCT  $\alpha'$ -martensite coloured in red but also the yellow-hued  $\epsilon$ -martensite. As described in the literature, this hexagonal phase reflects the intermediate step in the transformation sequence of the FCC austenite into BCT martensite [32, 41, 44, 261].

Figure 6.36 presents the fusion of a SEM image and the SIMS data of the same region. Here, the distribution of deuterium is represented by bright colour, whereas blue indicates regions with a relatively low intensity of the D signal.

Severe cracking and roughening of the surface are visible in the SEM micrograph taken after electrochemical charging and ToF-SIMS experiments. This can be attributed to a number of effects: The formation of martensite, which is connected to a shape deformation [251]; the so-called hydrogen-enhanced decohesion of the lattice (HEDE) and alterations in the stress state of the surface after charging [259]. It is evident that the above-mentioned mechanisms are not only responsible for crack formation. Djukic et al. e.g. reviewed recently the interplay of HELP and the HEDE mechanism in steels [140]. For this reason, it is assumed that surface cracking has developed as a result of the interaction of the described processes. Beyond that, other phenomena, such as the absorption-induced dislocation emission (AIDE) and hydrogen-enhanced



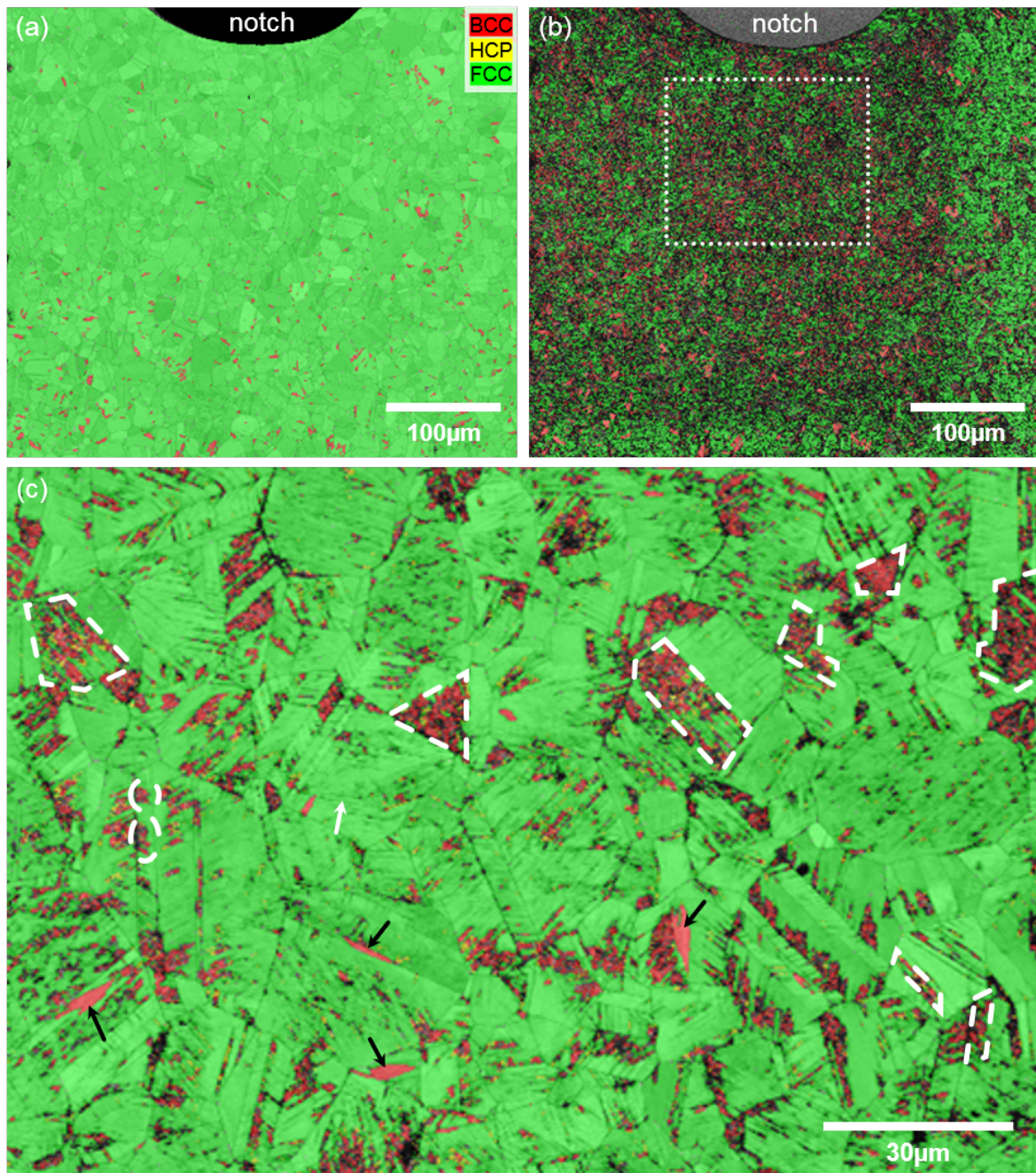


Figure 6.35: The overlay of pattern quality (PQ) and phase distribution map of the sample before charging is shown in (a). The same region after electrochemical charging for 120 h and ToF-SIMS experiments is depicted in (b). The dotted frame in (b) indicates the magnified area within the field of analysis in (c). Dashed white lines indicate some locations where martensite newly formed. Black arrows highlight some pre-existing  $\delta$ -ferrite islands whereas a white arrow marks slip bands.



strain-induced vacancy formation (HESIV), can take a part in the crack formation. Nevertheless, in the present study on AISI 304L steel, these two mechanisms should be of less importance [286]. This was already discussed in the previous chapters.

The distribution of deuterium in the matrix is heterogeneous. Areas with a higher intensity of deuterium-related signals (orange) can be found as well as locations with a relatively lower intensity (yellow) and regions where the signal was too weak to be detected (blue). Considering Figure 6.35(c) together with Figure 6.36(a), it becomes obvious that deuterium is dissolved in both the austenite and trapped by the newly formed martensite. Solute deuterium in the FCC phase after charging can be explained by its high solubility. The presence of deuterium in the BCC phase, however, stands against the common assumption of its low solubility for hydrogen and deuterium, respectively. Martensite contains a high number of defects. Especially dislocations that form during transformation are regarded as effective trapping sites for hydrogen, and in consequence, for deuterium [86]. Kim *et al.* showed furthermore that interfaces, grain boundaries and point defects within the newly formed martensite bind hydrogen [287]. The white arrow in Figure 6.35(c) and Figure 6.36 shows the accumulation of deuterium already at slip lines, i.e. the precursor of martensite. In addition to that, it is anticipated that deuterium may not only be trapped at these defects but also dissolved within the lattice. Due to the rapid  $\gamma \rightarrow \epsilon \rightarrow \alpha'$ -transformation, diffusion of deuterium was restricted so that the newly formed BCT matrix was supersaturated with deuterium.

It was already discussed in a published work [288] and in previous chapters (cf. Chapters 6.3.2, 6.4.3, 6.4.4) that deuterium can be incorporated into the newly formed BCT and HCP lattices: Deuterium entered the matrix, induced sufficiently high mechanical load to trigger  $\gamma \rightarrow \epsilon \rightarrow \alpha'$ -transformation and remained trapped at newly-formed defects and interfaces and supersaturated inside the lattice.

The present observations of deuterium being trapped by martensite support recent findings of Pu *et al.* [289]. The authors investigated the changes in hydrogen desorption resulting from martensitic transformation. In their work, bainitic steels with retained austenite were electrochemically charged, compressed and subsequently analysed by thermal desorption analysis (TDA). A decreased hydrogen effusion from the compressed samples in comparison to mechanically unloaded reference samples was measured. Supplementary X-ray diffraction measurements (XRD) suggested an increase in dislocation density from  $5 \cdot 10^{14}$  to  $4 \cdot 10^{15}/\text{m}^2$ , acting as traps for hydrogen.

Results contrasting the present observations were obtained e.g. by Koyama *et al.* [75, 89, 290]. The authors cooled down hydrogen pre-charged samples from different austenitic steel grades to cryogenic temperatures and determined the evolution of hydrogen. An increased hydrogen release rate during the formation of athermal  $\epsilon$ -martensite was observed. The explanation for this behaviour was the lower solubility and higher diffusivity of hydrogen in martensite in comparison to the parent austenite.

From these findings and the present results, the question arises of how similar solubility and diffusivity for hydrogen of  $\epsilon$ - and  $\alpha'$ -martensite are. It also has to be clarified in which way the trapping behaviour of strain- and stress-induced martensite differ from athermal martensite.

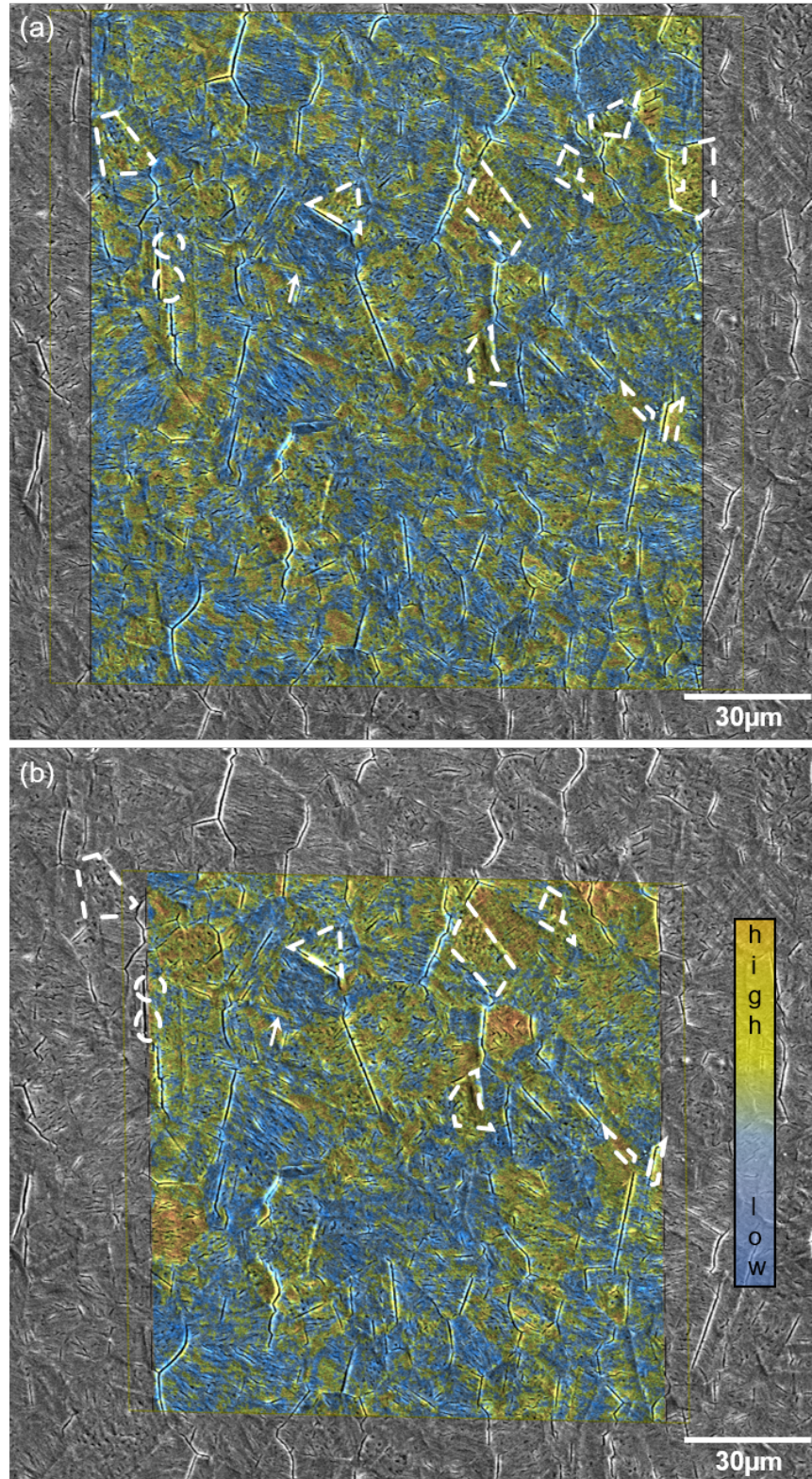


Figure 6.36: The overlay of an SEM micrograph and the SIMS data after PCA before (a) and during applying mechanical load (b). The distribution of deuterium and its covariant fragments is reflected as principal component two (PC2) in (a) and PC1 in (b). Brighter colours refer to a higher intensity of the signal. For a better orientation, the same regions as indicated in Figure 6.35(c) are marked here by dashed white lines too. The notch of the sample is located appr. 85 μm above the SIMS images.

A thorough and systematic comparison of athermal martensite transformation (AMT) and deformation-induced martensite transformation (DIMT) was done by Tian *et al.* [282]. For this purpose, the authors investigated several austenitic steel grades with nickel concentrations varying from 10.5 to 14 wt.-%. The formation and structure of AMT and DIMT in steels with a low stability of the austenite phase, i.e. low nickel concentration, was indicated by SEM and EBSD observations. From these results it can be anticipated that the currently investigated grade AISI 304L, possessing a relatively low stability of the  $\gamma$ -phase, behaves in the same way.

In order to fully exploit the information content of the ToF-SIMS results, principal component analysis (PCA) was applied [228]. This allowed to incorporate not only the deuterium signal but other deuterium-related fragments such as  $\text{OD}^-$ . The obtained principal components (PC) contain several peaks of different masses that were detected during SIMS analysis. The influence of each peak within the principal component is weighed which shows the contribution of an element to the PC. Deuterium together with several deuterium-related fragments is reflected by PC2 in the measurement *without* external mechanical load, shown in Figure 6.36(a). In contrast to that, PCA on the data gathered *during* applying mechanical loading resulted in the deuterium signals condensed in PC1. The first two to three PCs are typically containing the main variance and are therefore used for data interpretation [291]. The variance of higher PCs is usually very small or even zero. Consequently PC1 explains a higher amount of the total variance than PC2. The deuterium-related peaks had a higher variance after applying the mechanical load. This gives an indication of the stronger signal intensity as a result of the strain.

During mechanical loading of the specimen, the part of the sample opposite from the notch encountered compressive stress, while in the vicinity of the notch tensile stress prevailed. This was illustrated schematically in Figure 5.9 and by the FEM simulation in Figure 5.10. The highest tensile stress and strain occurred directly below the notch. The material was plastically strained in the notch root. The size of this plastic zone was approximately 65  $\mu\text{m}$ . The field of analyses was located about 85  $\mu\text{m}$  from the notch, where the material was deformed elastically. However, this was sufficient to induce a movement of deuterium towards the notch, viz. the area under tensile stress. This was energetically favourable since tensile stress expanded the lattice, offering more space for deuterium [292]. The comparison of Figure 6.36 (a) and (b) reveals that not only the overall intensity of the deuterium-related signals is higher in Figure 6.36 (b) as compared to (a). Additionally, the concentration of deuterium increases towards the upper part of the ROI, thus, towards the notch where the highest stress and strain are assumed to occur.

The sample was cooled down to a temperature of  $\approx -75 \pm 5^\circ\text{C}$  during the experiments. This was done to hamper diffusion of deuterium. Although diffusion does occur even at this low temperature, its strong influence as a possible artefact can be reduced here. To corroborate the viability of the PCA applied on the SIMS data, representative masses were selected and analysed. The  $\text{FeO}^-$  and  $\text{CrO}^-$  signals were selected, for iron and chromium are the main alloying elements of the investigated grade AISI 304L. Thus, the selected masses should not be subjected to alterations during mechanical loading. The same applies to the ubiquitously present hydrogen in the analysis chamber. That is why the signal of the fragment  $\text{OH}^-$  was chosen as well. Indeed, the comparison of each mass before and during mechanical loading did not show differences. For

this reason it is assumed that scaling of the data and principal component analyses did not bias the results. Therefore, it is believed that the re-distribution of deuterium occurred predominantly due to the strain-induced movement of deuterium as it was reported, e.g., by Lufrano *et al.* [292]. In their work the authors simulated hydrogen diffusion in four-point bend specimen and showed that the increased lattice spacing during bending decreased the chemical potential of hydrogen in solid solution. The resulting gradient of the chemical potential triggered movement of hydrogen towards the crack tip. Yokobori *et al.* confirmed this behaviour by numerical analyses [293, 294]. Their model showed that hydrogen diffuses along a stress gradient and accumulates in regions of maximum triaxial tensile stress.

Recently, McMahon *et al.* were able to confirm this by SIMS experiments [205]. They conducted fatigue tests at a stress ratio of 0.7 and a stress intensity range of  $\approx 11 \text{ MPa}\sqrt{m}$  on steel grade AISI 316. The tests took place under high-purity deuterium gas atmosphere and a pressure of 68.9 MPa. The distribution of deuterium in the vicinity of the fatigue crack was then imaged by subsequent NanoSIMS measurements. Dislocation tangles ahead and in the wake of the crack tip, i.e. within its plastic zone, as well as interfaces of MnS inclusions exhibited a higher concentration of deuterium than the surrounding material. From that, the authors concluded that dislocation-mediated transport of deuterium occurred and the role of inclusions as traps for hydrogen was evident.

This so-called *dislocation drag* of deuterium [96] is of less importance at the low strains shown in the present results. However, the mechanical bending-induced stress field was sufficient to prompt deuterium movement, resulting in an increased signal intensity. Therefore, it can be taken as an indication and proof of the *Gorsky effect*. An additional driving force could furthermore have been the tensile stresses that resulted from contraction of the lattice during deuterium effusion.

### AISI 316L

Similar observations as presented above were made on a sample made from the second investigated alloy AISI 316L. Figure 6.37(a) shows the fusion of the ToF-SIMS data and a SEM image of an *un-strained* specimen after 120 h of electrochemical charging, whereas Figure 6.37(b) shows the data of the same ROI that was acquired *during* mechanical load. As it was mentioned above, the application of the bending stress resulted in a displacement of the sample. That "revealed" a fresh and un-sputtered area of the surface that was cropped. Furthermore, few localised but strong outliers existed within the dataset. These stem from contaminations. Both flaws were masked by a *pixel mask* because otherwise they would have affected the interpretation of the data negatively. The pixel masks are indicated by dashed red lines in Figure 6.37. Dashed black lines in Figure 6.37(b) highlight some grains that exhibit a higher intensity of the deuterium *during* mechanical bending as compared to the initial state.

The white dotted lines frame the area of the images that represent the very same location in the phase distribution and inverse pole figure maps in the following illustration, Figure 6.38. Arrows mark newly formed martensite grains with a relatively high intensity of the deuterium



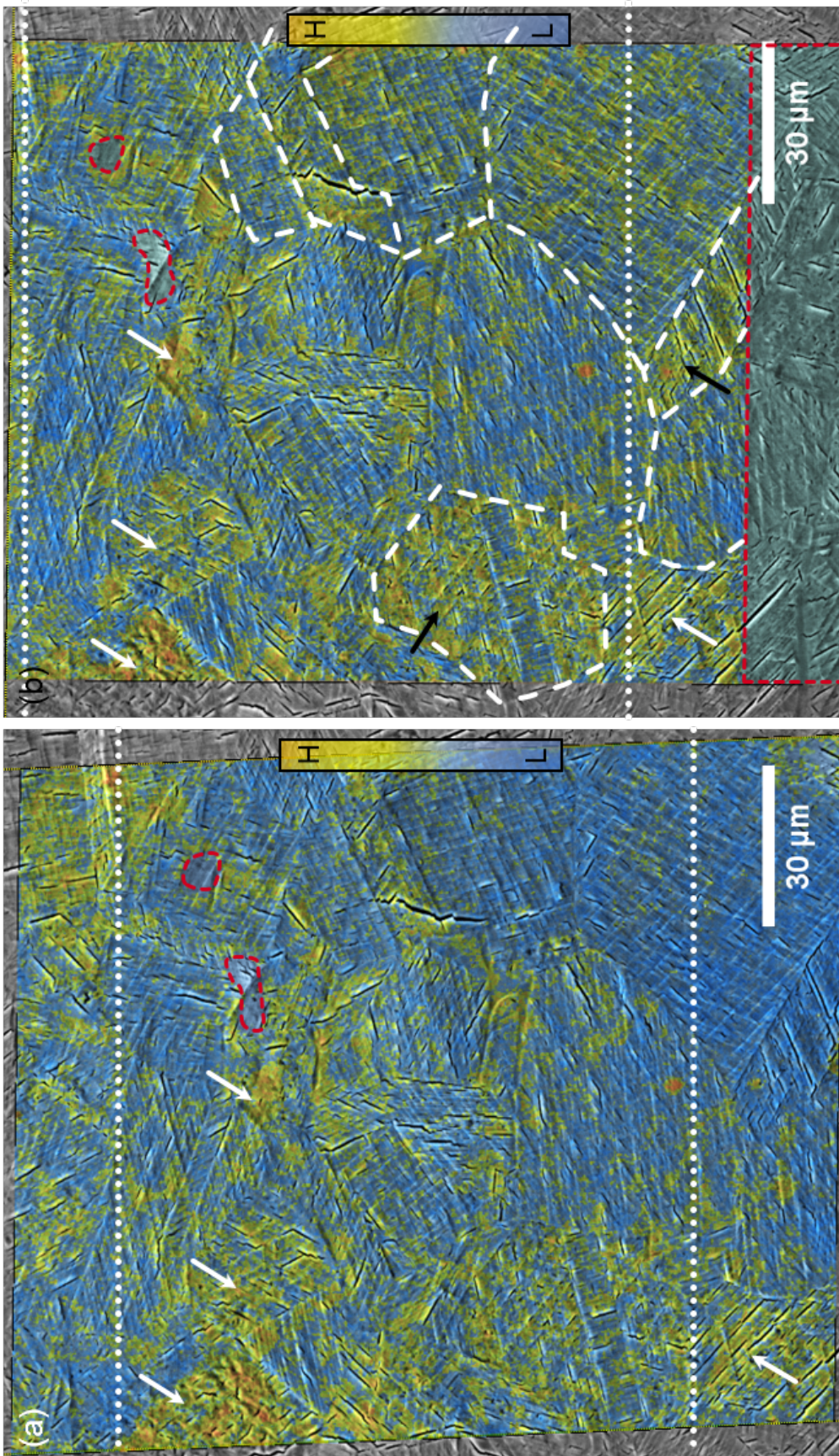


Figure 6.37: Data fusion of a SEM micrograph and the distribution of deuterium in AISI 316L, reflected by PC3, after 120 hours of charging without (a) and during mechanical load applied (b). The dotted white lines indicate the location where the EBSD micrograph was taken. The dashed red line shows the location of a so-called pixel mask, whereas dashed white lines highlight grains with higher D-intensity during load. White arrows exemplarily indicate newly formed martensite. Black arrows indicate newly formed martensite with a higher D-intensity during load. The notch is located approximately  $65\ \mu\text{m}$  above the SIMS image.



signal. The differences in colouring will be explained below. Some of these locations lie outside the ROI depicted here. However, they can be retrieved in the Appendix. EBSD micrographs in Figure A.23 and Figure A.24 give an overview of the specimen's surface before and after electrochemical charging and SIMS measurements. Additional higher-magnified images are presented in Figure A.25.  $\gamma \rightarrow \varepsilon \rightarrow \alpha'$ -phase transformation took place almost exclusively in grains with [111]-orientation or close to it. The phase distribution maps furthermore show that the formation of martensite was mainly due to the impact of deuterium. Because no sputter crater is visible, it leads to the assumption that the effect of the  $\text{Cs}^+$  beam was rather small.

The distribution of the signal intensity of deuterium and its related fragments in Figure 6.37 are reflected by PC3. As it was discussed with previous SIMS images, deuterium is spread in the surface heterogeneously. It is noteworthy that areas with the strongest signal refer to newly-formed martensite. Comparing Figure 6.37(a) and (b) delivers information about the effect of mechanical bending. The overall intensity increased after applying the external load. This becomes obvious especially in grains encircled by dashed black lines and can be interpreted as a higher concentration of deuterium within these grains. Consulting the corresponding phase distribution maps reveals that mainly *un*-transformed FCC grains enhanced in intensity. Like it was discussed in the case of steel AISI 304L, the mechanical load applied on the sample expanded lattice. This caused deuterium to move towards these energetically more favourable regions, offering more space in the interstitial sites.

Two former austenite grains that partially transformed into  $\varepsilon$ - and  $\alpha'$ -martensite are highlighted by black arrows and dashed black lines. Both locations show an increment of the intensity of the deuterium fragments (*viz.* PC3). In contrast to that are other martensitic domains that do not exhibit this increase. White arrows indicate those sites. The reason for this divergence may be due to a different "bonding" of deuterium within the HCP/BCC phase. Martensite grains that increased their intensity might be supersaturated with deuterium, allowing its stress-induced movement (black arrows). Martensite that deeply trapped deuterium (white arrows) did not enable this motion because of the strong binding energies between deuterium and e.g. dislocations (*cf.* Table 3.3). This might be the reason why notable changes before and during external mechanical load in these areas are not visible.

The following sketch illustrates the stress state in front of a notch/crack tip and the resulting mechanism responsible for hydrogen or deuterium motion, respectively. It was shown in Chapter 5.5 that a plastic zone evolves around the notch of the specimen when subjected to external mechanical load, induced by the 4PB sample holder. The magnitude of the plastic zone is in the order of  $65 \mu\text{m}$ . The highest load occurs at the elastic-plastic interface. In the regime of plastic deformation, movement of deuterium is mainly dislocation-mediated, whereas the Gorsky effect governs in the elastic regime.

One aim of the present work is to validate whether or not the four-point-bending sample holder, developed by Sobol [6], is a suitable means to stimulate hydrogen/deuterium motion by applying an external mechanical load. A mechanical bending stress simulates in-service condition of the investigated materials. Summarising, it can be said that the recent findings underpin previous observations and endorse the theory of stress-enhanced mobility of hydrogen according to the

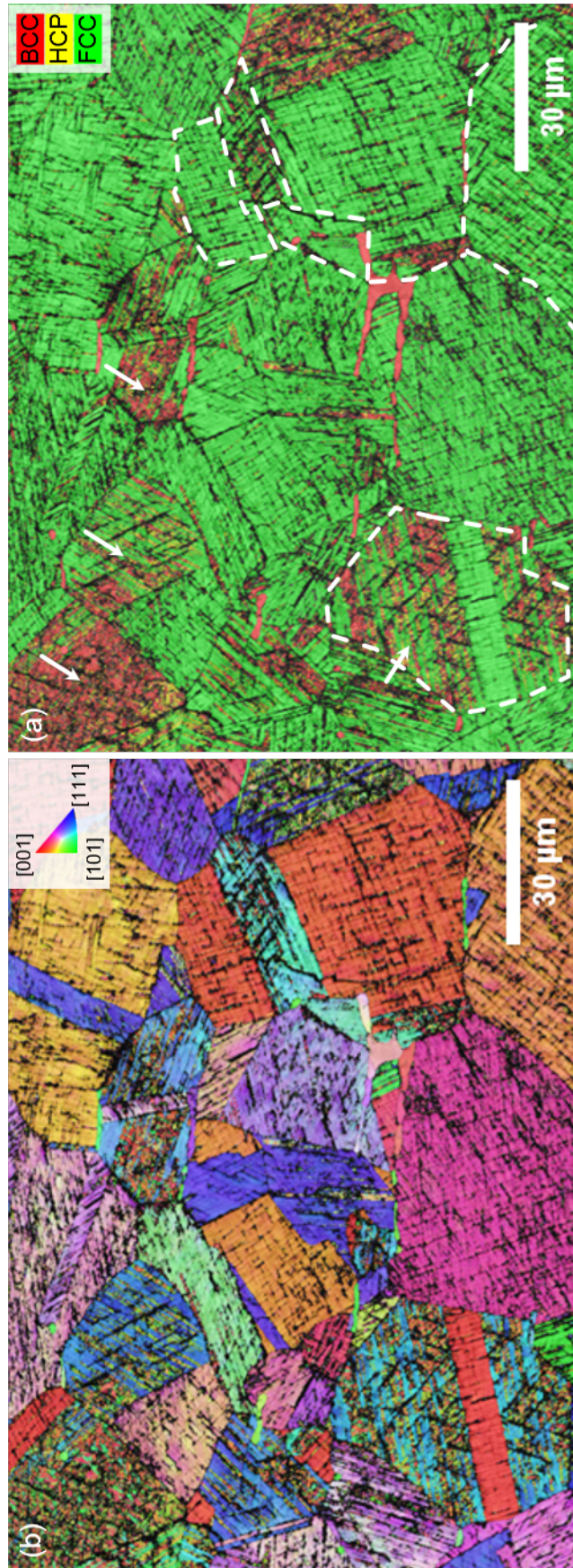


Figure 6.38: Phase distribution map (a) and inverse pole figure in  $z$ -direction (IPFZ) of a specimen made from AISI 316L grade after electrochemical charging for 120 h. Shown here is the same ROI as indicated by dotted white lines in Figure 6.37. White arrows mark newly formed deuterium-induced martensite grains with a relatively high intensity of the deuterium signal. For a better orientation, dashed white lines highlight the same grains as in Figure 6.37.

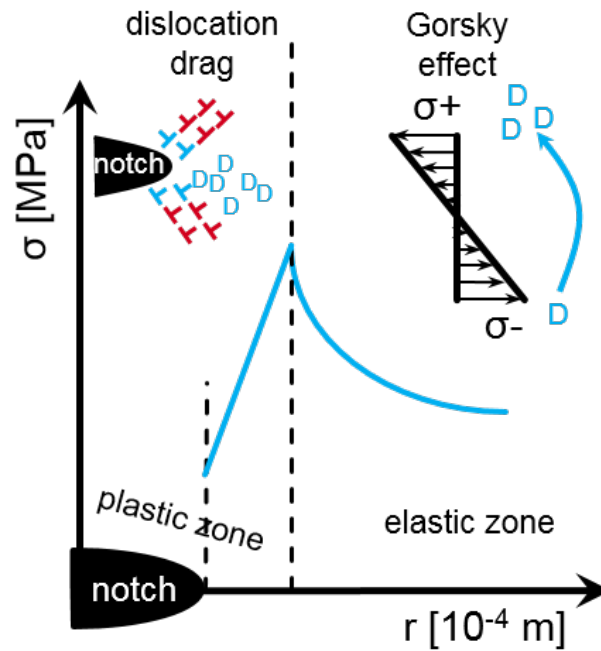


Figure 6.39: Schematic depiction of the stress distribution in front of a notch or a crack tip; the axis labels are adapted from Yokobori et al. [293]. The graph shows that the highest (tensile) stress builds up at the elastic-plastic interface. The main mechanisms for supporting hydrogen/deuterium movement are given for each regime. Blue dislocations represent deuterium-decorated dislocations.

Gorsky effect. However, the in-situ ToF-SIMS investigations on the duplex stainless steel 2205, conducted by Sobol in [6], might be revisited under some considerations. It is for instance not ascertained that the austenite phase in DSS behaves identical to the austenite in ASS.

As it was described above, in-situ experiments were carried out at temperatures of  $\approx -75 \pm 5^\circ\text{C}$  with a continuous connection of the sample holder to the cold finger of the SIMS (cf. Figure 5.8). Variations of the diffusivity of deuterium due to temperature changes can be thus neglected. In contrast to that, Sobol had to remove the sample holder during the application of mechanical load. Consequently, samples warmed up to  $\approx -45^\circ\text{C}$ . This of course is accompanied by an increased diffusivity of deuterium inside the metal lattice. An increased intensity of deuterium within the ferrite phase of the DSS 2205, as it was detected by ToF-SIMS, can still be taken as localised enrichment during mechanical loading. Hence, the unnecessary to increase the temperature during the experiments in the present study is a step forward that reduced another source of error.

## 7. Conclusions

The main goal of the present contribution was to investigate hydrogen-assisted damages, phase transformations and potential accumulation sites in the common and conventional austenitic stainless steels AISI 304L and 316L, respectively. The hydrogen-isotope deuterium was used as tracer and indicator for this purpose. Following conclusions can be drawn from the obtained results:

1. Electrochemical charging is a simple and easy way to introduce large amounts of hydrogen and deuterium into the lattice of the austenitic stainless steels AISI 304L and 316L. A concentration of the electrolyte of 0.05M  $D_2SO_4$  diluted in 99.9%  $D_2O$  combined with a current density of  $5\text{ mA/cm}^2$  is high enough to introduce deuterium already after 24 h. Longer charging times lead to higher concentrations. However, the usage of a so-called recombination poison such as  $NaAsO_2$  did not foster the uptake neither hydrogen nor deuterium. Its positive effect that is described frequently in the literature was not observed. On the contrary, adding  $NaAsO_2$  to the electrolyte caused precipitation of further substances on the sample surfaces and black shroud during charging, finally reducing the amount of deuterium absorbed by the specimen. Omitting of the frequently used recombination poison in this study turned out to be preferable. It should be revisited for future investigations, as it might hampers the ingress of deuterium and also due to its toxicity.
2. The longer the electrochemical charging time is, the more the surface of the specimen is damaged. This is expressed as an increased roughness, cracking and phase transformation. Due to the increased roughness of the surface, the grain structure of some specimens became unrecognisable in the SEM and phases undetectable in EBSD analysis. In combination with severe surface cracking, data fusion of SEM images and ToF-SIMS data was difficult and sometimes impossible.
3. The ratio *longer charging time = stronger damaged surface* is only true in tendency. Due to several additional influences, a direct correlation between charging time and martensite correlation can not be drawn reliably. Therefore, a comprehensive reflection on possible influencing factors of these results was delivered.
4. The present study evidently showed that deuterium-assisted damages in both alloy grades can be reflected in 1. crack formation and 2. transformation of the pristine  $\gamma$ -austenite into  $\alpha'$ -martensite with an intermediate step of the hexagonal  $\epsilon$ -phase.
  - 4.1 SEM investigations revealed that cracks almost exclusively formed along grain boundaries, i.e. intergranular, or other interfaces such as twins, slip bands or  $\gamma$ - $\alpha'$ -interfaces. This leads to the assumption that crack formation was due to high stress resulting from the mismatch of neighbouring (sub-)grains and newly formed BCT/HCP phases and the loss of cohesive strength of metallic bonds according to the HEDE mechanism.
  - 4.2 EBSD measurements revealed that martensite formed on preferred slip bands inside the austenite grains. It can be thus concluded that these martensitic fractions were

*strain-induced* [295–297]. Both types of martensite, HCP  $\epsilon$  and BCT  $\alpha'$ , developed in both investigated alloys. However, more  $\alpha'$  was produced in grade AISI 304L during similar charging times than in 316L grade. In the latter a higher fraction of  $\epsilon$ -martensite was observed. Considering the sequence of martensitic transformation, it became clear that this was due to the higher stability of the austenite in 316L. Here, the transformation process was, in tendency, not completed.

The formation of more fine deformation bands in steel grade AISI 316L in comparison to more block-like structures in AISI 304L was explained by extending the model of Tian *et al.* [264].

5. ToF-SIMS is a suitable instrument to map and depict the distribution of deuterium in metals. However, the inevitable step of sputtering the surface with caesium ions before analyses can also cause a  $\gamma \rightarrow \alpha'$ -phase transformation. Such effects might overlay and, thus, hide the effects of H/D proven by the results in this contribution. The optimal sputter energy and time has to be selected with great care. Especially in the case of 3 keV sputtering, phase transformations caused by deuterium can not be investigated, because the measurement technique itself altered the outcome of the experiment too much. Longer sputtering with a beam energy of 1 keV can still introduce martensite in grade AISI 304L, whereas 316L alloy is resilient against martensite formation for at least 5 min of sputtering.
6. Obtained ToF-SIMS and EBSD results and their comparison allowed to identify various accumulation sites for both hydrogen and deuterium. Hydrogen was detected along grain boundaries of steel grade AISI 316L but not in 304L. It is assumed that hydrogen accumulated along carbon and nitrogen segregations during the hot rolling process. In contrast to that, 304L grade was cold rolled, not giving hydrogen the possibility to diffuse and segregate at the grain boundaries.

The present work proved that martensite and its precursors, i.e. slip bands and stacking faults, are able to effectively trap deuterium. It was shown that both (1.) deuterium-induced *and* (2.) sputter-induced martensite can incorporate deuterium in their lattice. Here it is important to differentiate between the two sequences of martensite formation.

In the first case, it is assumed that deuterium induced high mechanical strains into the austenite. This might caused shear of atomic planes that consequently resulted in martensite. It has to be emphasised that such phase transformations are *not* caused by external deformations, but evidently by ingress of deuterium into the microstructure causing local deformations.

In the second case, deuterium was dissolved inside the austenite lattice without provoking  $\gamma \rightarrow \alpha'$ -transition, but certainly distorting the matrix. However, only the additional mechanical driving force of the  $\text{Cs}^+$ -beam finally caused martensite formation.

Regardless of the initiation mechanism, it shall be highlighted here that deuterium is not only causing a high number of newly formed dislocations but is also trapped by them. The



question whether deuterium was released temporarily from the new HCP/BCT phase and re-trapped or was not de-trapped at all, is beyond the scope of the present contribution.

In addition to that, deuterium might not only be deeply trapped at newly formed defects, such as dislocations and vacancies, but dissolved within the lattice. Due to the rapid  $\gamma \rightarrow \alpha'$ -transformation, diffusion of deuterium might be restricted so that the matrix was supersaturated with deuterium.

7. The finding that deuterium and, thus, hydrogen can be trapped inside martensite can be relevant for industrial applications. It is well known that FCC austenite possesses a high solubility but low diffusivity for hydrogen, whereas BCT martensite has a lower solubility and higher diffusivity for hydrogen as compared to its parent lattice. These altered diffusion properties are believed to facilitate hydrogen uptake that, in consequence, can induce more phase transformation. An unfavourable cycle may begin, accelerating the materials degradation. This idea can be at least partially confuted by the present findings. It is questionable if the diffusivity of hydrogen and deuterium in deformation-induced martensite is in the same order of magnitude as the velocity of diffusion in original BCC/BCT materials.
8. Martensitic transformation due to external mechanical load takes place on preferred slip systems where the highest *resulting* stress occurs. A slip systems is formed by a slip plane and a slip direction. In the cubic lattice, these systems are arranged in a way that only four distinct angles between the planes exist: 35.26°, 45°, 54.74° and 60°. SEM and EBSD micrographs of the sample's surfaces were done within the scope of the present study. By measuring the angles between the slip bands depicted by the micrographs, it was found that only these four angles exist. This delivers another indication that deuterium-induced phase transformation obeys the law of crystallography, Schmid's law and takes place in the same way as deformation-induced martensite formation.
9. The four-point-bending sample holder that was used in the current work to simulate load conditions in the sample and to stimulate deuterium motion was developed by Sobol [6]. It was shown that the sample holder successfully fulfils this task. This became obvious by comparing ToF-SIMS data collected *without* and *during* application of mechanical load on the specimen.

Because the ROIs that were analysed by ToF-SIMS *during* loading were located in the part of the respective sample that was deformed elastically, the results of the in-situ experiments suggest a stress-enhanced motion of deuterium. Because of the insufficient extent of the mechanical load applied by the piezo actuators, dislocation drag of deuterium can be mostly excluded. It is therefore assumed that the *Gorsky effect* was the main driving force and that deuterium moved towards energetically favourable regions, i.e. sites where the lattice was expanded due to resulting tensile stress.

## 8. Perspectives

1. O. Sobol laid the foundation of the present study by developing the four-point-bending sample holder that enables *in-situ* ToF-SIMS investigations during external mechanical load. One of the results obtained during the experiments was an inhomogeneous distribution of deuterium in the very vicinity of the notch of the specimen. A stepwise increase of the load accentuated the behaviour [6]. Formation and propagation of cracks due to mechanical bending was supposed to be the origin.

In order to validate both formation of cracks and re-distribution of deuterium close to the notch (i.e.  $\approx 5\ \mu\text{m}$ ) that are due to the mechanical load for the case of austenitic stainless steels AISI 304L and 316L, additional in-situ SIMS experiments have to follow the present study. Due to the very proximity of the notch, the *edge effect* has to be considered as a significant source of artefacts. Careful data treatment is inevitable.

2. Although the four-point-bending sample holder was proven to function successfully, its range of application can be augmented and enhanced for future experiments. The piezo actuators in their recent set-up are only able to apply a linear, monotonous load on the sample. Knowledge about the fatigue behaviour of steels under the influence of hydrogen is interesting for the research community and industry alike [121, 122, 151, 155, 298]. Applying a fatigue load on the 4PB specimen by simultaneous ToF-SIMS analyses of the deuterium behaviour would be a step beyond the state of the art and could validate experiments presented e.g. by McMahan *et al.* [205]. This can be achieved by writing a program that controls the piezo actuators to move with a certain frequency.
3. Electrochemical charging with an aqueous solution such as  $\text{D}_2\text{SO}_4$  is a fast, easy and relatively cheap method to introduce deuterium into the material. Data fusion for the enhanced analyses of the distribution of deuterium and charging-induced phase transformation is, however, not straight forward. This is mainly due to the high fugacity of the cathodic charging. Lowering the current density could provide a remedy but also result in corrosion of the specimen. Hajilou *et al.* used a glycerol-based electrolyte for their in-situ cantilever tests [299]. By that the authors not only maintained the integrity of the nano-cantilevers but also prevented local corrosion on the surface of the sample. This approach could be considered for further experiments.

A means to ensure a viable data fusion of SEM images and ToF-SIMS data even for highly damaged samples after longer electrochemical charging are nano-indentations. To this end, three to four indentation marks can be introduced before charging. It is crucial that these marks are situated within the posterior ROI of the SIMS experiments.

Another procedure to introduce deuterium into the specimen is autoclaving. That means the introduction of deuterium from the gas phase. This process does not only maintain the integrity of the surface, but is more close to real conditions e.g. in storage and transportation of hydrogen in the sectors of power-to-gas and fuel-cell technology. However, ensuring

---

the uptake of deuterium from the gaseous phase requires high pressure and temperature (As a rule of thumb a pressure of  $p=200$  bar and  $T=200^\circ\text{C}$ .). This goes along with high security standards of the charging facilities and high costs to purchase high-purity gaseous deuterium. Whether this approach is applicable on the 4PB samples investigated in the present study has to be carefully evaluated. However, it is not clear whether the knowledge gained on cathodically charged samples can be carried over to gaseously charged specimen. It is known that the impact of compressed gaseous hydrogen in terms of crack initiation, phase transformation and accumulation sites deviates from the one investigated in the present contribution.

4. A notch of approximately  $200\ \mu\text{m}$  diameter was introduced into the specimens. Its task was to act as stress concentration site during the application of external mechanical load. Up to-date a second property of this notch was neglected: Although the thickness of the samples was only about  $350\text{-}400\ \mu\text{m}$ , it is a three-dimensional object. The notch represents here an additional surface where deuterium can enter the metal during electrochemical charging. Analysing the inner part of the notch, i.e. from x- and y-direction, could yield further information. By cross-sectioning specimens after charging, ToF-SIMS and EBDS analyses of the surface and subsequent EBSD measurements can deliver two results. First, the depth into which the phase transformation reaches from the surface into the material (depending on the charging time) and second, the extend of phase transformation and other damages directly around the notch. First measurements were already conducted on ex-situ samples and published in [61]. However, further experiments are necessary, especially in respect to the adjusted surface treatment of the in-situ samples in comparison to the ex-situ samples.
5. The present study pointed out that deuterium can cause  $\gamma\rightarrow\varepsilon\rightarrow\alpha'$ -phase transformation in austenitic stainless steels AISI 304L and 316L and that this martensite is able to incorporate deuterium. The exact mechanism how this process happens and whether deuterium is (re-)trapped by newly formed dislocations or supersaturated within the HCP/BCC matrix can not be answered here. Higher magnified ToF-SIMS coupled with EBSD or electron channeling contrast imaging (ECCI) could provide further insight. ECCI is a powerful tool to observe the microstructure evolution induced by hydrogen with high lateral resolution [300]. Dislocations, dislocation tangles or stacking faults can be made visible by that SEM technique [64]. Additional carrier gas hot extraction or thermal desorption analyses (TDA) and subsequent calculations are able to determine the activation energies of hydrogen released from electrochemically charged samples. By that, deeply trapped, diffusible and supersaturated hydrogen might be differentiated. This approach was successfully carried out and described e.g. by Rhode *et al.* [301], Silverstein *et al.* [253] and Koyama *et al.* [302]. Together with the EBSD/ECCI and SIMS measurements, information about the underlying mechanisms and the locations of hydrogen, i.e. deuterium, accumulation sites can be provided.

6. The absorption of deuterium into the (sub-)surface of the specimen does not take place homogeneously. From that it can be concluded that the effusion of deuterium after charging is heterogeneous too. A study that combines SKPFM and EBSD data can be useful to tackle this issue. By means of EBSD measurements the grain orientation and additionally the possible martensite variants can be identified. Scanning Kelvin probe force microscopy gives information on the variation of the potential, i.e. changes in the local work function. These changes are interpreted as changes in the band structure of the oxide caused by hydrogen [303]. Correlating this information with structural information from EBSD can provide further insight into the orientation-dependent hydrogen-assisted damages in ASS. For this purpose several specimens have to be charged in stages with hydrogen and analysed by both EBSD and SKPFM. Subsequently, these samples will be stored for desorption under controlled atmosphere and repeatedly analysed by SKPFM and EBSD after distinct storage periods. By that a matrix is created that contains information about the diffusion *into* and effusion *from* the austenitic grades AISI 304L and 316L.
7. The present work proved that hydrogen can be accumulated at the grain boundaries of the steel grade AISI 316L. However, the exact mechanism and origin of the hydrogen remains unclear. Knowledge about the properties of the grain boundaries, e.g. type (random or special GB), misorientation angle and density, can deliver information about their trapping capacity. Atomic force microscopy (AFM) and designated electron backscatter diffraction (EBSD) measurements are suitable ways to gain information about the properties of GBs and should be combined with ToF-SIMS analysis in the future.
8. A common trend in the production of (austenitic stainless) steels is the process of *additive manufacturing*. Although there are different ways to produce parts and components via AM, it can be generally understood as a 3D printing process. This method gives not only a high degree of design flexibility, but also the ability to produce customised spare parts on-demand. That is why additively manufactured ASS are interesting for the hydrogen industry as well [172]. Because mechanical properties, corrosion resistance as well as diffusivity and solubility of hydrogen inside these alloys may vary dramatically from their conventionally produced counterparts, this opens a completely new field of study for materials science and engineering. Investigating additively manufactured 304L and 316L grades and comparing them to the "standard" grades is therefore of great interest. First SEM and ToF-SIMS investigations on AISI 316L-AM were already conducted and analysed. Additional measurements, including structural analyses by EBSD or XRD are necessary to create a comprehensive picture about the influence of hydrogen/deuterium. A main question will be whether or not deuterium induces phase transformation in AM steels too.
9. The present study delivered new and important insights into the impact of hydrogen on the structural integrity of the austenitic grades AISI 304L and 316L. However, the results of the EBSD analyses can be interpreted only qualitatively or semi-quantitatively. That is why further studies have to raise more quantitative data to correlate the extend of phase

transformation with the charging time and the amount of deuterium introduced. This can be achieved, e.g. by CGHE and XRD measurements.

10. Even though differences in the trapping behaviour, solubility and diffusivity between DIM, AM and charging-induced martensite were pointed out, further experiments are necessary. This is particularly relevant to investigate the properties of sputter-induced martensite. The two following experimental approaches were developed to this end. The first one aims to gain deeper insight into *charging-induced* martensite (I.), whereas the second focuses on *sputter-induced* martensite (II.).

### **I.**

1. Sample preparation → Removal of residual martensite
2. EBSD analyses → Verification by phase maps and inverse pole figures
3. Electrochemical charging → Introduction of deuterium to trigger  $\gamma \rightarrow \epsilon \rightarrow \alpha'$ -transformation
4. ToF-SIMS analysis → Localisation of deuterium accumulation sites
5. EBSD analysis → Verification of phase transformation and correlation with SIMS results
6. Desorption → Removal of diffusible and trapped deuterium at low temperatures
7. ToF-SIMS analysis → Localisation of potentially deeply trapped deuterium
8. Electrochemical charging → Introduction of deuterium at lower current density
9. ToF-SIMS analysis → Localisation of deuterium accumulation sites
10. EBSD analysis → Verification of possible new phase transformation and re-trapping at already existing charging-induced martensite

### **II.**

1. Sample preparation → Removal of residual martensite
  2. EBSD analyses → Verification by phase maps and inverse pole figures
  3. ToF-SIMS experiments → Deliberate introduction of sputter-induced martensite
  4. EBSD analysis → Verification of phase transformation
  5. Electrochemical charging → Introduction of deuterium
  6. ToF-SIMS analysis → Localisation of deuterium accumulation sites and verification whether or not sputter-induced martensite traps deuterium
  7. EBSD analysis → Verification of possible new phase transformation in the course of charging
11. Systematic studies of hydrogen-assisted damages by means of physical experiments are important to gain knowledge about the underlying mechanisms. However, complementary computer simulations as a valuable tool to broaden the scope of hydrogen research and to



deliver further insights gained, justifiably, more and more attention. Models and simulations are for instance able to describe the distribution, transport and diffusion of hydrogen atoms inside a steel lattice [292, 304–308], hydrogen-assisted cracking phenomena [309], the effect of hydrogen on void growth and coalescence [310] and many other aspects.

The initial distribution of deuterium inside the investigated steels AISI 304L and 316L after charging and its rearrangement during application of external load have to be verified by ToF-SIMS measurements. Additional simulations of the stress distribution induced by both deuterium and mechanical bending create a detailed picture of the actual processes.

12. A large variety of different metal alloys is nowadays used for applications where hydrogen in critical concentrations might occur. With respect to the booming hydrogen industry it becomes even more crucial to investigate a larger spectrum of alloy systems. The experimental procedure of electrochemical charging, SEM, EBSD and ToF-SIMS measurements has proven to deliver valuable information of the behaviour of ASS subjected to hydrogen. This approach can therefore help to better understand the hydrogen-assisted cracking behaviour e.g. of aluminium alloys, nickel-base alloys, titanium alloys, duplex stainless steels and martensitic stainless steels.

---

## Bibliography

- [1] Johnson, W. H. *Proceedings of the Royal Society of London* **23**(156-163), 168–179 (1874).
- [2] Intergovernmental Panel on Climate Change. <https://www.ipcc.ch/sr15/>, (2019). Accessed on 2019-08-14.
- [3] *Nature* **572**, 283 (2019). <https://www.nature.com/articles/d41586-019-02425-7>.
- [4] Zhang, L., Shen, H., Lu, K., Cao, W., Sun, Y., Fang, Y., Xing, Y., Du, Y., and Lu, M. *International Journal of Hydrogen Energy* **42**(50), 29888–29896 (2017).
- [5] The driving force. Managing hydrogen projects with Linde., (2020). Linde AG hydrogen brochure.
- [6] Sobol, O. *Hydrogen Assisted Cracking and Transport Studied by ToF-SIMS and Data Fusion with HR-SEM*. Thesis, Otto-von-Guericke Universität Magdeburg, (2018).
- [7] Murakami, Y. In *International Hydrogen Conference*, Somerday, B., Sofronis, P., and Jones, R., editors, 308–315. ASM International, (2008).
- [8] Woodtli, J. and Kieselbach, R. *Engineering Failure Analysis* **7**(6), 427–450 (2000).
- [9] Djukic, M. B., Zeravic, V. S., Bakic, G. M., Sedmak, A., and Rajicic, B. *Engineering Failure Analysis* **58**, 485–498 (2015).
- [10] Merkel, M. and Thomas, K.-H. *Taschenbuch der Werkstoffe (German)*. Carl Hanser Verlag, (2008).
- [11] Talonen, J. and Hänninen, H. *Steel Research International* **78**(3), 260–265 (2007).
- [12] Mine, Y., Horita, N., Horita, Z., and Takashima, K. *International Journal of Hydrogen Energy* **42**(22), 15415–15425 (2017).
- [13] Verhoeven, J. D. *Steel Metallurgy for the Non-Metallurgist*. ASM International, (2007).
- [14] *ASM Metals Handbook Desk Edition 2001*. ASM International, 2nd edition, (1998).
- [15] Papula, S. *Delayed Cracking of Metastable Low-Nickel Austenitic Stainless Steels*. Doctoral thesis, (2015).
- [16] De Cooman, B. C., Estrin, Y., and Kim, S. K. *Acta Materialia* **142**, 283–362 (2018).
- [17] San Marchi, C. Report, Sandia National Laboratories, (2005). Technical Reference on Hydrogen Compatibility of Materials Austenitic Stainless Steels: Type 304 & 304L.
- [18] Mente, T. *Numerische Simulation der wasserstoffunterstützten Rissbildung in austenitisch-ferritischen Duplexstählen (German)*. Thesis, Otto-von-Guericke-Universität, (2015).

- 
- [19] Hannula, S. P., Hänninen, H., and Tahtinen, S. *Metallurgical Transactions A - Physical Metallurgy and Materials Science* **15**(12), 2205–2211 (1984).
- [20] Handbook of Stainless Steel, (2013). Outokumpo Stainless Steel company flyer.
- [21] Martin, M., Weber, S., Theisen, W., Michler, T., and Naumann, J. *International Journal of Hydrogen Energy* **36**(24), 15888–15898 (2011).
- [22] Grassel, O., Krüger, L., Frommeyer, G., and Meyer, L. W. *International Journal of Plasticity* **16**(10-11), 1391–1409 (2000).
- [23] Koyama, M., Akiyama, E., Lee, Y. K., Raabe, D., and Tsuzaki, K. *International Journal of Hydrogen Energy* **42**(17), 12706–12723 (2017).
- [24] Lo, K. H., Shek, C. H., and Lai, J. K. L. *Materials Science & Engineering R-Reports* **65**(4-6), 39–104 (2009).
- [25] Takaki, S., Nanba, S., Imakawa, K., Macadre, A., Yamabe, J., Matsunaga, H., and Matsuoka, S. *International Journal of Hydrogen Energy* **41**(33), 15095–15100 (2016).
- [26] Biermann, H., Solarek, J., and Weidner, A. *steel research international* **83**(6), 512–520 (2012).
- [27] Kotecki, D. and Siewert, T. *Welding Research Supplement* , 171–178 (1992).
- [28] *Stainless Steels for Design Engineers*, book section in Austenitic Stainless Steels, 69–78. ASM (2008).
- [29] Garion, C., Skoczzeń, B., and Sgobba, S. *International Journal of Plasticity* **22**(7), 1234–1264 (2006).
- [30] Kim, J.-K. and De Cooman, B. C. *Materials Science and Engineering: A* **676**, 216–231 (2016).
- [31] Kim, J. W. and Byun, T. S. *Journal of Nuclear Materials* **396**(1), 1–9 (2010).
- [32] Linderov, M., Segel, C., Weidner, A., Biermann, H., and Vinogradov, A. *Materials Science and Engineering: A* **597**, 183–193 (2014).
- [33] Vasylyev, M. A., Mordyuk, B. N., Sidorenko, S. I., Voloshko, S. M., and Burmak, A. P. *Surface and Coatings Technology* **343**, 57–68 (2018).
- [34] Hecker, S. S., Stout, M. G., Staudhammer, K. P., and Smith, J. L. *Metallurgical Transactions A-Physical Metallurgy and Materials Science* **13**(4), 619–626 (1982).
- [35] Murr, L. E., Staudhammer, K. P., and Hecker, S. S. *Metallurgical Transactions A-Physical Metallurgy and Materials Science* **13**(4), 627–635 (1982).
- [36] Talonen, J. and Hänninen, H. *Acta Materialia* **55**(18), 6108–6118 (2007).
-

- [37] Rozenak, P. *Metallurgical and Materials Transactions A-Physical Metallurgy and Materials Science* **45A**(1), 162–178 (2014).
- [38] Huang, T. T., Dan, W. J., and Zhang, W. G. *Metallurgical and Materials Transactions A-Physical Metallurgy and Materials Science* **48a**(10), 4553–4564 (2017).
- [39] Wendler, M., Hauser, M., Fabrichnaya, O., Krüger, L., Weiß, A., and Mola, J. *Materials Science and Engineering: A* **645**, 28–39 (2015).
- [40] Wendler, M., Weiß, A., Krüger, L., Mola, J., Franke, A., Kovalev, A., and Wolf, S. *Advanced Engineering Materials* **15**(7), 558–565 (2013).
- [41] Tian, Y., Borgenstam, A., and Hedström, P. *Materials Today: Proceedings* **2**, S687–S690 (2015).
- [42] Chatterjee, S. and Bhadeshia, H. K. D. H. *Materials Science and Technology* **23**(9), 1101–1104 (2007).
- [43] Olson, G. B. and Cohen, M. *Metallurgical Transactions A* **6**(4), 791 (1975).
- [44] Weidner, A., Segel, C., and Biermann, H. *Materials Letters* **143**, 155–158 (2015).
- [45] Chun, Y. S., Kim, J. S., Park, K. T., Lee, Y. K., and Lee, C. S. *Materials Science and Engineering A-Structural Materials Properties Microstructure and Processing* **533**, 87–95 (2012).
- [46] Kruml, T., Polak, J., and Degallaix, S. *Materials Science and Engineering A-Structural Materials Properties Microstructure and Processing* **293**(1-2), 275–280 (2000).
- [47] Lecroisey, F. and Pineau, A. *Metallurgical Transactions* **3**(2), 391–400 (1972).
- [48] Martin, S., Wolf, S., Martin, U., Krüger, L., and Jahn, A. In *ESOMAT 2009*, (2009).
- [49] Galindo-Nava, E. I. *Scripta Materialia* **138**, 6–11 (2017).
- [50] Padilha, A. F. and Rios, P. R. *ISIJ international* **42**(4), 325–337 (2002).
- [51] Nolze, G. *Archives of Metallurgy and Materials* **51**(1), 15–22 (2006).
- [52] Hirth, J. P. *Metallurgical Transactions A-Physical Metallurgy and Materials Science* **11**(6), 861–890 (1980).
- [53] Li, Z., Brand, U., and Ahbe, T. *Precision Engineering* **45**, 110–117 (2016).
- [54] Borchers, C., Michler, T., and Pundt, A. *Advanced Engineering Materials* **10**(1-2), 11–23 (2008).
- [55] Byun, T. S., Hashimoto, N., and Farrell, K. *Acta Materialia* **52**(13), 3889–3899 (2004).
- [56] Fussik, R. and Weber, S. *Journal of Materials Science and Engineering A* **6**(5) (2016).

- 
- [57] Pontini, A. E. and Hermida, J. D. *Scripta Materialia* **37**(11), 1831–1837 (1997).
- [58] Han, G., He, J., Fukuyama, S., and Yokogawa, K. *Acta Materialia* **46**(13), 4559–4570 (1998).
- [59] Guo, E.-Y., Wang, M.-Y., Jing, T., and Chawla, N. *Materials Science and Engineering A-Structural Materials Properties Microstructure and Processing* **580**, 159–168 (2013).
- [60] Kalandyk, B., Zapa, R., Boroń, L., and Solecka, M. *Archives of Metallurgy and Materials* **59**(3), 1103–1106 (2014).
- [61] Röhsler, A., Sobol, O., Nolze, G., Unger, W. E. S., and Böllinghaus, T. *Journal of Vacuum Science & Technology B, Nanotechnology and Microelectronics: Materials, Processing, Measurement, and Phenomena* **36**(3), 03F103 (2018).
- [62] Gussev, M. N., Busby, J. T., Byun, T. S., and Parish, C. M. *Materials Science and Engineering A-Structural Materials Properties Microstructure and Processing* **588**, 299–307 (2013).
- [63] Samek, L., de Moor, E., Penning, J., and de Cooman, B. C. *Metallurgical and Materials Transactions A* **37A**, 109–124 (2006).
- [64] Weidner, A., Müller, A., Weiß, A., and Biermann, H. *Materials Science and Engineering: A* **571**, 68–76 (2013).
- [65] Mesquita, R. A., Schneider, R., Steineder, K., Samek, L., and Arenholz, E. *Metallurgical and Materials Transactions A* **44**(9), 4015–4019 (2013).
- [66] Lichtenfeld, J. A., Mataya, M. C., and Van Tyne, C. J. *Metallurgical and Materials Transactions A-Physical Metallurgy and Materials Science* **37A**(1), 147–161 (2006).
- [67] Yu, H. D., Guo, Y. J., and Lai, X. M. *Materials & Design* **30**(7), 2501–2505 (2009).
- [68] So, K. H., Kim, J. S., Chun, Y. S., Park, K. T., Lee, Y. K., and Lee, C. S. *ISIJ International* **49**(12), 1952–1959 (2009).
- [69] Shuro, I., Kobayashi, S., Nakamura, T., and Tsuzaki, K. *Journal of Alloys and Compounds* **588**, 284–289 (2014).
- [70] Ryu, J. H., Chun, Y. S., Lee, C. S., Bhadeshia, H. K. D. H., and Suh, D. W. *Acta Materialia* **60**(10), 4085–4092 (2012).
- [71] [http://www.worldstainless.org/transport\\_applications/automotive\\_applications](http://www.worldstainless.org/transport_applications/automotive_applications). Accessed: 2019-17-12.
- [72] Oberflächen von Outokumpu (German), (2012). Outokumpu Group company flyer.
- [73] Bal, B., Koyama, M., Gerstein, G., Maier, H. J., and Tsuzaki, K. *International Journal of Hydrogen Energy* **41**(34), 15362–15372 (2016).



- 
- [74] Chen, T. C., Chen, S. T., Kai, W., and Tsay, L. W. *Materials Characterization* **112**, 134–141 (2016).
- [75] Koyama, M., Abe, Y. J., Saito, K., Akiyama, E., Takai, K., and Tsuzaki, K. *Scripta Materialia* **122**, 50–53 (2016).
- [76] Zhang, L., Li, Z. Y., Zheng, J. Y., Zhao, Y. Z., Xu, P., Zhou, C. L., Zhou, C. S., and Chen, X. Y. *International Journal of Hydrogen Energy* **39**(35), 20578–20584 (2014).
- [77] Matsunaga, H. and Noda, H. *Metallurgical and Materials Transactions A-Physical Metallurgy and Materials Science* **42A**(9), 2696–2705 (2011).
- [78] Böllinghaus, T. *Wasserstoffunterstützte Schäden in metallischen Strukturwerkstoffen (german)*. habilitation dissertation, (1999).
- [79] Brilz, M., Biehler, J., Hoche, H., and Oechsner, M. *International Journal of Hydrogen Energy* **43**(22), 10496–10501 (2018).
- [80] Rhode, M. *Effect of hydrogen on weld joint microstructures of low alloyed steels applied in power plants*. Thesis, Otto-von-Guericke-Universität Magdeburg, (2015).
- [81] Harris, J. *American Chemical Society* **7**, 2528–2533 (1991).
- [82] Horikawa, K., Okada, H., Kobayashi, H., and Urushihara, W. *The Japan Institute of Metals* **50**(9), 2201–2206 (2009).
- [83] Yamabe, J., Awane, T., and Murakami, Y. *International Journal of Hydrogen Energy* **42**(38), 24560–24568 (2017).
- [84] Chen, Y., Santos, D. M. F., and Sequeira, C. A. C. *Hydrogen diffusion in austenitic stainless steels*, volume 258-260 of *Defect and Diffusion Forum*, 322–326. Trans Tech Publications Ltd, Zürich (2006).
- [85] Brass, A. M. and Chene, J. *Corrosion Science* **48**(10), 3222–3242 (2006).
- [86] Olden, V. *FE modelling of hydrogen induced stress cracking in 25% Cr duplex stainless steel*. Thesis, Norwegian University of Science and Technology, (2008).
- [87] Craidy, P., Briottet, L., and Santos, D. *International Journal of Hydrogen Energy* **40**(47), 17084–17090 (2015).
- [88] Bak, S. H., Abro, M. A., and Lee, D. B. *Metals* **6**(7), 8 (2016).
- [89] Koyama, M., Ogawa, T., Yan, D., Matsumoto, Y., Tasan, C. C., Takai, K., and Tsuzaki, K. *International Journal of Hydrogen Energy* **42**(42), 26423–26435 (2017).
- [90] Owczarek, E. and Zakroczymski, T. *Acta Materialia* **48**(12), 3059–3070 (2000).
- [91] Li, Y. F., Zhao, L. M., and Pan, H. L. *Materials and Structures* **46**(4), 621–627 (2013).

- 
- [92] Katsuta, H. and Furukawa, K. *Journal of Nuclear Science and Technology* **18**(2), 143–151 (1981).
- [93] Böllinghaus, T., Hoffmeister, H., and Middel, C. *Welding in the World* **37**(1), 16–23 (1996).
- [94] Völkl, J. and Alefeld, G. *Il Nuovo Cimento B Series 11* **33**(1), 190–204 (1976).
- [95] Fukai, Y. and Sugimoto, H. *Advances in Physics* **34**(2), 263–326 (1985).
- [96] Tien, J. K., Thompson, A. W., Bernstein, I. M., and Richards, R. J. *Metallurgical Transactions a-Physical Metallurgy and Materials Science* **7**(6), 821–829 (1976).
- [97] Lee, S. M., Park, I. J., Jung, J. G., and Lee, Y. K. *Acta Materialia* **103**, 264–272 (2016).
- [98] Fidelle, J. P., Broudeur, R., and Roux, C. In *Proceedings of the International Conference on the effect of hydrogen on materials*, (1975).
- [99] Hardie, D., Xu, J., Charles, E. A., and Wei, Y. *Corrosion Science* **46**(12), 3089–3100 (2004).
- [100] Koyama, M., Akiyama, E., and Tsuzaki, K. *Scripta Materialia* **66**(11), 947–950 (2012).
- [101] Tavares, S. S. M., Bastos, I. N., Pardal, J. M., Montenegro, T. R., and da Silva, M. R. *International Journal of Hydrogen Energy* **40**(47), 16992–16999 (2015).
- [102] Momotani, Y., Shibata, A., Terada, D., and Tsuji, N. *International Journal of Hydrogen Energy* , 1–9 (2016).
- [103] Pundt, A. and Kirchheim, R. *Annual reviews material* **36**, 555–608 (2006).
- [104] Grong, O. *Metallurgical Modelling of Welding*. The Institute of Materials, 2 edition, (1997).
- [105] Hoelzel, M., Danilkin, S. A., Ehrenberg, H., Töbrens, D. M., Udovic, T. J., Fuess, H., and Wipf, H. *Materials Science and Engineering A-Structural Materials Properties Microstructure and Processing* **384**(1-2), 255–261 (2004).
- [106] Krieger, W., Merzlikin, S. V., Bashir, A., Szczepaniak, A., Springer, H., and Rohwerder, M. *Acta Materialia* **144**, 235–244 (2018).
- [107] Park, Y. D., Maroef, I. S., and Olson, D. L. *Welding Journal* **81**(2), 27S–35S (2002).
- [108] Pu, S. D. and Ooi, S. W. *Materials Science and Engineering: A* **761** (2019).
- [109] Dabah, E. *Hydrogen Interaction with Supermartensitic Stainless Steel studied by Energy Dispersive X-Ray Diffraction*. Thesis, (2015).
- [110] Oriani, R. A. *Annual Review of Materials Science* **8**, 327–357 (1978).
- [111] Szummer, A. *Hydrogen Degradation of Ferrous Alloys*, chapter Phase Transformations Near the Crack Tip, 512–534. (1985).
-

- 
- [112] Nelson, H. *Hydrogen Embrittlement*, volume 25 of *Treatise on Materials Science and Technology*. Academic Press, New York, (1983).
- [113] Fisher, D. J. *Hydrogen Diffusion in Metals: A 30-Year Retrospective*, volume 167. Trans Tech Publication, (1999).
- [114] Koyama, M., Akiyama, E., Sawaguchi, T., Raabe, D., and Tsuzaki, K. *Scripta Materialia* **66**(7), 459–462 (2012).
- [115] Pan, C., Chu, W. Y., Li, Z. B., Liang, D. T., Su, Y. J., Gao, K. W., and Qiao, L. J. *Materials Science and Engineering: A* **351**(1–2), 293–298 (2003).
- [116] Song, J. and Curtin, W. A. *Acta Materialia* **59**(4), 1557–1569 (2011).
- [117] Di Cocco, V., Franzese, E., Iacoviello, F., and Natali, S. *Engineering Fracture Mechanics* **75**(3–4), 705–714 (2008).
- [118] Dmytrakh, I. M., Leshchak, R. L., Syrotyuk, A. M., and Barna, R. A. *International Journal of Hydrogen Energy* **42**(9), 6401–6408 (2017).
- [119] Kanezaki, T., Narazaki, C., Mine, Y., Matsuoka, S., and Murakami, Y. *International Journal of Hydrogen Energy* **33**(10), 2604–2619 (2008).
- [120] Kelestemur, M. H. and Chaki, T. K. *Fatigue & Fracture of Engineering Materials & Structures* **24**(1), 15–22 (2001).
- [121] Saintier, N., Awane, T., Olive, J. M., Matsuoka, S., and Murakami, Y. *International Journal of Hydrogen Energy* **36**(14), 8630–8640 (2011).
- [122] Matsuoka, S., Takakuwa, O., Okazaki, S., Yoshikawa, M., Yamabe, J., and Matsunaga, H. *Scripta Materialia* **154**, 101–105 (2018).
- [123] Whiteman, M. B. and Troiano, A. R. *Physica Status Solidi* **7**(2), K109–K110 (1964).
- [124] Laureys, A., Van den Eeckhout, E., Petrov, R., and Verbeken, K. *Acta Materialia* **127**, 192–202 (2017).
- [125] Sobol, O., Holzlechner, G., Nolze, G., Wirth, T., Eliezer, D., Böllinghaus, T., and Unger, W. E. S. *Materials Science and Engineering A* (2016).
- [126] Yang, Q. and Luo, J. L. *Materials Science and Engineering A-Structural Materials Properties Microstructure and Processing* **288**(1), 75–83 (2000).
- [127] Tiegel, M. C., Martin, M. L., Lehmberg, A. K., Deutges, M., Borchers, C., and Kirchheim, R. *Acta Materialia* **115**, 24–34 (2016).
- [128] Rozenak, P. and Loew, A. *Corrosion Science* **50**(11), 3021–3030 (2008).

- 
- [129] Saleh, A. A., Hejazi, D., Gazder, A. A., Dunne, D. P., and Pereloma, E. V. *International Journal of Hydrogen Energy* **41**(28), 12424–12435 (2016).
- [130] Beachem, C. D. *Metallurgical Transactions* **3**(2), 437–451 (1972).
- [131] Robertson, I. M., Sofronis, P., Nagao, A., Martin, M. L., Wang, S., Gross, D. W., and Nygren, K. E. *Metallurgical and Materials Transactions A-Physical Metallurgy and Materials Science* **46A**(6), 2323–2341 (2015).
- [132] Lynch, S. P. *NACE - International Corrosion Conference Series* 01 (2007).
- [133] Bond, G. M., Robertson, I. M., and Birnbaum, H. K. *Scripta Metallurgica* **20**(5), 653–658 (1986).
- [134] Lee, T. C., Robertson, I. M., and Birnbaum, H. K. *Philosophical Magazine A-Physics of Condensed Matter Structure Defects and Mechanical Properties* **62**(1), 131–153 (1990).
- [135] Dadfarnia, M., Novak, P., Ahn, D. C., Liu, J. B., Sofronis, P., Johnson, D. D., and Robertson, I. M. *Advanced Materials* **22**(10), 1128–1135 (2010).
- [136] Barnoush, A. and Vehoff, H. *Acta Materialia* **58**(16), 5274–5285 (2010).
- [137] Wang, S., Nagao, A., Edalati, K., Horita, Z., and Robertson, I. M. *Acta Materialia* **135**, 96–102 (2017).
- [138] Kirchheim, R. *International Journal of Materials Research* **100**(4), 483–487 (2009).
- [139] Robertson, I. M. *Engineering Fracture Mechanics* **68**(6), 671–692 (2001).
- [140] Djukic, M. B., Bakic, G. M., Sijacki Zeravcic, V., Sedmak, A., and Rajicic, B. *Engineering Fracture Mechanics* (2019).
- [141] Tanino, M., Komatsu, H., and Funaki, S. *Journal De Physique* **43**(NC-4), 503–508 (1982).
- [142] Khatak, H. S., Gnanamoorthy, J. B., and Rodriguez, P. *Metallurgical and Materials Transactions A-Physical Metallurgy and Materials Science* **27**(5), 1313–1325 (1996).
- [143] G, A. and Świątnicki, W. A. *Materials Chemistry and Physics* **81**(2-3), 496–499 (2003).
- [144] Zapffe, C. A. and Sims, C. E. *Transactions of the American Institute of Mining and Metallurgical Engineers* **145**, 225–261 (1941).
- [145] Buckley, J. R. and Hardie, D. *Materials Science and Technology* **9**(3), 259–263 (1993).
- [146] Iacoviello, F., Habashi, M., and Cavallini, M. *Materials Science and Engineering A-Structural Materials Properties Microstructure and Processing* **224**(1-2), 116–124 (1997).
- [147] Tsay, L. W., Lee, W. C., Luu, W. C., and Wu, J. K. *Corrosion Science* **44**(6), 1311–1327 (2002).

- [148] Yagodzinsky, Y., Saukkonen, T., Hänninen, H., Tuomisto, F., Barannikova, S., and Zuev, L. In *Effects of Hydrogen on Materials*, Somerday, B., Sofronis, P., and Jones, R., editors, 97+, (2009).
- [149] Martin, M., Weber, S., Izawa, C., Wagner, S., Pundt, A., and Theisen, W. *International Journal of Hydrogen Energy* **36**(17), 11195–11206 (2011).
- [150] Costa, L. R. O., Lemus, L. F., and dos Santos, D. S. *International Journal of Hydrogen Energy* **40**(47), 17128–17135 (2015).
- [151] Tsay, L. W., Young, M. C., and Chen, C. *Corrosion Science* **45**(9), 1985–1997 (2003).
- [152] Tsay, L. W., Liu, Y. C., Lin, D. Y., and Young, M. C. *Materials Science and Engineering A-Structural Materials Properties Microstructure and Processing* **384**(1-2), 177–183 (2004).
- [153] Tsay, L. W., Yu, S. C., and Huang, R. T. *Corrosion Science* **49**(7), 2973–2984 (2007).
- [154] Tsay, L. W., Liua, Y. F., Huang, R. T., and Kuo, R. C. *Corrosion Science* **50**(5), 1360–1367 (2008).
- [155] Kawamoto, K., Oda, Y., Noguchi, H., Fujii, H., Izumi, T., and Itoh, G. *Journal of Solid Mechanics and Materials Engineering* **3**(6), 898–909 (2009).
- [156] Bahrami, A., Zhang, Y. H., and Tubby, P. In *OMAE2011: Proceedings of the ASME 30th International Conference on Ocean, Offshore and Arctic Engineering*, volume 3, 79–92, (2011).
- [157] Barnoush, A., Kheradmand, N., and Hajilou, T. *Scripta Materialia* **108**, 76–79 (2015).
- [158] Williams, D. P. and Nelson, H. G. *Metallurgical Transactions* **1**(1), 63–& (1970).
- [159] John, C. S. and Gerberich, W. W. *Metallurgical Transactions* **4**(2), 589–594 (1973).
- [160] Lee, T. D., Goldenberg, T., and Hirth, J. P. *Metallurgical Transactions* **10A**, 199–208 (1979).
- [161] Hänninen, H. and Hakkarainen, T. *Corrosion* **36**(1), 47–51 (1980).
- [162] Ulmer, D. G. and Altstetter, C. J. *Acta Materialia* **39**(6), 1237–1248 (1991).
- [163] Mittal, S. C., Prasad, R. C., and Deshmukh, M. B. *ISIJ international* **34**(2), 211–216 (1994).
- [164] Delafosse, D. and Magnin, T. *Engineering Fracture Mechanics* **68**(6), 693–729 (2001).
- [165] Luu, W. C., Liu, P. W., and Wu, J. K. *Corrosion Science* **44**(8), 1783–1791 (2002).
- [166] Zakroczymski, T., G, A., and Świątnicki, W. *Corrosion Science* **47**(6), 1403–1414 (2005).



- 
- [167] Zucchi, F., Grassi, V., Monticelli, C., and TrabANELLI, G. *Corrosion Science* **48**(2), 522–530 (2006).
- [168] Au, M. *Materials Science and Engineering: A* **454–455**, 564–569 (2007).
- [169] Roychowdhury, S. and Kain, V. *Journal of Materials Engineering and Performance* **17**(5), 702–707 (2008).
- [170] Chen, T. C., Chen, S. T., and Tsay, L. W. *International Journal of Hydrogen Energy* **39**(19), 10293–10302 (2014).
- [171] Mine, Y., Koga, K., Kraft, O., and Takashima, K. *Scripta Materialia* **113**, 176–179 (2016).
- [172] Baek, S. W., Song, E. J., Kim, J. H., Jung, M., Baek, U. B., and Nahm, S. H. *Scripta Materialia* **130**, 87–90 (2017).
- [173] Wang, S., Nagao, A., Sofronis, P., and Robertson, I. M. *Acta Materialia* **144**, 164–176 (2018).
- [174] Rhode, M., Steger, J., Steppan, E., and Kannengiesser, T. *Welding in the World* **60**(4), 623–638 (2016).
- [175] Kesten, P., Pundt, A., Schmitz, G., Weisheit, M., Krebs, H. U., and Kirchheim, R. *Journal of Alloys and Compounds* **330**, 225–228 (2002).
- [176] Sathirachinda, N., Pettersson, R., Wessman, S., Kivisäkk, U., and Pan, J. *Electrochimica Acta* **56**(4), 1792–1798 (2011).
- [177] Nagashima, T., Koyama, M., Bashir, A., Rohwerder, M., Tasan, C. C., Akiyama, E., Raabe, D., and Tsuzaki, K. *Materials and Corrosion* **68**(3), 306–310 (2017).
- [178] Koyama, M., Rohwerder, M., Tasan, C. C., Bashir, A., Akiyama, E., Takai, K., Raabe, D., and Tsuzaki, K. *Materials Science and Technology* **33**(13), 1481–1496 (2017).
- [179] Miyauchi, N., Hirata, K., Murase, Y., Sakaue, H. A., Yakabe, T., Itakura, A. N., Gotoh, T., and Takagi, S. *Scripta Materialia* **144**, 69–73 (2018).
- [180] Oran, U. *Surface Chemical Characterization of Plasma-Chemically Deposited Polymer Films by Time-of-Flight Static Secondary Ion Mass Spectrometry*. Thesis, Freie Universität Berlin, (2005).
- [181] Benninghoven, A., Rüdenauer, F. G., and Werner, H. W. *Secondary Ion Mass Spectrometry*, volume 86. John Wiley & Sons, (1987).
- [182] De Chambost, E., Monsallut, P., Rasser, B., and Schumacher, M. *Applied Surface Science* **203–204**, 391–395 (2003).
- [183] Vickerman, J. C. and Briggs, D. *ToF-SIMS: Surface Analysis by Mass Spectrometry*, 789. IM Publications; SurfaceSpectra Ltd., Manchester, UK (2001).

- 
- [184] Betz, G. and Wehner, G. K. *Sputtering of Multicomponent Materials*, volume 2, 1–117. Springer (1981).
- [185] Straif, C. J. *The interaction of Bi cluster ions with molecular compounds*. Thesis, Technische Universität Wien, (2009).
- [186] Sigmund, P. *Sputtering processes: Collision cascades and spikes*, 121. Academic Press Inc., New York (1977).
- [187] Niehuis, E. and Grehl, T. *Dual Beam Depth Profiling*, 753–780. IM Publications and SurfaceSpectra Limited (2001).
- [188] Hoffmann, E. *Mass Spectrometry: Principles and Applications*. John Wiley & Sons Ltd., 3 edition, (2007).
- [189] Belu, A. M., Graham, D. J., and Castner, D. G. *Biomaterials* **24**(21), 3635–3653 (2003).
- [190] Grehl, T. *Improvement in ToF-SIMS Instrumentation for Analytical Application and Fundamental Research*. Thesis, Westfälische-Wilhelms Universität Münster, (2003).
- [191] Tuccitto, N., Giambianco, N., Marletta, G., and Licciardello, A. *Applied Surface Science* **255**(4), 1075–1078 (2008).
- [192] Kossoy, E., Khoptiar, Y., Cytermann, C., Shemesh, G., Katz, H., Sheinkopf, H., Cohen, I., and Eliaz, N. *Corrosion Science* **50**(5), 1481–1491 (2008).
- [193] Ravanel, X., Trouiller, C., Juhel, M., Wyon, C., Kwakman, L. F. T., and Leonard, D. *Applied Surface Science* **255**(4), 1415–1418 (2008).
- [194] Bloomfield, H. L. and Nie, H.-Y. *Surface and Interface Analysis* **49**(13), 1379–1386 (2017).
- [195] Frank, R. C., Baker, J. E., and Altstetter, C. J. *Metallurgical Transactions A-Physical Metallurgy and Materials Science* **13**(4), 581–584 (1982).
- [196] Gao, H., Cao, W., Fang, C., and Delosrios, E. R. *Fatigue & Fracture of Engineering Materials & Structures* **17**(10), 1213–1220 (1994).
- [197] Oltra, R. and Bouillot, C. *Experimental investigation of the role of hydrogen in stress corrosion cracking of duplex stainless steels*, chapter Hydrogen Transport and Cracking in Metals, 17–26. (1994).
- [198] Takai, K., Seki, J., and Homma, Y. *Materials Transactions Jim* **36**(9), 1134–1139 (1995).
- [199] Straub, F., Wirth, T., Hertwig, A., Hodoroba, V. D., Unger, W. E. S., and Böllinghaus, T. *Surface and Interface Analysis* **42**(6-7), 739–742 (2010).
- [200] Straub, F., Böllinghaus, T., Unger, W. E. S., and Mente, T. In *International Hydrogen Conference (IHC 2012)*, 505–513. ASME press, (2012).

- 
- [201] Sobol, O., Straub, F., Wirth, T., Holzlechner, G., Böllinghaus, T., and Unger, W. E. S. *Scientific Reports* **6**(19929) (2016).
- [202] Sobol, O., Nolze, G., Saliwan-Neumann, R., Eliezer, D., Böllinghaus, T., and Unger, W. E. S. *International Journal of Hydrogen Energy* **42**(39), 25114–25120 (2017).
- [203] Tanaka, T., Kawakami, K., and Hayashi, S. *Journal of Materials Science* **49**(11), 3928–3935 (2014).
- [204] Al Aboura, Y., Cook, A., Felisari, L., Akid, R., and Moore, K. L. In *International Conference on Metals and Hydrogen, Steelyhydrogen 2018*, volume 3. OCAS, (2018).
- [205] McMahon, G., Miller, B. D., and Burke, M. G. *npj Materials Degradation* **2**(1) (2018).
- [206] Dabah, E., Kannengiesser, T., Mente, T., Beyer, K., and Brauser, S. *Welding in the World* **57**(4), 561–567 (2013).
- [207] Silverstein, R., Sobol, O., Böllinghaus, T., Unger, W., and Eliezer, D. *Journal of Alloys and Compounds* **695**, 2689–2695 (2017).
- [208] Ningshen, S., Uhlemann, M., Schneider, F., and Khatak, H. S. *Corrosion Science* **43**(12), 2255–2264 (2001).
- [209] Pulkkinen, H., Papula, S., Todoshchenko, O., Talonen, J., and Hänninen, H. *Steel Research International* **84**(10), 966–974 (2013).
- [210] Schaeffler, A. L. *Metal Progress* **106**(1), 227–227 (1974).
- [211] Kim, S. J., Yun, D. W., Suh, D. W., and Kim, K. Y. *Electrochemistry Communications* **24**, 112–115 (2012).
- [212] Rozenak, R. and Bergman, R. *Materials Science and Engineering A-Structural Materials Properties Microstructure and Processing* **437**(2), 366–378 (2006).
- [213] Rozenak, P. and Eliezer, D. *Metallurgical Transactions A-Physical Metallurgy and Materials Science* **19**(3), 723–730 (1988).
- [214] Borruto, A., Palma, F., and Iavarone, M. *International Journal of Hydrogen Energy* **28**(8), 881–887 (2003).
- [215] Takai, K., Chiba, Y., Noguchi, K., and Nozue, A. *Metallurgical and Materials Transactions A-Physical Metallurgy and Materials Science* **33**(8), 2659–2665 (2002).
- [216] Michalska, J., Labanowski, J., and Cwiek, J. *Technologies and Properties of Modern Utilised Materials* **35** (2012).
- [217] Yamabe, J., Awane, T., and Murakami, Y. In *International Conference on Metals and Hydrogen, Steelyhydrogen 2018*, volume 3. OCAS, (2018).

- 
- [218] <https://www.bruker.com/products/x-ray-diffraction-and-elemental-analysis/eds-wds-ebds-sem-micro-xrf-and-sem-micro-ct/quantax-ebds/hardware/argus-fsebse-imaging-system.html>. accessed: 2019-05-03.
- [219] Holzlechner, G., Kubicek, M., Hutter, H., and Fleig, J. *Journal of Analytical Atomic Spectrometry* **28**(7), 1080–1089 (2013).
- [220] Kubicek, M., Holzlechner, G., Opitz, A. K., Larisegger, S., Hutter, H., and Fleig, J. *Applied Surface Science* **289**, 407–416 (2014).
- [221] Nickel Development Institute NiDI, (1974). *Materials for Cryogenic Service: Engineering Properties of Austenitic Stainless Steels*.
- [222] Ledbetter, H. M., Weston, W. F., and Naimon, E. R. *Journal of Applied Physics* **46**(9), 3855–3860 (1975).
- [223] Ledbetter, H. M. *Journal of Applied Physics* **52**(3), 1587–1589 (1981).
- [224] Czarkowski, P., Krawczynska, A. T., Slesinski, R., Brynk, T., Budniak, J., Lewandowska, M., and Kurzydowski, K. J. *Fusion Engineering and Design* **86**(9-11), 2517–2521 (2011).
- [225] Rasmussen, K. J. R. Report, Centre for Advanced Structural Engineering, (2001).
- [226] personal communication with Dr. T. Mente, Berlin 2019-06-04.
- [227] Wagner, M. S. *Applied Surface Science* **255**(4), 992–996 (2008).
- [228] Graham, D. J. and Castner, D. G. *Biointerphases* **7**(1), 10 (2012).
- [229] Lohninger, H. and Ofner, J. *Spectroscopy Europe* **26**(5), 5 (2014).
- [230] Bro, R. and Smilde, A. K. *Analytical Methods* **6**(9), 2812–2831 (2014).
- [231] Race, A. M. and Bunch, J. *Analytical and Bioanalytical Chemistry* **407**(8), 2047–2054 (2015).
- [232] Van de Plas, R., Yang, J., Spraggins, J., and Caprioli, R. M. *Nature Methods* **12**(4), 366–72 (2015).
- [233] Heller, D., ter Veen, R., Hagenhoff, B., and Engelhard, C. *Surface and Interface Analysis* **49**(10), 1028–1038 (2017).
- [234] Sobol, O., Holzlechner, G., Holzweber, M., Lohninger, H., Böllinghaus, T., and Unger, W. E. S. *Surface and Interface Analysis* **48**, 474–478 (2016).
- [235] Salmi, S., Rhode, M., Juttner, S., and Zinke, M. *Welding in the World* **59**(1), 137–144 (2015).

- 
- [236] San Marchi, C., Somerday, B. P., Zelinski, J., Tang, X., and Schiroky, G. H. *Metallurgical and Materials Transactions A-Physical Metallurgy and Materials Science* **38a**(11), 2763–2775 (2007).
- [237] Polyanskiy, V., Alekseeva, E., Belyaev, A., Polyanskiy, A., Tretyakov, D. A., and Yakovlev, Y. A. *Continuum Mechanics and Thermodynamics* (2019).
- [238] Latanision, R. M. and Oppenhauser, H. *Metallurgical Transactions* **5**, 483–492 (1974).
- [239] Robinson, S. L., Moody, N. R., Myers, S. M., Farmer, J. C., and Greulich, F. A. *Journal of the Electrochemical Society* **134**(8B), C424–C424 (1987).
- [240] Szummer, A., Jezierska, E., and Lublinska, K. *Journal of Alloys and Compounds* **293**, 356–360 (1999).
- [241] Ichitani, K. and Kanno, M. *Science and Technology of Advanced Materials* **4**(6), 545–551 (2003).
- [242] Lee, S. J., Ronevich, J. A., Krauss, G., and Matlock, D. K. *ISIJ International* **50**(2), 294–301 (2010).
- [243] Minkovitz, E. and Eliezer, D. *Journal of Materials Science Letters* **1**(5), 192–194 (1982).
- [244] Robinson, S. L., Moody, N. R., Myers, S. M., Farmer, J. C., and Greulich, F. A. *Journal of the Electrochemical Society* **137**(5), 1391–1397 (1990).
- [245] Michalska, J. *The effect of Hydrogen on Pitting Corrosion of Superaustenitic and Austenitic-Ferritic Stainless Steels*, volume 326-328 of *Defect and Diffusion Forum*, 620–625. Trans Tech Publications Ltd, Zürich (2012).
- [246] Griesche, A., Dabah, E., and Kannengiesser, T. *Canadian Metallurgical Quarterly* **54**(1), 38–42 (2015).
- [247] Hwang, B., Lee, T. H., and Kim, S. J. *Procedia Engineering* **10**, 409–414 (2011).
- [248] Gey, N., Petit, P., and Humpert, M. *Metallurgical and Materials Transactions A* **36A**, 3291–3299 (2005).
- [249] Krüger, L., Wolf, S., Martin, S., Martin, U., Jahn, A., Weiß, A., and Scheller, P. R. *steel research international* **82**(9), 1087–1093 (2011).
- [250] Virkkunen, I. *Thermal Fatigue of Austenitic and Duplex Stainless Steels*. Thesis, Helsinki University of Technology, (2001).
- [251] Bullough, R. and Bilby, B. A. *Proceedings of the Physical Society of London Section B* **69**(12), 1276–1286 (1956).
- [252] Turnbull, A. *International Journal of Hydrogen Energy* **40**(47), 16961–16970 (2015).

- 
- [253] Silverstein, R. *The Influence of Hydrogen on the Microstructure and Dynamic Strength of Duplex Stainless Steels*. Thesis, Ben-Gurion University of the Negev, (2015).
- [254] Pérez Escobar, D., Miñambres, C., Duprez, L., Verbeken, K., and Verhaege, M. *Corrosion Science* **53**(10), 3166–3176 (2011).
- [255] Hänninen, H., Tähtinen, S., and Kivilahti, J. In *3rd International Congress on Hydrogen and Materials*, 185–190, (1982).
- [256] Dabah, E., Kannengiesser, T., Eliezer, D., and Böllinghaus, T. *Materials Science and Engineering A-Structural Materials Properties Microstructure and Processing* **528**(3), 1608–1614 (2011).
- [257] Hänninen, H. and Hakkarainen, T. *Metallurgical and Materials Transactions A* **10A** (1979).
- [258] Mathias, H., Nadiv, S., and Katz, Y. *Metal Science* **3**, 129–137 (1978).
- [259] Mathias, H., Katz, Y., and Nadiv, S. In *Advances in Fracture Research*, 2743–2751. Pergamon, (1982).
- [260] Miyazaki, M., Isobe, K., and Murao, T. Technical report, Nippon Steel, (2013).
- [261] Weidner, A., Glage, A., Martin, S., Man, J., Klemm, V., Martin, U., Polák, J., Rafaja, D., and Biermann, H. *International Journal of Materials Research* **102**(11), 1374–1377 (2011).
- [262] Weidner, A., Martin, S., Klemm, V., Martin, U., and Biermann, H. *Scripta Materialia* **64**(6), 513–516 (2011).
- [263] Claeys, L., Depover, T., De Graeve, I., and Verbeken, K. *Materials Characterization* **156** (2019).
- [264] Tian, Y., Gorbato, O., Borgenstam, A., Ruban, A., and Hedström, P. *Metallurgical and Materials Transactions A* **48A** 10 (2016).
- [265] Masoumi, M., Silva, C. C., Beres, M., Ladino, D. H., and de Abreu, H. F. G. *International Journal of Hydrogen Energy* **42**(2), 1318–1326 (2017).
- [266] Fu, J. W. and Yang, Y. S. *Journal of Alloys and Compounds* **580**, 191–194 (2013).
- [267] Cao, Y., Li, H. L., Szpunar, J. A., and Shmayda, W. T. *Materials Science Forum* **408-412**, 1139–1144 (2002).
- [268] Tähtinen, S., Kivilahti, J., and Hänninen, H. In *3rd International Congress on Hydrogen and Materials*, 185–190, (1982).
- [269] Mathias, H., Katz, Y., and Nadiv, S. In *Metal-Hydrogen Systems*, VEZIROĞLU, N., editor, 225–249. Pergamon (1982).



- 
- [270] Izawa, C., Wagner, S., Martin, M., Weber, S., Pargeter, R., Michler, T., Uchida, H. H., and Pundt, A. *Journal of Alloys and Compounds* **580**, S13–S17 (2013).
- [271] Ooi, S. W., Yan, P., and Vegter, R. H. *Materials Science and Technology* **35**(1), 12–25 (2019).
- [272] Dabah, E., Lisitsyn, V., and Eliezer, D. *Materials Science and Engineering A-Structural Materials Properties Microstructure and Processing* **527**(18-19), 4851–4857 (2010).
- [273] Bechtle, S., Kumar, M., Somerday, B. P., Launey, M. E., and Ritchie, R. O. *Acta Materialia* **57**(14), 4148–4157 (2009).
- [274] Oudriss, A., Creus, J., Bouhattate, J., Conforto, E., Berziou, C., Savall, C., and Feaugas, X. *Acta Materialia* **60**(19), 6814–6828 (2012).
- [275] Zamanzade, M., Müller, C., Velayarce, J. R., and Motz, C. *International Journal of Hydrogen Energy* **44**(14), 7706–7714 (2019).
- [276] Gavriljuk, V. and Teus, S. *Metallofizika i Noveishie Tekhnologii* **39**, 457–464 (2017).
- [277] Kulkova, S., Kulkov, S. S., Bakulin, A., Hocker, S., and Schmauder, S. *International Journal of Hydrogen Energy* **37**, 6666–6673 (2012).
- [278] Morsdorf, L., Jeannin, O., Barbier, D., Mitsuhashi, M., Raabe, D., and Tazan, C. C. *Acta Materialia* **121**, 202–214 (2016).
- [279] Pressouyre, G. M. *Metallurgical Transactions A-Physical Metallurgy and Materials Science* **10**(10), 1571–1573 (1979).
- [280] Kumnick, A. J. and Johnson, H. H. *Acta Metallurgica* **28**(1), 33–39 (1980).
- [281] Béréš, M., Wu, L., Santos, L. P. M., Masoumi, M., da Rocha Filho, F. A. M., da Silva, C. C., de Abreu, H. F. G., and Gomes da Silva, M. J. *International Journal of Hydrogen Energy* **42**(21), 14786–14793 (2017).
- [282] Tian, Y., Borgenstam, A., and Hedström, P. *Journal of Alloys and Compounds* **766**, 131–139 (2018).
- [283] Tian, Y. *Martensitic Transformation in Stainless Steels*. Thesis, KTH Royal Institute of Technology, (2018).
- [284] Hua, Z. L., An, B., Iijima, T., Gu, C. H., and Zheng, J. Y. *Scripta Materialia* **131**, 47–50 (2017).
- [285] Enomoto, M., Cheng, L., Mizuno, H., Watanabe, Y., Omura, T., Sakai, J., Yokoyama, K., Suzuki, H., and Okuma, R. *Metallurgical and Materials Transactions E* **1**(4), 331–340 (2014).

- 
- [286] Hatano, M., Fujinami, M., Arai, K., Fujii, H., and Nagumo, M. *Acta Materialia* **67**, 342–353 (2014).
- [287] Kim, J. S., Lee, Y. H., Lee, D. L., Park, K. T., and Lee, C. S. *Materials Science and Engineering A-Structural Materials Properties Microstructure and Processing* **505**(1-2), 105–110 (2009).
- [288] Röhslér, A., Sobol, O., Unger, W. E. S., and Böllinghaus, T. *International Journal of Hydrogen Energy* **44**, 12228–12238 (2019).
- [289] Pu, S., Turk, A., Lenka, S., and Ooi, S. *Scripta Materialia* **170**, 38–42 (2019).
- [290] Koyama, M., Bashir, A., Rohwerder, M., Merzlikin, S. V., Akiyama, E., Tsuzaki, K., and Raabe, D. *Journal of the Electrochemical Society* **162**(12), C638–C647 (2015).
- [291] Varmuza, K. and Filzmoser, P. *Technometrics* **52**, 468–469 (2010).
- [292] Lufitano, J. and Sofronis, P. *Acta Materialia* **46**(5), 1519–1526 (1998).
- [293] Yokobori, A. T., Nemoto, T., Satoh, K., and Yamada, T. *Engineering Fracture Mechanics* **55**(1), 47–60 (1996).
- [294] Yokobori, A. T., Chinda, Y., Nemoto, T., Satoh, K., and Yamada, T. *Corrosion Science* **44**(3), 407–424 (2002).
- [295] Fahr, D. *Metallurgical Transactions* **2**, 1883–1892 (1971).
- [296] Olson, G. B. and Cohen, M. *Journal of the Less Common Metals* **28**(1), 107–118 (1972).
- [297] Wang, Z. and Beese, A. M. *Acta Materialia* **131**, 410–422 (2017).
- [298] Chen, X., Zhou, C., Zheng, J., and Zhang, L. *International Journal of Hydrogen Energy* **43**(6), 3342–3352 (2018).
- [299] Hajilou, T., Deng, Y., Rogne, B. R., Kheradmand, N., and Barnoush, A. *Scripta Materialia* **132**, 17–21 (2017).
- [300] Luo, H., Li, Z. M., Chen, Y. H., Ponge, D., Rohwerder, M., and Raabe, D. *Electrochemistry Communications* **79**, 28–32 (2017).
- [301] Rhode, M., Schaupp, T., Münster, C., Mente, T., Böllinghaus, T., and Kannengiesser, T. *Welding in the World* **63**(2), 511–526 (2018).
- [302] Koyama, M., Springer, H., Merzlikin, S. V., Tsuzaki, K., Akiyama, E., and Raabe, D. *International Journal of Hydrogen Energy* **39**(9), 4634–4646 (2014).
- [303] Evers, S., Senoz, C., and Rohwerder, M. *Science and Technology of Advanced Materials* **14**(1) (2013).

- [304] Mente, T. and Böllinghaus, T. *Welding in the World* **56**(11-12), 66–78 (2012).
- [305] Lufrano, J., Sofronis, P., and Birnbaum, H. K. *Journal of the Mechanics and Physics of Solids* **44**(2), 179–205 (1996).
- [306] Dadfarnia, M., Martin, M. L., Nagao, A., Sofronis, P., and Robertson, I. M. *Journal of the Mechanics and Physics of Solids* **78**, 511–525 (2015).
- [307] Ahn, D. C., Sofronis, P., and Dodds, R. *International Journal of Fracture* **145**(2), 135–157 (2007).
- [308] Yazdipour, N., Dunne, D., and Pereloma, E. *Effect of Grain Size on the Hydrogen Diffusion Process in Steel Using Cellular Automaton Approach*, volume 706-709 of *Materials Science Forum*, 1568–1573. Trans Tech Publications Ltd, Stafa-Zurich (2012).
- [309] Mente, T. and Böllinghaus, T. *Welding in the World* **58**(2), 205–216 (2014).
- [310] Liang, Y., Ahn, D. C., Sofronis, P., Dodds, R. H., and Bammann, D. *Mechanics of Materials* **40**(3), 115–132 (2008).

## A. Appendix

### A.1. Results of the sputter tests

#### AISI 304L

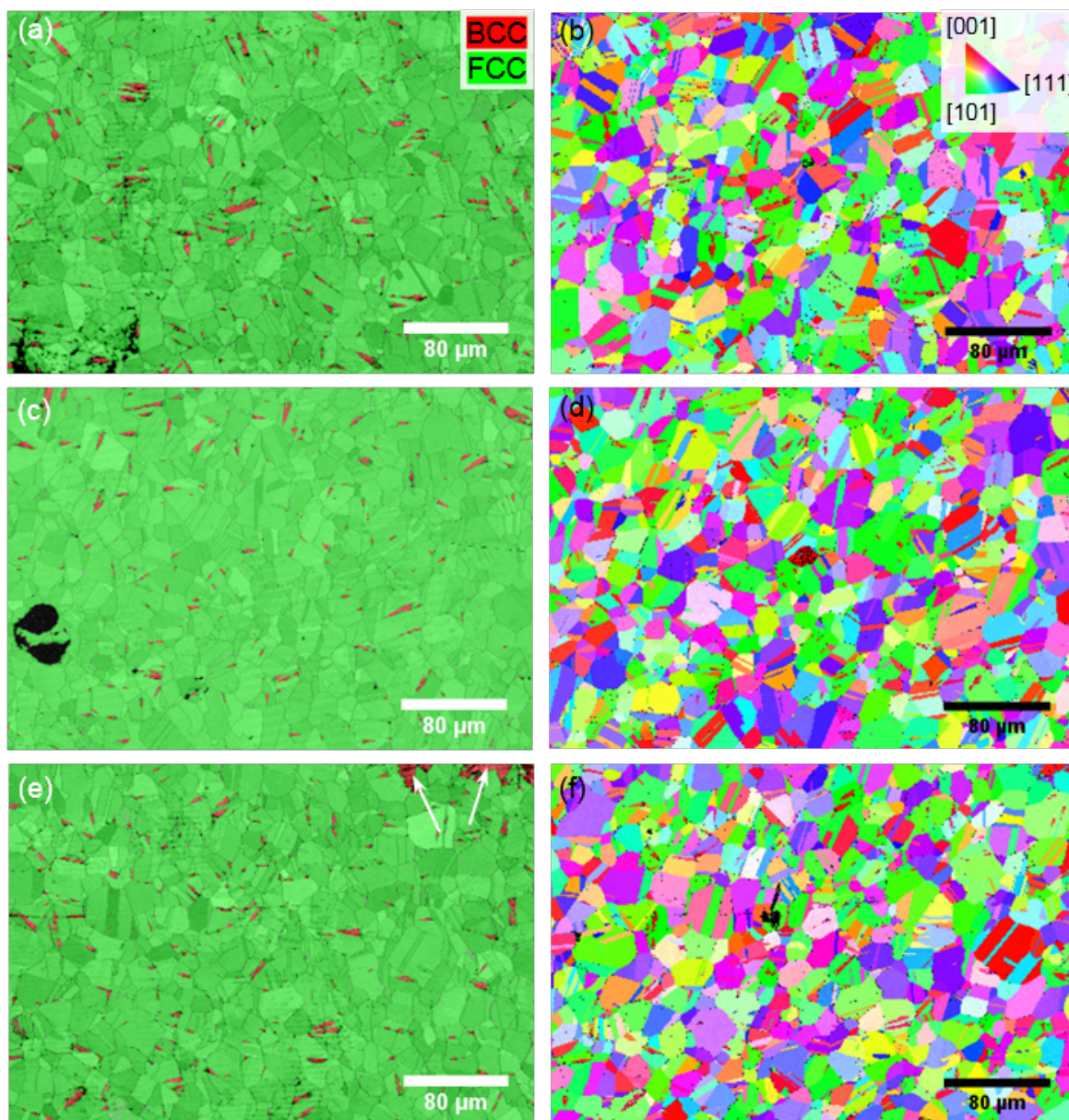


Figure A.1: Phase and pattern quality maps of AISI 304L after sputtering with 3 keV  $\text{Cs}^+$  at  $-80^\circ\text{C}$  for (a) 10 s, (c) 30 s and (e) 60 s and the corresponding inverse pole figures in z-direction (IPF-Z) in (b), (d) and (f), respectively. Every ROI was sputtered only once in order to not accumulate the impact of the  $\text{Cs}^+$ -beam. The white arrows in (e) indicate sputter damages deliberately induced for navigation.



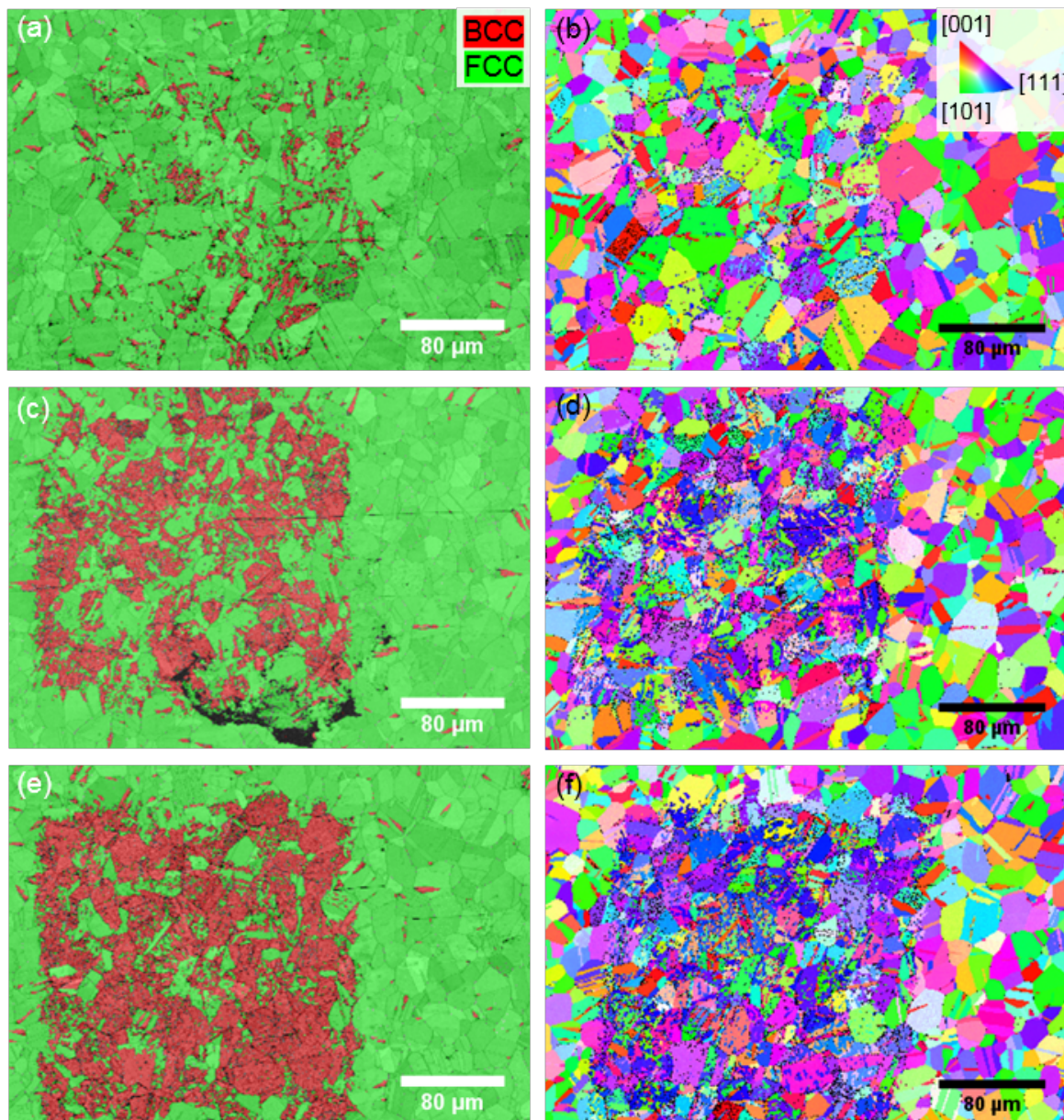


Figure A.2: Phase and pattern quality maps of AISI 304L after sputtering with 3 keV  $\text{Cs}^+$  at  $-80^\circ\text{C}$  for (a) 120 s, (c) 210 s and (e) 300 s and the corresponding inverse pole figures in z-direction (IPF-Z) in (b), (d) and (f), respectively. Every ROI was sputtered only once in order to not accumulate the impact of the  $\text{Cs}^+$ -beam.



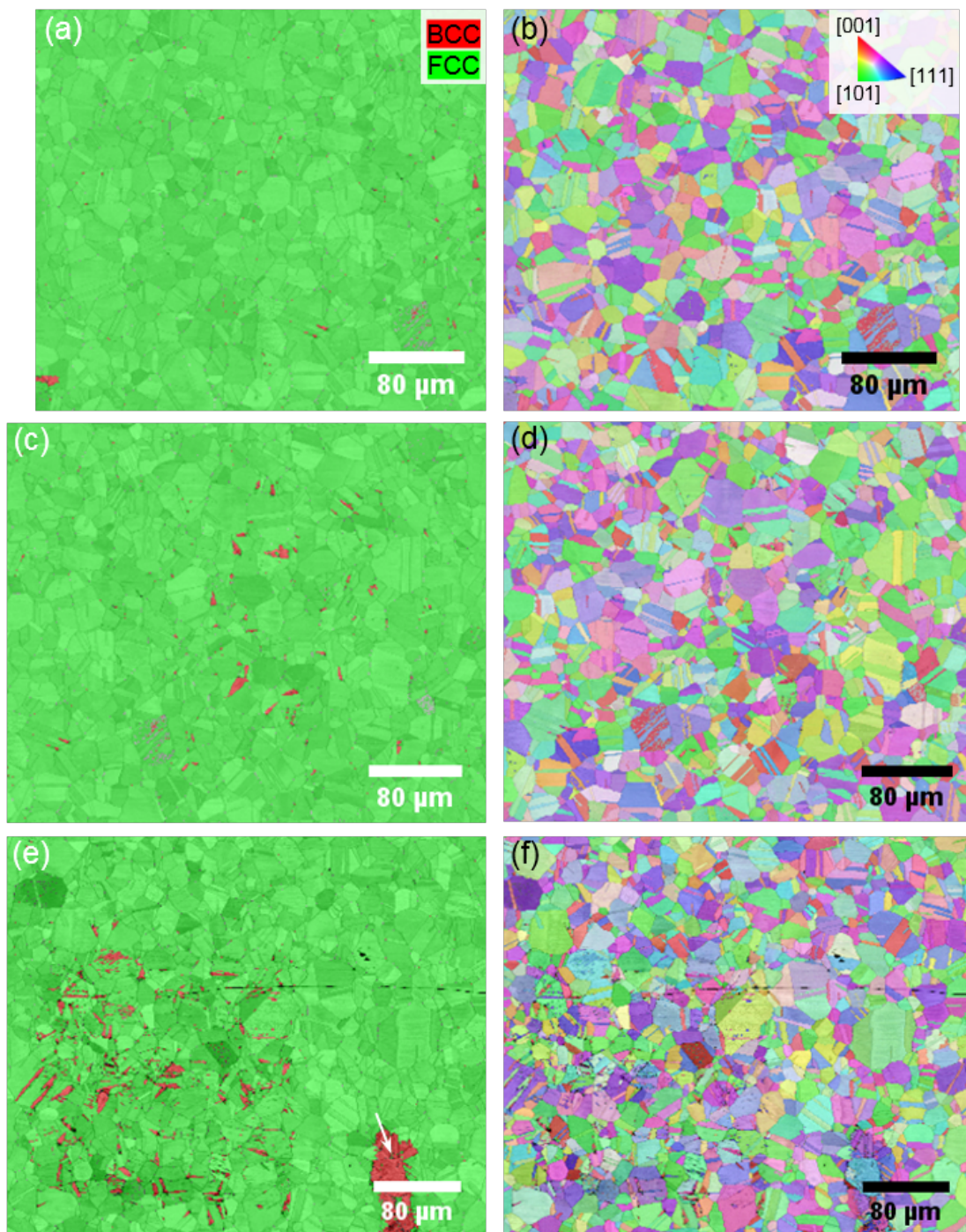


Figure A.3: Phase and pattern quality maps of AISI 304L after sputtering with 3 keV  $\text{Cs}^+$  at 20°C for (a) 10 s, (c) 30 s and (e) 60 s and the corresponding inverse pole figures in z-direction (IPF-Z) in (b), (d) and (f), respectively. Every ROI was sputtered only once in order to not accumulate the impact of the  $\text{Cs}^+$ -beam. The arrow in (e) indicates a sputter damage deliberately induced for navigation.



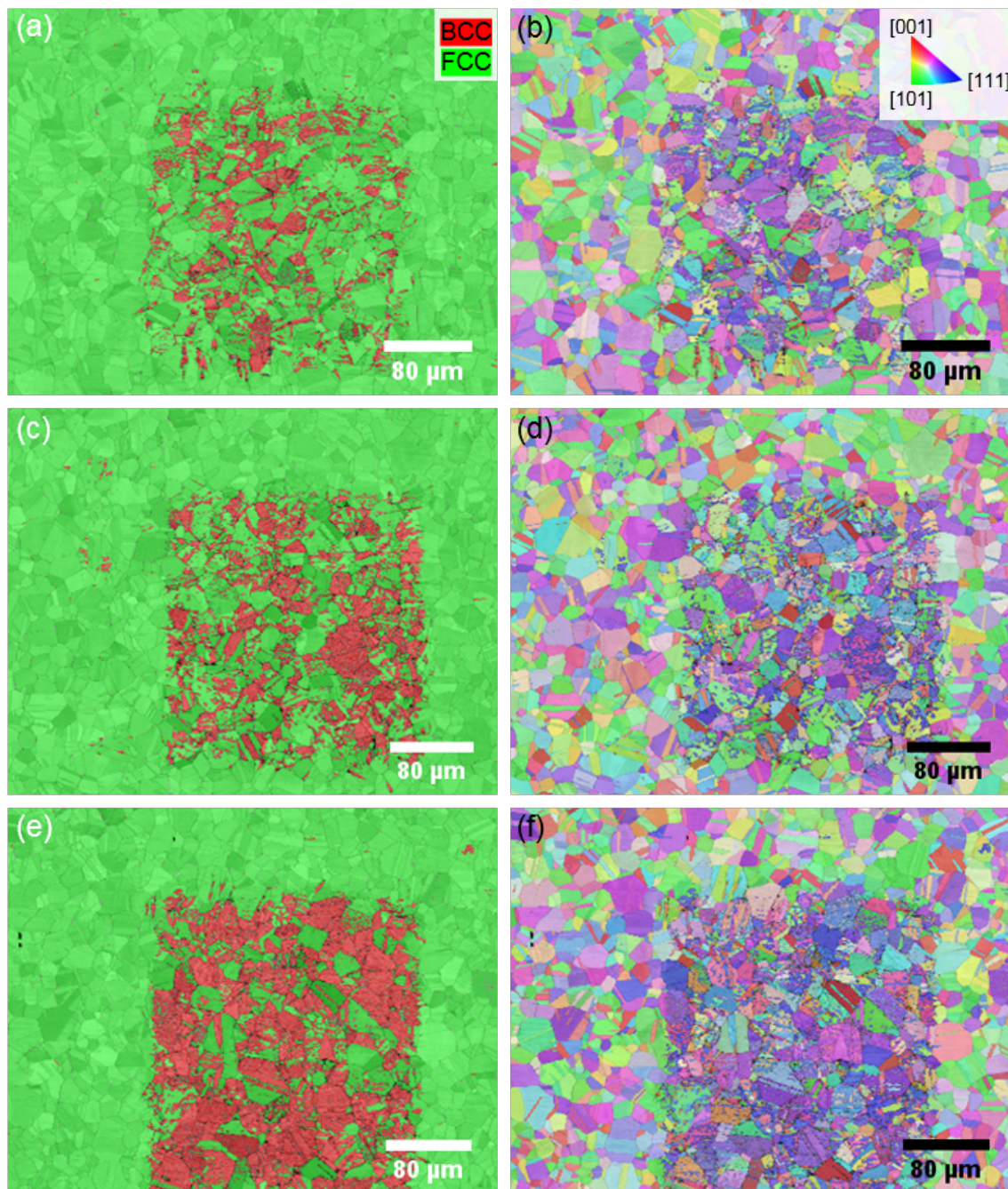


Figure A.4: Phase and pattern quality maps of AISI304L after sputtering with 3 keV  $\text{Cs}^+$  at 20°C for (a) 120 s, (c) 210 s and (e) 300 s and the corresponding inverse pole figures in z-direction (IPF-Z) in (b), (d) and (f), respectively. Every ROI was sputtered only once in order to not accumulate the impact of the  $\text{Cs}^+$ -beam.



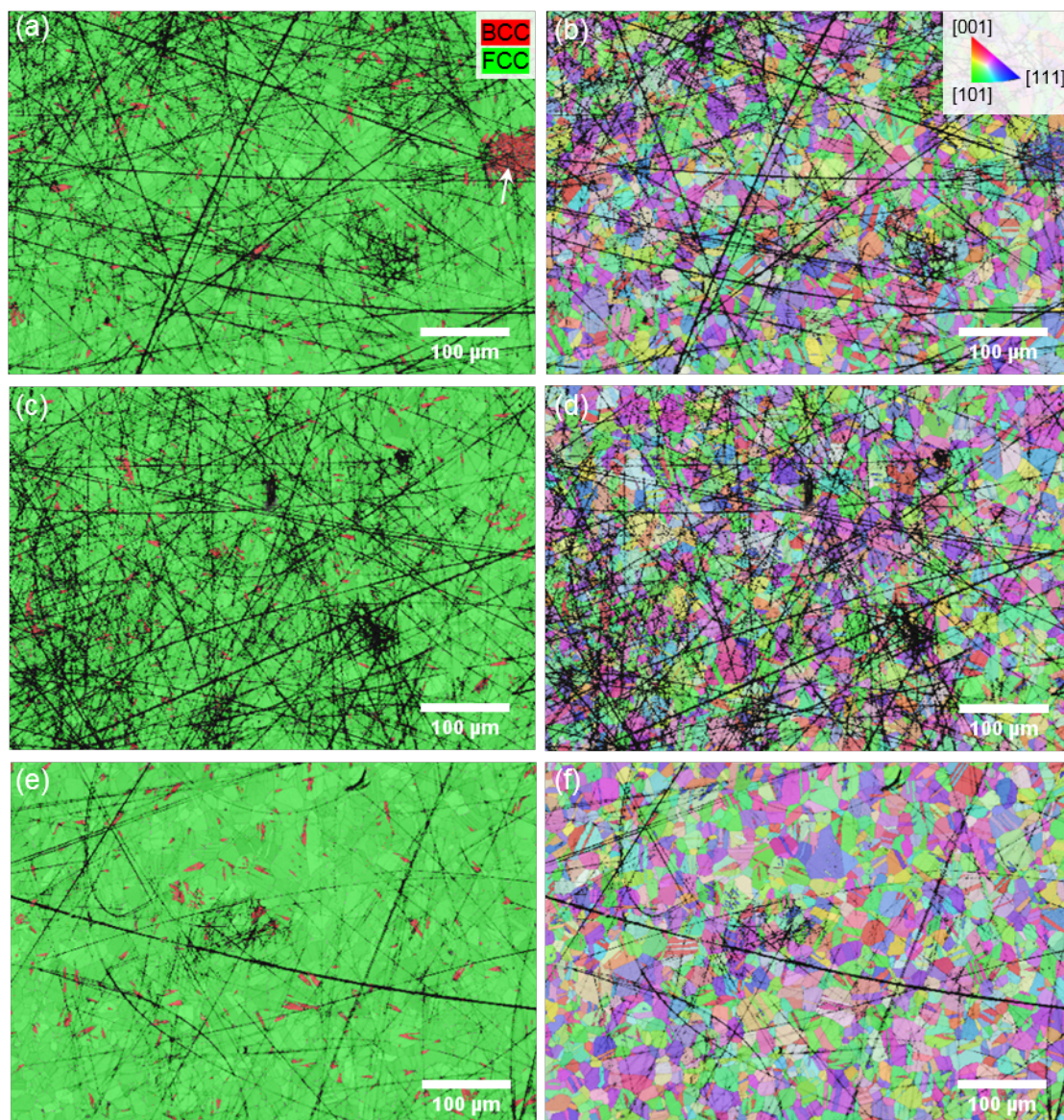


Figure A.5: Phase and pattern quality maps of AISI 304L after sputtering with  $1 \text{ keV Cs}^+$  at  $-80^\circ\text{C}$  for (a) 10 s, (c) 30 s and (e) 60 s and the corresponding inverse pole figures in  $z$ -direction (IPF-Z) in (b), (d) and (f), respectively. Every ROI was sputtered only once in order to not accumulate the impact of the  $\text{Cs}^+$ -beam. The white arrow in (a) indicates a sputter damage deliberately induced for navigation.



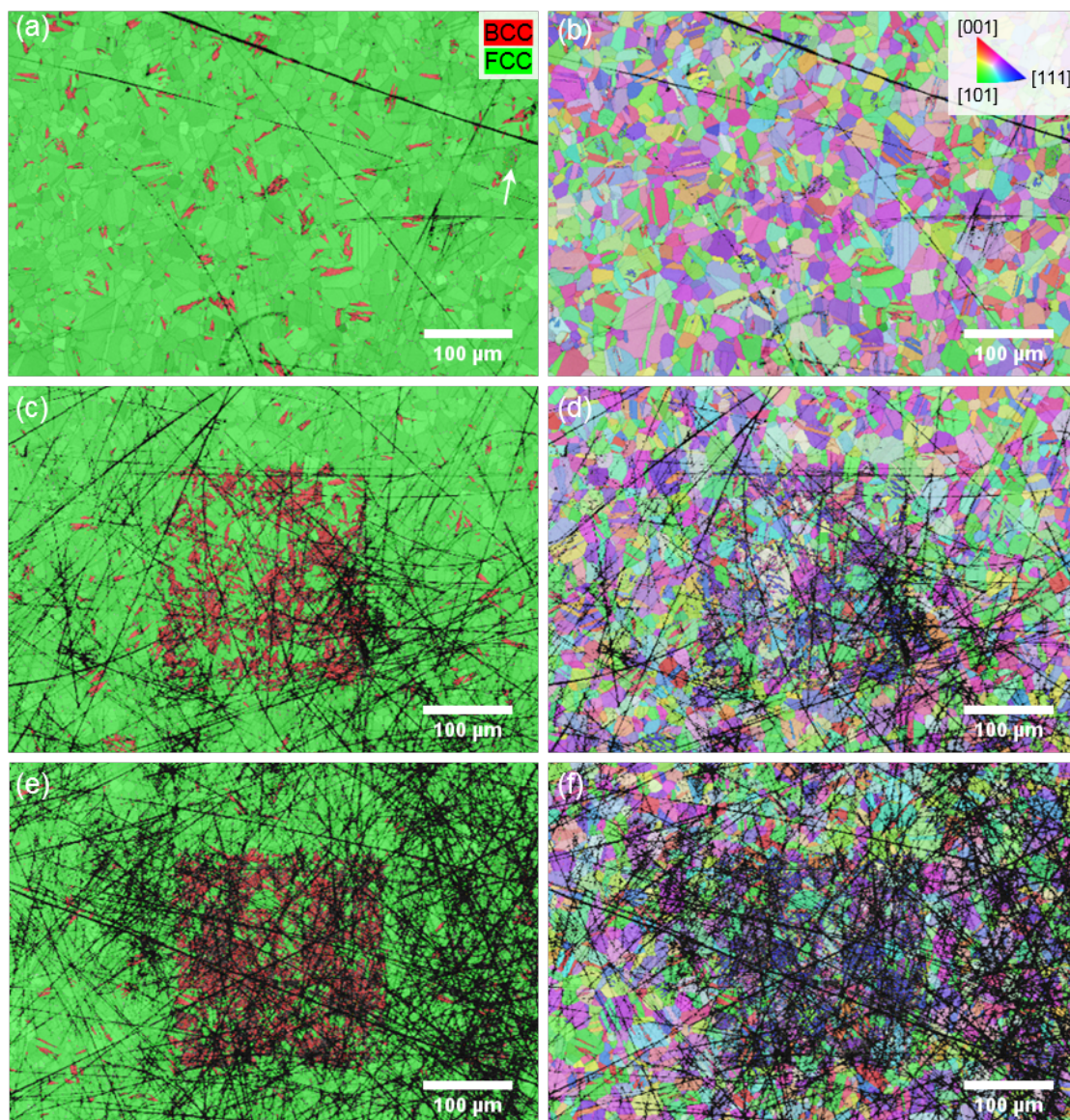


Figure A.6: Phase and pattern quality maps of AISI 304L after sputtering with  $1 \text{ keV Cs}^+$  at  $-80^\circ\text{C}$  for (a) 120 s, (c) 210 s and (e) 300 s and the corresponding inverse pole figures in z-direction (IPF-Z) in (b), (d) and (f), respectively. Every ROI was sputtered only once in order to not accumulate the impact of the  $\text{Cs}^+$ -beam.



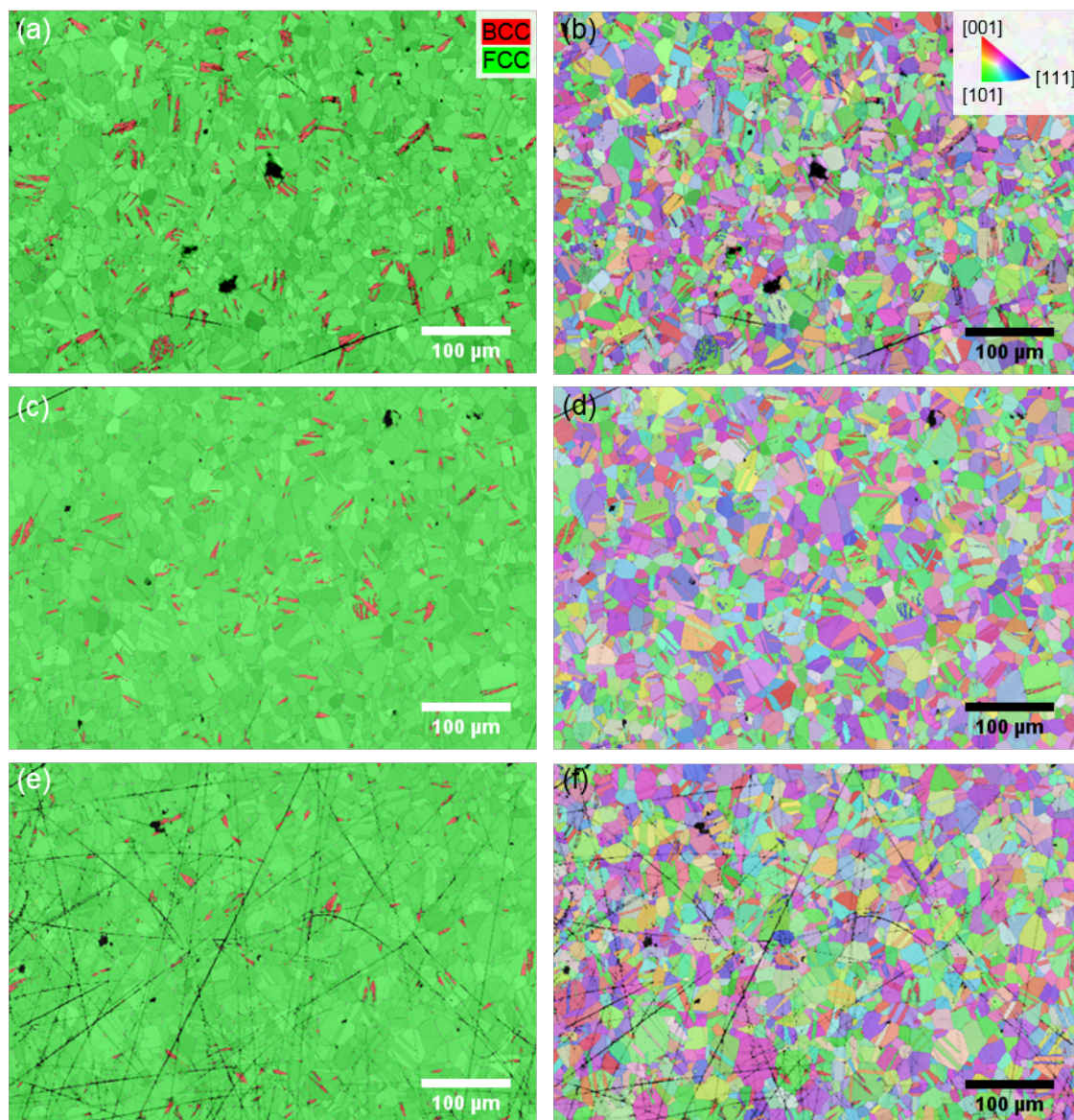


Figure A.7: Phase and pattern quality maps of AISI 304L after sputtering with  $1 \text{ keV Cs}^+$  at  $20^\circ\text{C}$  for (a) 10 s, (c) 30 s and (e) 60 s and the corresponding inverse pole figures in  $z$ -direction (IPF-Z) in (b), (d) and (f), respectively. Every ROI was sputtered only once in order to not accumulate the impact of the  $\text{Cs}^+$ -beam.



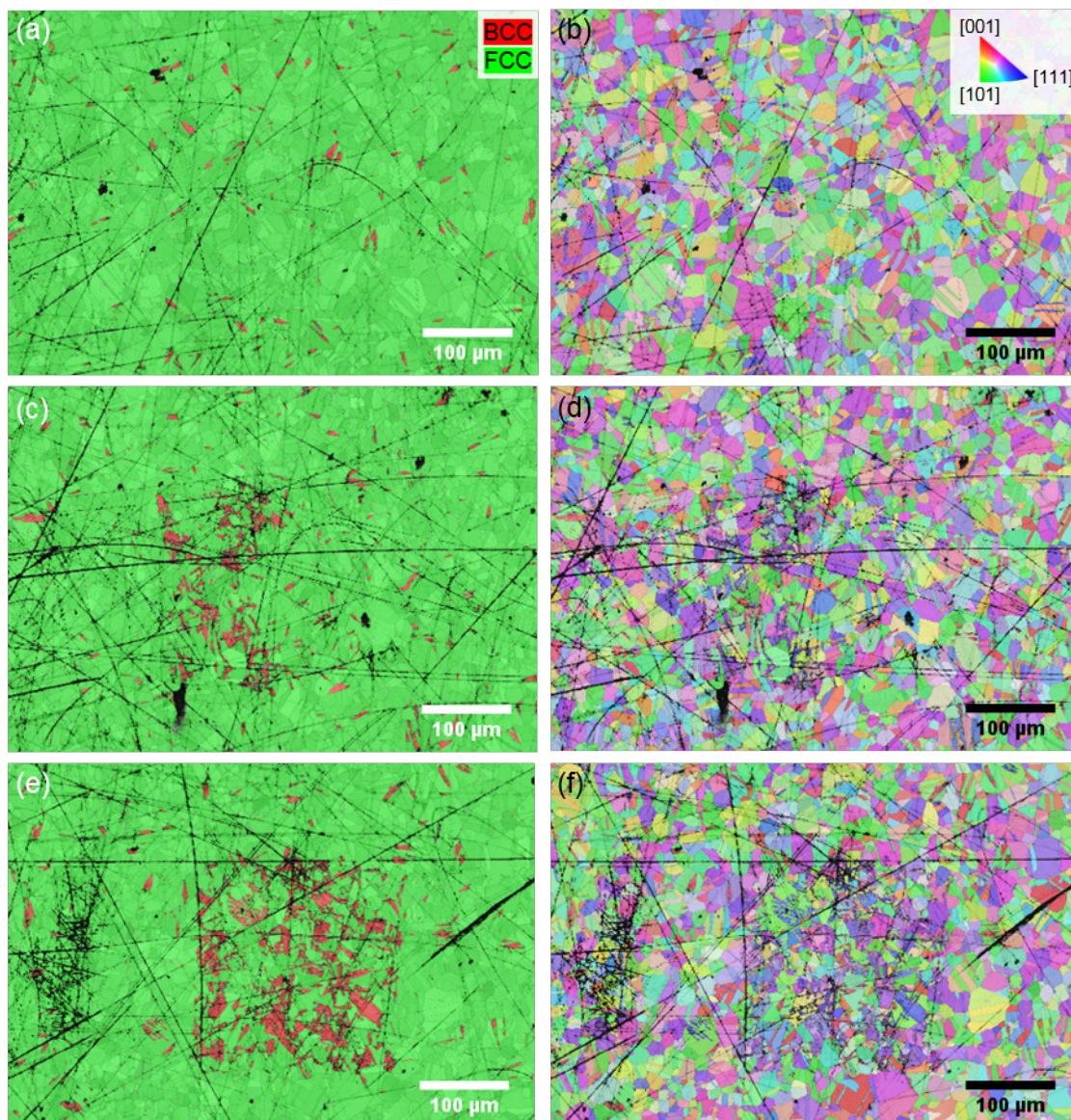


Figure A.8: *Phase and pattern quality maps of AISI304L after sputtering with 1 keV  $\text{Cs}^+$  at 20°C for (a) 120 s, (c) 210 s and (e) 300 s and the corresponding inverse pole figures in z-direction (IPF-Z) in (b), (d) and (f), respectively. Every ROI was sputtered only once in order to not accumulate the impact of the  $\text{Cs}^+$ -beam.*



## AISI 316L

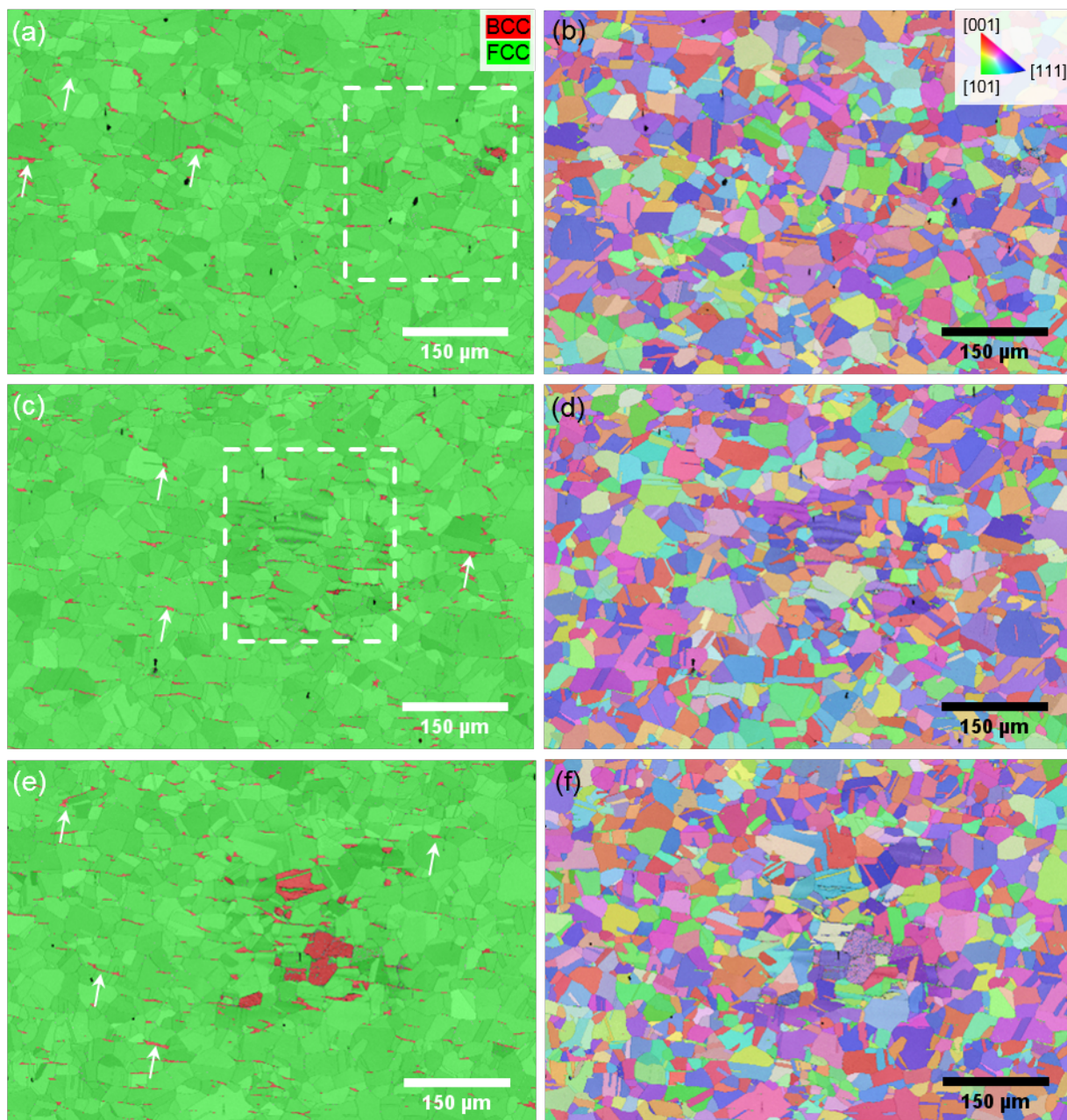


Figure A.9: Phase and pattern quality maps of AISI 316L after sputtering with  $3 \text{ keV Cs}^+$  at  $-80^\circ\text{C}$  for (a) 10 s, (c) 30 s and (e) 60 s and the corresponding inverse pole figures in  $z$ -direction (IPF-Z) in (b), (d) and (f), respectively. Every ROI was sputtered only once in order to not accumulate the impact of the  $\text{Cs}^+$ -beam. White arrows mark some of the centre line segregations that developed during solidification after the continuous casting process.



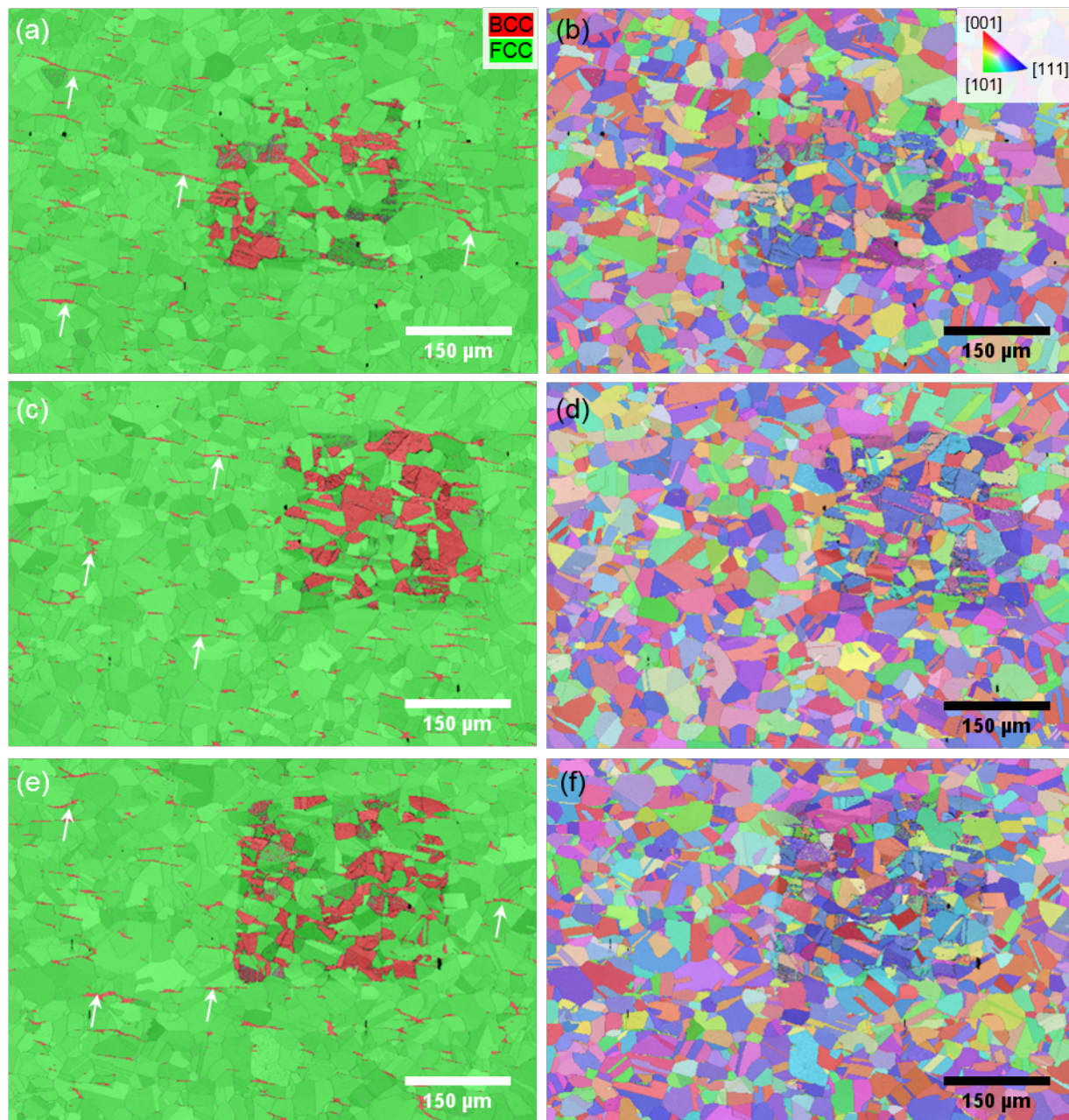


Figure A.10: Phase and pattern quality maps of AISI 316L after sputtering with 3 keV  $\text{Cs}^+$  at  $-80^\circ\text{C}$  for (a) 120 s, (c) 210 s and (e) 300 s and the corresponding inverse pole figures in z-direction (IPF-Z) in (b), (d) and (f), respectively. Every ROI was sputtered only once in order to not accumulate the impact of the  $\text{Cs}^+$ -beam. White arrows mark some of the centre line segregations that developed during solidification after the continuous casting process.



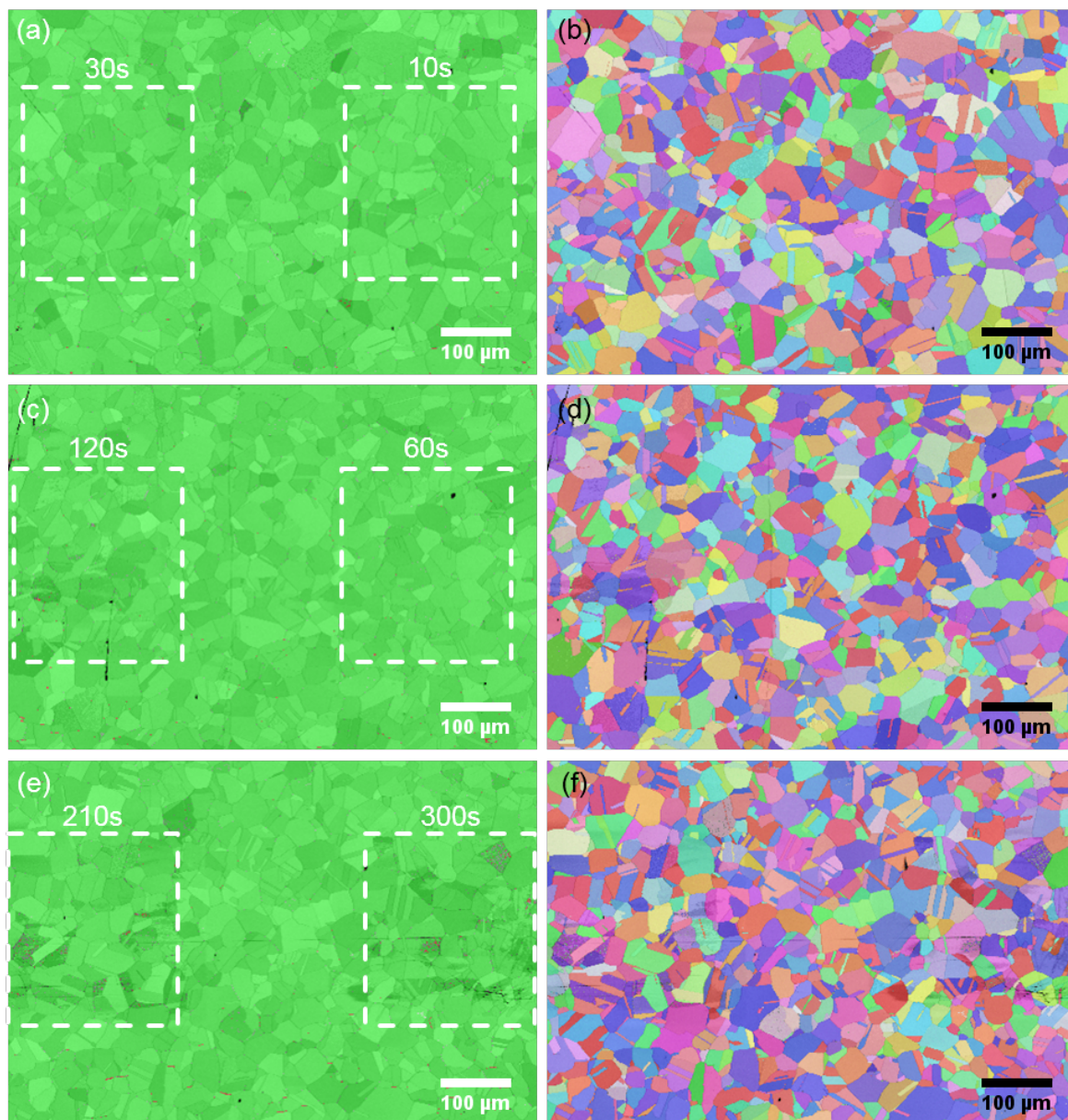


Figure A.11: Phase and pattern quality maps of AISI 316L after sputtering with  $3 \text{ keV Cs}^+$  at  $20^\circ\text{C}$  for (a) 10 and 30 s, (c) 60 and 120 s and (e) 210 and 300 s and the corresponding inverse pole figures in  $z$ -direction (IPF-Z) in (b), (d) and (f), respectively. Every ROI was sputtered only once in order to not accumulate the impact of the  $\text{Cs}^+$ -beam. The dotted frames indicate the sputtered regions.

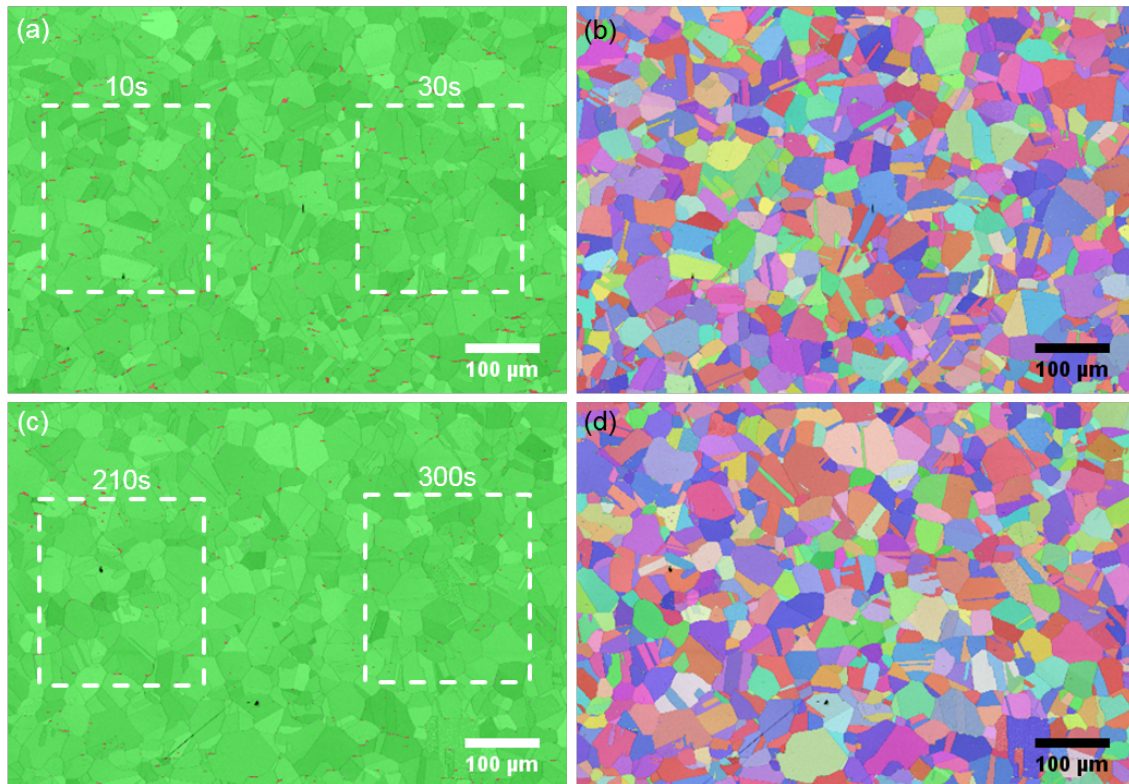


Figure A.12: Phase and pattern quality maps of AISI 316L after sputtering with  $1 \text{ keV Cs}^+$  at  $20^\circ\text{C}$  for (a) 10 and 30 s, (c) 210 and 300 s and the corresponding inverse pole figures in z-direction (IPF-Z) in (b) and (d), respectively. Every ROI was sputtered only once in order to not accumulate the impact of the  $\text{Cs}^+$ -beam. The dotted frames indicate the sputtered regions.



## A.2. SEM micrographs

AISI 304L

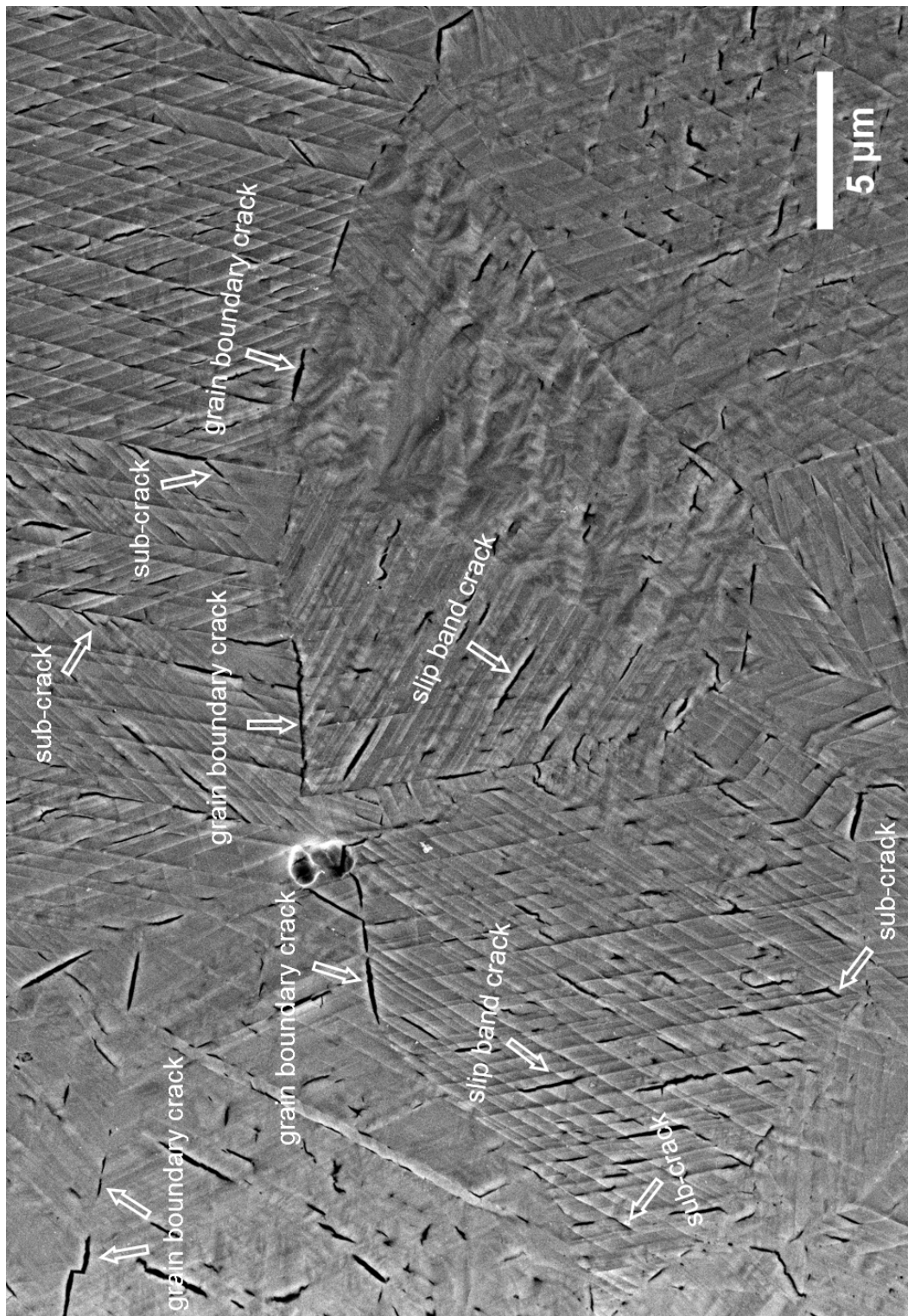


Figure A.13: SEM micrographs of alloy grade 304L after electrochemical charging for 72h. Some prominent features are highlighted.

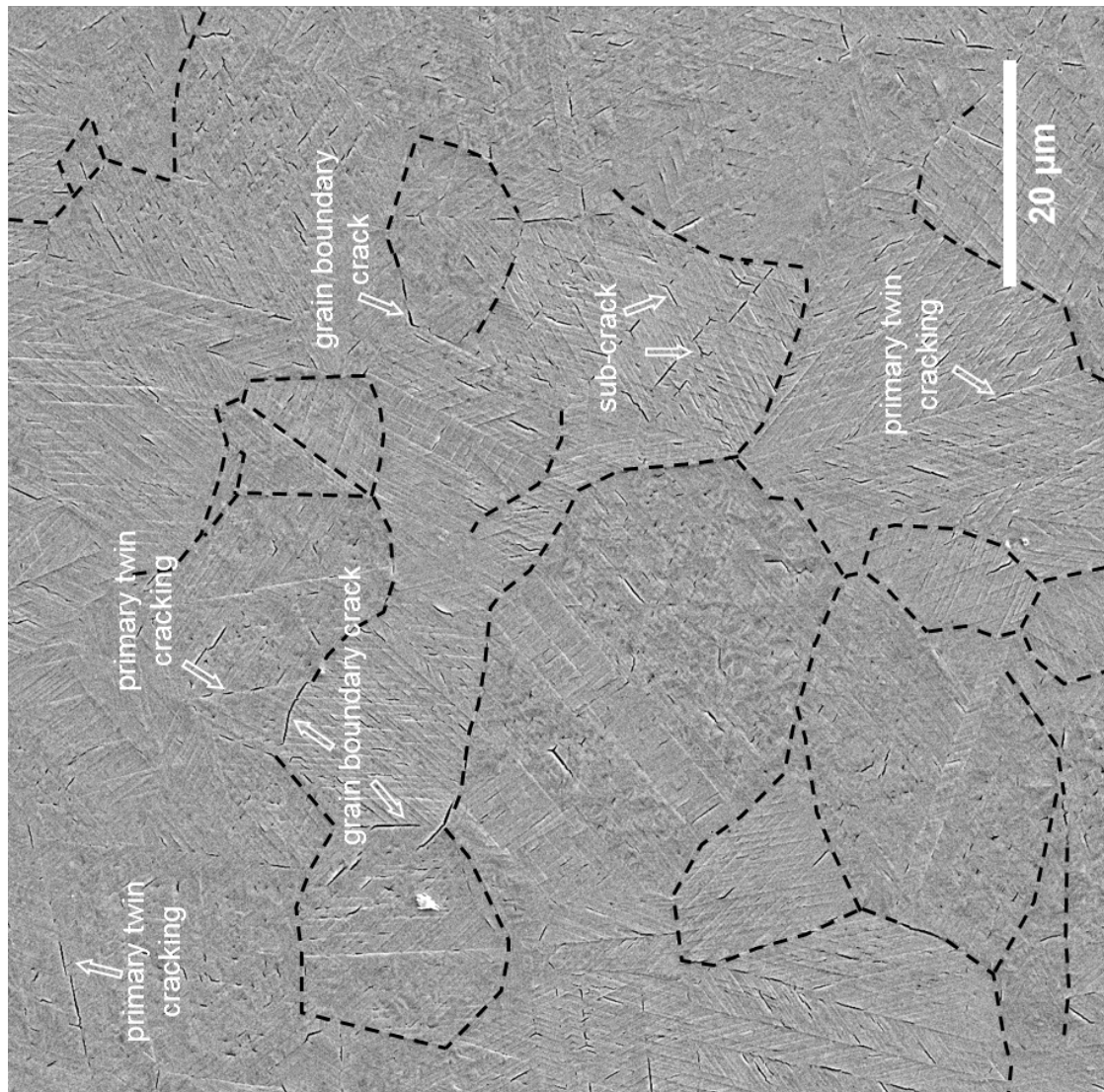


Figure A.14: SEM micrographs of alloy grade 304L after electrochemical charging for 72h. Some prominent features are labelled. The dashed black line indicates grain and twin boundaries.



## AISI 316L

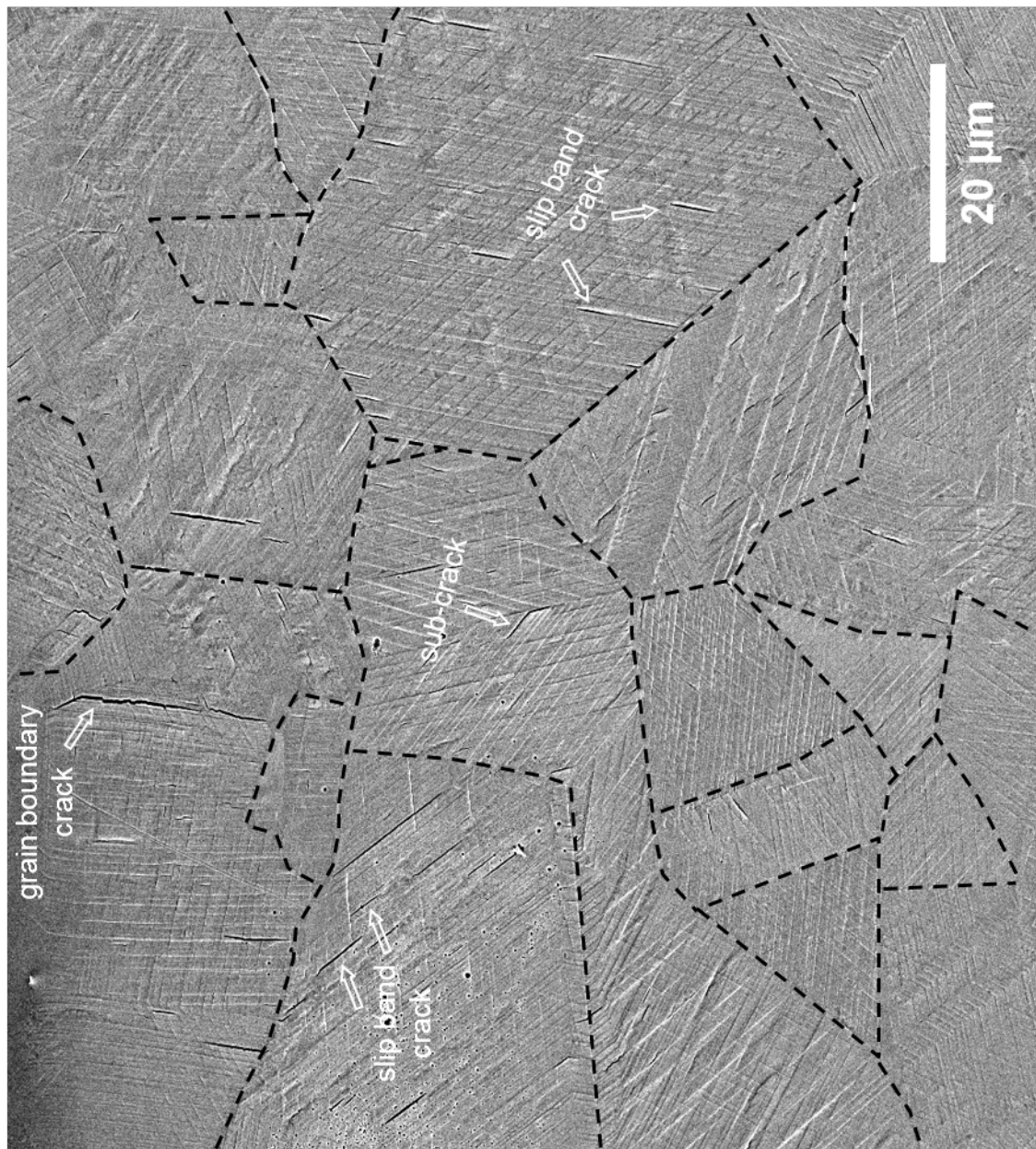


Figure A.15: SEM micrographs of alloy grade 316L after electrochemical charging for 24 h. Some prominent features are labelled. The dashed black line indicates grain and twin boundaries.

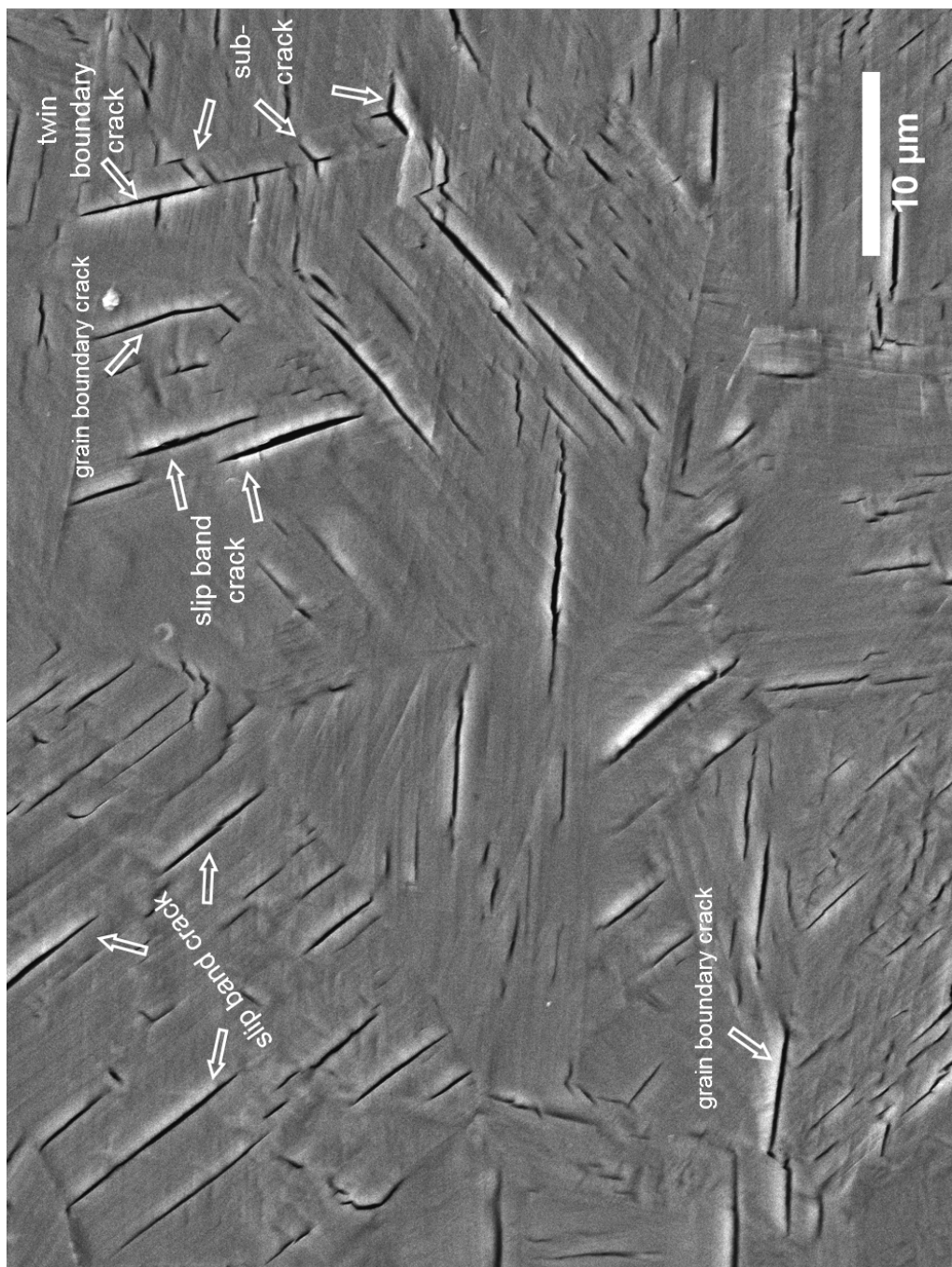


Figure A.16: SEM micrographs of alloy grade 316L after electrochemical charging for 120 h. Some prominent features are highlighted.

## A.3. EBSD results

## AISI 304L

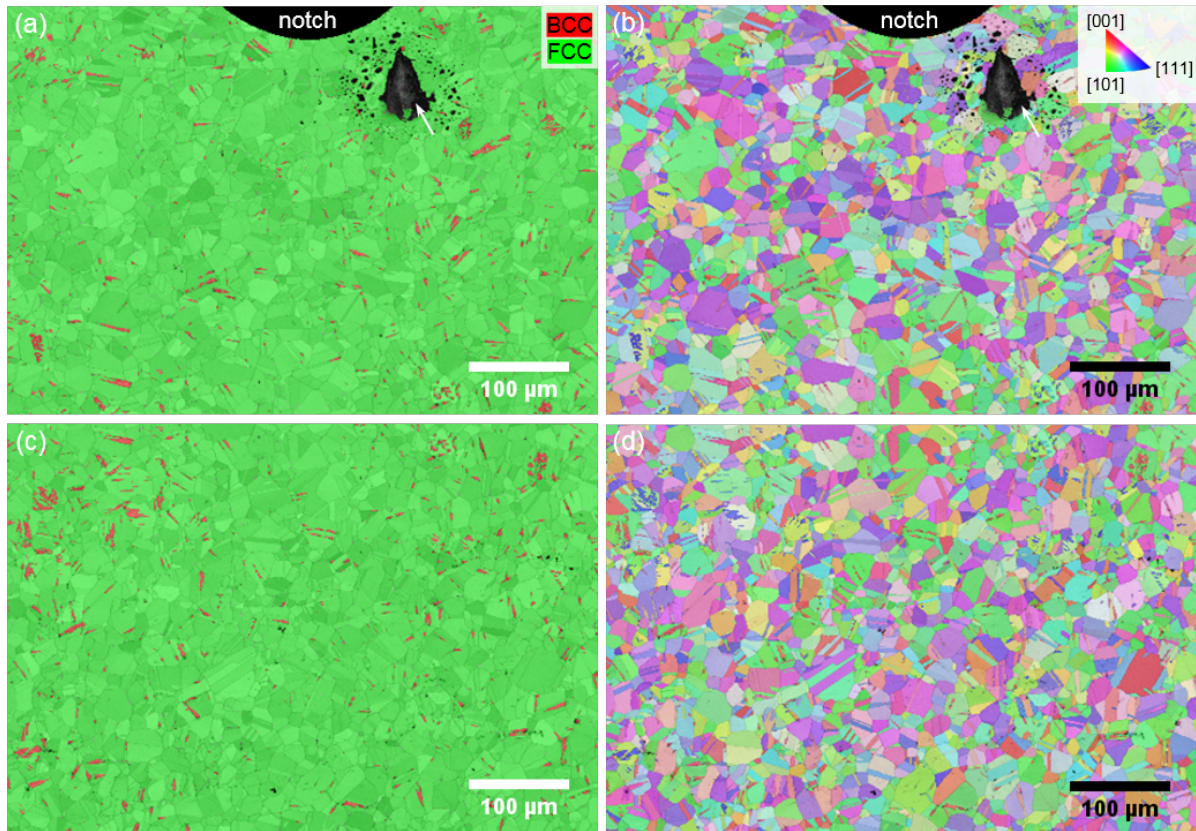


Figure A.17: Phase and pattern quality maps of AISI 304L after electrochemical polishing directly below the notch (a) and further away from it (c). The corresponding inverse pole figures in z-direction (IPF-Z) are given in (b) and (d), respectively. White arrows highlight contaminations from the polishing step.



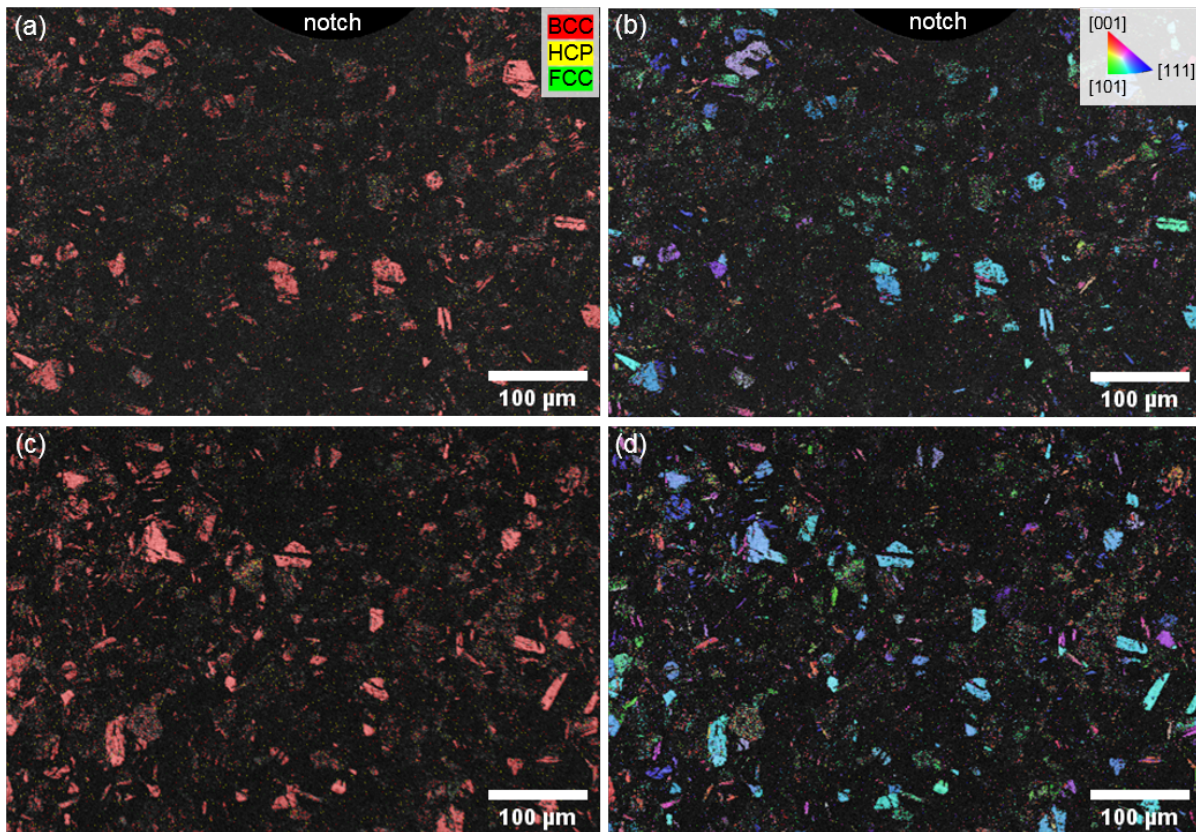


Figure A.18: *Phase and pattern quality maps of AISI 304L after 24 h of electrochemical charging and ToF-SIMS measurements directly below the notch (a) and further away from it (c). The corresponding inverse pole figures in z-direction (IPF-Z) are given in (b) and (d), respectively. Black pixels refer to measurement positions where none of the pre-defined phases could be indexed. The reason for the high number of damages on the surfaces remains unclear but is probably due to sample transport.*

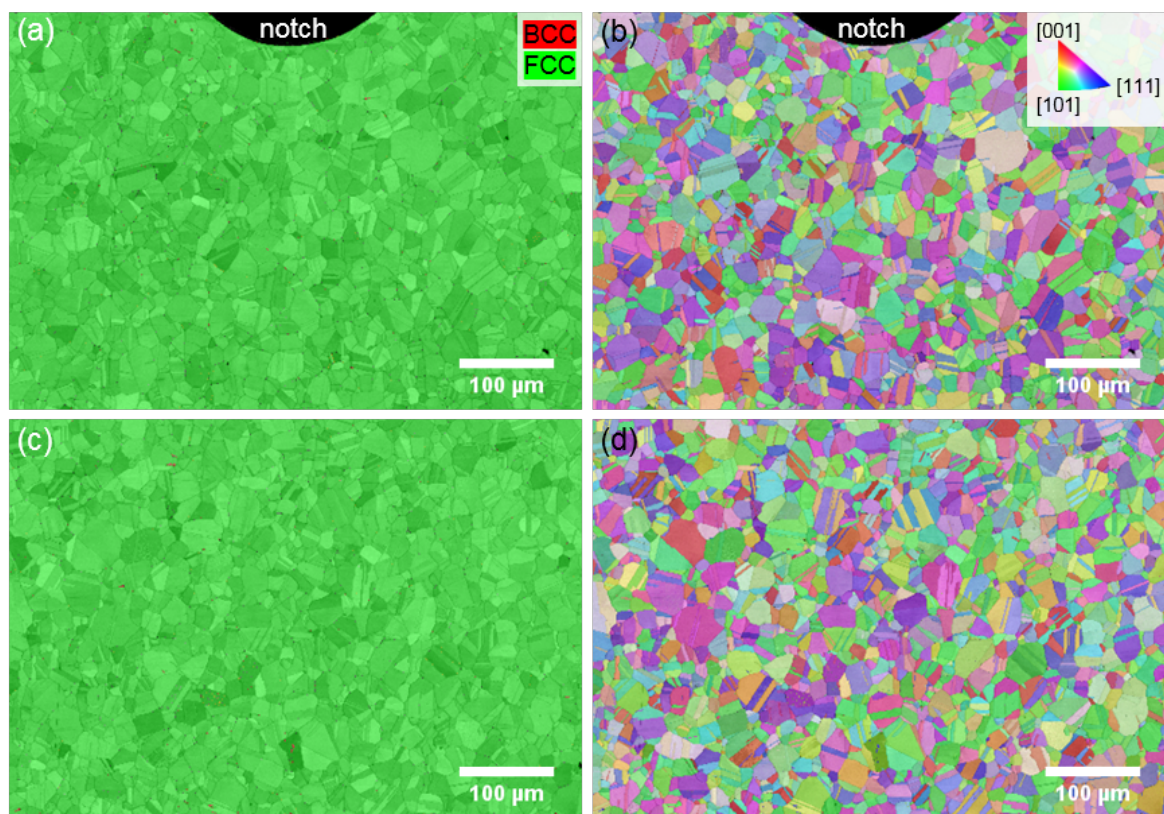


Figure A.19: Phase and pattern quality maps of AISI 304L after electrochemical polishing directly below the notch (a) and further away from it (c). The corresponding inverse pole figures in z-direction (IPF-Z) are given in (b) and (d), respectively.



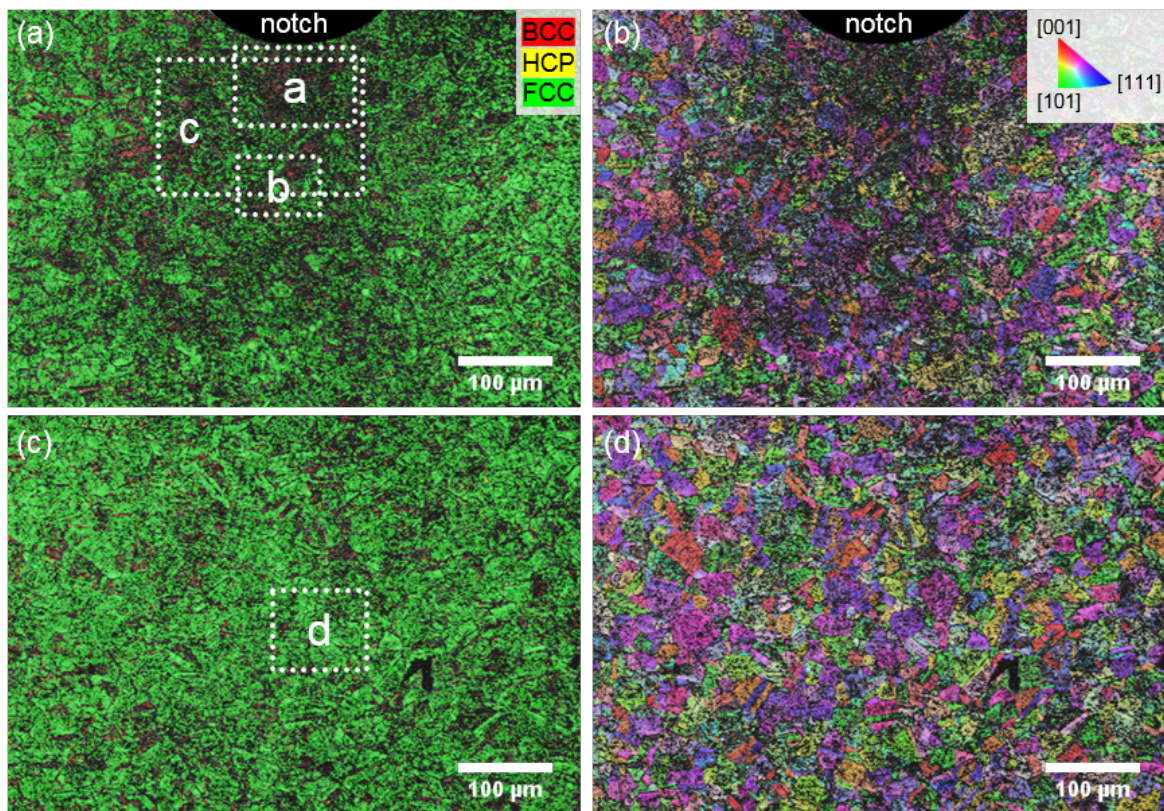


Figure A.20: Phase and pattern quality maps of AISI 304L after charging for 72 h and ToF-SIMS investigation. (a) shows the region directly below the notch, (c) a location farther from it. The corresponding inverse pole figures in z-direction (IPF-Z) are given in (b) and (d). The dotted squares indicate the location of higher magnified micrographs in Figure A.21.



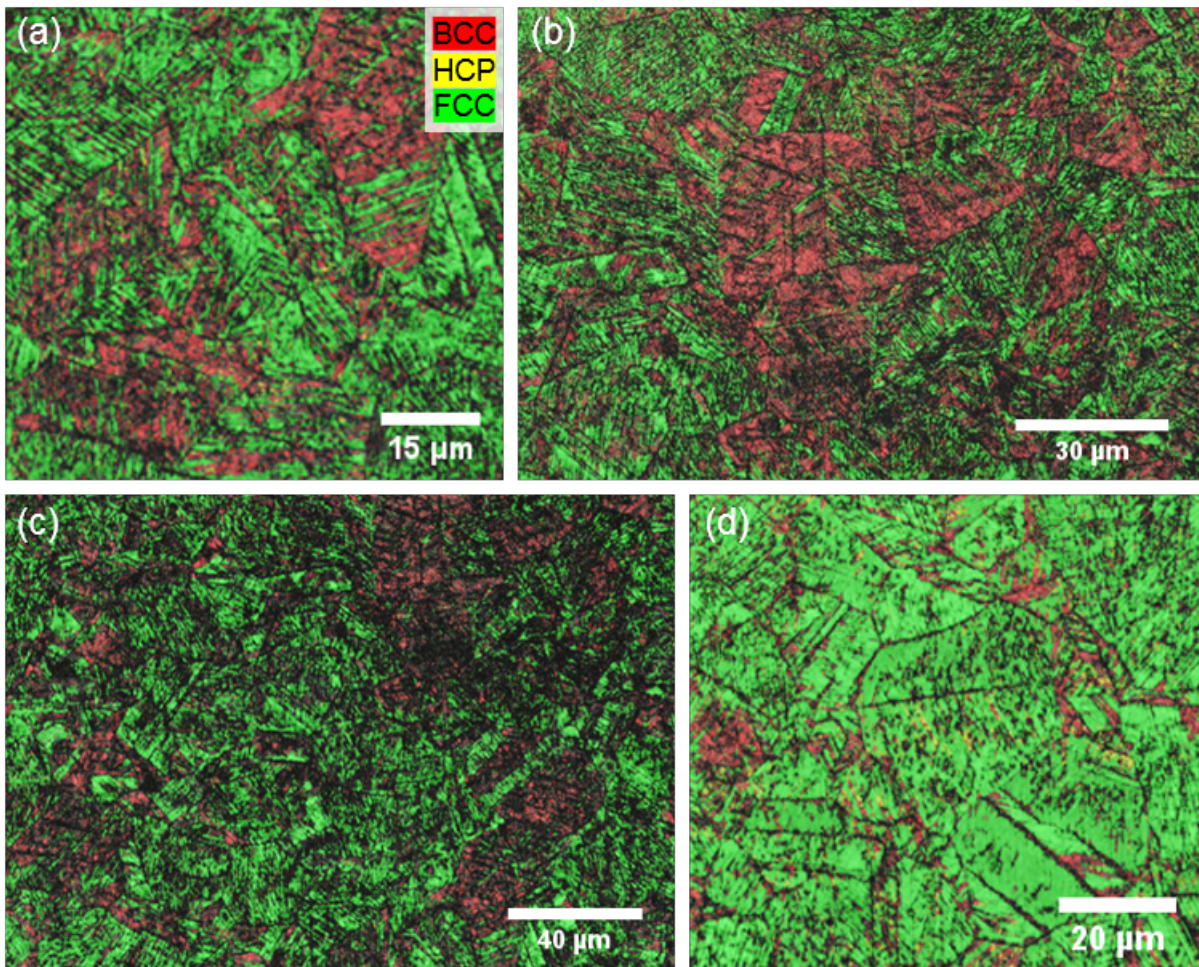


Figure A.21: *Higher-magnified micrographs of specific ROIs within the images shown Figure A.20.*



## AISI 316L

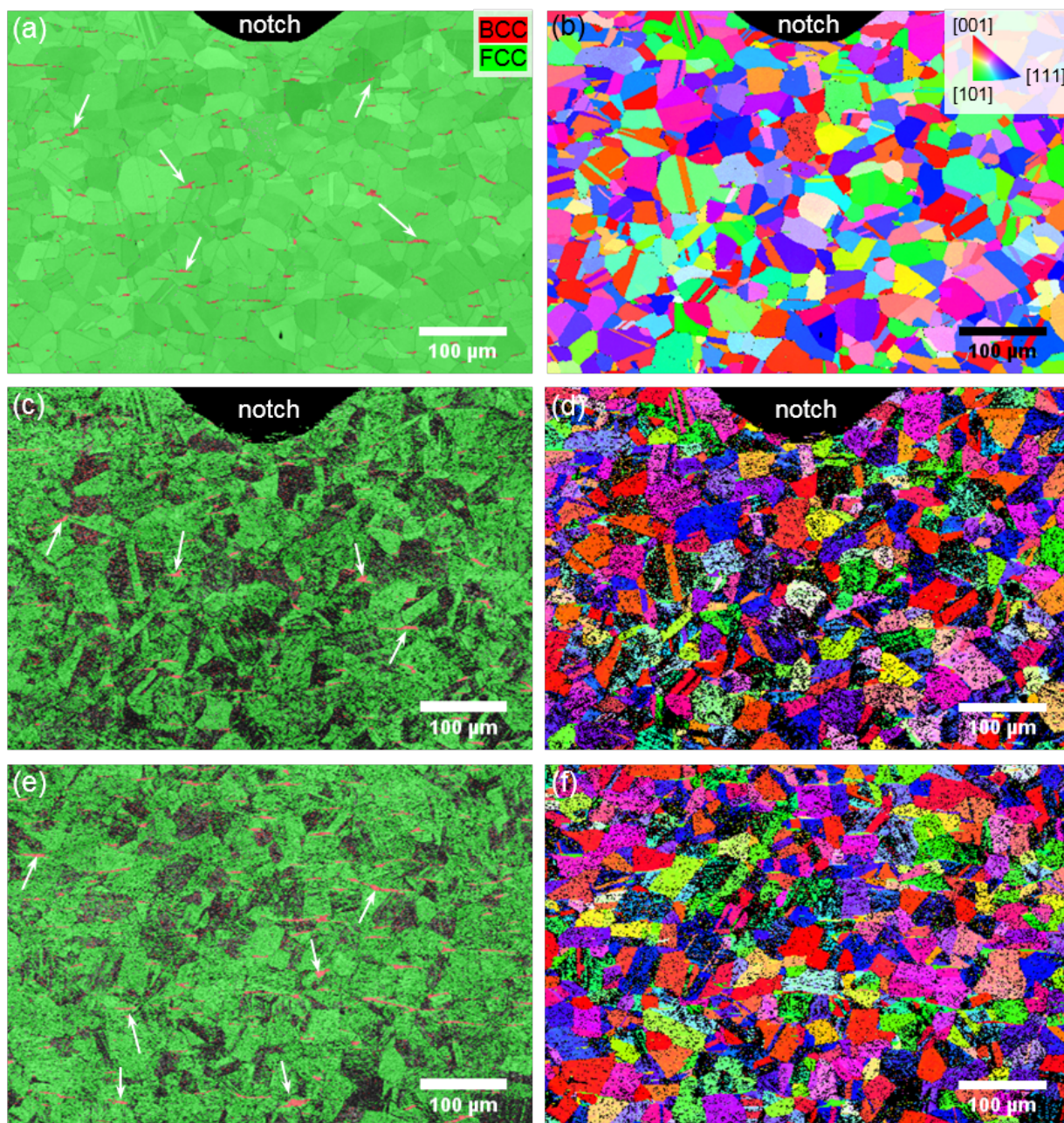


Figure A.22: Phase and pattern quality maps of AISI 316L before (a) and after electrochemical charging with deuterium for 72 h and ToF-SIMS analysis in (c) and (e). The corresponding inverse pole figures in  $z$ -direction (IPF-Z) are given in (b), (d) and (f). The white arrows indicate exemplarily the centre segregations. These developed during solidification after the continuous casting process. Black pixels refer to measurement positions where none of the pre-defined phases could be indexed.



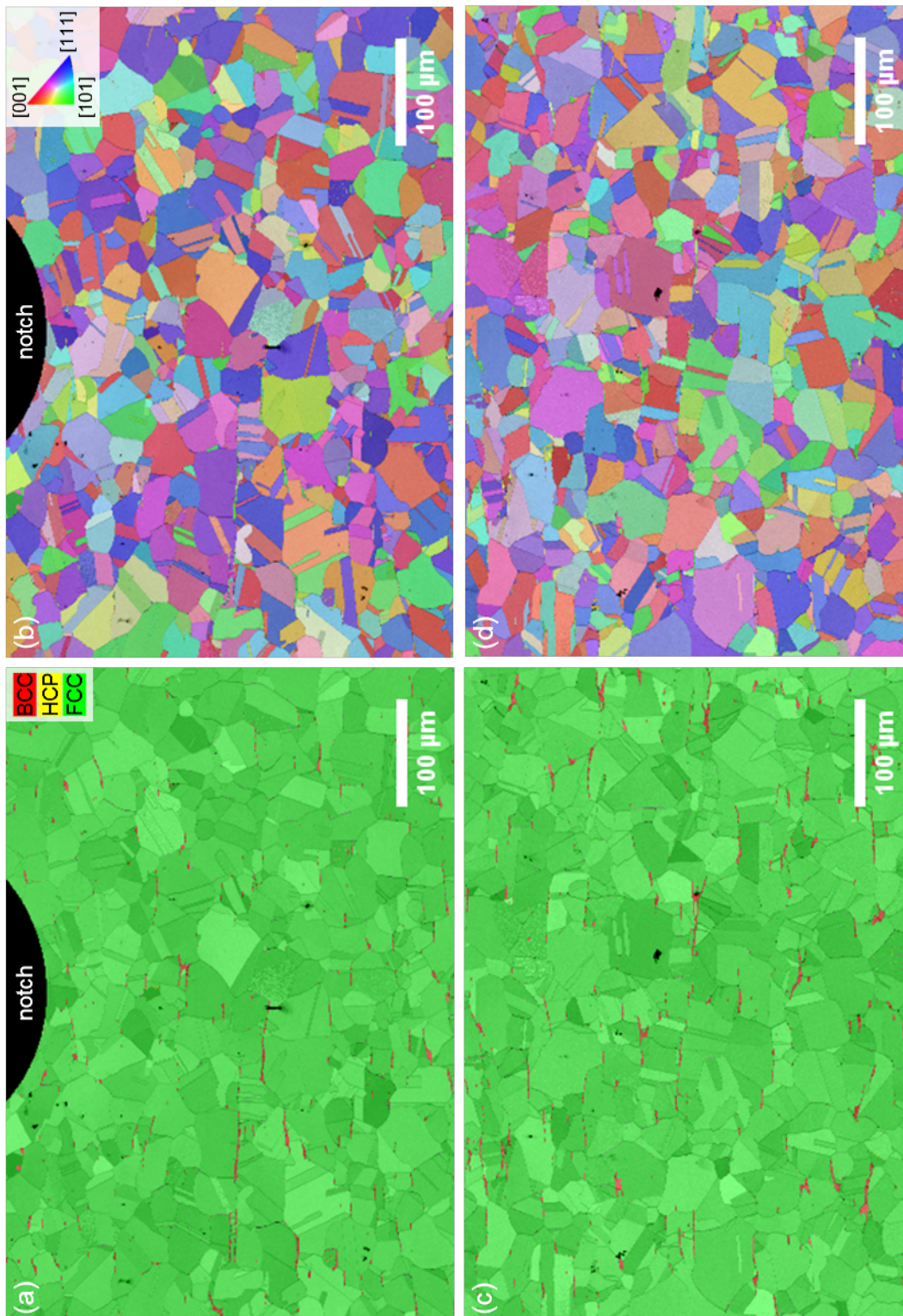


Figure A.23: Phase and pattern quality maps of AISI 316L directly below the notch (a) and farther from it (c). The corresponding inverse pole figures in  $z$ -direction (IPF-Z) are given in (b) and (d). Black pixels refer to measurement positions where none of the pre-defined phases could be indexed and are due to contaminations.



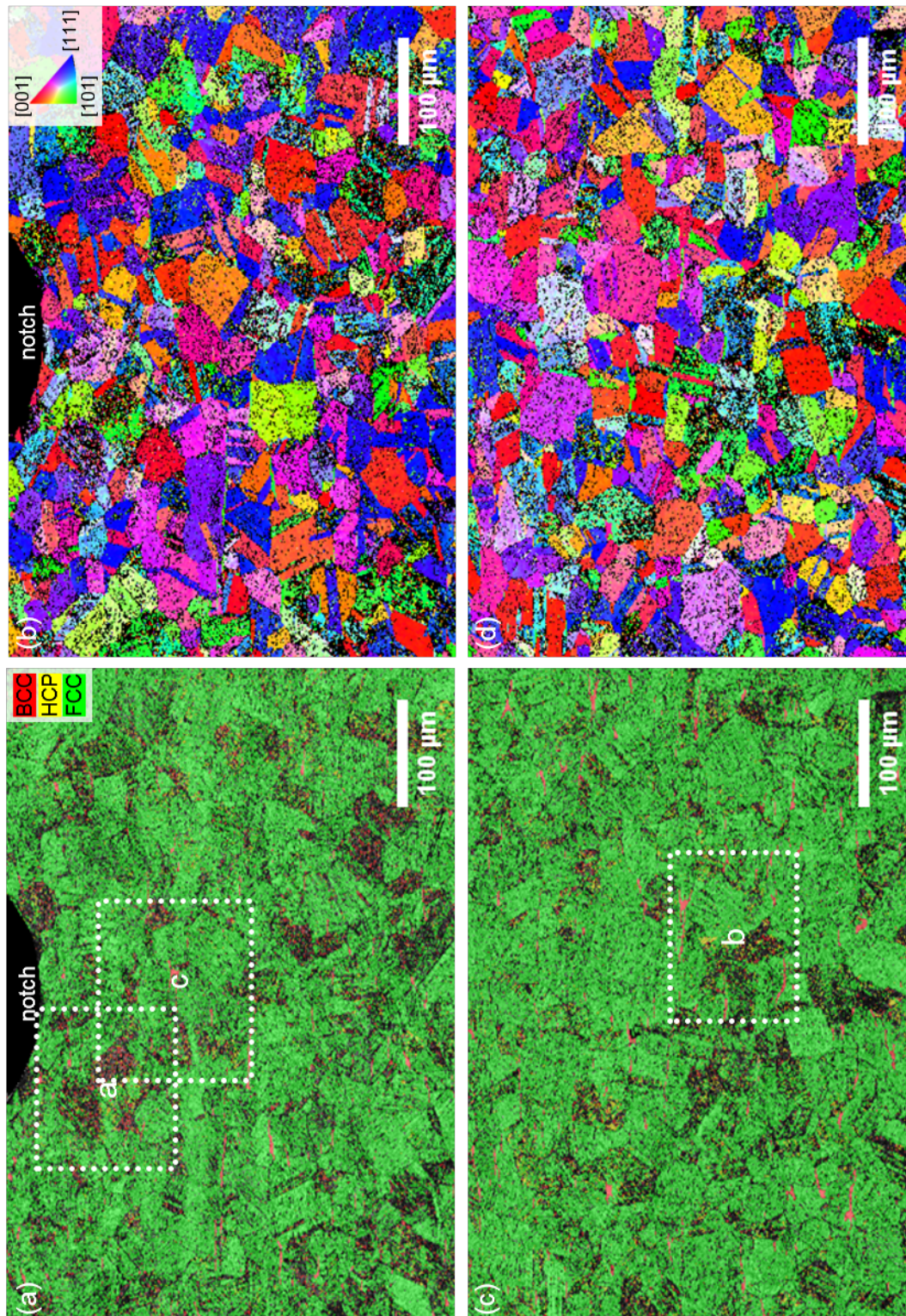


Figure A.24: Phase and pattern quality maps of AISI 316L of the same locations shown in Figure A.23 after electrochemical charging with deuterium for 72h and ToF-SIMS analysis in (a) and (c). The corresponding inverse pole figures in  $z$ -direction (IPF-Z) are given in (b) and (d). The white dotted squares marked with **a**, **b**, **c** indicate positions where high magnification measurements were taken. They are shown in Figure A.25.



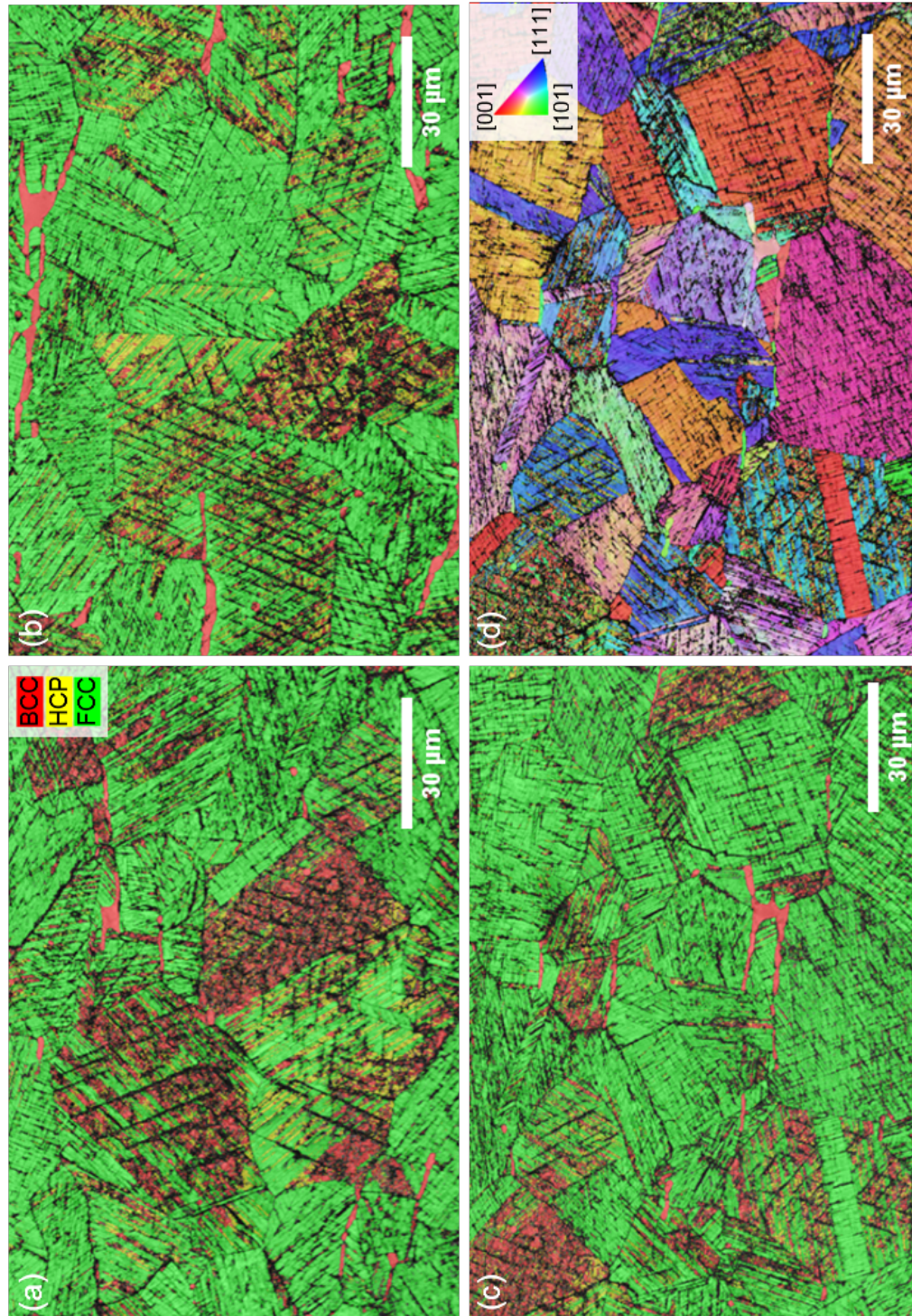


Figure A.25: Higher magnified phase and pattern quality maps of AISI 316L of the positions highlighted in Figure A.24 (a)-(c). The corresponding inverse pole figure in  $z$ -direction (IPF-Z) of (c) is given (d).



## A.4. ToF-SIMS results

## AISI 304L

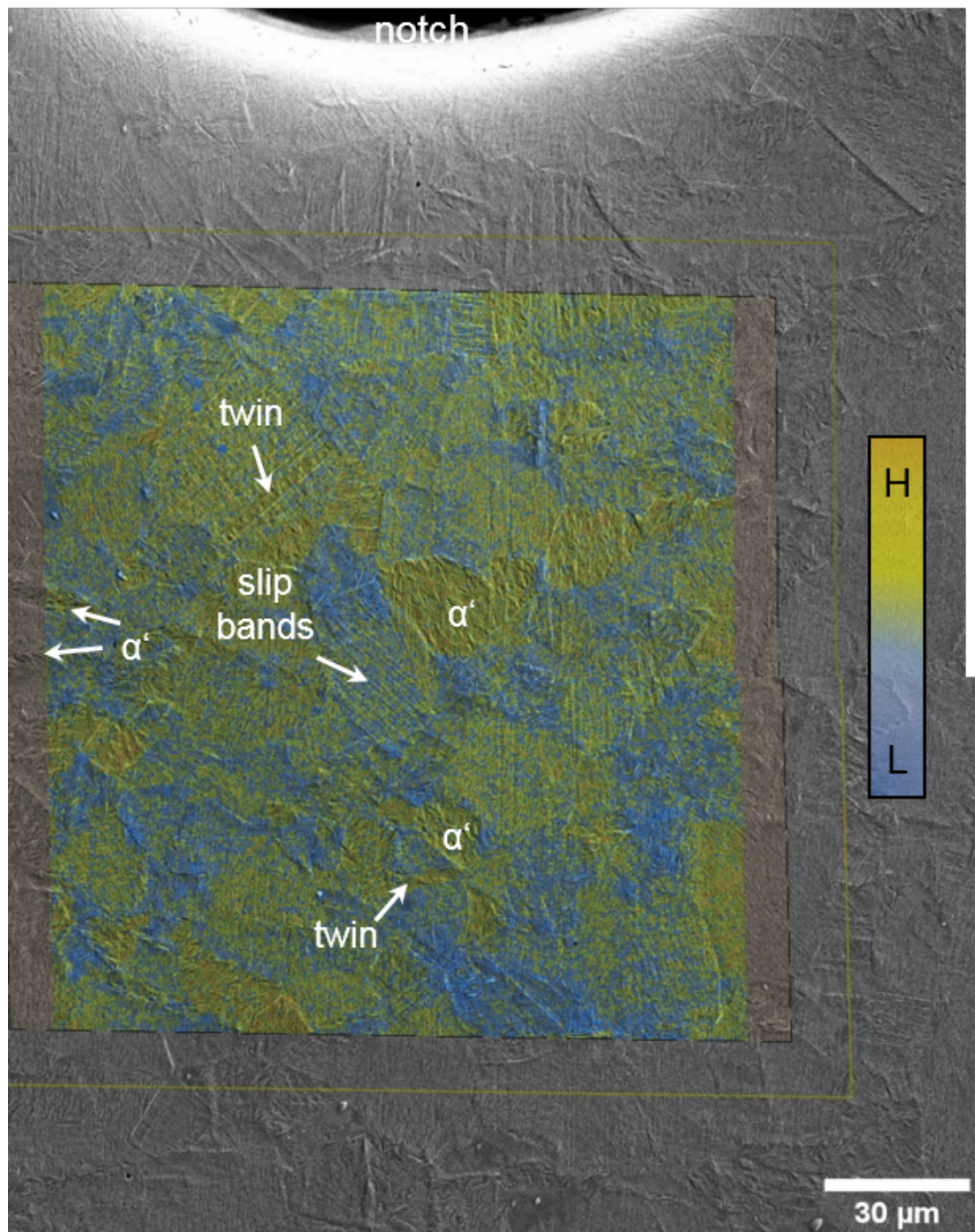


Figure A.26: Data fusion of a SEM micrograph and ToF-SIMS data of a sample charged for 24 h. Because the SEM images did not cover the complete ROI of the SIMS measurements, they were stitched. The distribution of deuterium and its covariants is given as the PC3. Some prominent features where deuterium was trapped are marked.

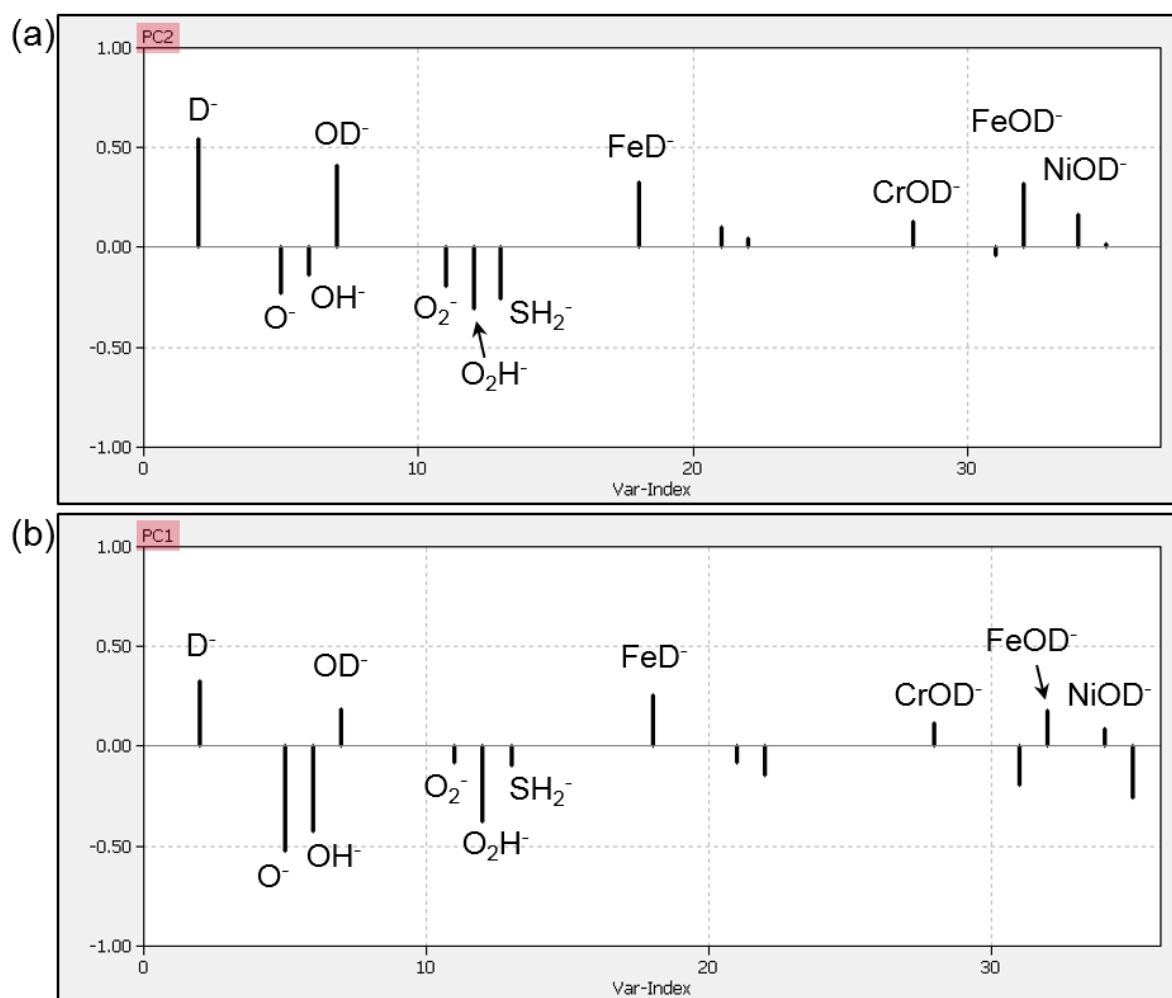


Figure A.27: Loadings plots of the PCA results that are depicted in Figure 6.36. (a) shows the results without external mechanical load as PC2 and (b) during mechanical load as PC1.

## AISI 316L

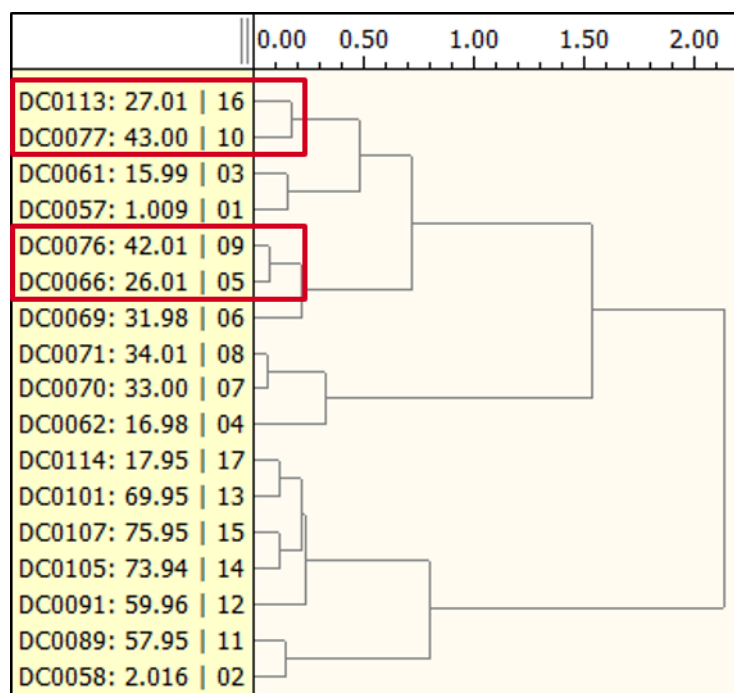


Figure A.28: Dendrogram of the hierarchical cluster analysis (HCA) from the corresponding image in Figure 6.29. The masses 27 ( $CNH^-$ ) and 43 ( $CNOH^-$ ) form a separate sub-branch from masses 26 ( $CN^-$ ) and 42 ( $CNO^-$ ) inside the main cluster. The presence of other masses like 32 ( $O_2^-$ ,  $S^-$ , resp.) within this main cluster can be explained with the surface contaminations.



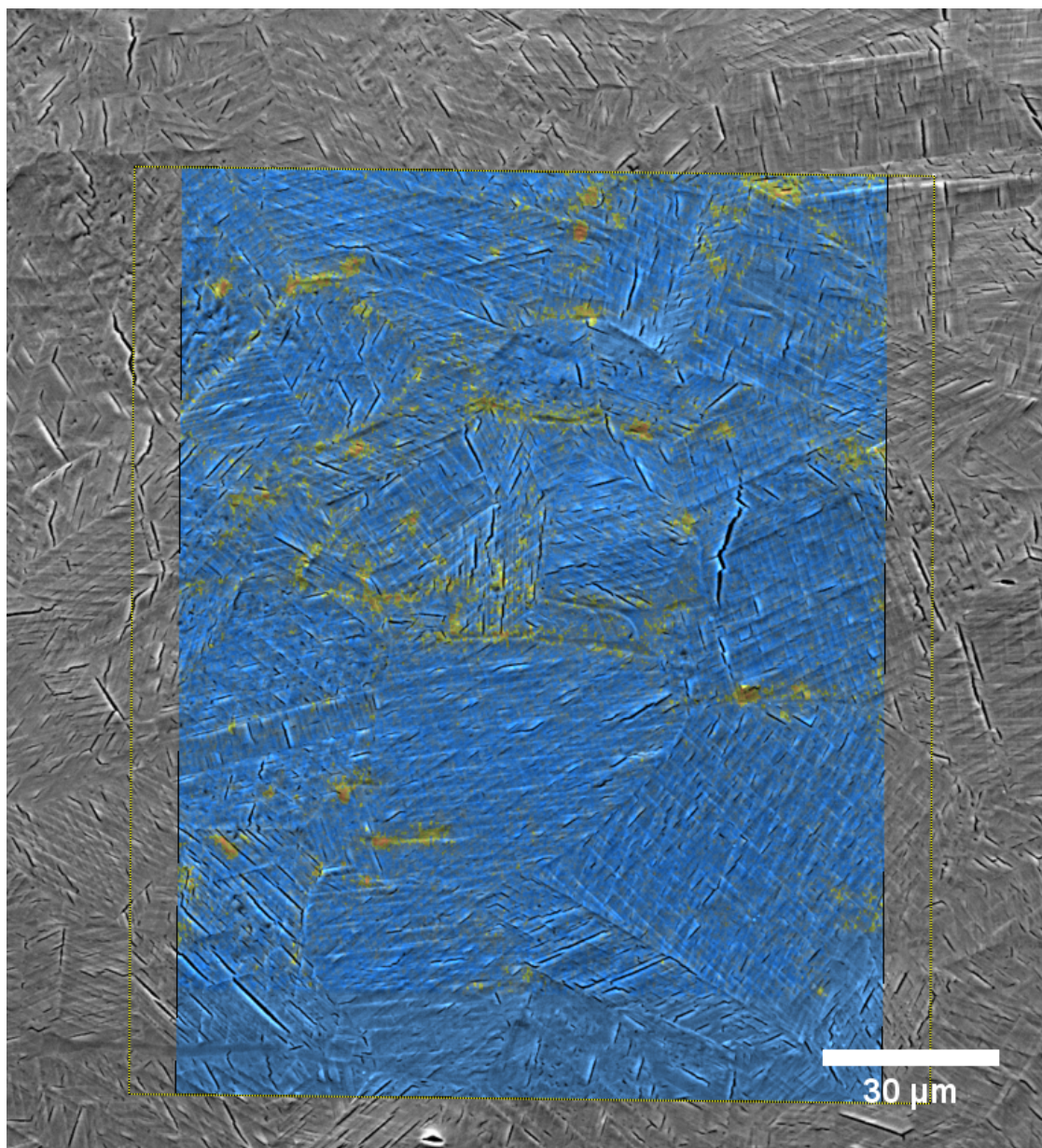


Figure A.29: *Data fusion of a SEM micrograph and SIMS data after electrochemical charging for 120 h. The signal of the fragment  $CNOH^-$  in AISI 316L is shown by bright colour. The notch is located approximately  $80\ \mu\text{m}$  above the SIMS image.*

---

## List of Figures

1.1. Hydrogen compressor unit as part of a hydrogen fuel station engineered by <i>Linde GmbH</i> and run by <i>H2 Mobility Deutschland GmbH &amp; Co. KG</i> [5]. Hydrogen is compressed up to 860 bar and pumped to the dispenser. All the piping is manufactured from austenitic stainless steel AISI 316. . . . .	2
2.1. The explosion of a hydrogen storage tank destroyed big parts of a factory, causing immense economic costs [8]. . . . .	4
2.2. Failure of a boiler tube as part of a power plant, investigated by Djukic <i>et al.</i> [9].	5
3.1. The iron-carbon phase diagram showing the areas of different phases in dependence of the temperature and carbon content. Note that the figure is simplified and not all constituents are labelled. Adapted from Merkel and Thomas [10]. . . . .	7
3.2. The extract of the left side of the Fe-C diagram shows (a) an enlarged, open $\gamma$ -area and (b) an extended, closed $\gamma$ -region, bordered by secondary phases. Figure according to Merkel and Thomas [10]. . . . .	10
3.3. Isothermal section of Fe-Cr-Ni phase diagram at 1100°C with the composition of the AISI 304 alloy marked. Figure according to Verhoeven [13]. . . . .	11
3.4. Classification of austenitic stainless steels regarding their chemical composition according to the <i>American Society for Metals</i> [28]. . . . .	12
3.5. Classification of metastable austenitic steels regarding the chemical composition and their resulting deformation behaviour. . . . .	13
3.6. Schematic stress-strain-curves of a TWIP, a TRIP and a steel without these hardening behaviours. . . . .	13
3.7. Schematic depiction of the temperature profile of Gibbs free energy as the main driving force for martensitic transformation. . . . .	15
3.8. Schematic depiction of the temperature regimes for athermal, stress-induced and strain-induced martensite formation, according to Wendler <i>et al.</i> [40]. . . . .	15
3.9. Sequence of the formation of intrinsic and extrinsic stacking faults in FCC materials according to De Cooman <i>et al.</i> [16]. . . . .	17
3.10. Description of BCC martensite (blue) within the FCC structure (black) in the ideal, undistorted unit cell. . . . .	18
3.11. Description of BCC martensite (blue) within the FCC structure (black) considering the movement of atomic planes and the resulting orientation relationships during martensitic transformation according to Bain, Pitsch, Nishiyama-Wassermann and Kurdjumov-Sachs. Note that the models possess more than the one given symmetry-equivalent variant. . . . .	19
3.12. Stress-strain curves of AISI 304 alloys after tensile tests at different temperatures. The dependence of the strain-hardening behaviour is obvious. According to Byun <i>et al.</i> [55]. . . . .	21
3.13. Possible sources for the ingress of hydrogen atoms into the material and their possible recombination at internal interfaces. Figure following Böllinghaus [78]. .	25

3.14. Schematic depiction of the adsorption and absorption process of hydrogen in acidic (a) and alkaline solutions (b). . . . .	26
3.15. A moving hydrogen-decorated dislocation (a) passes two obstacles (b) where part of the hydrogen cloud is stripped off. Pipe diffusion along the dislocation restores the atmosphere as dislocation moves further (c). According to Tien <i>et al.</i> [96]. . . . .	29
3.16. Octahedral and tetrahedral lattice sites in (a) FCC and (b) BCC structures of steels. The size of the respective interstices $d$ is given for every site. Figure according to Grong [104]. . . . .	30
3.17. Overview of different trapping sites in the microstructure of metals. Figure follows Koyama <i>et al.</i> [23]. . . . .	31
3.18. Important factors that influence hydrogen-assisted damages. . . . .	32
3.19. Reduction of mechanical tensile strength and ductility of the steel Fe-18Mn-1.2C in the presence of hydrogen [114]. . . . .	33
3.20. Electronic charge-density-difference contours for (a) a $\Sigma 3$ grain boundary (GB) and (b) the free surface (FS) in BCC iron. Blue colour indicates an electron deficit, red contours an excess of electrons. Figure taken from [135]. . . . .	37
3.21. Fracture surfaces of tensile specimen from AISI 304 steel with different hydrogen contents. A ductile-to-brittle transition occurs with higher amounts of hydrogen. Adapted from Au <i>et al.</i> [168]. . . . .	40
3.22. Schematic depiction of the liquid metal ion gun (LMIG) to generate, accelerate and focus a bismuth ion beam for analysis, adapted from <i>IONTOF GmbH</i> . . . . .	44
3.23. Schematic depiction of the different sputter regimes depending on the mass and kinetic energy of the primary ion. Scheme following Sigmund [186]. . . . .	45
3.24. Schematic depiction of the function of a time-of-flight detector. Primary ions hit the surface and sputter secondary ions with the masses $m_1 < m_2 < m_3 < m_4$ from the surface. They are extracted, pass the flight tube and hit the detector with a time offset that indicates their mass. . . . .	46
5.1. Optical micrographs of the investigated grades AISI 304L (a) and AISI 316L (b) after etching with Beraha II. White arrows mark ferritic and martensitic fractions that stem from the production process. They are not distinguishable from each other with the means of optical microscopy. . . . .	51
5.2. The Schaeffler-diagram plots the expected phases of steels depending on their nickel- and chromium-equivalent. The locations of the investigated materials are marked by dots. Figure according to Kotecki <i>et al.</i> [27]. . . . .	51
5.3. Sample dimensions for ex-situ (a) and in-situ experiments (b) in millimetres. . . . .	52
5.4. Schematic depiction of the sample preparation of the in-situ samples. . . . .	53
5.5. Schematic drawing of the facility for the electrochemical charging of the material with hydrogen and deuterium, respectively. . . . .	54
5.6. Detector unit of <i>Bruker</i> with the FSE detectors above and BSE detectors below. At the centre is the $e^-$ -flash <sup>HR</sup> system with the Kikuchi patterns schematised. Based on [218]. . . . .	56

---

5.7.	Sketch of the orientation distribution of the grains in a polycrystalline material and how to interpret inverse pole figures. The IPF-Z maps show the grain orientation parallel to the normal direction $\mathbf{z}$ of the material's surface. . . . .	57
5.8.	Depiction of the four-point-bending device used for the in-situ experiments in the ToF-SIMS, developed by Sobol [6]. . . . .	59
5.9.	Schematic depiction of the points of load transmission into the specimen. The plastic zone that might deploy under sufficient load is illustrated in red directly beneath the notch. Further, the directions of tensile ( $\sigma+$ ) and compressive ( $\sigma-$ ) stress within the in-situ specimen under load are shown. Dimensions are given in millimetres. . . . .	59
5.10.	Reproduction of the results of the finite element analysis of the grade AISI 304L under mechanical load with the software <i>Inkscape</i> . (a) shows the first principal strain and (b) the first principal stress $S1$ that reflect the highest strain and stress, respectively. These occur in x-direction, i.e. normal to the notch, when the specimen is bended. The original simulation was done by Dr. Tobias Mente with <i>ANSYS</i> [226]. . . . .	60
5.11.	Temperature profile for the CGHE measurements (red line) and the evolution of the ion current (blue line) representing hydrogen ions effusing from the sample. .	62
5.12.	Schematic depiction of a quadrupole mass spectrometer according to Salmi <i>et al.</i> [235]. . . . .	63
5.13.	Penetration depth (i.e. diffusion length) of deuterium during electrochemical charging for different charging times (cf. Chapter 3.2.2). The diffusion coefficients were taken from [90–92]. . . . .	64
6.1.	Optical micrographs of samples made from AISI 304L charged for (a) 24, (b) 48 and (c) 72 h with 0.05M $D_2SO_4$ and 0.01M $NaAsO_2$ as recombination poison. The sputter crater of the ToF-SIMS examinations is visible as a square in every image.	65
6.2.	Phase maps of AISI 304L before (a)+(b) sputtering and after sputtering with a 3keV $Cs^+$ -beam for 3 min (c) and 3.5 min (d), respectively. The dotted line margins the sputtered area. Black regions refer to areas where Kikuchi pattern (i.e. the diffraction patterns) could not be indexed. . . . .	67
6.3.	Overlay of phase and pattern quality maps of AISI 304L before (a) and after electrochemical charging for 48 h and SIMS analyses (c). The respective inverses pole figures in z-direction are given in (b) and (d). The surface of the specimen was sputtered with a 3keV $Cs^+$ -beam for 3 min before SIMS analyses. A white dotted frame margins the sputtered area. . . . .	69
6.4.	Evolution of the austenite fraction in dependence of the sputter time and the temperature regime. Every measurement spot was sputtered once to not accumulate damages. The sputter beam energy was <b>1 keV</b> . The inlet is a magnification of the graphs showing the alloy 316L sputtered at room temperature and $-80^\circ C$ . . . . .	72

---



---

6.5. Evolution of the austenite fraction in dependence of the sputter time and the temperature regime. Every measurement spot was sputtered once to not accumulate damages. The sputter beam energy was <b>3 keV</b> . . . . .	73
6.6. SEM images of the microstructure of the investigated steel AISI 304L (a) before and (b) after electrochemical charging for <b>24 h</b> . The respective phase distribution maps are displayed in (c) and (d). Red colour represents BCC-like phases ( $\delta$ -ferrite, martensite), while green-coloured areas indicate FCC phase. Black pixels refer to measurement positions with no solutions. The dotted lines in (c) highlight some grain and twin boundaries. . . . .	76
6.7. SEM images of microstructure of the investigated steel AISI 304L (a) before and (b) after electrochemical charging for <b>48 h</b> . (c) and (d) display the respective phase distribution maps collected by EBSD. Red colour represents BCC-like phases ( $\delta$ -ferrite, martensite), while green-coloured areas indicate FCC phase. Black pixels refer to measurement positions with no solutions. The dotted lines in (c) highlight some grain and twin boundaries. . . . .	77
6.8. Fusion of ToF-SIMS data and SEM images of the sample charged for (a) 24 and (b) 48 h, respectively. Depicted is the distribution of deuterium and its co-covariants as the principal component two (PC2). The colour bar represents the intensity of the deuterium signal, whereas orange means a relatively high and blue a relatively low intensity. . . . .	79
6.9. Evolution of internal mechanical stresses during electrochemical charging (a) and during outgassing (b). According to Mathias <i>et al.</i> [259] . . . . .	82
6.10. SEM micrographs of the surface of grades AISI 304L (a) and 316L (b) after electrochemical charging for 120 h. The dashed lines mark some grain boundaries and twin boundaries. Microscopic features such as cracks and slip bands are marked by arrows. . . . .	83
6.11. Sequence of hydrogen-assisted cracking in steels can be described by the formation of primary twins (a), the formation of grain boundary cracks due to loss of cohesive strength with concomitant cracking of primary twins and the formation of secondary twins (b) and finally the evolution of sub-cracks (c). Adapted from Koyama <i>et al.</i> [114]. . . . .	84
6.12. Phase and pattern quality maps of AISI 316L after preparation directly below the notch (a) and further away from it (c). The corresponding inverse pole figures in z-direction (IPF-Z) are given in (b) and (d). White arrows mark some of the <i>centre line segregations</i> that developed during solidification after the continuous casting process. . . . .	85

---

6.13. Phase and pattern quality maps of AISI 316L after electrochemical charging for 24 h and ToF-SIMS analysis in (a) and (c). The corresponding inverse pole figures in z-direction (IPF-Z) are given in (b) and (d). White squares labelled [a] and [b] mark positions where high-resolution images were taken from. These images are depicted in Figure 6.14. The white dotted line margins the region that was influenced by the sputter beam in the ToF-SIMS. . . . .	86
6.14. Phase and pattern quality maps of AISI 316L after electrochemical charging for 24 h and ToF-SIMS analysis. The images were taken from a sputtered (a) and a non-sputtered area (b) that are shown in Figure 6.13(a) and (c), respectively. . .	87
6.15. Phase and pattern quality maps of AISI 304L before (a) and after electrochemical charging for 48 h (c) and the corresponding inverse pole figures in z-direction (IPF-Z) in (b) and (d), respectively. Note that the sample was <i>not</i> polished electrochemically. The martensite fraction remained from the production process and was not fully removed by mechanical grinding. . . . .	89
6.16. Phase and pattern quality maps of AISI 304L after electrochemical polishing in (a) and (c) and the corresponding inverse pole figures in z-direction (IPF-Z) in (b) and (d). Black pixels refer to measurement positions where none of the pre-defined phases could be indexed. . . . .	90
6.17. Phase and pattern quality maps of AISI 304L after electrochemical charging for 72 h and ToF-SIMS analysis (a) and the corresponding inverse pole figure in z-direction (IPF-Z) in (b). The higher magnified ROIs, marked by dotted squares, are shown in (c) and (d). White arrows mark BCC phase that existed already <i>before</i> charging. . . . .	91
6.18. Image (a) shows the phase and pattern quality map of an un-sputtered area distant from the notch of the same sample shown in Figure 6.17. The white square indicates the location of the higher-magnified region in (b). . . . .	92
6.19. Phase and pattern quality maps of AISI 316L after electrochemical charging with deuterium for 72 h and ToF-SIMS analysis in (a) and (c). The corresponding inverse pole figures in z-direction (IPF-Z) are given in (b) and (d), respectively. White squares in (a) and (c) mark positions where high-resolution images were taken. These magnifications of a <i>sputtered</i> and <i>un-sputtered</i> area are shown in (e) and (f), respectively. White arrows indicate exemplary the centre line segregations. Black pixels refer to measurement positions where none of the pre-defined phases could be indexed. . . . .	93
6.20. Formation of deformation-induced martensite and mechanical twins in austenitic stainless steel in dependence of the nickel concentration and, thus, stacking fault energy. Adapted and extended from Tian <i>et al.</i> [264]. . . . .	94

6.21. Phase and pattern quality maps of AISI 304L before (a) and after electrochemical charging with deuterium for 120 h and ToF-SIMS analysis in (c) and (e). The corresponding inverse pole figures in z-direction (IPF-Z) are given in (b), (d) and (f). Higher magnified images of locations labelled with a-d are given in Figure 6.22. The white arrows indicate contaminations or damages on the surface that are due to sample preparation. Black pixels refer to measurement positions where none of the pre-defined phases could be indexed. . . . .	96
6.22. Higher magnification micrographs of selected areas in the phase maps shown in Figure 6.21 (c) and (e), respectively. ROIs (a) and (b) lie <i>within</i> the sputter crater, while (c) and (d) stem from the non-sputtered surface. White arrows indicate martensite or $\delta$ -ferrite that existed already <i>before</i> charging. . . . .	97
6.23. Phase and pattern quality maps of AISI 316L before (a) and after electrochemical charging with deuterium for 120 h and ToF-SIMS analysis in (c) and (e). The corresponding inverse pole figures in z-direction (IPF-Z) are given in (b), (d) and (f). The white arrows indicate exemplary the centre segregations. Black pixels refer to measurement positions where none of the pre-defined phases could be indexed. . . . .	99
6.24. Phase and pattern quality maps of the same sample as in Figure 6.23 in (a). Positions where high-resolution micrographs were taken are marked by white squares and shown in (b), (c) and (d). White arrows in (d) emphasise primary cracks that are located on slip bands and branch out into sub-cracks. Black pixels refer to measurement positions where none of the pre-defined phases could be indexed. . . . .	100
6.25. High resolution phase distribution and phase quality maps of AISI 316L after electrochemical charging with deuterium for 120 h and ToF-SIMS analysis. The micrographs stem from regions <i>outside</i> the areas shown in the overview in Figure 6.23 and therefore reflect un-sputtered material. Black pixels refer to measurement positions where none of the pre-defined phases could be indexed. White arrows indicate cracks rimmed by a small strip of austenite. . . . .	101
6.26. According to Cao <i>et al.</i> [267], absorption and diffusion of hydrogen in FCC materials is anisotropic. The present findings are in agreement with those findings.	102
6.27. Schmid's law (a), visualised by a cylinder model, describes the resulting shear stress when a tensile stress is applied. Some slip planes and directions in FCC structures are outlined in (b). Due to the translation symmetry of the cubic system, these are sufficient to describe the major slip systems. . . . .	103
6.28. Phase distribution maps of three samples made from AISI 316L after electrochemical charging for 72 h. Micrographs (a), (c) and (e) show ROIs directly underneath the notch that were <i>sputtered</i> , while (b), (d) and (f) show <i>un-sputtered</i> ROIs below. The white dotted line in (d) separates the image into a sputtered (above) and an un-sputtered region (below). The numbers give the fraction of austenite within the respective image. . . . .	106

---

6.29. Data fusion of a SEM micrograph and the signal of $\text{CNOH}^-$ in AISI 316L after 72 h of charging. The white circle indicates a region with the high intensity that is partially due to contaminations on the surface. The notch is visible in black at the bottom of the image. . . . .	109
6.30. Fusion of a SEM image and ToF-SIMS data (a) and phase and pattern quality maps (b) of AISI 304L after electrochemical charging for 48 h. The colour scale in (a) refers to the signal intensity of the $\text{D}^-$ and $\text{OD}^-$ fragments after PCA. A white square in (b) indicates the location of ROI analysed by SIMS; the arrow highlights slip bands and newly formed martensite. . . . .	112
6.31. Phase and pattern quality maps of the sputtered area below the notch of AISI 304L after electrochemical charging for 48 h (a) and fusion of a SEM image and ToF-SIMS data of the same ROI (b). It was sputtered for 2.5 min with a $3\text{ keV Cs}^+$ -beam. A white square in (a) and (b) indicates the location of ROI analysed by SIMS. The colour scale in (b) refers to the signal intensity of the $\text{D}^-$ and $\text{OD}^-$ fragments after PCA. . . . .	113
6.32. Data fusion of a SEM micrograph and ToF-SIMS data of a 304L steel sample charged for 72 h. The distribution of deuterium is reflected by PC2. The dotted line in (a) and (b) indicates the edges of SIMS and EBSD image. Dashed lines highlight special features such as grain and twins/sub-grain boundaries inside it. White arrows highlight accumulation of deuterium at grain and twin boundaries. . . . .	116
6.33. Phase distribution and corresponding inverse pole figure maps of AISI 304L before (a) and (b), respectively and after charging for 72 h and ToF-SIMS investigation in (c) and (d), respectively. The dotted square indicate the location of higher magnified micrographs in Figure 6.32(b). . . . .	117
6.34. Data fusion of a SEM micrograph and ToF-SIMS data of a sample charged for 72 h (a) and the phase distribution map in (b). The distribution of deuterium and its covariants is given as the PC3. The notch is visible as a black shadow at the bottom of (a). The white frame margins the location where the EBSD image stems from, white arrows indicate remains of $\epsilon$ -martensite. . . . .	119
6.35. The overlay of pattern quality (PQ) and phase distribution map of the sample <i>before</i> charging is shown in (a). The same region <i>after</i> electrochemical charging for 120 h and ToF-SIMS experiments is depicted in (b). The dotted frame in (b) indicates the magnified area within the field of analysis in (c). Dashed white lines indicate some locations where martensite newly formed. Black arrows highlight some pre-existing $\delta$ -ferrite islands whereas a white arrow marks slip bands. . . . .	121

---



- 
- 6.36. The overlay of an SEM micrograph and the SIMS data after PCA *before* (a) and *during* applying mechanical load (b). The distribution of deuterium and its covariant fragments is reflected as principal component two (PC2) in (a) and PC1 in (b). Brighter colours refer to a higher intensity of the signal. For a better orientation, the same regions as indicated in Figure 6.35(c) are marked here by dashed white lines too. The notch of the sample is located appr.  $85\ \mu\text{m}$  above the SIMS images. . . . . 123
- 6.37. Data fusion of a SEM micrograph and the distribution of deuterium in AISI 316L, reflected by PC3, after 120 hours of charging *without* (a) and *during* mechanical load applied (b). The dotted white lines indicate the location where the EBSD micrograph was taken. The dashed red line shows the location of a so-called *pixel mask*, whereas dashed white lines highlight grains with higher D-intensity *during* load. White arrows exemplary indicate newly formed martensite. Black arrows indicate newly formed martensite with a higher D-intensity *during* load. The notch is located approximately  $65\ \mu\text{m}$  above the SIMS image. . . . . 126
- 6.38. Phase distribution map (a) and inverse pole figure in z-direction (IPFZ) of a specimen made from AISI 316L grade after electrochemical charging for 120 h. Shown here is the same ROI as indicated by dotted white lines in Figure 6.37. White arrows mark newly formed deuterium-induced martensite grains with a relatively high intensity of the deuterium signal. For a better orientation, dashed white lines highlight the same grains as in Figure 6.37. . . . . 128
- 6.39. Schematic depiction of the stress distribution in front of a notch or a crack tip; the axis labels are adapted from Yokobori *et al.* [293]. The graph shows that the highest (tensile) stress builds up at the elastic-plastic interface. The main mechanisms for supporting hydrogen/deuterium movement are given for each regime. Blue dislocations represent deuterium-decorated dislocations. . . . . 129
- A.1. Phase and pattern quality maps of AISI 304L after sputtering with **3 keV**  $\text{Cs}^+$  at **-80°C** for (a) 10 s, (c) 30 s and (e) 60 s and the corresponding inverse pole figures in z-direction (IPF-Z) in (b), (d) and (f), respectively. Every ROI was sputtered only once in order to not accumulate the impact of the  $\text{Cs}^+$ -beam. The white arrows in (e) indicate sputter damages deliberately induced for navigation. . . . . i
- A.2. Phase and pattern quality maps of AISI 304L after sputtering with **3 keV**  $\text{Cs}^+$  at **-80°C** for (a) 120 s, (c) 210 s and (e) 300 s and the corresponding inverse pole figures in z-direction (IPF-Z) in (b), (d) and (f), respectively. Every ROI was sputtered only once in order to not accumulate the impact of the  $\text{Cs}^+$ -beam. . . . . ii
- A.3. Phase and pattern quality maps of AISI 304L after sputtering with **3 keV**  $\text{Cs}^+$  at **20°C** for (a) 10 s, (c) 30 s and (e) 60 s and the corresponding inverse pole figures in z-direction (IPF-Z) in (b), (d) and (f), respectively. Every ROI was sputtered only once in order to not accumulate the impact of the  $\text{Cs}^+$ -beam. The arrow in (e) indicates a sputter damage deliberately induced for navigation. . . . . iii
-



---

A.12.Phase and pattern quality maps of AISI 316L after sputtering with <b>1 keV</b> Cs <sup>+</sup> at <b>20°C</b> for (a) 10 and 30 s, (c) 210 and 300 s and the corresponding inverse pole figures in z-direction (IPF-Z) in (b) and (d), respectively. Every ROI was sputtered only once in order to not accumulate the impact of the Cs <sup>+</sup> -beam. The dotted frames indicate the sputtered regions. . . . .	xii
A.13.SEM micrographs of alloy grade 304L after electrochemical charging for 72 h. Some prominent features are highlighted. . . . .	xiii
A.14.SEM micrographs of alloy grade 304L after electrochemical charging for 72 h. Some prominent features are labelled. The dashed black line indicates grain and twin boundaries. . . . .	xiv
A.15.SEM micrographs of alloy grade 316L after electrochemical charging for 24 h. Some prominent features are labelled. The dashed black line indicates grain and twin boundaries. . . . .	xv
A.16.SEM micrographs of alloy grade 316L after electrochemical charging for 120 h. Some prominent features are highlighted. . . . .	xvi
A.17.Phase and pattern quality maps of AISI 304L after electrochemical polishing directly below the notch (a) and further away from it (c). The corresponding inverse pole figures in z-direction (IPF-Z) are given in (b) and (d), respectively. White arrows highlight contaminations from the polishing step. . . . .	xvii
A.18.Phase and pattern quality maps of AISI 304L after 24 h of electrochemical charging and ToF-SIMS measurements directly below the notch (a) and further away from it (c). The corresponding inverse pole figures in z-direction (IPF-Z) are given in (b) and (d), respectively. Black pixels refer to measurement positions where none of the pre-defined phases could be indexed. The reason for the high number of damages on the surfaces remains unclear but is probably due to sample transport.	xviii
A.19.Phase and pattern quality maps of AISI 304L after electrochemical polishing directly below the notch (a) and further away from it (c). The corresponding inverse pole figures in z-direction (IPF-Z) are given in (b) and (d), respectively. .	xix
A.20.Phase and pattern quality maps of AISI 304L after charging for 72 h and ToF-SIMS investigation. (a) shows the region directly below the notch, (c) a location farther from it. The corresponding inverse pole figures in z-direction (IPF-Z) are given in (b) and (d). The dotted squares indicate the location of higher magnified micrographs in Figure A.21. . . . .	xx
A.21.Higher-magnified micrographs of specific ROIs within the images shown Figure A.20.	xxi
A.22.Phase and pattern quality maps of AISI 316L before (a) and after electrochemical charging with deuterium for 72 h and ToF-SIMS analysis in (c) and (e). The corresponding inverse pole figures in z-direction (IPF-Z) are given in (b), (d) and (f). The white arrows indicate exemplary the centre segregations. These developed during solidification after the continuous casting process. Black pixels refer to measurement positions where none of the pre-defined phases could be indexed. .	xxii

---

- 
- A.23. Phase and pattern quality maps of AISI 316L directly below the notch (a) and farther from it (c). The corresponding inverse pole figures in z-direction (IPF-Z) are given in (b) and (d). Black pixels refer to measurement positions where none of the pre-defined phases could be indexed and are due to contaminations. . . . . xxiii
- A.24. Phase and pattern quality maps of AISI 316L of the same locations shown in Figure A.23 after electrochemical charging with deuterium for 72 h and ToF-SIMS analysis in (a) and (c). The corresponding inverse pole figures in z-direction (IPF-Z) are given in (b) and (d). The white dotted squares marked with **a**, **b**, **c** indicate positions where high magnification measurements were taken. They are shown in Figure A.25. . . . . xxiv
- A.25. Higher magnified phase and pattern quality maps of AISI 316L of the positions highlighted in Figure A.24 (a)-(c). The corresponding inverse pole figure in z-direction (IPF-Z) of (c) is given (d). . . . . xxv
- A.26. Data fusion of a SEM micrograph and ToF-SIMS data of a sample charged for 24 h. Because the SEM images did not cover the complete ROI of the SIMS measurements, they were stitched. The distribution of deuterium and its covariants is given as the PC3. Some prominent features where deuterium was trapped are marked. . . . . xxvi
- A.27. Loadings plots of the PCA results that are depicted in Figure 6.36. (a) shows the results *without* external mechanical load as PC2 and (b) *during* mechanical load as PC1. . . . . xxvii
- A.28. Dendrogram of the hierarchical cluster analysis (HCA) from the corresponding image in Figure 6.29. The masses 27 ( $\text{CNH}^-$ ) and 43 ( $\text{CNOH}^-$ ) form a separate sub-branch from masses 26 ( $\text{CN}^-$ ) and 42 ( $\text{CNO}^-$ ) inside the main cluster. The presence of other masses like 32 ( $\text{O}_2^-$ ,  $\text{S}^-$ , resp.) within this main cluster can be explained with the surface contaminations. . . . . xxviii
- A.29. Data fusion of a SEM micrograph and SIMS data after electrochemical charging for 120 h. The signal of the fragment  $\text{CNOH}^-$  in AISI 316L is shown by bright colour. The notch is located approximately  $80 \mu\text{m}$  above the SIMS image. . . . . xxix



---

**List of Tables**

3.1. Influence of alloying elements on the phase stability [10]. . . . .	6
3.2. Stacking fault energies in metastable austenitic steels and their influence on the deformation behaviour. . . . .	20
3.3. Trapping sites for hydrogen in metallic alloys and the respective activation energy needed for de-trapping. . . . .	32
3.4. Overview of hydrogen mapping techniques [175–179]. . . . .	42
5.1. Chemical composition of the investigated materials according to the supplier and measured by an optical emission spectrometer (OES). All values are given in wt.-%.	50
5.2. Juxtaposition of the different sample preparation techniques that were tested in the scope of the present work. . . . .	53
5.3. Parameters of the electrochemical charging processes. . . . .	54
6.1. Calculated amount of hydrogen from the CGHE measurements in AISI 304L after charging for 24 and 48 h, respectively. All values are given in <i>ppm</i> . . . . .	66
6.2. Details of the sputter tests on the grades AISI 304L and 316L. Both procedures were done at room temperature and -80°C, respectively. . . . .	69
6.3. Calculated $M_{d30}$ -temperatures and determined ASTM grain size numbers of the AISI 304L and 316L steel grades, respectively. For the calculation both the chemical composition given by the supplier and the composition determined by OES were used. . . . .	70
6.4. Stacking fault energies of the AISI 304L and 316L steel grades, respectively. For the calculation both the chemical composition given by the supplier and the composition determined by OES were used. The underlying equations were taken from [40, 48]. . . . .	70
6.5. Critical values of sputter times, energies and temperatures that can act as guideline for further experiments. . . . .	75
6.6. Angles between planes and directions in cubic crystal systems. . . . .	100

## List of Publications

### Poster Presentations

Röhslers, A., Sobol, O., Nolze, G., Unger, W.E.S., Böllinghaus, Th.; *The use of time-of-flight secondary ion mass spectrometry for the investigation of hydrogen-induced effects in austenitic steel AISI 304L*. The 21st International Conference on Secondary Ion Mass Spectrometry (2017)

Röhslers, A., Sobol, O., Nolze, G., Unger, W.E.S., Böllinghaus, Th.; *In-situ observation of the hydrogen behaviour in austenitic stainless steel by time-of-flight secondary ion mass spectrometry during mechanical loading*. International Conference on Metals and Hydrogen SteelyHydrogen2018 (2018)

Röhslers, A., Sobol, O., Nolze, G., Böllinghaus, Th. Unger, W.E.S.; *Analysis of deuterium in austenitic stainless steel AISI 304L by Time-of-Flight Secondary Ion Mass Spectrometry*. SIMS Europe 2018 (2018)

### Papers

Röhslers, A., Sobol, O., Nolze, G., Unger, W.E.S., Böllinghaus, Th.; *The use of time-of-flight secondary ion mass spectrometry for the investigation of hydrogen-induced effects in austenitic steel AISI 304L*. Journal of Vacuum Science & Technology B, Nanotechnology and Microelectronics: Materials, Processing, Measurement and Phenomena **36**, 03F103 (2018)

Sobol, O., Röhslers, A., Straub, F., Nolze, G., Saliwan-Neumann, R., Eliezer, D., Böllinghaus, Th., Unger, W.E.S.; *Deuterium assisted cracking in standard and lean duplex stainless steels: A ToF-SIMS and EBSD study*. Proceedings of the Third International Conference on Metals and Hydrogen SteelyHydrogen2018, **H02** (2018)

Röhslers, A., Sobol, O., Unger, W. E. S., Böllinghaus, Th. *Comprehensive study of deuterium-induced effects in austenitic stainless steel AISI 304L*. International Journal of Hydrogen Energy, **44**, 12228-12238, (2019)

Röhslers, A., Sobol, O., Hänninen, H., Böllinghaus, Th. *In-situ ToF-SIMS analyses of deuterium re-distribution in austenitic steel AISI 304L under mechanical load* Scientific Reports 10, (2020).